UNIVERSITY OF CALIFORNIA
RIVERSIDE

Development and Optimization of Magnesium Alloys and Oxide Surface Treatments for Orthopedic Implant Applications

A Dissertation submitted in partial satisfaction
of the requirements for the degree of

Doctor of Philosophy

in

Bioengineering

by

Aaron Franco Cipriano

March 2016

Dissertation Committee
Dr. Huinan Liu, Chairperson
Dr. Valentine Vullev
Dr. Masaru Rao

The Dissertation of Aaron Franco Cipriano is approved:

Committee Chairperson

University of California, Riverside

Acknowledgements

A heartfelt THANK YOU to all the individuals who provided inspiration, guidance, and support to make possible this dissertation and enable my growth as a scientist:

My advisor, Dr. Huinan Liu, for her guidance and incessant support throughout my graduate school experience. As my Ph.D. advisor, she encouraged me and gave me the freedom to actively pursue collaborations as well as identify new exciting opportunities for biomaterials research. I admire her vision and fierce dedication to facilitate the clinical translation of novel biomaterials.

The Biomaterials and Nanomedicine research group. To the 2011/2012 members – Jackie, Ian, Maria, Meriam, Yen – for welcoming a younger and unexperienced version of me and for teaching me many of the tools and methods that helped me throughout my dissertation work. To the 2012-2015 members, thank you for your friendship and support, and for making the days spent in lab enjoyable. I hope to see each one of you grow into the scientists you aspire to be.

My dissertation committee at UC Riverside, Dr. Valentine Vullev and Dr. Masaru Rao, for kind support and invaluable advice during the yearly meetings. Also, Dr. Ren-Guo Guan (Northeastern U), Dr. Yufeng Zhang (Peking University), Dr. Serkan Inceglou, (LLU), Dr. Gary Botimer, (LLU), Dr. David Carter (UC Riverside), Dr. Krassimir Bozhilov (UC Riverside), Dr. Jon Wergedal (VA Hospital, Loma Linda), and Nancy Lowen (VA Hospital, Loma Linda) for collaborating and/or their

advice that led to the successful completion of one or more aspects in this dissertation.

All of the undergraduate and intern students with whom I had the pleasure to work with and mentor, and who in large part helped me complete the work described herein: Amy Sallee, Christopher Miller, Belinda Le, Myla Tayoba, Jorge Sanchez, Marisa Lopez, Alan Lin, Mayra Cortez, Idalia Ramirez, and Pedro Soria, Jr.

The UC Riverside Dissertation Year Program (DYP) for funding; the Stem Cell Center at UC Riverside for support; and, the Central Facility for Advanced Microscopy and Microanalysis (CFAMM) and Institute for Integrative Genome Biology (IIGB) at UC Riverside for instrument use.

Finally, my family in California – Carlos, Ruth, Carlos, Beto – I am forever indebted for giving me a home away from home.

The text of this dissertation, in part, is a reprint of the material as it appears in:

Cipriano AF, et al. Preparation, degradation, and cytocompatibility of anodically oxidized MgO surface treatments for biomedical applications. *In preparation*, 2016.

Cipriano AF, et al. The in vivo degradation of as-drawn Mg-4Zn-1Sr intramedullar pins and associated peri-implant bone remodeling in the rat tibia. *In preparation*, 2016.

Cipriano AF, et al. A comparative study on the degradation of Mg-4Zn-xSr alloys and their cytocompatibility using the direct culture method. *In preparation*, 2016.

Cipriano AF, et al. Cytocompatibility and Early Inflammatory Response of Human Endothelial Cells in Direct Culture with Mg-Zn-Sr Alloys. Submitted to *Acta Biomaterialia*, 2016.

Cipriano AF, et al. Investigation on Magnesium-Zinc-Calcium alloys and bone marrow derived mesenchymal stem cell responses in direct culture. *Acta Biomaterialia*. 12(1): 298-321, 2015.

Cipriano AF, et al. In vitro degradation of four Magnesium-Zinc-Strontium alloys and their cytocompatibility with human embryonic stem cells. *Journal of Materials Science: Materials in Medicine*. 24(4): 989-1003, 2013.

Dedication

I dedicate this dissertation to my family,

To my wife, Natalie, for being my best friend, confidant, partner in crime, mother to Nallie and Mango, and for making me smile when I needed it the most.

To my parents, Cruz y Ruby Cipriano, for their unwavering support, for teaching me the value of good education and hard work, and for instilling in me quality values.

To my brother, Dr. Bani H. Cipriano, for being the best older brother I could ask for and for being a role model in life.

I love you all.

Riverside, CA. February, 2016.

ABSTRACT OF THE DISSERTATION

Development and Optimization of Magnesium Alloys and Oxide Surface Treatments for Orthopedic Implant Applications

by

Aaron Franco Cipriano

Doctor of Philosophy, Graduate Program in Bioengineering
University of California, Riverside, March 2016
Dr. Huinan Liu, Chairperson

The potential of Magnesium (Mg)-based temporary biodegradable metallic implants relies most heavily on the mechanical and electrochemical properties of Mg, as well as on the fact that the human body contains a large amount of Mg ions and can effectively metabolize the degradation products of Mg. To realize the benefits of Mg for orthopedic fixation device applications, however, it is critical to engineer the rate of Mg degradation in the body based on end-goal design specifications. Firstly, we developed and studied Mg-xZn-0.5Ca alloys, Mg-4Zn-xSr alloys, and anodically oxidized surface treatments, all of which present innovative strategies to engineer the corrosion rates, mechanical properties, and/or improve cell-biomaterial interactions to meet clinical requirements. Secondly, we developed and implemented physiologically relevant *in vitro* models to evaluate cellular responses at the cell-biomaterial interface between various mammalian cell types and Mg-based biomaterials. Optimization of the methods allowed us to identify key aspects that influence Mg degradation *in vitro* and cellular responses to concomitant degradation products, thereby providing more

comprehensive *in vitro* method for examining and screening bioresorbable materials compared with current standards. Lastly, we evaluated for the first time the *in vivo* degradation and host-response to Mg-4Zn-1Sr alloys, not only to evaluate and optimize performance of our novel materials, but also to identify factors that affect degradation and bridge the existing gap between *in vitro* and *in vivo* measurements of Mg-based biomaterials. Collectively, the results and conclusions of this dissertation supported the promising potential of bioresorbable Mg-based biomaterials for musculoskeletal implant applications. It is likely that the solution that enables clinical translation of Mg-based biomaterials will be a combination of biomedical-designed alloys and surface treatments/coatings. Furthermore, this dissertation provided design guidelines and *in vitro* tools to screen and optimize: alloy composition, degradation rates, cytocompatibility, and cellular responses at the cell-biomaterial interface to fine tune Mg-based biomaterials for specific implant applications.

Table of contents

List of figures

List of tables

Chapter 1 - Introduction

1.1. Magnesium-based biodegradable implants and the rapid degradation in physiological fluids

Magnesium (Mg)-based biomaterials specifically designed for biodegradable implant applications have been the focus of biomedical research since the early 2000s [1-3]. Mechanical and electrochemical properties of Mg make these metallic biomaterials superior candidates, compared with currently used materials, for temporary biodegradable implants in multiple biomedical applications [1-4]. Titanium (Ti) alloy orthopedic implants, which are widely used, are limited by: stress shielding on surrounding bone; necessity of revision surgeries for implant removal; distortion on post-operative evaluation by magnetic resonance imaging (MRI); and, release of harmful wear particulates which have been associated with long-term implant loosening and failure [5-8]. Likewise, bioabsorbable polymer-based orthopedic implants, an alternative to permanent metallic implants, are limited by: lack of mechanical strength needed for load bearing implants [9]; breakage during surgery (and associated patient complications) [10-18]; and, acidic degradation products which can lead to tissue inflammation [19]. In contrast, Mg-based implants have mechanical properties that more closely approximate those of human cortical bone, they are also biodegradable, biocompatible, osteoconductive, and have anti-bacterial properties [1-3, 20, 21]. Most notable is the fact that the human body contains a large amount of Mg ions and can

effectively metabolize the degradation products of Mg [1-3]. Specifically, Mg is one of the most abundant cations in intracellular and extracellular fluids in the body and is essential for bone and tooth formation. The level of Mg in the extracellular fluid ranges between 0.7 and 1.05 mM, where homeostasis is maintained by the kidney and intestine [22]. Therefore, temporary biodegradable metallic implants are idealized to be superior alternatives to permanent implants in that they would eliminate the need for implant removal surgeries following healing of the damaged tissue. By doing so, Mg-based biodegradable implants could reduce the burden on the healthcare system by mitigating risks and costs [23, 24].To realize the benefits of Mg for medical implant applications, however, it is critical to control the rate of Mg degradation (i.e. corrosion) in the body. The informed reader is directed to the following review articles that discuss in detail the mechanisms and factors that affect Mg alloy corrosion [25, 26].

1.2. Solutions to address the rapid degradation of Mg for biomedical applications

Late 20th-century automotive and defense industries drove improvements in metallurgical processing and allowed for the development and wide-spread implementation of die-cast Mg alloys (i.e. Mg-9Al-1Zn, wt. %; AZ91) with superior corrosion resistance and mechanical performance [27, 28]. Further motivation to increase the corrosion resistance of Mg-based materials for structural applications led to the development of coatings and surface treatments, including:

electrochemical plating, conversion coatings, hydride coatings, anodization, gas-phase deposition, laser surface alloying/cladding, and organic/polymer coatings [29]. Several possibilities, obtained from the development for structural applications, could be implemented to tailor the degradation rate of Mg-based materials for biomedical applications as long as alloying elements, surface treatments, and/or coatings result in a biologically compatible material. In fact, research in this area has not only focused on tailoring the degradation rate, but also in improving the bioactivity, osseointegration, and tissue-implant interaction of Mg-based biomaterials [1-3]. Specifically, we developed, implemented, and optimized Mg alloys and anodically oxidized surface treatments to tailor the corrosion rates, mechanical properties, and/or improve cell-biomaterial interactions to enable clinical translation of Mg-based biomaterials.

1.2.1. Crystalline ternary Mg-Zn-Ca biomedical alloys

The crystalline Mg-Zinc (Zn)-Calcium (Ca) ternary alloys have been of particular interest in the past few years for biomedical applications [30-42]. Mg-Zn-Ca alloys have been developed and actively investigated since the late 1990s to improve the creep resistance and mechanical properties of Mg alloys for high-temperature and lightweight structural applications. The addition of low-cost Ca into the Mg-Zn alloy was intended to improve the precipitation hardening ability of Mg alloys and replace aluminum (Al) as an alloying element [43-53]. From the materials science perspective, the addition of Ca into Mg alloys provided three key

benefits. Namely, Ca improved room-temperature mechanical properties and creep resistance mainly due to the formation of fine Mg_2Ca precipitates [49, 53]; improved the oxidation resistance by changing the native porous oxide to a thermally-stable protective compact oxide layer [54]; and reduced the grain size of alloys when adding approximately 0.5-1.0 wt. % Ca [55, 56]. The maximum solubility of Ca in Mg is 1.0 - 1.6 atomic (at.) % at room temperature in the equilibrium state [41, 57]. The addition of Zn as an alloying element improved tensile and creep strength [58], increased age hardening response [43], reduced grain size, and improved alloy castability [53]. The maximum solubility of Zn in Mg was reported to be 2 weight (wt.) % at room temperature in the equilibrium state [32]. The addition of 1-4 wt. % Zn (when Ca < 1.0 wt. %) resulted in Mg-Zn-Ca alloys with corrosion (or degradation) rates promising for biomedical applications [32, 33, 36, 38, 42, 45]. In this study, a fixed content of 0.5 wt. % Ca and a maximum of 4 wt. % Zn were selected based on numerous Mg-Zn-Ca studies favoring as-cast Mg alloys with low Ca content (< 1 at. %) and Zn/Ca at. % ratio < 5 [32, 33, 36, 38, 42, 45].

From the perspective of medical applications, Mg-Zn-Ca alloys are attractive because all the alloying elements are naturally present in the human body and can be naturally metabolized and released. Specifically, Mg is a critical cation and cofactor in numerous intracellular processes [59], Zn participates in over 300 enzymatic processes [60], and Ca is a key element for bone formation and remodeling, and is essential for a variety of cellular functions [61]. Despite the

tremendous potential of Mg-Zn-Ca alloys for biomedical applications, so far only a handful of investigations focused on the cytocompatibility and biocompatibility aspects of these materials. For example, in 2011 and 2013, respectively, Zhang et al. and Yin et al. both investigated the cytocompatibility of Mg-Zn-Ca alloy extracts with L-929 fibroblasts for 7 days (per ISO 10993-5 standard) and concluded that the as-cast Mg-4.0Zn-0.2Ca (wt. %) alloy [32, 41] and as-cast Mg-xZn-1.0Ca (x = 1, 2, 3 wt. %) alloys [33] had a cytotoxicity grade of 0-1, which made them suitable candidates for biomedical applications. Furthermore, results from *in vivo* studies using as-cast Mg-Zn-Ca alloys indicated peri-implant bone formation [32, 40], unchanged blood serum Mg^{2+} ion concentrations, and retention of implant mechanical properties [39], even though the formation of hydrogen gas pockets [40] and minor inflammatory responses [39] were observed. Additionally, Zhang et al. reported that the dynamics at the implant-tissue interface caused a heterogeneous interfacial composition of carbon (C), oxygen (O), Mg, Ca, and phosphorus (P) with distinct Ca/P ratios [32]. Although these results supported Mg-Zn-Ca alloys for orthopedic implant applications, the mechanisms explaining how bone cells interact with these alloys at the implant-tissue interface remains elusive.

1.2.2. Crystalline ternary Mg-Zn-Sr biomedical alloys

Crystalline ternary Mg-Zn-Strontium (Sr) ternary alloys were specifically developed and manufactured for biomedical applications [62]. The selection of Zn and Sr as alloying elements resided in the fact that each of them can potentially

improve the mechanical and corrosion properties when alloyed with Mg [62, 63]. Zn has the same crystal structure as Mg and a 6.2 wt. % maximum solubility in Mg, where the solubility decreases as the temperature decreases. Addition of Zn can also provide the advantages of solution strengthening. Furthermore, solid solution of Zn in the α-Mg matrix phase increases the electric potential of the matrix and improves corrosion resistance. In fact, 4.0-6.0 wt.% Zn was optimal for maximizing Mg alloy strength and corrosion resistance, which was induced by strengthening effects of the intermetallic MgZn phase [64-67]. Although Sr has a limited solid solubility (0.11 wt.%; 0.03 at. %) in the Mg alloy, the addition of Sr can refine the microstructure [68], increase the mechanical properties, improve the creep properties, and increase corrosion resistance of Mg alloys [69].

From a biomedical perspective, Zn was selected as an alloying element because it is an important element in the body and participates in the syntheses of enzymes [60]. Sr was added because it has similar chemical characteristics as Ca, and accumulates mainly in trabecular bones [70, 71]. In addition, Sr ranelate (a Sr compound) has been proven to be beneficial for increasing bone mass and structural integrity in osteoporotic patients [72, 73], and its addition to hydroxyapatite cements has been shown to improve cement degradation and biocompatibility properties [33]. First studies on Mg-Zn-Sr alloys for biomedical applications showed superior mechanical and degradation properties as compared with pure Mg [62]. The improvement of properties resulted in part from grain refinement induced by dispersion of intermetallic compounds, namely $Zn_{13}Sr$,

which was formed due to the addition of both Zn and Sr as alloying elements [62, 74]. Although these results provided first evidence of the potential for Mg-Zn-Sr alloys, cell culture studies using a physiologically relevant *in vitro* model are necessary to determine the degradation in cell culture media, cytocompatibility, and cellular responses at cell-biomaterial interface with this novel family of alloys. Additionally, first studies evaluating the *in vivo* degradation and host-response are also necessary to determine clinical translation of Mg-Zn-Sr alloys.

1.2.3. Anodically oxidized surface modifications

Anodic oxidation (or anodization) is an electrolytic passivation process through which a thick (5-30 µm), stable, and protective oxide film can be grown on various metals, including Mg and its alloys [29, 75]. In the electrolytic cell, direct current generated by a power source drives uniform current flow from the metallic anode (working electrode) to the cathode (counter electrode) through the electrolyte and growth of a metallic oxide layer is initiated [76]. Furthermore, the anodic behavior of Mg and its alloys, and resulting characteristics of the passivation film, is strongly influenced by processing parameters including: alloy composition, magnitude and duration of the applied current/voltage, and electrolyte properties (composition, concentration, temperature, pH, etc.) [29, 75, 76]. Several industrial processes (e.g. Dow 17, HAE, Magoxid, Tagnite) have been implemented to successfully anodize Mg and its alloys for structural applications; however, many of these processes use either hazardous compounds (i.e. chromates and/or fluorides) as

electrolyte additives or necessitate high current densities for producing arc-induced oxidation [29, 75]. In an effort to develop an environmentally-friendly and toxic-free anodic oxidation process for Mg-based materials, Lei et al. investigated potentiostatic anodization of Mg-Zn-Ca alloys in aqueous 6 or 10 M KOH electrolytes followed by annealing [77, 78]. The authors demonstrated that the Mg-Zn-Ca behaved as an active-passive metal in the 6 M KOH electrolyte. Specifically, commercially pure Mg [79] and Mg-Zn-Ca alloys [78] showed four distinct processes in the 6 M KOH electrolyte: cathodic, which led to active metal dissolution to Mg^{2+} ions; passivation, which led to formation of Mg hydroxide ($Mg(OH)_2$); secondary oxidation, which led to the formation of Mg oxide (MgO); and transpassive, which results in oxygen evolution. In contrast, Mg-Zn-Ca alloys only showed cathodic, passivation, and transpassive processes in the 10 M KOH electrolyte [78]. Following anodization in the passivation region, an annealing step at a heating rate of 100 °C/hr followed by 6 hours at 450 °C was recommended to ensure retention of oxide structure and allow dehydration and conversion of $Mg(OH)_2$ to MgO [77, 78, 80]. Furthermore, Lei et al. demonstrated enhanced corrosion resistance of the anodized and annealed Mg alloys using the 10 M KOH electrolyte, compared with non-treated controls, through *in vitro* measurements in 3.5% NaCl or Hank's solution [77, 78]. In order to translate the potential of anodization using a 10 M KOH electrolyte to improve the corrosion resistance of Mg-based biomaterials, *in vitro* cell culture studies are necessary to determine the degradation in cell culture media, cytocompatibility, and cellular responses at cell-

biomaterial interface with anodically oxidized surface treatments. In fact, to our knowledge, cellular responses at the cell-biomaterial interface with surface treated Mg-based materials are very sparse in literature.

1.3. *In vitro* cell culture methods to study the degradation of Mg-based biomaterials and associated cellular responses

Current cytocompatibility and cytotoxicity testing of Mg alloys in literature are mostly based on the extract culture method (ISO 10993-5 and 10993-12), which is also called non-contact or media extract method because the cells are only exposed to certain concentrations of media extracts from degraded samples and are not in the same culture as the samples. These ISO standards were originally developed for testing the cytocompatibility of non-degradable materials [81]; however, they were widely adopted to study Mg or Mg alloys mainly due to the simplicity of methodology [81, 82]. The limitations of the extract-based culture method become apparent when comparing with the direct culture method (i.e. cells are directly cultured together with Mg alloy samples). The direct culture method takes the dynamic degradation processes of Mg alloys into account and makes it possible to probe cell behaviors directly on the alloy surfaces, even though culturing cells directly on the highly dynamic Mg alloy surface is more technically challenging. It is widely accepted that the degradation of Mg-based materials produces soluble degradation products (i.e., Mg^{2+} ions and hydroxide [OH^-] ions), insoluble precipitates, and hydrogen gas, along with the changes in surface

topography. All of these can influence homeostasis of the biological environment and therefore affect cellular processes at the implant site, but cannot be captured effectively using the extract-based culture method. For example, the changing surface topography of Mg-based materials could play an important role in modulating cell functions by contact-based cues. A growing body of literature provided evidence for the modulatory effects of micro- and nano-scale surface features on cell adhesion, proliferation, morphology, and differentiation [83-87]. Since the extract-based culture method can potentially obscure subtle effects of Mg alloy degradation on cells, we introduced the direct culture method to complement the extract-based culture method.

We introduced the cell-based direct culture method to characterize and screen Mg-based biomaterials along with cellular responses to the degradation of these metallic biomaterials. The direct culture method introduced the advantages of predicting degradation rates, testing cytocompatibility with solubilized degradation products, and probing cellular responses at the cell-substrate interface, all in a single platform [88]. In the direct culture method, the cells directly attached onto the Mg-based sample surfaces were designated as *direct contact*, while the cells attached to the culture plate surrounding the samples but not in direct contact with the samples were designated as *indirect contact*. The direct contact aspect of the direct culture method allowed us to probe the dynamic cell-biomaterial interface directly, while the indirect contact aspect of the same culture offered a means to compare our results with the results from extract-based culture method in

literature. Although physiologically relevant *in vitro* models, such as the direct culture method, are necessary for initial rapid screening of cytocompatibility and cytotoxicity of engineered biomaterials [89], *in vivo* evaluations at a later-stage remain imperative for clinical translation since the gap between *in vitro* and *in vivo* studies remains unresolved [90, 91].

1.4. Objectives

This dissertation presents four main research objectives:

1. Develop and optimize properties of novel Mg-based biomaterials with engineered corrosion rates to meet clinical requirements. Specifically, Mg-xZn-0.5Ca (x = 0.5, 1.0, 2.0, or 4.0 wt. %) alloys, Mg-4Zn-xSr (x = 0.15, 0.5, 1.0, 1.5 wt. %) alloys, and anodically oxidized commercially pure Mg (99.9% purity).

2. Develop and implement the direct *in vitro* culture method which is intended to mimic *in vivo* physiological conditions and evaluate cell responses at the cell-biomaterial interface (*direct contact*) and on the culture plate (*indirect contact*; exposure to solubilized degradation products) surrounding the Mg-based biomaterial. Additionally, a systematic comparison with other cell lines (and respective culture media) in the direct culture would allow us to: (i) identify key aspects that affect the *in vitro* degradation of Mg-based biomaterials, (ii) identify the capabilities of different cell lines in detecting cytotoxic effects induced by the degradation of Mg-based biomaterials, and (iii) identify the effect of

solubilized degradation products on distinct cellular responses (e.g. viability, morphology, inflammation, etc.).

3. Utilize the developed *in vitro* model to quantify the degradation rate of novel Mg alloys and anodically oxidized Mg, as well as determine cytocompatibility and cellular responses at the cell-biomaterial interface. The *in vitro* model will be a useful tool to screen and optimize the degradation, cytocompatibility, and interaction with cells of Mg-based biomaterials.

4. Determine *in vivo* degradation and host-response to novel biomaterials using small animal models. Evaluation of the *in vivo* degradation will allow us to identify factors that affect degradation and bridge the existing gap between *in vitro* and *in vivo* measurements of Mg-based biomaterials.

1.5. References

[1] Staiger MP, Pietak AM, Huadmai J, Dias G. Magnesium and its alloys as orthopedic biomaterials: A review. Biomaterials. 2006;27:1728-34.

[2] Witte F, Hort N, Vogt C, Cohen S, Kainer KU, Willumeit R, et al. Degradable biomaterials based on magnesium corrosion. Curr Opin Solid State Mater Sci. 2008;12:63-72.

[3] Zheng YF, Gu XN, Witte F. Biodegradable metals. Mater Sci Eng, R. 2014;77:1-34.

[4] Hermawan H, Dubé D, Mantovani D. Developments in metallic biodegradable stents. Acta Biomater. 2010;6:1693-7.

[5] Breen DJ, Stoker DJ. Titanium lines: A manifestation of metallosis and tissue response to titanium alloy megaprostheses at the knee. Clin Radiol. 1993;47:274-7.

[6] Beuf O, Briguet A, Lissac M, Davis R. Magnetic resonance imaging for the determination of magnetic susceptibility of materials. J Magn Reson B. 1996;112:111-8.

[7] Ludeke KM, Roschmann P, Tischler R. Susceptibility artefacts in NMR imaging. Magn Reson Imaging. 1985;3:329-43.

[8] Petersilge CA, Lewin JS, Duerk JL, Yoo JU, Ghaneyem AJ. Optimizing imaging parameters for MR evaluation of the spine with titanium pedicle screws. AJR Am J Roentgenol. 1996;166:1213-8.

[9] Tran N, Webster TJ. Nanotechnology for bone materials. Wiley Interdiscip Rev Nanomed Nanobiotechnol. 2009;1:336-51.

[10] Lembeck B, Wulker N. Severe cartilage damage by broken poly-L-lactic acid (PLLA) interference screw after ACL reconstruction. Knee Surg Sports Traumatol Arthrosc. 2005;13:283-6.

[11] Smith CA, Tennent TD, Pearson SE, Beach WR. Fracture of Bilok interference screws on insertion during anterior cruciate ligament reconstruction. Arthroscopy. 2003;19:E115-17.

[12] Baums MH, Zelle BA, Schultz W, Ernstberger T, Klinger HM. Intraarticular migration of a broken biodegradable interference screw after anterior cruciate ligament reconstruction. Knee Surg Sports Traumatol Arthrosc. 2006;14:865-8.

[13] Shafer BL, Simonian PT. Broken poly-L-lactic acid interference screw after ligament reconstruction. Arthroscopy. 2002;18:E35.

[14] Sidhu DS, Wroble RR. Intraarticular migration of a femoral interference fit screw. A complication of anterior cruciate ligament reconstruction. Am J Sports Med. 1997;25:268-71.

[15] Takizawa T, Akizuki S, Horiuchi H, Yasukawa Y. Foreign body gonitis caused by a broken poly-L-lactic acid screw. Arthroscopy. 1998;14:329-30.

[16] Bostman O, Hirvensalo E, Makinen J, Rokkanen P. Foreign-body reactions to fracture fixation implants of biodegradable synthetic polymers. J Bone Joint Surg Br. 1990;72:592-6.

[17] Kwak JH, Sim JA, Kim SH, Lee KC, Lee BK. Delayed intra-articular inflammatory reaction due to poly-L-lactide bioabsorbable interference screw used in anterior cruciate ligament reconstruction. Arthroscopy-the Journal of Arthroscopic and Related Surgery. 2008;24:243-6.

[18] Walton M, Cotton NJ. Long-term in vivo degradation of poly-L-lactide (PLLA) in bone. J Biomater Appl. 2007;21:395-411.

[19] Beevers DJ. Metal vs bioabsorbable interference screws: initial fixation. Proc Inst Mech Eng H. 2003;217:59-75.

[20] Hort N, Huang Y, Fechner D, Störmer M, Blawert C, Witte F, et al. Magnesium alloys as implant materials – Principles of property design for Mg–RE alloys. Acta Biomater. 2010;6:1714-25.

[21] Lock JY, Wyatt E, Upadhyayula S, Whall A, Nuñez V, Vullev VI, et al. Degradation and antibacterial properties of magnesium alloys in artificial urine for potential resorbable ureteral stent applications. J Biomed Mater Res, A. 2014;102:781-92.

[22] Liu H. The effects of surface and biomolecules on magnesium degradation and mesenchymal stem cell adhesion. J Biomed Mater Res A. 2011;99:249-60.

[23] Amini AR, Wallace JS, Nukavarapu SP. Short-Term and Long-Term Effects of Orthopedic Biodegradable Implants. J Long Term Eff Med Implants. 2011;21:93-122.

[24] Jiang Y, Jia T, Wooley PH, Yang S-Y. Current research in the pathogenesis of aseptic implant loosening associated with particulate wear debris. Acta Orthop Belg. 2013;79:1-9.

[25] Song G, Atrens A. Understanding Magnesium Corrosion—A Framework for Improved Alloy Performance. Adv Eng Mater. 2003;5:837-58.

[26] Song GL. Corrosion and protection of magensium alloys. Beijing: Chemistry Industry Press. 2006:211.

[27] Harbodt K. Chapter 1: History. In: Friedrich HE, Mordike BL, editors. Magnesium Technology: Metallurgy, Design Data, Applications. Berlin, Heidelberg: Springer Berlin Heidelberg; 2006. p. 1-28.

[28] Mordike BL, Ebert T. Magnesium: Properties — applications — potential. Mater Sci Eng, A. 2001;302:37-45.

[29] Gray JE, Luan B. Protective coatings on magnesium and its alloys — a critical review. J Alloy Compd. 2002;336:88-113.

[30] Rosalbino F, Negri S, Saccone A, Angelini E, Delfino S. Bio-corrosion characterization of Mg–Zn–X (X = Ca, Mn, Si) alloys for biomedical applications. J Mater Sci Mater Med. 2010;21:1091-8.

[31] Xu Z, Smith C, Chen S, Sankar J. Development and microstructural characterizations of Mg–Zn–Ca alloys for biomedical applications. Mater Sci Eng, B. 2011;176:1660-5.

[32] Zhang BP, Wang Y, Geng L. Research on Mg-Zn-Ca Alloy as Degradable Biomaterial. In: Pignatello R, editor. Biomaterials - Physics and Chemistry. Rijeka, Croatia: InTech; 2011. p. 183-204.

[33] Zhang B, Hou Y, Wang X, Wang Y, Geng L. Mechanical properties, degradation performance and cytotoxicity of Mg–Zn–Ca biomedical alloys with different compositions. Mater Sci Eng, C. 2011;31:1667-73.

[34] Du H, Wei Z, Liu X, Zhang E. Effects of Zn on the microstructure, mechanical property and bio-corrosion property of Mg–3Ca alloys for biomedical application. Mater Chem Phys. 2011;125:568-75.

[35] Gao JH, Guan SK, Ren ZW, Sun YF, Zhu SJ, Wang B. Homogeneous corrosion of high pressure torsion treated Mg–Zn–Ca alloy in simulated body fluid. Mater Lett. 2011;65:691-3.

[36] Bakhsheshi-Rad HR, Abdul-Kadir MR, Idris MH, Farahany S. Relationship between the corrosion behavior and the thermal characteristics and microstructure of Mg–0.5Ca–xZn alloys. Corros Sci. 2012;64:184-97.

[37] Cho SY, Chae S-W, Choi KW, Seok HK, Han HS, Yang SJ, et al. Load-bearing capacity and biological allowable limit of biodegradable metal based on degradation rate in vivo. J Biomed Mater Res, B. 2012;100B:1535-44.

[38] Sun Y, Zhang B, Wang Y, Geng L, Jiao X. Preparation and characterization of a new biomedical Mg–Zn–Ca alloy. Mater Design. 2012;34:58-64.

[39] Cho SY, Chae S-W, Choi KW, Seok HK, Kim YC, Jung JY, et al. Biocompatibility and strength retention of biodegradable Mg-Ca-Zn alloy bone implants. J Biomed Mater Res, B. 2013;101B:201-12.

[40] Cha P-R, Han H-S, Yang G-F, Kim Y-C, Hong K-H, Lee S-C, et al. Biodegradability engineering of biodegradable Mg alloys: Tailoring the electrochemical properties and microstructure of constituent phases. Sci Rep. 2013;3.

[41] Yin P, Li N, Lei T, Liu L, Ouyang C. Effects of Ca on microstructure, mechanical and corrosion properties and biocompatibility of Mg–Zn–Ca alloys. J Mater Sci Mater Med. 2013;24:1365-73.

[42] Cipriano AF, Miller CT, Liu H. Cytocompatibility of Magnesium-Zinc-Calcium Alloys with Bone Marrow Derived Mesenchymal Stem Cells. In: B. Mishra MIaTC, editor. Advanced Materials Research, THERMEC 2013 Supplement. Las Vegas, NV: Trans Tech Publ; 2014. p. 1-6.

[43] Nie JF, Muddle BC. Precipitation hardening of Mg-Ca(-Zn) alloys. Scr Mater. 1997;37:1475-81.

[44] Jardim PM, Solórzano G, Sande JBV. Second phase formation in melt-spun Mg–Ca–Zn alloys. Mater Sci Eng, A. 2004;381:196-205.

[45] Gao X, Zhu SM, Muddle BC, Nie JF. Precipitation-hardened Mg–Ca–Zn alloys with superior creep resistance. Scr Mater. 2005;53:1321-6.

[46] Oh JC, Ohkubo T, Mukai T, Hono K. TEM and 3DAP characterization of an age-hardened Mg–Ca–Zn alloy. Scr Mater. 2005;53:675-9.

[47] Bamberger M, Levi G, Sande JB. Precipitation hardening in Mg-Ca-Zn alloys. Metall and Mat Trans A. 2006;37:481-7.

[48] Levi G, Avraham S, Zilberov A, Bamberger M. Solidification, solution treatment and age hardening of a Mg–1.6 wt.% Ca–3.2 wt.% Zn alloy. Acta Mater. 2006;54:523-30.

[49] Ortega Y, Monge MA, Pareja R. The precipitation process in Mg–Ca–(Zn) alloys investigated by positron annihilation spectroscopy. J Alloy Compd. 2008;463:62-6.

[50] Zhou T, Chen D, Chen Z-h. Microstructures and properties of rapidly solidified Mg-Zn-Ca alloys. T Nonferr Metal Soc. 2008;18:s101-s6.

[51] Geng L, Zhang BP, Li AB, Dong CC. Microstructure and mechanical properties of Mg–4.0Zn–0.5Ca alloy. Mater Lett. 2009;63:557-9.

[52] Oh-ishi K, Watanabe R, Mendis CL, Hono K. Age-hardening response of Mg–0.3 at.%Ca alloys with different Zn contents. Materials Science and Engineering: A. 2009;526:177-84.

[53] Farahany S, Bakhsheshi-Rad HR, Idris MH, Abdul Kadir MR, Lotfabadi AF, Ourdjini A. In-situ thermal analysis and macroscopical characterization of Mg–xCa and Mg–0.5Ca–xZn alloy systems. Thermochim Acta. 2012;527:180-9.

[54] You B-S, Park W-W, Chung I-S. The effect of calcium addition to magnesium on the microstructure and compositional changes of oxide film formed at high temperature. Mater Trans. 2001;42:1139-41.

[55] Zhang E, Yang L. Microstructure, mechanical properties and bio-corrosion properties of Mg–Zn–Mn–Ca alloy for biomedical application. Mater Sci Eng, A. 2008;497:111-8.

[56] Hirai K, Somekawa H, Takigawa Y, Higashi K. Effects of Ca and Sr addition on mechanical properties of a cast AZ91 magnesium alloy at room and elevated temperature. Mater Sci Eng, A. 2005;403:276-80.

[57] Hagihara K, Fujii K, Matsugaki A, Nakano T. Possibility of Mg- and Ca-based intermetallic compounds as new biodegradable implant materials. Mater Sci Eng, C. 2013;33:4101-11.

[58] Boehlert CJ, Knittel K. The microstructure, tensile properties, and creep behavior of Mg–Zn alloys containing 0–4.4 wt.% Zn. Materials Science and Engineering: A. 2006;417:315-21.

[59] McCarthy JT, Kumar R. Divalent Cation Metabolism: Magnesium. Hoboken, New Jersey, USA: Wiley-Blackwill; 1999.

[60] Coleman JE. Zinc proteins: enzymes, storage proteins, transcription factors, and replication proteins. Annu Rev Biochem. 1992;61:897-946.

[61] Parfitt AM. Calcium Homeostasis. Physiology and Pharmacology of Bone: Springer Berlin Heidelberg; 1993. p. 1-65.

[62] Guan RG, Cipriano AF, Zhao ZY, Lock J, Tie D, Zhao T, et al. Development and Evaluation of a Magnesium-Zinc-Strontium Alloy for Biomedical Applications – Alloy Processing, Microstructure, Mechanical Properties, and Biodegradation. Mater Sci Eng, C. 2013;33:3661-9.

[63] Brar HS, Wong J, Manuel MV. Investigation of the mechanical and degradation properties of Mg-Sr and Mg-Zn-Sr alloys for use as potential biodegradable implant materials. J Mech Behav Biomed. 2012;7:87-95.

[64] Xu L, Zhang E, Yin D, Zeng S, Yang K. In vitro corrosion behaviour of Mg alloys in a phosphate buffered solution for bone implant application. J Mater Sci Mater Med. 2008;19:1017-25.

[65] Maeng DY, Kim TS, Lee JH, Hong SJ, Seo SK, Chun BS. Microstructure and strength of rapidly solidified and extruded Mg-Zn alloys. Scr Mater. 2000;43:385-9.

[66] Somekawa H, Osawa Y, Mukai T. Effect of solid-solution strengthening on fracture toughness in extruded Mg–Zn alloys. Scr Mater. 2006;55:593-6.

[67] Gao X, Nie JF. Characterization of strengthening precipitate phases in a Mg–Zn alloy. Scr Mater. 2007;56:645-8.

[68] Gu XN, Xie XH, Li N, Zheng YF, Qin L. In vitro and in vivo studies on a Mg-Sr binary alloy system developed as a new kind of biodegradable metal. Acta Biomater. 2012;8:2360-74.

[69] Bai X, Hu W-J, Zhang L-Q, Wang G, Luo X. Effect of Sr on microstructures and mechanical properties of AZ91 Mg alloys. Chin J Nonferr Met. 2008;18:1596-16011601.

[70] Gu XN, Xie XH, Li N, Zheng YF, Qin L. In vitro and in vivo studies on a Mg-Sr binary alloy system developed as a new kind of biodegradable metal. Acta Biomater. 2012.

[71] Dahl SG, Allain P, Marie PJ, Mauras Y, Boivin G, Ammann P, et al. Incorporation and distribution of strontium in bone. Bone. 2001;28:446-53.

[72] Marie PJ, Ammann P, Boivin G, Rey C. Mechanisms of Action and Therapeutic Potential of Strontium in Bone. Calcif Tissue Int. 2001;69:121-9.

[73] Meunier PJ, Roux C, Seeman E, Ortolani S, Badurski JE, Spector TD, et al. The Effects of Strontium Ranelate on the Risk of Vertebral Fracture in Women with Postmenopausal Osteoporosis. New Engl J Med. 2004;350:459-68.

[74] Borkar H, Hoseini M, Pekguleryuz M. Effect of strontium on flow behavior and texture evolution during the hot deformation of Mg–1 wt%Mn alloy. Materials Science and Engineering: A. 2012;537:49-57.

[75] Blawert C, Dietzel W, Ghali E, Song G. Anodizing Treatments for Magnesium Alloys and Their Effect on Corrosion Resistance in Various Environments. Adv Eng Mater. 2006;8:511-33.

[76] Cipriano AF, Miller CT, Liu H. Vertically Aligned TiO2 Nanotubes on Metallic Substrates: A Review of Anodic Growth Mechanisms and Biomedical Applications J Biomed Nanotechnol. 2014.

[77] Lei T, Ouyang C, Tang W, Li L-F, Zhou L-S. Enhanced corrosion protection of MgO coatings on magnesium alloy deposited by an anodic electrodeposition process. Corros Sci. 2010;52:3504-8.

[78] Lei T, Ouyang C, Tang W, Li L-F, Zhou L-S. Preparation of MgO coatings on magnesium alloys for corrosion protection. Surf Coat Tech. 2010;204:3798-803.

[79] Cai Z, Lu D, Li W, Liang Y, Zhou H. Study on anodic oxidation of magnesium in 6M KOH solution by alternative current impedance. Int J Hydrogen Energy. 2009;34:467-72.

[80] Yoshida T, Tanaka T, Yoshida H, Funabiki T, Yoshida S, Murata T. Study of Dehydration of Magnesium Hydroxide. J Phys Chem. 1995;99:10890-6.

[81] Fischer J, Pröfrock D, Hort N, Willumeit R, Feyerabend F. Reprint of: Improved cytotoxicity testing of magnesium materials. Mater Sci Eng, B. 2011;176:1773-7.

[82] Xin Y, Hu T, Chu PK. In vitro studies of biomedical magnesium alloys in a simulated physiological environment: A review. Acta Biomater. 2011;7:1452-9.

[83] Cipriano AF, De Howitt N, Gott SC, Miller CT, Rao MP, Liu H. Bone Marrow Stromal Cell Adhesion and Morphology on Micro- and Sub-Micropatterned Titanium. J Biomed Nanotechnol. 2014;10:660-8.

[84] Wang PY, Li WT, Yu J, Tsai WB. Modulation of osteogenic, adipogenic and myogenic differentiation of mesenchymal stem cells by submicron grooved topography. J Mater Sci Mater Med. 2012;23:3015-28.

[85] Hasirci V, Pepe-Mooney BJ. Understanding the cell behavior on nano-/micro-patterned surfaces. Nanomed. 2012;7:1375-89.

[86] Matsuzaka K, Walboomers F, de Ruijter A, Jansen JA. Effect of microgrooved poly-l-lactic (PLA) surfaces on proliferation, cytoskeletal organization, and mineralized matrix formation of rat bone marrow cells. Clin Oral Implants Res. 2000;11:325-33.

[87] Liu H, Slamovich EB, Webster TJ. Increased osteoblast functions among nanophase titania/poly(lactide-co-glycolide) composites of the highest nanometer surface roughness. J Biomed Mater Res A. 2006;78:798-807.

[88] Cipriano AF, Sallee A, Guan R-G, Zhao Z-Y, Tayoba M, Sanchez J, et al. Investigation of magnesium–zinc–calcium alloys and bone marrow derived mesenchymal stem cell response in direct culture. Acta Biomater. 2015;12:298-321.

[89] Kirkpatrick CJ, Mittermayer C. Theoretical and practical aspects of testing potential biomaterials in vitro. J Mater Sci Mater Med. 1990;1:9-13.

[90] Witte F, Fischer J, Nellesen J, Crostack H-A, Kaese V, Pisch A, et al. In vitro and in vivo corrosion measurements of magnesium alloys. Biomaterials. 2006;27:1013-8.

[91] Kirkland NT, Birbilis N, Staiger MP. Assessing the corrosion of biodegradable magnesium implants: A critical review of current methodologies and their limitations. Acta Biomater. 2012;8:925-36.

Chapter 2 – *In vitro* degradation of four Magnesium-Zinc-Strontium alloys and their cytocompatibility with human embryonic stem cells

2.1. Background

An *in vitro* cytocompatibility study was designed based on H9 human embryonic stem cells (hESC) to assess the degradation and subtle cellular effects of four distinct ZSr41 alloys in comparison with pure Mg. The H9 hESC model was used to mimic physiological environment because of its greater sensitivity to known toxicants [1, 2]. The sensitive H9 hESC *in vitro* model could potentially improve the detection or screening of toxicological effects of new biomaterials by monitoring cell adhesion, proliferation, and differentiation. The use of *in vitro* hESC model in this study was inspired by the successful implementation and validation of the embryonic stem cell test (EST), which was based on mouse ESC (mESC). The EST took advantage of mESC sensitivity to more accurately predict the toxicity of new compounds [3, 4]. Additional benefits of the H9 hESC-based model include human relevance, availability, unlimited proliferation ability and the ease of genetic modification [5, 6]. *In vitro* gene modification techniques, such as gene transfection to express green fluorescent protein (GFP), enable cell sorting and evaluation of differentiation for downstream applications [7, 8]. Furthermore, since the degradation rate and mode of Mg are responsive to dissolved ions and other components in the surrounding solution [9-13], cell culture media provides a physiologically relevant model to test degradation of Mg-based alloys.

This study presents a comparison of the degradation and cytocompatibility of four distinct ZSr41 Mg alloys in the hESC cell culture as compared with pure polished Magnesium (P-Mg) control. The ZSr41 alloys were composed of 94.5-95.85 wt. % Mg, 4 wt. % Zn and 0.15-1.5 wt.% Sr.

2.2. Materials and methods

2.2.1. Preparation of Mg-Zn-Sr alloys (ZSr41) and Mg control

The amount of Strontium (Sr) added into each alloy was as follows: 0.15 wt.% Sr for ZSr41A; 0.5 wt.% Sr for ZSr41B; 1.0 wt.% Sr for ZSr41C; and 1.5 wt.% Sr for ZSr41D. These alloys were produced by a metallurgical process consisting of melting, casting, rolling, and heat treatment. First, a stainless steel crucible was preheated to 690-700 °C, and then argon gas was blown into the stainless steel crucible. Pure Mg ingots with a purity of 99.9% were heated and melted in the stainless steel crucible. Argon gas with a flow rate of 6L/ min was blown into the alloy during heating and melting to protect the alloy from oxidation. After the Mg ingots melted, preheated metallic Zn and Sr were added into the magnesium and the mixture was stirred slightly to make the alloy elements react sufficiently. After the melting process, the alloy was held at 690-700 °C for 30 min, deslagged, and cast as ingots at 720 °C. The ingots were rolled at 380 °C into sheets with a thickness of 1 mm. The alloy sheets were then aged at 175 °C for 8 hrs. The produced ZSr41 alloy sheets were cut to 5x5 mm squares using a notcher (Model No. 100, Whitney Metal Tools Co.) for degradation and cell studies. Control P-Mg

(as rolled, Goodfellow Co.) sheets of 99.9% purity and thickness of 250 μm were cut into 5x5 mm squares as well for degradation and cell studies.

Samples of ZSr41A, B, C, D and P-Mg were all prepared in the same manner according to the following procedures: first, the 5x5 mm squares were polished using 600, 800, and 1200 grit silicon carbide abrasive papers (Ted Pella, Inc.) to remove surface oxides. After surface polishing, ZSr41 and P-Mg samples had a silver-white color. Each sample was subsequently ultrasonically cleaned (VWR, Model 97043-036) for 15 min in 200 proof ethanol (Koptec), individually weighed (M_0), and disinfected under ultraviolet (UV) radiation in a class II biosafety cabinet for 4 hours on each side prior to degradation and cell culture experiments.

2.2.2. Surface characterization of ZSr41 alloys prior to cell culture

Prior to cell culture, the surface microstructures of ZSr41A, ZSr41B, ZSr41C, ZSr41D, and P-Mg were characterized using a field emission scanning electron microscope (FESEM; Philips XL-30). Surface composition and elemental distribution were analyzed using energy dispersive X-ray spectroscopy (EDS; EDAX). An accelerating voltage of 25 kV was used to obtain SEM images and perform EDS analysis.

2.2.3. H9 human embryonic stem cell culture

H9 human embryonic stem cells (H9 hESCs) were stably transfected with green fluorescence protein (GFP) at the octamer-binding transcription factor 4

(OCT4) promoter site using Gene Juice (Novagen), knockout Dulbecco's modified eagle's medium (KO-DMEM/F12; Invitrogen) and plasmid pCAG-eGFP-Internal Ribosome entry site (IRES)-Puromycin-R. These transfected hESCs can be closely monitored for differentiation under fluorescence microscope. Feeder-free conditions in a T-25 flask (Falcon) with Geltrex™ matrix (Invitrogen) and mTeSR®1 media (STEMCELL Technologies) were used to maintain the H9-OCT4 hESCs. Upon verification of 80-90% confluency under optical microscope, the H9-OCT4 hESCs were passaged using Accutase (Innovative Cell Technologies) in conjunction with glass beads to provide gentle mechanical detachment.

Morphology and fluorescence of H9-OCT4 hESCs was observed using a fluorescence microscope (Nikon Eclipse Ti) to ensure hESCs were normal and healthy prior to the co-culture with Mg alloys. Cell morphology was determined using phase contrast images. Fluorescence images were used to determine the viability and differentiation of hESCs. Phase contrast images and fluorescence images were merged using NIS-Elements Imaging Software (Nikon).

2.2.4. Culturing of H9-OCT4 hESCs with ZSr41 alloys

The immersion method was used to investigate ZSr41 alloy and P-Mg degradation. Two 12-well plates (BD Falcon) were prepared by covering the wells with cold Geltrex™ matrix (Invitrogen) in DMEM media (Invitrogen 11965092) (1:50) for 24 hours. The excess Geltrex™ solution was aspirated and H9-OCT4 ESCs were seeded (passage 15) onto the wells with mTeSR®1 media and

maintained for 24 hours under standard cell culture conditions (that is, a sterile, 37 °C, 5% CO_2/95% air, humidified environment).

After the initial 24-hour incubation period, the mTeSR®1 media was removed and replenished with fresh media. The ZSr41A, B, C and D samples and Mg controls were placed into trans-well inserts (Corning) and positioned within the wells where H9-OCT4 ESCs were cultured. Positive control for cytocompatibility consisted of mTeSR®1 media with H9-OCT4 hESCs only without any Mg samples. The hESCs with ZSr41 alloy and P-Mg samples and positive controls were then incubated in the Nikon Biostation CT under standard cell culture conditions. The mTeSR®1 media was replaced with fresh media every 24 hours to more closely mimic *in vivo* conditions where the circulation system regularly takes away soluble degradation products from the local site of implantation [14]. All degradation and cell culture experiments were performed in triplicate.

2.2.4.1. In vitro degradation of ZSr41 alloys

Following preparation, the samples were incubated for a total of 72 h. In order to more closely mimic *in vivo* conditions where the circulatory system regularly removes soluble degradation products from the local implantation site, incubation intervals were set as 24 h. At each prescribed incubation interval, the culture media was removed and collected to measure pH levels and ionic concentrations. After the media collection, the same amount of fresh culture media was added into each well under sterile conditions. Cautions were taken to avoid disrupting degradation

products on the specimen surface while removing the culture media along with any soluble degradation products found within. The pH levels were measured using a calibrated pH meter (VWR, Model SB70P) after each prescribed incubation interval. The concentration of Mg ions in the collected media was measured using inductively coupled plasma atomic emission spectroscopy (ICP-AES; Perkin Elmer Optima 2000 DV). Ionic concentrations were obtained by comparison with a standard curve generated from samples of $MgCl_2 \cdot 6H_2O$ with known concentrations of 250, 125, 62.5, 31.25, and 15.63 ppm. Oversaturated media samples were diluted with DI water to obtain values within the range of the standard curve. At the end of the 72 h incubation period, each sample was individually weighed (M_f) and the values were used to calculate mass loss per exposed surface area with respect to incubation time using the following equation (Eq. 1.1):

$$M_{loss} = (M_0 - M_f)/(L*W+2*L*t+2*W*t) \qquad \text{(Eq. 1.1)}$$

where M_0 is the initial sample mass, M_f is the final sample mass, L is the sample length (5 mm), W is the sample width (5 mm) and t is the sample thickness (1 mm for ZSr41 and 250 µm for P-Mg).

2.2.4.2. *In vitro* cytocompatibility of ZSr41 alloys with hESCs

Phase contrast and fluorescence images of two random points of each well were captured using Nikon Biostation CT at every 6 h intervals to evaluate cell viability in response to ZSr41 and P-Mg degradation products throughout the 72 h

incubation period. The hESCs were continuously observed during the 72 h incubation period to obtain detailed information on dynamic cellular responses corresponding to the early stage of *in vivo* implant performance. Cellular responses to the implants immediately after insertion are critical for the long-term success of implants, and, therefore, should be monitored closely. Nikon Biostation enabled the continuous *in situ* imaging of hESCs co-cultured with ZSr41 alloys and controls. The areas covered by viable H9 hESC colonies showing positive OCT4 stem cell marker were manually outlined in images using ImageJ software. Numerical area of cell coverage for each sample was subsequently normalized against initial (t = 0) cell coverage in order to monitor the change of viable cell colony coverage over time.

2.2.4.3. Surface characterization of ZSr41 alloys after cell culture

After 72 h of cell culture, the surfaces of ZSr41A, ZSr41B, ZSr41C, ZSr41D, and P-Mg were characterized using the FESEM (Philips XL-30) at a 25kV accelerating voltage. Sample surface composition and elemental distribution were analyzed using EDS at the 25kV accelerating voltage.

2.2.5. Statistical Analyses

In vitro degradation and cytocompatibility experiments were run in triplicate. Parametric numerical data sets were analyzed using standard analysis of variance (ANOVA), whereas non-parametric numerical data sets were analyzed using

Kruskal-Wallis analysis, both followed by standard post hoc tests with the Holm-Bonferroni correction; statistical significance was considered at $p<0.05$.

2.3. Results

2.3.1. Surface morphology and composition of ZSr41 alloys

Scanning electron micrographs of the four ZSr41 alloys before *in vitro* degradation showed different surface topography (Figure 2.1, A-E). Different amounts, sizes, and distribution of precipitated phases (white particles) were observed on the surfaces of ZSr41B, C, and D. Precipitate size ranged from 1 to 5 µm and the amount present on the alloys increased in this order: ZSr41B<ZSr41C<ZSr41D. In contrast, there were no precipitates observed on ZSr41A and P-Mg. The darker regions visible in SEM images of the samples showed a higher amount of Oxygen (O), indicating the formation of an oxide layer (Figure 2.2). Additionally, micron-sized pores were visible on the surface of P-Mg, but not on the surfaces of any of the ZSr41 alloys. Overall, the surface of the samples appeared smooth, but residual trace lines induced by polishing were visible on the surfaces.

EDS spectra and quantitative analyses at 5,000x magnification confirmed increasing levels of Sr in the ZSr41 alloys in the following order: ZSr41 A< ZSr41B<ZSr41C (Figure 2.1, A'-E' EDS spectra). All ZSr41 alloys had close to 4 wt. % Zn according to EDS quantitative analyses. EDS analyses also confirmed

the presence of Mg on the surface of all ZSr41 alloys, as clearly seen through the prevalent peak near 1.25 keV on all spectra. A low percentage of O (less than 4 wt. % on all samples) was found in all four ZSr41 alloys and P-Mg surfaces, indicating the presence of oxides even after polishing.

Additionally, EDS analyses were also performed at 25,000x magnification in order to investigate the composition of the precipitates visible on the surfaces of the ZSr41 alloys (Figure 2.3, A-E). EDS spectra of the highlighted area of precipitates (white particulate features) at the higher magnification (Figure 2.3, A'-E' EDS spectra) indicated higher concentrations of Sr and Zn as compared with the composition detected on the overall surfaces of the alloys at the lower magnification. EDS analysis of the highlighted precipitates showed 13.79 wt. % Sr in ZSr41D, 11.60 wt. % Sr in ZSr41C, and 10.24 wt.% Sr in ZSr41B. In contrast, EDS analysis of ZSr41A at 25,000x magnification was done on the entire surface rather than a selected area due to the lack of precipitates and showed only 1.37 wt. % Sr.

2.3.2. *In vitro* degradation results of ZSr41 alloys

Mass loss of ZSr41 alloys and P-Mg is an important measurement for quantification of the degradation rate when co-cultured with hESCs. Statistical analysis of the total mass loss per unit area over 72 h degradation period indicated differences among the ZSr41 alloys and P-Mg according to ANOVA [$F(4,10) = 20.619$, $p < 0.001$], as shown in Figure 2.4. Post hoc pair-wise comparison tests

revealed significantly less mass loss for ZSr41A, B, and C alloys when compared to P-Mg. Among the four ZSr41 alloys, ZSr41B and ZSr41C exhibited similar mass loss, and ZSr41D showed significantly greater amount of mass loss when compared to the other compositions of ZSr41.

As Mg and Mg alloy degrade, soluble degradation products, i.e., Mg ions (Mg^{2+}) and hydroxide ions (OH^-), are the other two important indicators of degradation rate. Figure 2.5 shows pH change of cell culture media over time as a result of degradation of Mg and ZSr41 alloys. Analysis of the pH values of immersion media showed that ZSr41A degradation did not induce significant pH increase throughout all time intervals as compared with the other ZSr41 alloys and P-Mg. The pH increase of immersion media cultured with ZSr41D was the highest among all the ZSr41 alloys and P-Mg tested. When comparing the pH change of the media containing ZSr41 alloys and P-Mg control with the blank control (cells and media only), the results showed that degradation products from P-Mg and ZSr41 alloys caused an increase in pH, while the blank control caused a decrease in pH. The decrease in pH for blank control was due to the metabolic activities of cells. Results also indicated a significant increase in pH during the initial 24 h of culture as a result of initial degradation of ZSr41B, ZSr41C, and P-Mg.

Figure 2.6 shows Mg ion concentration over time in the media cultured with Mg and ZSr41 alloys. The results indicated significant differences in the ICP-AES data of Mg ion concentration according to ANOVA [$F(4,10) = 13.69$, $p < 0.05$]. Post hoc

pair-wise comparison tests combined with Holm-Bonferroni correction only detected significant difference between ZSr41A and ZSr41D. The media co-cultured with the ZSr41A alloy showed the lowest Mg ion concentration over the 72 h immersion. The cell culture media in contact with the ZSr41D alloy showed the greatest Mg ion concentration at the end of 72 h culture period. Mg ion concentration in cell culture media in contact with most ZSr41 alloys and P-Mg increased to an initial maximum after 24 h of immersion, and decreased after 48 and 72 h immersion. The ZSr41B and ZSr41C alloys showed similar behavior to P-Mg in terms of Mg ion concentration.

The results of average Mg ion, Sr, and Zn concentrations in the cell culture media during the first 48 h of culture are summarized in Table 2.1. The results showed that Mg ion concentration in the media containing ZSr41A (13.6±0.8 mM) was the lowest, and ZSr41B (18.4±0.6 mM) was the highest. ZSr41C and ZSr41D alloys showed Mg ion concentrations of 18.0±2.9 mM, and 17.0±2.3 mM, respectively. P-Mg showed Mg ion concentration of 17.4±1.6 mM. Additionally, the concentrations of Zn and Sr induced by the degradation of ZSr41 alloys were calculated based on the original Zn and Sr percentages in the respective ZSr41 alloys and the respective Mg ion concentrations during the initial 48 h of culture. The calculated Zn concentration showed that ZSr41A had the lowest value (0.200±0.0120 mM), while ZSr41B, C, and D showed the values of 0.270±0.0092 mM, 0.270±0.0430 mM, and 0.250±0.0340 mM, respectively. As for Sr, the results showed that Sr concentration in the media containing ZSr41A (0.006±0.0003 mM)

was the lowest, and ZSr41D (0.071±0.0096 mM) was the highest. ZSr41B and ZSr1C showed Sr concentrations of 0.025±0.0009 mM and 0.050±0.0080 mM, respectively.

Figure 2.7 shows the total combined amount of Mg dissolved in the media during the 72 h cell culture. The total amount was calculated by first multiplying the Mg ion concentration measured at each prescribed time interval by the volume of each sample and then combining the total Mg collected at 24, 48 and 72 h time points. The results confirmed that the total Mg ions induced by ZSr41A alloy degradation was the lowest when compared to the other ZSr41 alloys and P-Mg.

The results of mass loss, pH change and Mg ion concentration, together, confirmed the degradation rate of Mg alloys of interest in the following order, starting from slowest degradation: ZSr41A<ZSr41B~ZSr41C<ZSr41D.

2.3.3. *In vitro* cytocompatibility results of ZSr41 alloys with hESC

Fluorescence images from the 72 h cell culture study showed improved H9 hESC cytocompatibility with ZSr41 alloys compared with P-Mg, of which, ZSr41A alloy showed the best cytocompatibility overall. Normalized coverage of viable hESC colonies was determined through quantitative analyses of the fluorescence and phase contrast images and the results are plotted in Figure 2.8. Linear growth and proliferation of hESC colonies were observed in the positive control (blank, cells only, no Mg samples). All four ZSr41 alloys and P-Mg control eventually led

to cell death, but at a different rate. The ZSr41 alloys prolonged the cell survival as compared with P-Mg control. After 30 h of culture, all of the ZSr41 alloys exhibited coverage of viable cell colonies. In contrast, almost no viable hESC colonies were visible in the co-culture with P-Mg at the 30 h time interval. After 48 h of culture, almost no viable cells were present in the co-cultures with ZSr41B, C and D, but some viable cell colonies were still observed in the co-culture with ZSr41A. At the end of the 72 h study, ZSr41A alloy was the only one in which viable cell colonies were still observed in its co-culture.

Therefore, the 30 h time interval was chosen as the critical time point for further statistical analysis, because, at this time point, viable cell colonies were still present in the co-culture with ZSr41 alloys while the amount of viable cells in the co-culture with P-Mg was nearly zero (Figure 2.9). The Kruskal-Wallis test for non-parametric data showed significant differences in the means of viable cell colony coverage at 30 h [X^2 (5, N = 18) = 12.5041, $p < 0.05$]. The pair-wise comparison test revealed significantly less amounts of viable cell colonies in the co-cultures with ZSr41B, C, and D alloys and P-Mg when compared to the blank positive control (cells only). No statistically significant difference was detected between ZSr41A and the blank positive control at 30 h.

Phase contrast and fluorescence images of hESCs in Figure 2.10 indicated that ZSr41A was the only alloy where viable cells were present in co-culture at the end of 72 h study. Comparison of the cell response to the ZSr41 alloys and P-Mg in

Figure 2.10 also showed a slightly better cell viability in the culture with the ZSr41C sample than that for the ZSr41B, D, and P-Mg samples. All Mg-based samples exhibited an initial increase in cell coverage followed by a steady decrease over time due to the following reasons. During the initial interval (0-14 h), the hESCs lost their closely packed organization and began to disperse. Thus, the coverage area of viable cell colony appeared larger. In comparison with the blank positive control with cells only, all Mg-based samples showed a decrease in percentage of viable cell colony coverage after initial period.

In summary, the cell viability results confirmed that the cytocompatibility of the ZSr41 alloys following this order, starting from the most cytocompatible: ZSr41A>ZSr41C>ZSr41B~ZSr41D>P-Mg.

2.3.4. Surface morphology and composition of ZSr41 alloys after cell culture

The ZSr41 alloys were characterized after degradation in the cell culture, as shown in Figure 2.11 and 2.12. Figure 2.11 shows the surface morphology and composition at 1,000x magnification where apparent degradation products were observed on all four ZSr41 alloys and P-Mg control. The ZSr41B, ZSr41D, and P-Mg showed severe local corrosion and similar surface morphology. Less severe but localized corrosion along the grain boundaries was seen in ZSr41A and ZSr41C alloys. When compared to the grain size visible in P-Mg, the grains in the ZSr41 alloys were considerably smaller due to the refining effect of Sr [15]. Among

the ZSr41 alloys, the grain refinement effect of Sr was more pronounced in ZSr41A, ZSr41B and ZSr41C. Figure 2.12 shows the surface morphology of ZSr41 alloys and P-Mg at 5,000x magnification. Formation of nano-sized needle-like surface features was identified on ZSr41B, ZSr41D and P-Mg. SEM images at 5,000x magnification further confirmed that ZSr41A and ZSr41C alloys degraded in a similar fashion, i.e., localized degradation at the grain boundaries.

The results of EDS analyses at 1,000x magnification indicated the presence of Chlorine (Cl) on the surface of the samples that exhibited more aggressive corrosion, namely ZSr41B, ZSr41D and P-Mg (Figure 2.11, A'-E' EDS spectra). In addition to Cl, other elements, including Mg, Zn, Sr, O, Ca, Phosphorus (P), and Carbon (C) were identified on the surface of the post-degraded samples. Ca, P and C and the increasing amount of O were precipitated from the cell culture media. Importantly, less amount of O (~36 wt. %) was found on the surfaces of ZSr41A and ZSr41C than that found on the surface of ZSr41B, ZSr41D and P-Mg (~50 wt. %) which experienced more aggressive corrosion. EDS analyses also detected more Ca and P on the surface of ZSr41A and ZSr41C as compared with ZSr41B and ZSr41D.

2.4. Discussion

Degradation properties and cytocompatibility of Mg alloys are correlated design criteria and are equally important for the development of better Mg alloys to meet clinical needs. In this study, four ZSr41 alloys were developed based on the

beneficial effects of Zn and Sr on Mg alloy properties, and their degradation properties and cytocompatibility were investigated for medical applications. The ZSr41 alloys were co-cultured *in vitro* with hESCs to study the alloy degradation and interactions with cells in a physiologically simulated and sensitive environment.

The results of this study provided evidence on how fast these ZSr41 Mg alloys degraded in the cell culture, and how the cells responded to degradation products. ZSr41A alloy exhibited superior cytocompatibility and slower degradation as compared with ZSr41B, ZSr41C, ZSr41D, and P-Mg. Specifically, ZSr41A showed less mass loss during 72 h of co-culturing with hESCs, indicating a slower degradation. Furthermore, ZSr41A had a less pronounced effect on pH increase of cell culture media as compared with the other alloys and P-Mg. The ICP-AES results on Mg ion concentration further confirmed that less amount of Mg ions was solubilized in the cell culture media during the degradation of ZSr41A at each prescribed time, as compared to the other ZSr41 alloys and P-Mg control. In addition, the average Mg ion, and calculated Zn and Sr concentrations in the cell culture media were below the therapeutic dosages that have been shown to be beneficial for humans (Table 2.1) [16-18]. The slower release of soluble degradation products (Mg ions and hydroxide ions) from the ZSr41A alloy may have contributed to the improved cell viability around ZSr41A.

The results of this *in vitro* study showed that the viability of the H9 hESCs improved in the co-culture with ZSr41A when compared with the co-culture with the other ZSr41 alloys and P-Mg. The lower Mg ion concentration induced by slower degradation of ZSr41A was speculated to be one of the major contributing factors. Specifically, the results showed that viability of hESCs improved at an Mg ion concentration (48 h average) of 13.6±0.8 mM for ZSr41A, when compared with ZSr41B, C, D, and P-Mg, which had concentrations in the range of 17.0±2.3 to 18.4±0.6 mM. These results are within the Mg lethal dosage (LD50) previously reported in literature (Table 2.1) [19]. Specifically, Feyerabend et al. reported that the LD50 tested with different cell lines *in vitro* was between 50 mM and 73 mM during a 48 h incubation period [19]. Due to the inherent differences between H9 hESC and HUCPV cells tested in literature, the Mg ion concentration at LD50 was much lower for the H9 hESC (< 18 mM) than that for HUCPV (73 mM) [19]. In other words, this comparison suggested a greater sensitivity associated with the h9-hESC model. Additionally, the calculated Zn and Sr concentrations were also much lower than the respective lethal dosage reported in literature (Table 2.1) [20, 21]. However, in order to confirm the comparison of cytotoxicity evaluation between the models based on the H9 hESCs and other cell lines (such as HUCPV), further *in vitro* studies would be beneficial if the exact same cell culture procedures were followed to evaluate the cytotoxicity of the same Mg alloy [22].

Addition of 0.15 wt. % Sr to Mg alloys (ZSr41A) resulted in formation of dispersed intermetallic phases and considerably improved degradation and

cytocompatibility properties for clinical applications. However, continuous increase of the amount of Sr in Mg alloys (ZSr41B, ZSr41C and ZSr41D) did not show evident benefits. It has been shown that the solubility of Sr in Mg is between 0.11 and 0.15 wt. % at 450-570 °C [23]. Other studies have reported that addition of 0.1 to 0.3 wt. % Sr to AZ91 Mg alloys resulted in refinement of the alloy microstructure [24]. Previous results indicated that ZSr41 with 1 wt. % Sr resulted in grain refinement of the alloy as a result of formation of $Zn_{13}Sr$, a dispersed intermetallic phase. During solidification, the $Zn_{13}Sr$ phase was pushed to the crystal growth edge of the primary α-Mg phase to restrain the growth of dendrites and led to grain refinement [25]. The grain refinement behavior was clearly identifiable in SEM images of ZSr41A but not as obvious for ZSr41D (1.5 wt. % Sr addition). The lack of grain refinement observed in ZSr41D could be explained by the limited solubility of Sr in Mg and would agree with other studies which showed that addition of more than 0.7 wt. % Sr to an Mg-based alloy did not lead to grain refinement, but instead resulted in easier recrystallization that decreased mechanical properties of Mg-based alloys [26]. In addition, as the amount of Sr added into Mg alloys increased, the corrosion rate of Mg alloys also accelerated due to the increased formation of galvanic couples between the Mg matrix and intermetallic Mg-Zn-Sr phases [27]. These results indicated that the addition of Sr to the Mg-Zn alloy was critical and beneficial. Specifically, 0.15 wt. % was optimal for the improvement of mechanical properties and corrosion properties of the material.

The degradation results of this *in vitro* study indicated that the presence of physiological ions and other components in the culture media might also contributed to the degradation mode and rate of ZSr41 alloys. Witte et al. also speculated that tissue oxygen, water content, carbon dioxide, the physiological salt concentration in blood, and the cellular metabolism were responsible for the degradation of magnesium *in vivo* [28]. For example, the presence of Cl^- ions was only detected on the surfaces of ZSr41B, ZSr41D, and P-Mg by EDS, but not on ZSr41A and ZSr41C. Meanwhile, SEM images showed that ZSr41B, D, and P-Mg exhibited more severe corrosion after 72 h cell culture, as compared with ZSr41A and C. These results matched the literature report that Cl ions (Cl^-) contributed to severe pitting corrosion in Mg alloys due to the formation of highly soluble magnesium chloride [29]. The cytocompatibility results showed a similar trend as the degradation results, i.e., prolonged and improved cell viability in the co-cultures with ZSr41A and ZSr41C as compared with ZSr41B, ZSr41D and P-Mg. The correlation between the degradation and cytocompatibility results was apparent when considering them together.

In summary, this study pointed out that the degradation properties and cytocompatibility of the Mg-Zn-Sr ternary alloys were highly dependent on the amounts of Sr added. The ZSr41A alloy with 0.15 wt. % Sr was the most promising candidate for biomedical applications due to its slower degradation and improved cell viability. However, further *in vitro* studies with primary cell cultures and *in vivo*

studies in an actual implant environment are necessary to obtain a more thorough cytocompatibility assessment prior to translating to clinical applications [22, 30].

2.5. Conclusion

This first *in vitro* study of Mg-Zn-Sr ternary alloys using a hESC-based model enabled the sensitive screening of four distinct alloy compositions for biomedical implant applications. The results showed enhanced cytocompatibility with the ZSr41A alloy compared to the other ZSr41 alloy compositions studied. Enhanced cell viability with ZSr41A alloy was due to its slower degradation, as indicated by less mass loss, less pH increase in media, and lower Mg ion concentration detected in media. The slower degradation of ZSr41A alloy can be attributed to the grain refining effects of Sr and the effects of Zn and Sr on corrosion resistance. In this study, the hESC culture model was used due to its inherent sensitivity to degradation products. The H9 hESC model can serve as an initial *in vitro* screening model to demonstrate the biocompatibility and biosafety of novel biomaterials at the early stage. However, long-term cell studies and animal studies in response to the new ZSr41 alloys are still needed in order to translate this new alloy to clinical applications.

2.6. Figures and tables

Figure 2.1: Surface characterization (low magnification) of ZSr41 alloys.
(A-E) Scanning electron micrographs of (A) ZSr41A, (B) ZSr41B, (C) ZSr41C, (D) ZSr41D, and (E) P-Mg after surface polishing at a magnification of 5,000x. (A'-E') EDS spectra and surface elemental composition (wt. %) of (A') ZSr41A, (B') ZSr41B, (C') ZSr41C, (D') ZSr41D, and (E') P-Mg. Accelerating voltage was 25 kV. Scale bars = 10 µm.

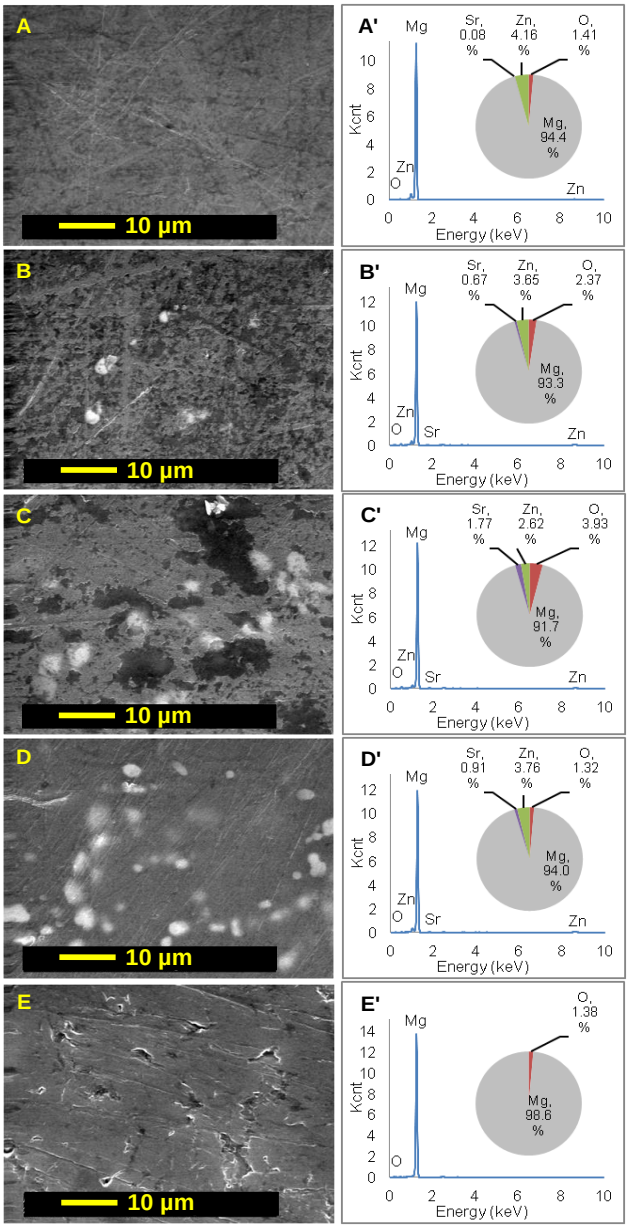

Figure 2.2: Surface characterization of oxidized regions in ZSr41 alloys.
(A) Scanning electron micrograph of ZSr41C at a 25 kV accelerating voltage with a magnification of 25,000x. Scale bar = 2 µm. (A') EDS spectrum and surface elemental composition (wt. %) of the highlighted area on the ZSr41C surface.

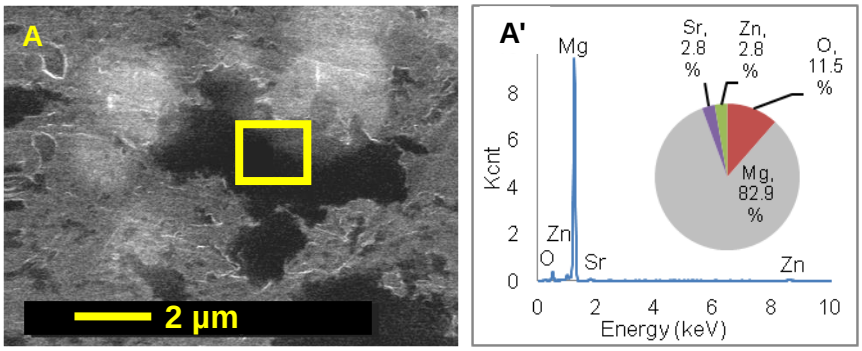

Figure 2.3: Surface characterization (high magnification) of ZSr41 alloys.
(A-E) Scanning electron micrographs of (A) ZSr41A, (B) ZSr41B, (C) ZSr41C, (D) ZSr41D, and (E) P-Mg after surface polishing at a magnification of 25,000x. (A'-E') EDS spectra and surface elemental composition (wt. %) of (A') ZSr41A, (B') ZSr41B highlighted area, (C') ZSr41C highlighted area, (D') ZSr41D highlighted area, and (E') P-Mg. Accelerating voltage was 25 kV. Scale bars = 2 µm.

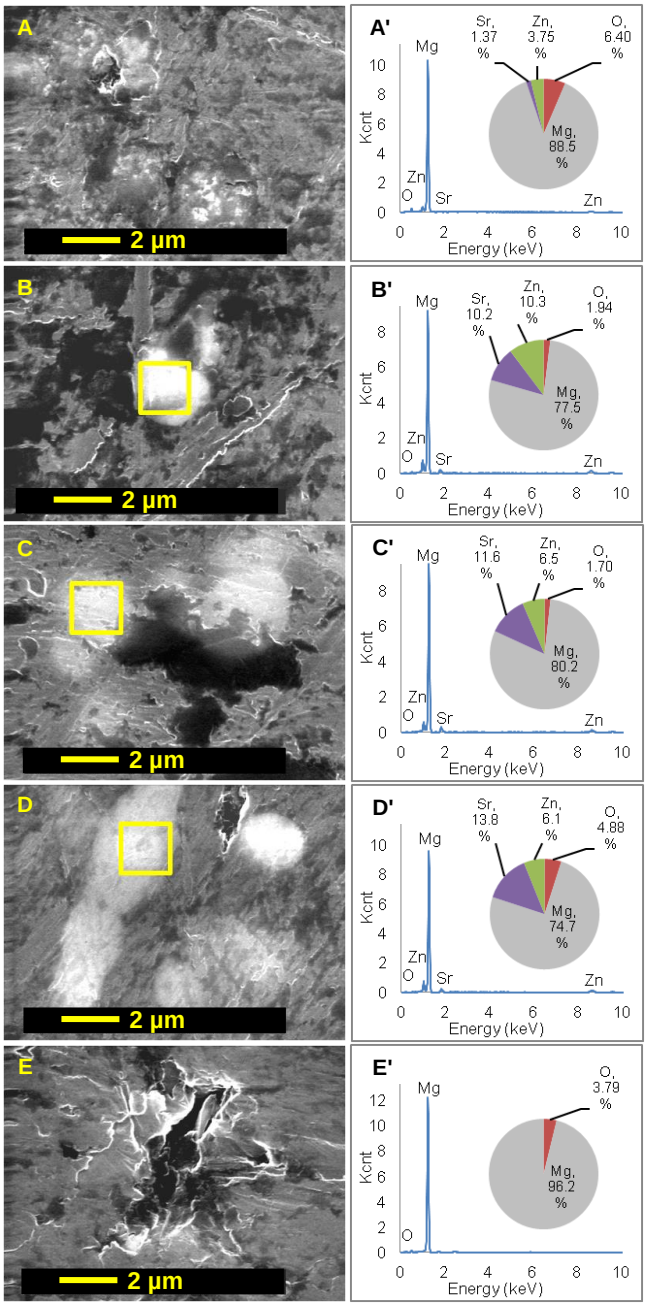

Figure 2.4: Total mass loss per unit area of ZSr41 alloys and the control after culturing with H9 hESC for 72 h.
Values are mean ± SEM; n =3; *p < 0.05 compared to ZSr41D; **p < 0.05 compared to P-Mg.

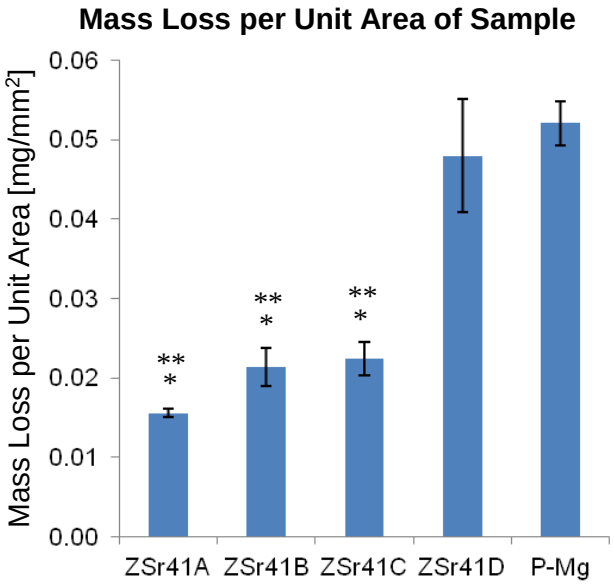

Figure 2.5: pH change of H9 hESC culture media as a result of degradation of ZSr41 alloys, P-Mg, and blank control (cells only).
Values are mean ± SEM; n =3; $p < 0.05$ when comparing ZSr41A to other ZSr41 compositions, P-Mg, and blank control at all time points.

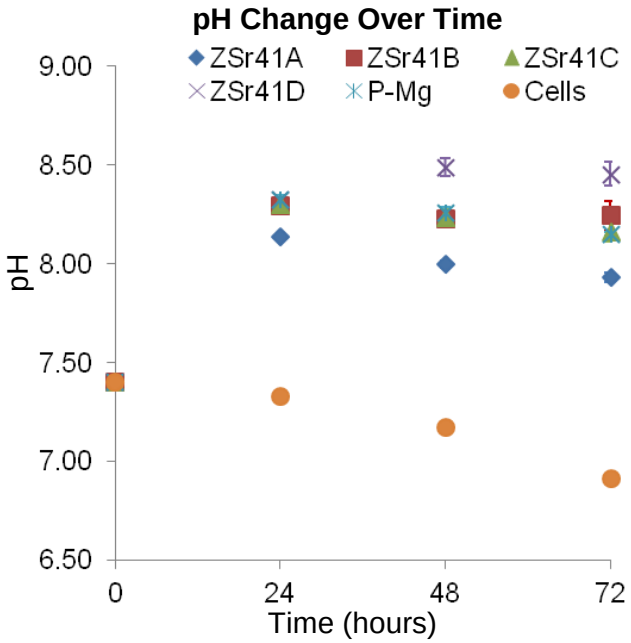

Figure 2.6: The change of Mg ionic concentration in the cell culture media as a result of degradation of ZSr41 alloys and P-Mg.
Mg ions in the media but not from Mg degradation were subtracted. Values are mean ± SEM; n = 3. Post hoc pair-wise comparison tests combined with Holm-Bonferroni correction only detected significant difference between ZSr41A and ZSr41D. Note: mg/L = ppm.

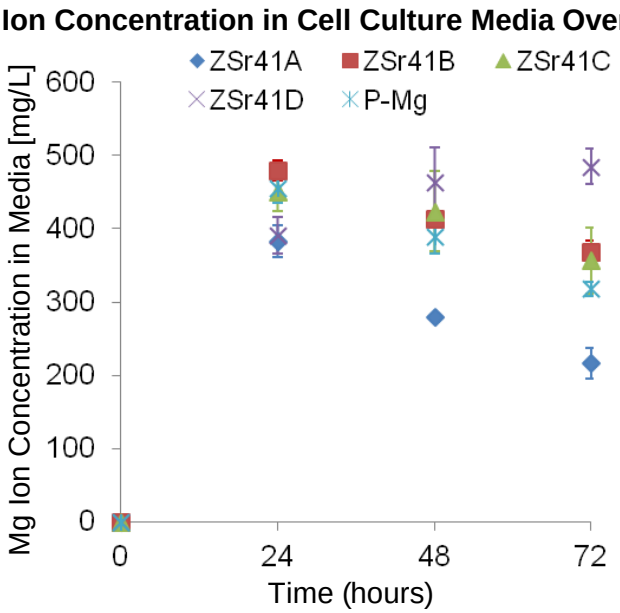

Figure 2.7: Total combined amount of Mg dissolved in the cell culture media over 72 hours as a result of degradation of ZSr41 alloys and P-Mg.
The total amount was calculated by first multiplying the Mg ion concentration measured at each prescribed time interval by the volume of each sample and then combining the total Mg collected at 24, 48 and 72 h time points. Values are mean ± SEM; n = 3; *$p < 0.05$ compared to ZSr41A.

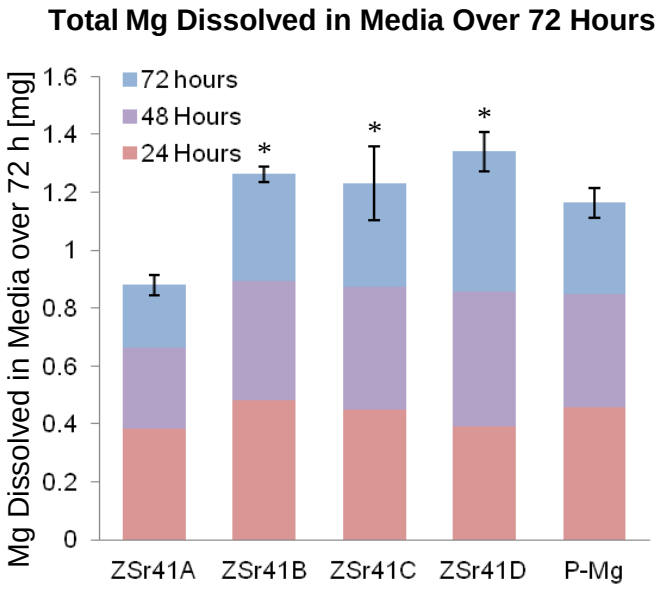

Figure 2.8: The change of viable H9 hESC colony coverage over time after exposure to ZSr41 alloys and P-Mg degradation products as compared with the blank positive control (cells only, no Mg samples).
The coverage area of viable cell colonies at each time point was normalized by the initial cell coverage area at time zero.

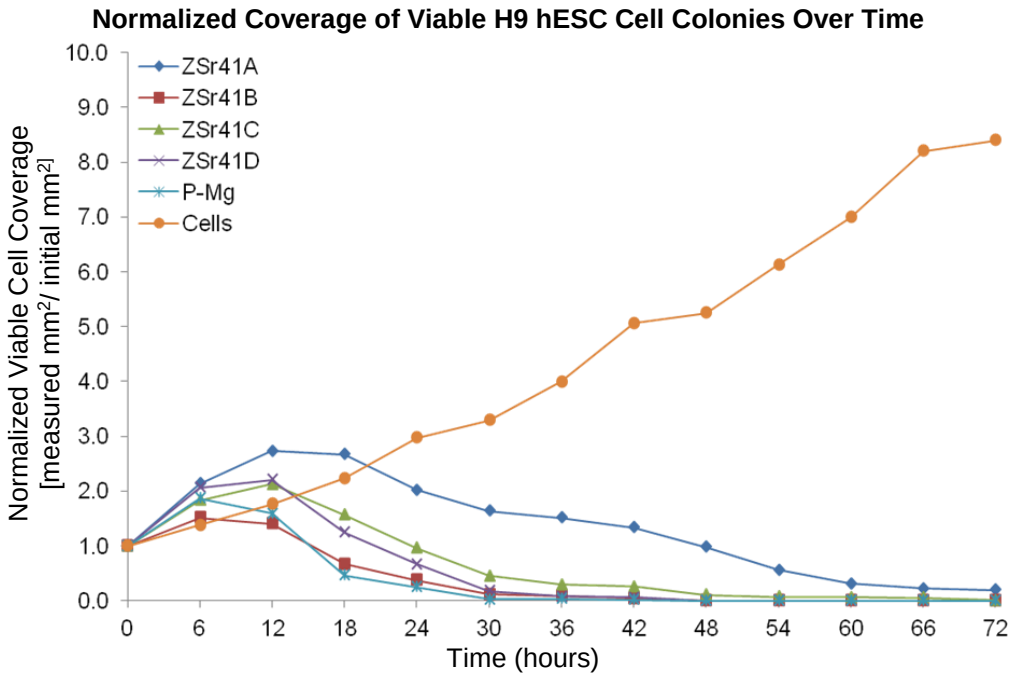

Figure 2.9: Normalized viable H9 hESC colony coverage after exposure to ZSr41 alloy and P-Mg degradation products for 30 h as compared with the blank positive control (cells only, no Mg samples).
The coverage area of viable cell colonies was normalized by the initial cell coverage area at time zero. Values are mean ± SEM; n =3; *$p < 0.05$ when comparing ZSr41B, C, D, and P-Mg with the blank positive control (cells only). No statistically significant difference was detected between ZSr41A and the blank positive control.

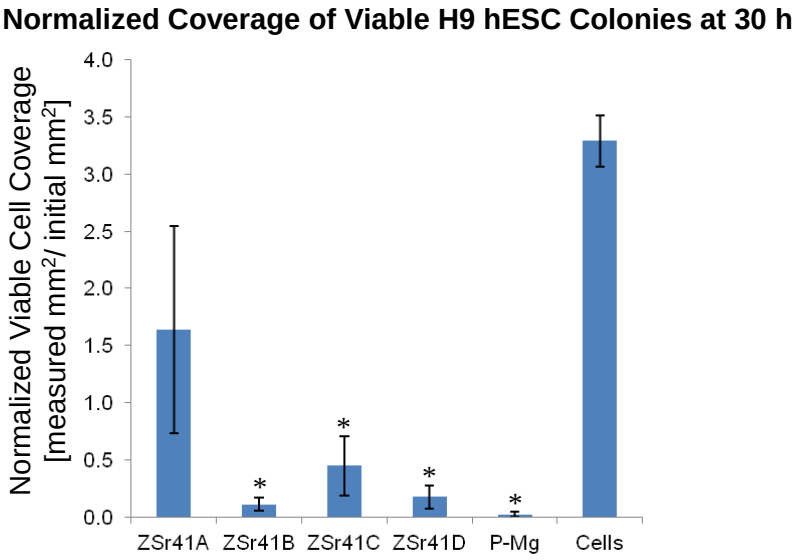

Figure 2.10: Montage of merged fluorescence and phase contrast images of H9 hESCs when co-cultured with ZSr41 alloys, P-Mg, and blank positive control (cells only) at the prescribed time intervals during the 72 h of cell culture.
All images in the montage have the same magnification as shown by the 400 µm scale bar.

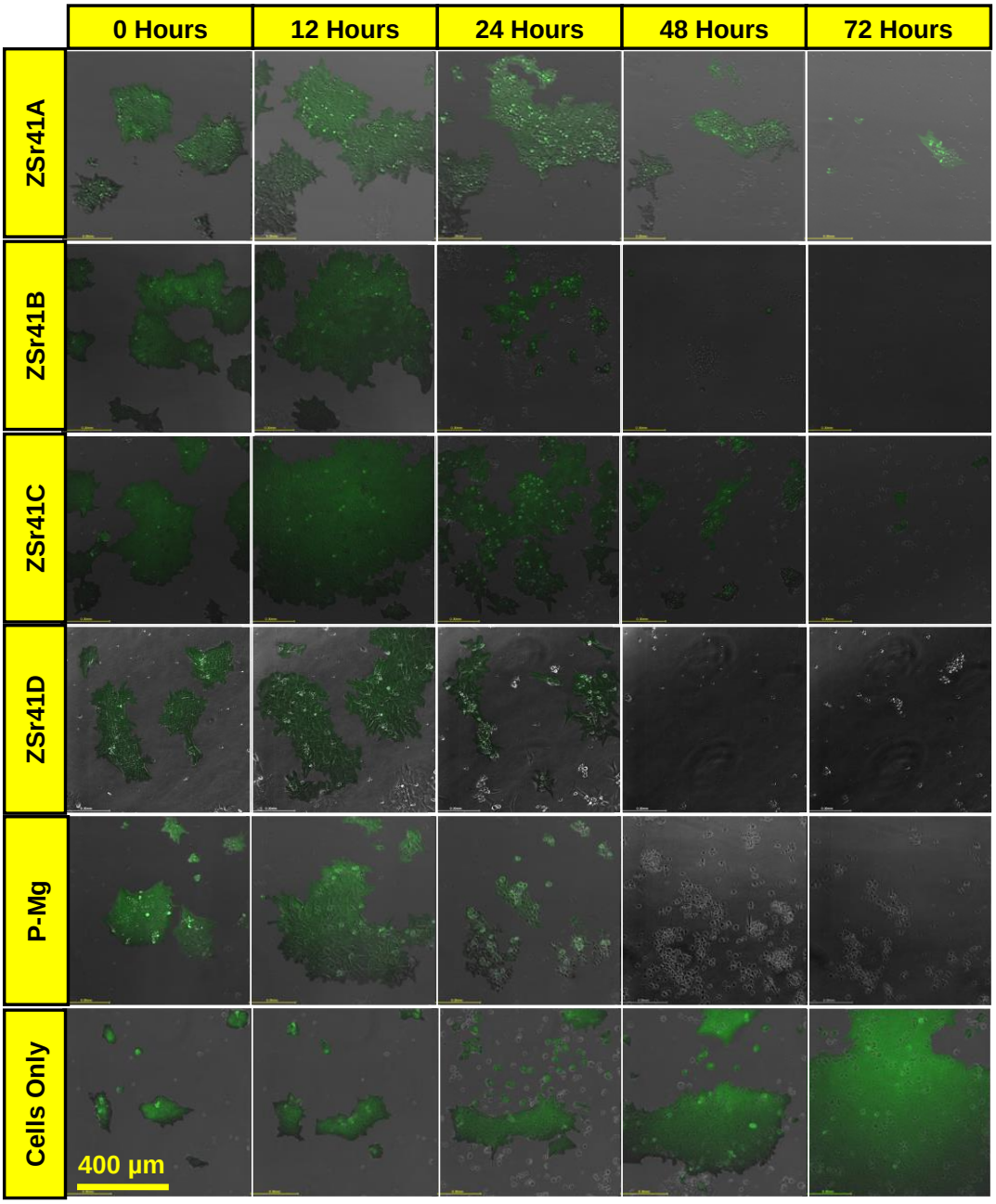

Figure 2.11: Surface characterization (low magnification) of ZSr41 alloys post-incubation with H9-hESCs for 72 hrs.

(A-E) Scanning electron micrographs of (A) ZSr41A, (B) ZSr41B, (C) ZSr41C, (D) ZSr41D, and (E) P-Mg after 72-h degradation in hESC culture at a magnification of 1,000x. (A'-E') EDS spectra and surface elemental composition (wt. %) of (A') ZSr41A, (B') ZSr41B, (C') ZSr41C, (D') ZSr41D, and (E') P-Mg. Accelerating voltage was 25 kV. Scale bars = 50 µm.

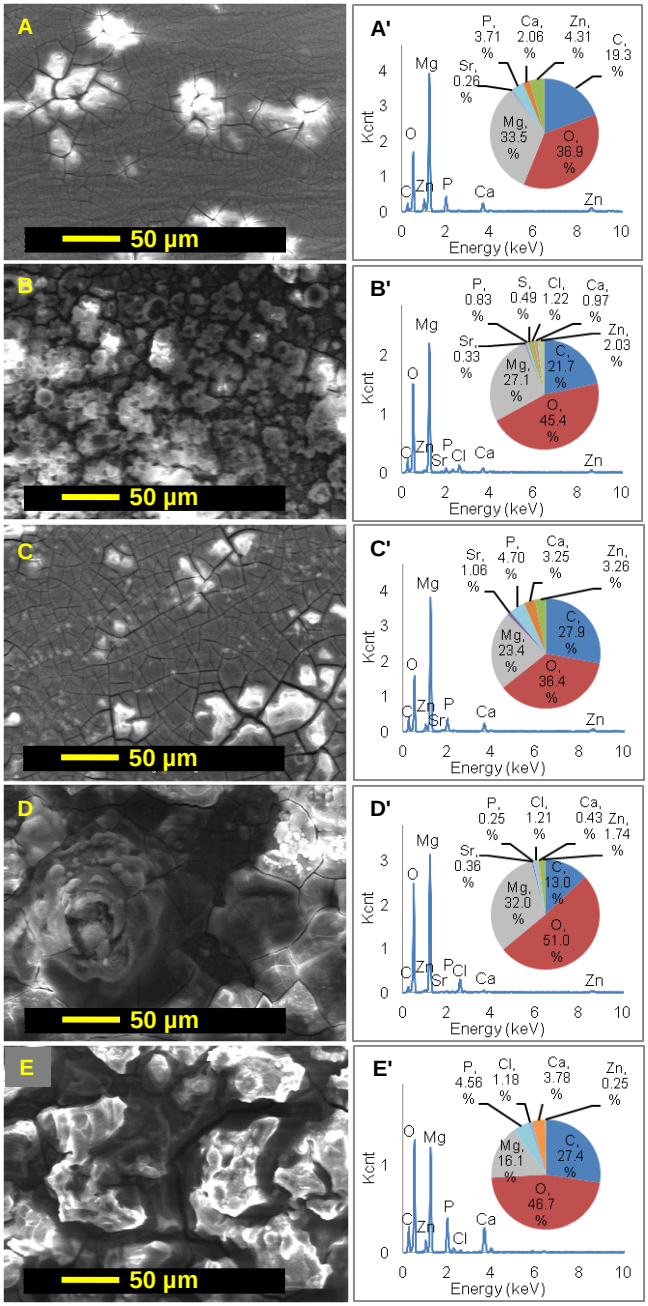

Figure 2.12: Surface characterization (high magnification) of ZSr41 alloys post-incubation with H9-hESCs for 72 hrs.

Scanning electron micrographs of (A) ZSr41A, (B) ZSr41B, (C) ZSr41C, (D) ZSr41D, and (E) P-Mg after 72-h degradation in hESC culture at a magnification of 5,000x. Accelerating voltage was 25 kV. Scale bars = 10 µm.

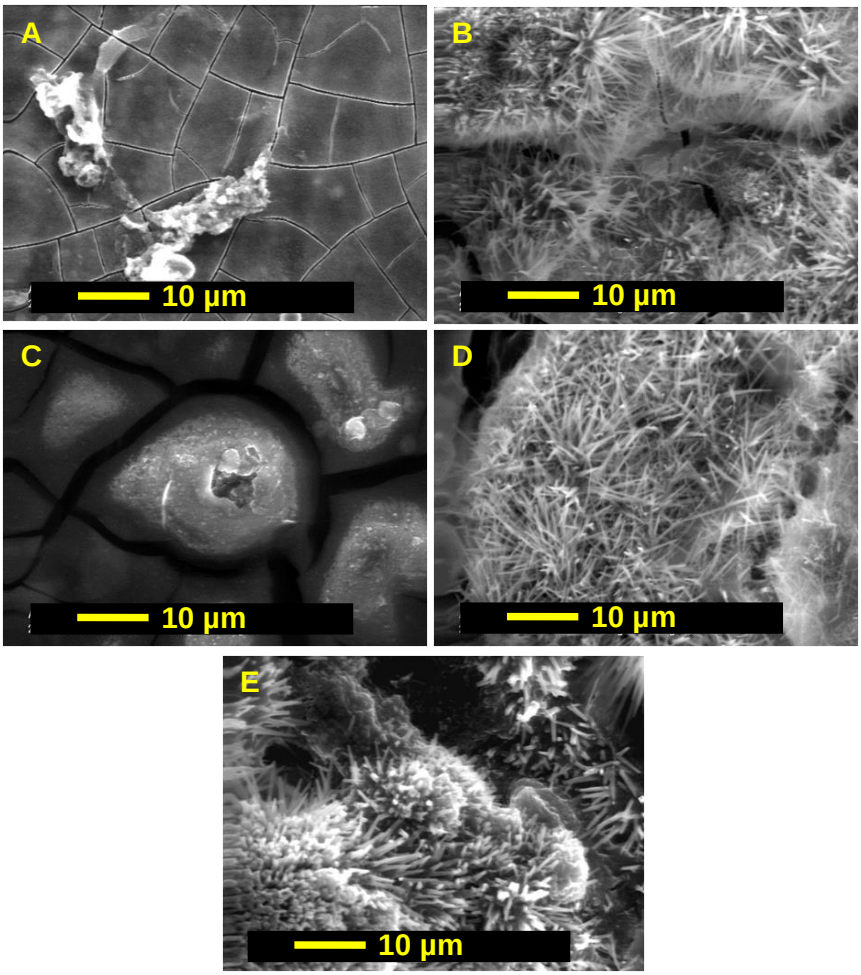

Table 2.1: The average Mg ion concentrations, the calculated Zn and Sr concentrations in the media co-cultured with the ZSr41 alloys and P-Mg during the first 48-hour culture period in comparison with the respective therapeutic daily dosages and the lethal dosages (LD50) of Mg, Zn and Sr.

Mg, Zn and Sr at the therapeutic daily dosage level showed clinical benefits to patients [16-18]. Lethal dosage of Mg ions (in the form of $MgCl_2$) was detected *in vitro* by literature [19]. Lethal dosage of Zn (in the form of $ZnSO_4$) was detected by intravenous administration to dogs [20]. Lethal dosage of Sr (in the form of $SrCl_2$) was detected by intravenous administration to mice [21]. Mg ion concentrations induced by degradation of ZSr41 alloys were below the LD50 of Mg ion concentrations reported in [19], indicating the greater sensitivity of hESC model in detecting subtle cytotoxic effects.

	Mg Ion Concentration [mM]	**Zn Concentration [mM]**	**Sr Concentration [mM]**
ZSr41A	13.6±0.8	0.200±0.0120	0.006±0.0003
ZSr41B	18.4±0.6	0.270±0.0092	0.025±0.0009
ZSr41C	18.0±2.9	0.270±0.0430	0.050±0.0080
ZSr41D	17.0±2.3	0.250±0.0340	0.071±0.0096
P-Mg	17.4±1.6	N/A	N/A
Therapeutic Daily Dosage	24-40 [17]	0.9 [18]	5.9 [16]
Lethal Dosage (LD50)	50-73 [19]	3.7 [20]	33.8 [21]

2.7. References

[1] Laschinski G, Vogel R, Spielmann H. Cytotoxicity test using blastocyst-derived euploid embryonal stem cells: A new approach to in vitro teratogenesis screening. Reprod Toxicol. 1991;5:57-64.

[2] Talbot P, Lin S. Mouse and Human Embryonic Stem Cells: Can They Improve Human Health by Preventing Disease? Curr Top Med Chem. 2011;11:1638-52.

[3] Seiler AE, Spielmann H. The validated embryonic stem cell test to predict embryotoxicity in vitro. Nat Protoc. 2011;6:961-78.

[4] West PR, Weir AM, Smith AM, Donley ELR, Cezar GG. Predicting human developmental toxicity of pharmaceuticals using human embryonic stem cells and metabolomics. Toxicol Appl Pharm. 2010;247:18-27.

[5] Davila JC, Cezar GG, Thiede M, Strom S, Miki T, Trosko J. Use and Application of Stem Cells in Toxicology. Toxicological Sciences. 2004;79:214-23.

[6] Adler S, Pellizzer C, Hareng L, Hartung T, Bremer S. First steps in establishing a developmental toxicity test method based on human embryonic stem cells. Toxicol In Vitro. 2008;22:200-11.

[7] Eiges R, Schuldiner M, Drukker M, Yanuka O, Itskovitz-Eldor J, Benvenisty N. Establishment of human embryonic stem cell-transfected clones carrying a marker for undifferentiated cells. Curr Biol. 2001;11:514-8.

[8] Hidaka K, Lee JK, Kim HS, Ihm CH, Iio A, Ogawa M, et al. Chamber-specific differentiation of Nkx2.5-positive cardiac precursor cells from murine embryonic stem cells. FASEB J. 2003;17:740-2.

[9] Johnson I, Perchy D, Liu H. In vitro evaluation of the surface effects on magnesium-yttrium alloy degradation and mesenchymal stem cell adhesion. J Biomed Mater Res A. 2011;100A:477–85.

[10] Guan RG, Johnson I, Cui T, Zhao T, Zhao ZY, Li X, et al. Electrodeposition of hydroxyapatite coating on Mg-4.0Zn-1.0Ca-0.6Zr alloy and in vitro evaluation of degradation, hemolysis, and cytotoxicity. J Biomed Mater Res A. 2012;100:999-1015.

[11] Xin Y, Huo K, Tao H, Tang G, Chu PK. Influence of aggressive ions on the degradation behavior of biomedical magnesium alloy in physiological environment. Acta Biomater. 2008;4:2008-15.

[12] Rettig R, Virtanen S. Composition of corrosion layers on a magnesium rare-earth alloy in simulated body fluids. J Biomed Mater Res Part A. 2009;88:359-69.

[13] Zainal Abidin NI, Martin D, Atrens A. Corrosion of high purity Mg, AZ91, ZE41 and Mg2Zn0.2Mn in Hank's solution at room temperature. Corros Sci. 2011;53:862-72.

[14] Liu H. The effects of surface and biomolecules on magnesium degradation and mesenchymal stem cell adhesion. J Biomed Mater Res A. 2011;99:249-60.

[15] Yang M, Pan F, Cheng R, Tang A. Effect of Mg–10Sr master alloy on grain refinement of AZ31 magnesium alloy. Mater Sci Eng, A. 2008;491:440-5.

[16] Marie PJ, Ammann P, Boivin G, Rey C. Mechanisms of Action and Therapeutic Potential of Strontium in Bone. Calcif Tissue Int. 2001;69:121-9.

[17] Noronha JL, Matuschak GM. Magnesium in critical illness: metabolism, assessment, and treatment. Intensive Care Med. 2002;28:667-79.

[18] Fosmire GJ. Zinc toxicity. Am J Clin Nutr. 1990;51:225-7.

[19] Feyerabend F, Fischer J, Holtz J, Witte F, Willumeit R, Drücker H, et al. Evaluation of short-term effects of rare earth and other elements used in magnesium alloys on primary cells and cell lines. Acta Biomater. 2010;6:1834-42.

[20] Winek CL, Buehler EV. Intravenous toxicity of zinc pyridinethione and several zinc salts. Toxicol Appl Pharmacol. 1966;9:269-73.

[21] Kroes R, den Tonkelaar EM, Minderhoud A, Speijers GJ, Vonk-Visser DM, Berkvens JM, et al. Short-term toxicity of strontium chloride in rats. Toxicology. 1977;7:11-21.

[22] Pizzoferrato A, Ciapetti G, Stea S, Cenni E, Arciola CR, Granchi D, et al. Cell culture methods for testing biocompatibility. Clin Mater. 1994;15:173-90.

[23] Zhang Z, Couture A, Luo A. An investigation of the properties of Mg-Zn-Al alloys. Journal Name: Scripta Materialia; Journal Volume: 39; Journal Issue: 1; Other Information: PBD: 5 Jun 1998. 1998:Medium: X; Size: pp. 45-53.

[24] Liu SF, Liu LY, Kang LG. Refinement role of electromagnetic stirring and strontium in AZ91 magnesium alloy. J Alloy Compd. 2008;450:546-50.

[25] Guan RG, Cipriano AF, Zhao ZY, Lock J, Tie D, Zhao T, et al. Development and Evaluation of a Magnesium-Zinc-Strontium Alloy for Biomedical Applications – Alloy Processing, Microstructure, Mechanical Properties, and Biodegradation. Mater Sci Eng, C. 2013;33:3661-9.

[26] Borkar H, Hoseini M, Pekguleryuz M. Effect of strontium on flow behavior and texture evolution during the hot deformation of Mg–1 wt%Mn alloy. Mater Sci Eng, A. 2012;537:49-57.

[27] Gu XN, Xie XH, Li N, Zheng YF, Qin L. In vitro and in vivo studies on a Mg-Sr binary alloy system developed as a new kind of biodegradable metal. Acta Biomater. 2012.

[28] Witte F. The history of biodegradable magnesium implants: a review. Acta Biomater. 2010;6:1680-92.

[29] Witte F, Hort N, Vogt C, Cohen S, Kainer KU, Willumeit R, et al. Degradable biomaterials based on magnesium corrosion. Curr Opin Solid State Mater Sci. 2008;12:63-72.

[30] Ziats NP, Miller KM, Anderson JM. In vitro and in vivo interactions of cells with biomaterials. Biomaterials. 1988;9:5-13.

Chapter 3 – Investigation on Magnesium-Zinc-Calcium alloys and bone marrow derived mesenchymal stem cell responses in direct culture

3.1. Background

The objective of this study was to characterize the as-cast Mg-xZn-0.5Ca (x = 0.5, 1.0, 2.0, or 4.0 wt. %) alloys, and determine adhesion and morphology of bone marrow derived mesenchymal stem cells (BMSCs) at the interface with the Mg-xZn-0.5Ca alloys, using the direct culture method *in vitro*. The use of BMSCs for this *in vitro* study was motivated by their important roles in early implant osseointegration and bone regeneration *in vivo* [1]. Other research groups have also supported the applicability of BMSCs for testing the cytocompatibility of Mg-based materials for orthopedic applications [2]. It has also been suggested that the degradation of Mg-based materials in Dulbecco's Modified Eagle Medium (DMEM) resembled *in vivo* conditions more closely due to the presence of physiologically relevant ions and proteins [3-5]. To highlight the significance and novelty of this study in comparison with the state-of-the-art, a thorough review on the history and current development of as-cast crystalline Mg-Zn-Ca ternary alloys is summarized in Table 3.1 [6-26]. To our knowledge, this is the first comprehensive report on (i) the interactions of BMSCs with the degradation products at the dynamic cell-substrate interface under direct contact condition, (ii) the effects of degradation products on adhesion, morphology and viability of BMSCs surrounding the substrate under indirect contact condition, (iii) the *in vitro* degradation of as-cast

Mg-xZn-0.5Ca (x = 0.5, 1.0, 2.0, or 4.0 wt. %) alloys in the presence of BMSCs, and (iv) the respective effects of each soluble degradation product on BMSC behaviors to elucidate the mechanisms of BMSC responses to alloy degradation. This study provides mechanistic insights on BMSC responses to the promising Mg-Zn-Ca alloys for musculoskeletal applications as a function of increasing Zn content, demonstrates the subtle modulatory effects of surface topography and degradation products on BMSC behaviors, and establishes the *in vitro* model and methodology that can be standardized for screening bioresorbable alloys for musculoskeletal applications.

3.2. Materials and methods

3.2.1. Preparation of Mg-xZn-0.5Ca alloy and Mg control

The Mg-Zn-Ca alloys in this study had a nominal composition of x = 0.5, 1.0, 2.0, or 4.0 wt. % Zn and 0.5 wt. % Ca in the Mg matrix. These alloys were designated according to their Zn content as 0.5Zn, 1Zn, 2Zn, and 4Zn, respectively. The alloy was produced by a metallurgical process consisting of melting and casting. Briefly, a stainless steel crucible (Shenyang General Furnace Manufacturing Co., Ltd, Liaoning, China) was first preheated in a customized electrical-resistance furnace (Shenyang General Furnace Manufacturing Co., Ltd) to 400-500°C and 99.95% pure Mg ingots (Yinguang Magnesium Industry Group Co., Ltd., Shanxi, China) were melted under an argon (Ar) gas protected environment. Commercially available bulk metallic Zn (99.5%; HuLuDao Zinc

Industry Co., Ltd., Liaoning, China) and Ca (99.9% Yinguang Magnesium Industry Group Co., Ltd.) were preheated to remove moisture, added into the Mg, and the mixture was stirred and heated for 20 min at 700-720 °C. The mixture was then degassed with hexachloroethane and deslagged to ensure purity of the alloy melt, and cast as ingots at 720 °C. Subsequently, the Mg-xZn-0.5Ca ingots were cut into (0.44 ± 0.06) mm thick sheets using a wire electric discharge machine (Agiecut 200 VHP, AgieCharmilles, LincoInshire, IL, USA). Commercially pure Mg sheets (99.9%, as rolled; Goodfellow Co., Coraopolis, PA, USA) with a nominal thickness of 0.5 mm (0.47 ± 0.02 measured) was studied as a control in this study. The as-produced Mg-xZn-0.5Ca and pure Mg sheets were cut into (5.04 ± 0.34) mm x (5.08 ± 0.29) mm squares for surface characterization, electrochemical tests, and *in vitro* cell culture experiments.

3.2.2. Microstructure characterization

Prior to degradation and cell experiments, the microstructure of the Mg-xZn-0.5Ca alloys and Mg control was characterized using a scanning electron microscope (SEM; Nova NanoSEM 450, FEI Co., Hillsboro, OR, USA). For microstructure characterization, the samples were ground with SiC abrasive paper (Ted Pella Inc., Redding, CA, USA) up to 1200 grit, and fine polished up to 0.25 µm with polycrystalline diamond paste (Physical Test Solutions, Culver City, CA, USA). Surface elemental composition and distribution were analyzed with energy dispersive x-ray spectroscopy (EDS) using a Nova NanoSEM 450 equipped with

an X-Max50 detector and AZtecEnergy software (Oxford Instruments, Abingdon, Oxfordshire, UK). An accelerating voltage of 20 kV was used to obtain SEM images and perform EDS analysis. Additionally, x-ray diffraction (XRD; Empyrean, PANalytical, Westborough, MA, USA) was used to analyze the crystal structures of the phases present. All XRD spectra were acquired using Cu Kα radiation (45 kV, 40 mA) at a step size of 0.006 degree, and dwell time of 50 sec using a PIXcel 1D detector (PANalytical). Phase identification was performed using the HighScore software (PANalytical).

3.2.3. Electrochemical testing

Potentiodynamic polarization (PDP) curves were obtained using a potentiostat (Model 273A, Princeton Applied Research, Oak Ridge, TN, USA) with a three-electrode cell configuration and acquired with PowerSuite 2.50.0 software (Princeton Applied Research). The Mg-xZn-0.5Ca and Mg samples were connected to copper wire using copper tape and embedded in epoxy resin as the working electrode, platinum foil was used as the counter electrode, and a silver/silver chloride (Ag/AgCl) electrode was used as reference. Embedding the Mg-based samples in epoxy resin (Cat# ULTRA-3000R-32, Pace Technologies, Tucson, AZ, USA) was to expose only one 5 x 5 mm surface (0.25 cm^2). The epoxy resin also insulated the electrical connection between the sample and the copper wire. A 5 x 5 mm face of the embedded metallic samples was then ground with SiC abrasive paper up to 1200 grit and ultrasonically cleaned for 15 min in separate

baths of acetone and ethanol prior to electrochemical experiments. Revised simulated body fluid (r-SBF) at pH 7.4 was used as the electrolyte and maintained at 37.5 °C during PDP scans. The composition of r-SBF is the same as human blood plasma and described elsewhere [27]. PDP scans were obtained without equilibration of the working electrode. The potential was scanned from 0.5 to -3.5 V at a scanning rate of 20 mV s^{-1}. Values for corrosion potential (E_{corr}) and corrosion current density (J_{corr}) were extrapolated from the PDP curves according to ASTM G102-89 standard. All potentials are in reference to Ag/AgCl electrode.

3.2.4. BMSC responses and *in vitro* degradation of Mg-xZn-0.5Ca alloys

3.2.4.1. Preparation of BMSC culture

Following a protocol approved by the University of California at Riverside (UCR) Institutional Animal Care and Use Committee (IACUC), BMSCs were harvested from the marrow cavity of the femur and tibia of three-week-old female Sprague Dawley rat weanlings after euthanasia by CO_2. Specific details regarding BMSC extraction, isolation and culture are described previously [28]. Briefly, the distal and proximal ends of the bones were dissected and the bone marrow was flushed out of the bone cavity and collected using Dulbecco's Modified Eagle Medium (DMEM; Sigma Aldrich, St. Louis, MO, USA) supplemented with 10% fetal bovine serum (FBS; HyClone, Logan, UT, USA) and 1% penicillin/streptomycin (P/S; Invitrogen, Grand Island, NY, USA). Hereafter, DMEM + 10% FBS + 1% P/S is referred to as DMEM. The collected cells were then filtered through a 70-μm

nylon strainer to remove cell aggregates and tissue debris. The filtered BMSCs were cultured in DMEM under standard cell culture conditions (i.e., 37 ºC, 5%/95% CO_2/air, humidified sterile environment) to 90-95% confluency. Subsequently, BMSCs were detached using Trypsin (Invitrogen) and passaged up to the second passage (P2) for culture with Mg-xZn-0.5Ca alloys.

3.2.4.2. Direct culture of BMSCs with Mg-xZn-0.5Ca alloys

Prior to cell culture experiments, the Mg-xZn-0.5Ca alloy and Mg samples were ground with SiC abrasive paper up to 1200 grit, ultrasonically cleaned for 15 min in separate baths of acetone and ethanol, individually weighed (M_0), and sterilized under ultraviolet (UV) radiation for 4 hr on each side. Non-culture treated glass slides (Cat#12-544-1, Fisher Scientific, Hampton, NH, USA) with a thickness of 1 mm were cut into 5 x 5 mm squares, cleaned in acetone and ethanol, sterilized under UV radiation, and used as a reference. All the samples were placed in standard 12-well cell culture treated plates and rinsed with 2 mL of DMEM to calibrate the osmotic pressure. Subsequently, BMSCs (P2) were seeded directly onto the surfaces of the samples at a density of $4x10^4$ cells cm^{-2} and incubated in 3 mL of DMEM under standard cell culture conditions for 24, 48, and 72 hr. A positive control, designated as "cells" group, consisted of BMSCs cultured only with DMEM in the wells, i.e. without any samples. DMEM alone was also used as a blank reference and designated as “DMEM” group. In order to more closely mimic *in vivo* conditions where the circulation system regularly takes away soluble

degradation products from the local site of implantation [29], the cell culture media was collected for analysis and replenished with 3 mL of fresh media (pH 7.4) at every 24 hr interval.

3.2.4.3. Characterization of the BMSCs in direct contact with Mg-xZn-0.5Ca alloys

The interface between the BMSC monolayer and Mg-xZn-0.5Ca alloys, Mg, and glass samples at 24, 48, and 72 hr incubation was characterized using SEM. Additionally, corresponding surface elemental composition, and element distribution maps were acquired with EDS. The samples used for SEM and EDS analysis were removed from the wells and dip-rinsed in phosphate buffered saline (PBS) to remove non-adherent cells. Adherent cells were fixed with 3% glutaraldehyde in 0.1 M potassium phosphate buffer for 1 hr. After fixation, the samples were again dip-rinsed in PBS followed by a serial dehydration in increasing ethanol concentration (50%, 75%, 90%, 2x100%; 10 min each). The samples were then critical-point dried (Autosamdri-815, Tousimis Research Corp., Rockville, MD, USA) and sputter coated (Model 108, Cressington Scientific Instruments Ltd., Watford, UK) with platinum/palladium at 20 mA and 40 sec sputter time.

3.2.4.4. Quantification of BMSC adhesion and morphology under direct versus indirect contact conditions

BMSC adhesion and morphology on the surface of the samples (*direct contact* with the sample) and on culture plate surrounding the respective samples (*indirect contact* with the sample) was evaluated at 24, 48, and 72 hr of incubation through fluorescence microscopy. The results from the culture plates were grouped separately and designated as “plate”. The samples in direct contact with BMSCs were removed from the wells and dip-rinsed in PBS to remove non-adherent cells. The corresponding wells were washed separately with PBS to remove non-adherent cells. Adherent cells, both on the sample surface and on the plates, were separately fixed with 4% formaldehyde (10% neutral buffered formalin; VWR, Radnor, PA, USA) and stained with 4',6-diamidino-2-phenylindole dilactate (DAPI; Invitrogen) nucleic acid stain and Alexa Flour® 488 F-actin stain for fluorescence imaging. Adherent cells on the sample surface and on the culture plate surrounding the sample were visualized using a fluorescence microscope (Eclipse Ti and NIS software, Nikon, Melville, NY, USA) with a 10x objective lens at the same exposure condition and analyzed using Image J (NIH, Bethesda, MD, USA). Cell adhesion per group was quantified by counting the DAPI-stained cell nuclei at five random locations on the sample surface and at nine random locations on the culture plate at each prescribed incubation interval. Cell adhesion density was calculated as the number of adherent cells per unit area. Cell morphology was quantified by manually outlining twenty cells per image per group (on both sample surface and

culture plate) in ImageJ and obtaining values for average F-actin area per BMSC nucleus, maximum Feret diameter (D_{max}) of cells, and Feret diameter aspect ratio of cells (D_{max}/D_{min}). D_{min} is the minimum Feret diameter.

3.2.4.5. *In vitro* degradation of Mg-xZn-0.5Ca alloys in the BMSC culture

At each prescribed incubation interval, the *in vitro* degradation of the Mg-xZn-0.5Ca alloys and Mg was evaluated through measurements of pH and ionic concentrations of the collected media, and through the change in mass of each sample. The pH of the media at each incubation interval was measured immediately after collection using a calibrated pH meter (Model SB70P, VWR). The concentration of Mg^{2+}, Zn^{2+}, and Ca^{2+} ions in the collected media was measured using inductively coupled plasma optical emission spectroscopy (ICP-OES; Optima 8000, Perkin Elmer, Waltham, MA, USA). In order to minimize matrix effects in ICP-OES, the collected DMEM aliquots were diluted to 1:100 solutions in DI water. Ionic concentrations were then obtained from calibration curves generated using Mg, Zn, and Ca standards (Perkin Elmer) diluted to ranges of 0.5-5.0, 0.1-1.0, and 0.1-1.0 mg/L respectively. Finally, the initial (M_o) and final masses of each sample at each time point (M_i) were used to calculate the change in mass (percentage) with respect to initial mass (M_i/M_o)*100.

3.2.4.6. Effects of media alkalinity and Mg^{2+} ion concentration on BMSC viability and morphology

In order to identify which factor(s) modulated BMSC viability or morphology, separate experiments evaluating the effects of increasing Mg^{2+} ion concentration and increase in pH in the cell culture media were carried out. BMSCs (P2) were seeded in standard 12-well cell culture treated plates at a density of $4x10^4$ cells cm^{-2} and incubated in 3 mL of DMEM under standard cell culture conditions for 24 hr. Subsequently, the media was removed and replenished with 3 mL of (i) DMEM with pH values intentionally adjusted to 7.4, 8.1, 8.5, 9.0, and 9.5, or (ii) DMEM supplemented with respective Mg^{2+} ion concentrations of 0, 2, 4, 10, 20, 30, and 40 mM. BMSCs were then incubated under standard cell culture conditions with the adjusted media conditions for another 24 hr. Specific details used for adjusting pH and supplementing Mg^{2+} ions are described elsewhere [30]. When using $MgCl_2•6H_2O$ to prepare the cell culture media supplemented with Mg^{2+} ions, the measured Mg^{2+} ion concentrations in the supplemented media were less than the theoretical calculations because $MgCl_2•6H_2O$ is highly hygroscopic. Depending on the degree of salt hydration, the actual Mg^{2+} ion concentrations measured by ICP-OES were 1.3, 2.6, 6.7, 13.1, 21.1, and 27.6 mM respectively, instead of the theoretical values of 2, 4, 10, 20, 30, and 40 mM. DMEM incubated for 24 hr without cells was used as a blank reference. Adhered cells were fixed and stained, and viability and morphology of adhered BMSCs was analyzed and quantified using the same method described above. BMSC behaviors after 24 hr of incubation was

evaluated to compare with direct culture experiments (direct and indirect contact) since our cytocompatibility experiments with Mg-xZn-0.5Ca alloys consisted of repeated 24 hr incubation intervals (for a total of 72 hr). The culture media after 24 hr incubation with BMSCs was analyzed for change in pH and Mg^{2+} ion concentration as described above.

3.2.5. Statistical analyses

Electrochemical, cell adhesion and morphology through fluorescence, *in vitro* degradation, and alkalinity and Mg^{2+} ion experiments were run in triplicate. All data sets were tested for normal distribution and homogeneous variance. Parametric data sets were analyzed using one-way analysis of variance (ANOVA) followed by the Tukey HSD *post hoc* test. Data sets with normal distribution but heterogeneous variance were analyzed using one-way ANOVA (homogeneous variance not assumed) followed by the Games-Howell *post hoc* test. Non-parametric data sets were analyzed using the Kruskal-Wallis test followed by either the Nemenyi *post hoc* test (equal sample sizes) or the Dunn *post hoc* test (unequal sample sizes). Statistical significance was considered at $p < 0.05$.

3.3. Results

3.3.1. Microstructure of Mg-xZn-0.5Ca alloys

Figure 3.1 shows SEM micrographs of the microstructures of Mg-xZn-0.5Ca alloys and Mg control. The 0.5Zn alloy (Figure 3.1a) showed an α-Mg matrix and

continuous network of eutectic second phase which had a lamellar structure located primarily at the grain boundaries. The composition of the phases was verified through EDS point analyses (Figure 3.2). EDS results for 0.5Zn (Figure 3.2a and 3.2b) showed that the α-Mg matrix of 0.5Zn (point 3) was slightly enriched with Zn (0.87 at. %; 2.47 wt. %), which was less than the Zn content at point 1 and 2 of the second phase (13.83 at. % and 5.76 at. % for point 1 and 2, respectively). The bright second phase (point 1) was a Mg-Zn-Ca ternary phase with a Zn/Ca at. % ratio of 1.5, and the dark second phase (point 2) was also a Mg-Zn-Ca ternary phase with a Zn/Ca at. % ratio of 1.5 but contained higher Mg compared with point 1 (bright phase). The 1Zn alloy (Figure 3.1b) showed an α-Mg matrix, and the eutectic second phase was not a continuous network but rather finely dispersed with two visibly distinct regions. EDS results for 1Zn (Figure 3.2c and 3.2d) showed that the α-Mg matrix of 1Zn (point 6) was also slightly enriched with Zn (0.43 at. %; 1.24 wt. %), which was less than the Zn content at point 4 and 5 of the second phase (9.3 at. % and 7.06 at. % for point 4 and 5, respectively). The bright second phase (point 4) was a Mg-Zn-Ca ternary phase with a Zn/Ca at. % ratio of 1.0, and the dark second phase (point 5) was also a Mg-Zn-Ca ternary phase with a Zn/Ca at. % ratio of 0.6. Both secondary phases in the 1Zn alloy showed a similar Mg content. The 2Zn alloy (Figure 3.1c) showed an α-Mg matrix and a larger amount of fine secondary phases than 0.5Zn and 1Zn. Similar to 1Zn, the second phase in 2Zn was not a continuous network but rather finely dispersed granules located along the grain boundaries. Inspection of the second phase of 2Zn showed that

the dark spots pertained to the α-Mg matrix of the alloy. EDS results for 2Zn (Figure 3.2e and 3.2f) showed that the α-Mg matrix of 2Zn (point 8) was enriched with Zn (1.04 at. %; 2.9 wt. %), and the bright second phase (point 7) was a Mg-Zn-Ca ternary phase with a much greater Zn content (8.11 at. %) and a Zn/Ca at. % ratio of 1.6. The 4Zn alloy (Figure 3.1d) showed an α-Mg matrix, and a network of coarsely granular secondary phases which did not contain visibly distinct regions (i.e. bright/dark phases). EDS results for 4Zn (Figure 3.2g and 3.2h) showed that the α-Mg matrix of 4Zn (point 10) was enriched with Zn (1.57 at. %; 4.35 wt. %), and the bright second phase (point 9) was a Mg-Zn-Ca ternary phase with a much greater Zn content (20.71 at. %) and a Zn/Ca at. % ratio of 2.2. The Zn content in the secondary phase of the 4Zn alloy was dramatically higher (20.7 at. %) compared with the other Mg-xZn-0.5Ca alloys. EDS analysis of all second phases showed that they contained approximately 2 at. % aluminum (Al). Figure 3.1e shows the surface of the commercially pure Mg used as a control. Figure 3.1f shows a quantification of surface elemental composition through EDS area analysis of the Mg-xZn-0.5Ca alloys and pure Mg control at 600x magnification. Increasing Zn content was observed in each of the alloys. Specifically, 0.5Zn contained 0.64 wt. %, 1Zn contained 1.15 wt. %, 2Zn contained 2.4 wt. %, and 4Zn contained 4.44 wt. %. Ca content in all alloys was approximately 0.3 wt. %. Al peaks were not found at the low magnification EDS analysis, indicating that only trace amounts of Al were contained within the Mg-xZn-0.5Ca alloys. C and traces of O were found on the surface of all metallic samples. The surface elemental

composition (wt. %) of the glass slides used as reference for cell culture experiments was 61.97% O, 20.24% silicon (Si), 13.35% sodium (Na), 2.77% Mg, 0.95% Ca, and 0.71% potassium (K), as determined using EDS analysis (spectrum not shown).

XRD spectra for the phases in the 0.5Zn, 1Zn, 2Zn, and 4Zn alloys are shown in Figure 3.3 (curves a, b, c, and d respectively). The phases were identified according to patterns in the Inorganic Crystal Structure Database (ICSD): 01-071-6543 for Mg, 01-073-4526 for Mg_2Ca, 00-012-0266 for $Ca_2Mg_6Zn_3$, and 01-074-7069 for MgZn. The XRD pattern of 0.5Zn confirmed an α-Mg phase accompanied with Mg_2Ca and $Ca_2Mg_6Zn_3$ phases. Addition of 1-2 wt. % Zn (1Zn and 2Zn alloys, respectively) caused the Mg_2Ca phase to disappear and only α-Mg and $Ca_2Mg_6Zn_3$ phases were confirmed. Addition of 4 wt. % Zn (4Zn alloy) caused the precipitation of a Mg-Zn binary phase and α-Mg, $Ca_2Mg_6Zn_3$, and MgZn phases were confirmed.

3.3.2. Corrosion properties of Mg-xZn-0.5Ca alloys from electrochemical testing

PDP curves obtained for the polished samples showed that the initial corrosion (or degradation) behavior of the Mg-xZn-0.5Ca alloys and pure Mg control were similar. The median PDP trace with the most representative corrosion potential (E_{corr}) and corrosion current density (J_{corr}) for each sample type was plotted in Figure 3.4a. When compared with the pure Mg control, the PDP curves showed that the 2Zn alloy was slightly more cathodic, 0.5Zn was similar, and 1Zn and 4Zn

were slightly more anodic. Results based on the Tafel extrapolation of the PDP curves (Figure 3.4b) showed significant differences between E_{corr} [ANOVA; F (4, 10) = 10.969, p = 1.118x10^{-3}] and J_{corr} [ANOVA; F (4, 10) = 7.0155, p = 5.866x10^{-3}] among the metallic samples studied. Specifically, *post hoc* pairwise comparisons showed that the average E_{corr} value for 2Zn (-1.342 V) was significantly more cathodic when compared with 0.5Zn (-1.504 V), 1Zn (-1.606 V), 4Zn (-1.531 V), but not significantly lower than the pure as-rolled Mg control (-1.433 V). In contrast, only the average E_{corr} value for 1Zn was significantly more anodic when compared with pure Mg. In addition, average J_{corr} values were 22.174 mA cm^{-2} for 0.5Zn, 16.755 mA cm^{-2} for 1Zn, 21.914 mA cm^{-2} for 2Zn, 24.244 mA cm^{-2} for 4Zn, and 25.271 mA cm^{-2} for Mg. Statistical analysis showed a significantly lower J_{corr} value for 1Zn when compared with 4Zn and Mg.

3.3.3. BMSCs in direct contact with Mg-xZn-0.5Ca alloys

Analysis of the BMSC-substrate interface after 24, 48, and 72 hr culture showed distinct changes in surface topography and elemental composition for the Mg-xZn-0.5Ca alloys and Mg control compared with the glass reference. Additionally, cell-substrate interactions were determined through a qualitative assessment of BMSC morphologies at each incubation time point in response to the characteristics of the substrate interface.

Figure 3.5 shows the characterization of the cell-substrate interface for 0.5Zn, 1Zn, 2Zn, 4Zn, Mg, and glass at an original magnification of 150x (Figure 3.5a-

3.5f) and 4,000x (Figure 3.5a-3.5f insets), respectively, after 24 hr of direct culture and direct contact with the sample substrates. The color mapping in each image represents surface elemental distribution measured by EDS, where red = Mg, green = C, yellow = O, white = Si, pink = K and Na, orange = P, purple = Ca, and blue = Zn. Surface cracks (indicated with white arrows) and deposited degradation products (delineated with circles) were observed on the surfaces of all Mg-xZn-0.5Ca alloys and Mg. The cell morphology observed on the surface of all metallic samples showed relatively compact cell bodies compared with highly spread cells observed on the surface of the glass reference. These two distinct cell morphologies were referred as anisotropic and isotropic spreading, respectively [31]. Careful analysis showed that in addition to adhered and spread cells, spherical cells were also observed on the surface of all metallic samples and prominently on the glass reference (Figure 3.5f); EDS analysis confirmed that these spherical cells were in fact compact cell bodies. The insets in Figures 3.5a thru 3.5f show high magnification scanning electron micrographs (4,000x magnification) of cell protrusions (filopodia and lamellipodia) extending at the interface with each respective sample. These high magnification images showed cell protrusions bridging over surface cracks on all metallic samples. Quite notably, each sample exhibited a distinct sub-micron topography and distribution of surface cracks. Qualitatively, the highest degree of sub-micron spreading among the metallic samples was observed on the surface of Mg. Figure 3.5g summarizes the elemental composition (in wt. %) results obtained from EDS analyses at 150x

magnification. Increasing Zn content was detected on the surface of the Mg-xZn-0.5Ca alloys: 0.39%, 0.9%, 1.6%, and 3.35% for 0.5Zn, 1Zn, 2Zn, and 4Zn, respectively; as expected, Zn was not detected on the Mg or glass samples. In addition, all metallic samples showed approximately similar Ca deposition content: 1.23%, 1.62%, 1.34%, 1.31%, and 1.19% for 0.5Zn, 1Zn, 2Zn, 4Zn, and Mg, respectively; Ca was also detected on the glass reference (3.12%). Notably, the metallic samples all had a higher P deposition content when compared with the glass reference. Specifically, 4.63%, 6.28%, 4.46%, 5.69%, 4.05%, and 0% for 0.5Zn, 1Zn, 2Zn, 4Zn, Mg, and glass, respectively.

Figure 3.6 shows the characterization of the cell-substrate interface for 0.5Zn, 1Zn, 2Zn, 4Zn, Mg, and glass at an original magnification of 150x (Figure 3.6a-3.6f) and 2,500x (Figure 3.6a-3.6f insets), respectively, after 48 hr of direct culture and direct contact with the sample substrates. Surface cracks (indicated with white arrows) and degradation products (delineated with circles) were observed on the surfaces of all Mg-xZn-0.5Ca alloys and Mg, but were most prominent on the surface of the 4Zn sample (Figure 3.4d); the 0.5Zn, 1Zn, and Mg samples showed similar degradation behavior. Similar to the glass sample after 24 hr culture, spherical cells were observed on the surface of the glass reference (Figure 3.6f). The cells on the surface of the metallic substrates showed anisotropic spreading, but not as anisotropic as compared with their counterparts at the 24 hr culture; the glass reference continued to show prominent isotropic spreading. The cell monolayer was observed to be more continuous on the surface of the metallic

samples at this incubation period than at the 24 hr. The insets in Figures 3.6a thru 3.6f show high magnification scanning electron micrographs (2,500x magnification) of cell protrusions (filopodia and lamellipodia) extending at the interface with each respective sample. The differences in the sub-micron topography, such as plate-like patches on 4Zn and sub-micron cracks on Mg observed at the 24 hr incubation interval (Figures 3.5d and 3.5e, respectively), faded and all metallic samples displayed similar sub-micron features. Cell protrusions continued to extend across degradation cracks and even near areas of aggressive corrosion such as those seen on the surface of 4Zn (Figure 3.6d). Figure 3.6g summarizes the quantitative elemental composition results obtained from EDS analyses (in wt. %) at 150x magnification. Increasing Zn content was again detected on the surface of the Mg-xZn-0.5Ca alloys: 0.68%, 1.02% 2.03%, and 3.55% for 0.5Zn, 1Zn, 2Zn, and 4Zn respectively; as expected, Zn was not detected on the Mg or glass samples. In contrast to their counterparts at the 24 hr culture, the Mg-xZn-0.5Ca alloy samples showed different Ca deposition: 3.52% 1.27%, 1.22%, 3.75%, and 2.34% for 0.5Zn, 1Zn, 2Zn, 4Zn, and Mg, respectively; Ca was also detected on the glass sample (3.58%) which was similar to the value measured at 24 hr. The metallic samples all had a higher P deposition content when compared with the glass reference: 10.07%, 5.85%, 5.14%, 7.18%, 7.19%, and 0% for 0.5Zn, 1Zn, 2Zn, 4Zn, Mg, and glass, respectively.

Figure 3.7 shows the characterization of the cell-substrate interface for 0.5Zn, 1Zn, 2Zn, 4Zn, Mg, and glass at an original magnification of 150x (Figure 3.7a-

3.7f) and 2,500x (Figure 3.7a-3.7f insets), respectively, after 72 hr of direct culture and direct contact with the sample substrates. Surface cracks (indicated with white arrows) and degradation products (delineated with circles) were observed on the surfaces of all Mg-xZn-0.5Ca alloys and Mg. Alloy 0.5Zn showed a larger amount of degradation cracks compared with alloys 1Zn and 2Zn. Both 1Zn and 2Zn alloys showed similar characteristics in terms of the size and distribution of degradation cracks, and debris. In addition, the localized degradation observed on the surface of the 4Zn sample at 48 hr progressed into aggressive localized corrosion at 72 hr as seen in Figure 3.7d (circles were not used since areas of aggressive corrosion were prominently distributed all over the surface). The cells on the 1Zn and 2Zn samples showed a higher degree of isotropic spreading than their counterparts at the 48 hr culture, and the cells on the 0.5Zn and 4Zn samples continued to show signs of anisotropic spreading. In contrast to the glass samples at the 24 and 48 hr, the glass sample at 72 hr showed that almost all BMSCs had isotropic spreading (Figure 3.7f). The cell monolayer was observed to be relatively continuous on the surface of 1Zn, 2Zn, and Mg, but disrupted on the surface of the 0.5Zn and 4Zn samples due to the changes in surface topography caused by degradation. In contrast, the cell monolayer was nearly confluent on the surface of the glass reference with no spherical cells observed. The insets in Figures 3.7a thru 3.7f show high magnification scanning electron micrographs (2,500x magnification) of protrusions (filopodia and lamellipodia) extending at the interface with each respective sample. The cells observed on alloys 0.5Zn and 4Zn, where

degradation was more aggressive, showed abnormally extended protrusions. The cells on 1Zn, 2Zn, and Mg continued to bridge across the degradation cracks. Figure 3.7g summarizes the quantitative elemental composition results obtained from EDS analyses (in wt. %) at 150x magnification. Similar to the 24 and 48 hr samples, increasing Zn content was detected on the surface of the Mg-xZn-0.5Ca alloys: 0.71%, 0.81%, 2.24%, and 3.2% for 0.5Zn, 1Zn, 2Zn, and 4Zn, respectively; Zn was still not detected on the Mg or glass samples. The Mg-xZn-0.5Ca alloy samples continued to show different Ca deposition: 5.02%, 0.98%, 2.26%, 8.1%, and 2.74% for 0.5Zn, 1Zn, 2Zn, 4Zn, and Mg, respectively; Ca was also detected on the glass sample (2.94%) which was similar to the values measured at 24 and 48 hr. The metallic samples all had a higher P deposition content when compared with the glass reference, specifically, 11.05%, 3.23%, 7.99%, 10.47%, 6.96%, and 0% for 0.5Zn, 1Zn, 2Zn, 4Zn, Mg, and glass, respectively.

Common observations of BMSCs in direct contact with the substrates at all 3 time points (24, 48, and 72 hr) include the following: (1) BMSCs were able to attach to all Mg-based substrates; however, cell morphology on the Mg-based substrates differed and BMSCs showed more isotropic spreading on the glass reference than on the Mg-based substrates. (2) All Mg-based samples showed prominent Mg and O content (most likely in the form of MgO and/or $Mg(OH)_2$ from Mg degradation); and, P and Ca were detected on all Mg-based samples, indicating mineral precipitation. (3) EDS elemental distribution maps on the Mg-based samples after 72 hr of direct culture with BMSCs (Figure 3.8), showed that O was largely co-

localized with P and Ca, especially when the degradation was most evident (e.g., 0.5Zn and 4Zn samples at 72 hr). This O-P-Ca co-localized effect was not observed on the glass sample. Taken together, these observations indicated that Mg degradation products possibly attracted mineral deposition. (4) All samples showed C content, which was attributed to adhered cells, proteins, and extracellular matrix produced by cells. To assess possible correlation between surface composition and BMSC adhesion, elemental distribution maps of Mg, O, P, and Ca were cross-examined with the C distribution map; however, no detectable evidence indicated that surface chemistry would modulate the BMSC adhesion onto the Mg-xZn-0.5Ca alloys.

3.3.4. BMSC adhesion and proliferation in direct culture with the samples under direct and indirect contact conditions

Fluorescence images from the 24, 48, and 72 hr direct cultures on the surfaces of Mg-xZn-0.5Ca alloys, Mg control, and glass reference substrates (direct contact) are shown in Figure 3.9. Attached cells were observed on all substrates studied throughout the 72 hr culture. Fluorescence images from the culture plate surrounding each corresponding sample (indirect contact; image not shown) also showed adherent cells for all groups throughout the 72 hr culture. Similar to the observations from SEM analyses, the cells on the surface of the metallic samples showed a higher degree of anisotropic spreading, while the cells on the glass reference showed a preference towards isotropic spreading.

Results of BMSC adhesion density at 24, 48, and 72 hr direct cultures on the surfaces of Mg-xZn-0.5Ca alloys, Mg control, and glass reference substrates (direct contact with the sample) are summarized in Figure 3.10a. Results of BMSC adhesion on the tissue culture plates surrounding each sample (indirect contact with the sample) are summarized in Figure 3.10b. Statistically significant differences for cell adhesion density were detected neither on the sample surface at 24, 48, and 72 hr direct cultures, nor on the culture plates surrounding the sample at 24 and 72 hr. The only statistically significant difference detected using ANOVA was for the mean cell adhesion density on the culture plate at 48 hr [F (6, 17) = 9.6085, p = 1.092×10^{-4}]. *Post hoc* pairwise comparison showed a significantly lower BMSC adhesion density on the plate of 0.5Zn sample when compared with 1Zn, 2Zn, Mg, and cells only (positive control) conditions. Similarly, BMSC adhesion density on the 4Zn sample was found to be significantly lower compared with 2Zn and Mg. Additionally, 1Zn, 2Zn and Mg were all found to have a significantly higher BMSC adhesion density when compared with the glass reference. While the BMSC adhesion density on the surface of the sample (Figure 3.10a) showed no statistically significant differences, a general tendency of lower mean adhesion density was observed on the surface of the 4Zn sample. Further analysis of BMSC adhesion on the plates (Figure 3.10b) showed an increasing number of cells over time for all groups which was indicative of cell proliferation.

3.3.5. BMSC morphology in direct culture with the samples under direct and indirect contact conditions

Results of F-actin area per adhered BMSC nucleus at 24, 48, and 72 hr direct cultures on the surfaces of the samples (direct contact with the sample) and tissue culture plates surrounding the samples (indirect contact with the sample) are summarized in Figure 3.11. ANOVA confirmed statistical differences in the mean F-actin area per adhered BMSC nucleus on the surface of the samples (Figure 3.11a) at 24 hr [F (5, 12) = 12.784, p = 1.838×10^{-4}], 48 hr [F (5, 12) = 64.585, p = 2.96×10^{-8}], and 72 hr [F (5, 12) = 11.074, p = 3.653×10^{-4}]. Specifically, at 24 hr, *post hoc* pairwise comparisons showed significantly larger cells on the glass reference when compared with all metallic samples, and significantly smaller cells on 1Zn when compared with 0.5Zn, 2Zn, and Mg. At 48 hr, *post hoc* pairwise comparisons showed significantly larger cells on the glass reference when compared with the metallic samples; cells on Mg were significantly smaller when compared with 2Zn and 4Zn, cells on 4Zn were significantly larger when compared with 0.5Zn and 1Zn; and cells were significantly smaller on 0.5Zn when compared with 2Zn. At 72 hr, *post hoc* pairwise comparisons showed significantly smaller cells on the 0.5Zn sample when compared with all other groups tested. Furthermore, ANOVA also confirmed statistical differences in the mean F-actin area per adhered BMSC nucleus on the plates surrounding the samples (Figure 3.11b) at 24 hr [F (6, 17) = 6.881, p = 7.715×10^{-4}] and 48 hr [F (6, 17) = 4.0043, p = 1.109×10^{-2}]. No statistically significant differences were detected at 72 hr. *Post*

hoc pairwise comparisons at 24 hr showed significantly larger cells on the glass reference plate compared with the cells on the 0.5Zn, 1Zn, 2Zn, and Mg plates. Significantly larger cells were also found in the cells-only plate (positive control) when compared with the 2Zn plate. Additionally, *post hoc* pairwise comparisons at 48 hr showed significantly smaller cells on the Mg plate when compared with the cells on the 4Zn plate and cells-only plate.

Results from the quantification of D_{max} and diameter-based aspect ratio of adhered BMSCs at 24, 48, and 72 hr direct cultures on the surfaces of the samples (direct contact with the sample) and tissue culture plates surrounding the samples (indirect contact with the sample) are summarized in Figure 3.12. ANOVA (without homogeneous variance) confirmed statistical differences in the mean D_{max} of adhered BMSCs on the surface of the samples (Figure 3.12a) at 24 hr [F (5, 60) = 10.7478, p = 1.554×10^{-5}] and 48 hr [F (5, 60) = 8.1842, p = 1.135×10^{-4}]. No statistically significant differences were detected at 72 hr. Specifically, at 24 hr, *post hoc* pairwise comparisons showed that BMSCs on the surface of 1Zn had a significantly smaller D_{max} when compared with 0.5Zn, 4Zn, Mg, and the glass reference; D_{max} of BMSCs on the surface of 2Zn were significantly smaller when compared with 0.5Zn and the glass reference. At 48 hr, *post hoc* pairwise comparisons showed that BMSCs on the surface of 0.5Zn had a significantly smaller D_{max} when compared with 1Zn, 2Zn, and 4Zn; D_{max} of BMSCs on the surface of the glass reference were significantly larger when compared with 0.5Zn, 1Zn, 4Zn, and Mg. Moreover, ANOVA confirmed statistical differences in the mean

D_{max} of adhered BMSCs on the plates surrounding the samples (Figure 3.12b) only at 24 hr [F (6, 73) = 5.7963, p = 5.603x10^{-5}]; no statistically significant differences were found at 48 and 72 hr. *Post hoc* pairwise comparisons at 24 hr showed BMSCs on the plate surrounding the 0.5Zn sample had a significantly smaller D_{max} when compared with both glass reference and cells-only positive control; D_{max} of BMSCs on the plate surrounding the 1Zn sample was significantly smaller than the glass reference; and D_{max} of BMSCs on the plate surrounding the Mg sample was significantly smaller when compared with both glass reference and cells-only positive control. The aspect ratios of BMSCs on the surface of the samples (direct contact with the sample) and on the culture plate surrounding the samples (indirect contact with the sample) were calculated based on D_{max}/D_{min}, as summarized in Figures 3.12c and 3.12d, respectively. Statistical analyses of this data did not show any significant differences in cell aspect ratio at any time point. All analyzed cells showed an approximate aspect ratio of two, which means that in general, D_{max} was twice as large as the D_{min} and the general shape was elliptical. The fluorescence images in Figure 3.12d demonstrate the BMSCs with an aspect ratio of 1 or 2.

3.3.6. *In vitro* degradation of Mg-xZn-0.5Ca alloys during direct culture with BMSCs

Results of pH measurements of the collected media at 24, 48, and 72 hr are summarized in Figure 3.13a. The pH of DMEM (blank reference) showed different values at each incubation interval. DMEM uses a sodium bicarbonate ($NaHCO_3$)

buffer system that causes an alkaline shift when 5-10% CO_2 is not present [32]. Since the pH measurements of the collected media did not take place at 5-10% CO_2 and caused an alkaline shift of the baseline, we normalized the changes in the experimentally measured pH values by the mean change in blank DMEM at each time interval (DMEM pH was set at 7.4 immediately before replenishing). The normalized pH values for each group at each prescribed interval are summarized in Figure 3.13b. The normalized net pH change of the collected media could then be considered as either an alkaline change (> 1) or an acidic change (< 1), relative to the baseline, as a result from the degradation of Mg-based samples and/or cell metabolism. ANOVA (without homogeneous variance) confirmed statistical differences in the mean normalized pH values at the 24 hr time point [F (6, 60) = 29.5268, p = 1.63×10^{-9}]. *Post hoc* pairwise comparisons showed a significantly more alkaline media for the 0.5Zn, 1Zn, 2Zn, 4Zn, and Mg samples when compared with the glass reference and cells-only positive control. Additionally, the Kruskal-Wallis test for non-parametric data was used to confirm statistical differences in the normalized pH values at the 48 hr time point [X^2 (6, N = 42) = 21.977, p = 1.223×10^{-3}]. *Post hoc* pairwise comparisons showed a significantly more alkaline media for the 0.5Zn sample when compared with the glass reference, and a significantly more alkaline media for the 4Zn sample when compared with both glass reference and cells-only positive control. Furthermore, ANOVA confirmed statistical differences in the mean normalized pH values at the 72 hr time point [F (6, 17) = 18.057, p = 1.624×10^{-6}]. *Post hoc* pairwise comparisons

showed a significantly more alkaline media for the 2Zn sample when compared with 0.5Zn and cells-only positive control, and significantly more alkaline for the 4Zn sample when compared with all other groups. The normalized change in media pH for both glass and cells-only positive control at all incubation intervals was slightly more acidic, which was indicative of cell metabolism [30].

Figure 3.13c shows results of the change in mass at each time point relative to the initial mass of each metallic sample. No statistically significant differences were observed at the 24 hr time point. In contrast, ANOVA confirmed significant differences in the mean mass change at the 48 hr time point [F (4, 10) = 38.21, p = 4.972×10^{-6}]. *Post hoc* pairwise comparisons showed a significant mass gain on the Mg sample when compared with all the Mg-xZn-0.5Ca alloy samples. Moreover, the Kruskal-Wallis test was used to determine statistically significant differences in the mass change at the 72 hr time point [X^2 (4, N = 15) = 10.9, p = 2.771×10^{-2}]. Specifically, *post hoc* pairwise comparisons showed a significant mass gain on the Mg sample when compared with the 1Zn and 2Zn samples.

Results of Mg^{2+}, Zn^{2+}, and Ca^{2+} ion concentrations for all incubation time points are summarized in Figure 3.14. The Kruskal-Wallis test was used to confirm statistically significant differences in Mg^{2+} ion concentrations (Figure 3.14a) at 24 hr [X^2 (7, N = 84) = 65.8105, p = 1.033×10^{-11}], 48 hr [X^2 (7, N = 57) = 41.8486, p = 5.561×10^{-7}], and 72 hr [X^2 (7, N = 30) = 24.9312, p = 7.804×10^{-4}]. At 24 hr, *post hoc* pairwise comparisons showed significantly higher Mg^{2+} ion concentrations in

the media of the 0.5Zn, 1Zn, 2Zn, and 4Zn samples when each was compared with glass reference and cells-only positive control, and DMEM blank reference. Significantly higher Mg^{2+} ion concentration was also found for the media of the pure Mg sample when compared with the cells-only positive control and DMEM blank reference. At 48 hr, *post hoc* pairwise comparisons showed significantly higher Mg^{2+} ion concentrations in the media of the 0.5Zn and 1Zn samples only when compared with the cells-only positive control; significantly higher Mg^{2+} ion concentration was also found for the 4Zn sample media when compared with the cells-only positive control and DMEM blank reference. At 72 hr, *post hoc* pairwise comparisons showed significantly higher Mg^{2+} ion concentration only in the media of the 4Zn sample when compared with glass reference and DMEM blank reference. During all prescribed time intervals, the measured values of the media cultured with glass reference, cells-only positive control, and DMEM blank reference were in close agreement with literature values for Mg^{2+} ion concentration in DMEM [30]. In addition, the Kruskal-Wallis test was used to confirm statistically significant differences in Zn^{2+} ion concentrations (Figure 3.14b) at 24 hr [X^2 (7, N = 84) = 27.6874, $p = 2.505 \times 10^{-4}$] and 48 hr [X^2 (7, N = 57) = 22.0935, $p = 2.448 \times 10^{-3}$]; at the 72 hr incubation, the results were parametric and ANOVA was used to confirm statistical differences in the mean concentrations [F (7, 22) = 12.521, $p = 2.224 \times 10^{-6}$]. At 24 hr, *post hoc* pairwise comparisons showed a significantly higher Zn^{2+} ion concentration in the media of the 4Zn sample when compared with 1Zn, Mg, glass reference, cells-only positive control, and DMEM blank reference. At 48

hr, *post hoc* pairwise comparisons showed a significantly higher Zn^{2+} ion concentration in the media of the 4Zn sample when compared with 0.5Zn, cells-only positive control, and DMEM blank reference. At 72 hr, *post hoc* pairwise comparisons showed a significantly higher Zn^{2+} ion concentration in the media of the 4Zn sample when compared with all other groups. Moreover, ANOVA was used to confirm statistically significant differences in Ca^{2+} ion concentrations (Figure 3.14c) at 72 hr [F (7, 22) = 7.0426, p = 1.834×10^{-4}]; no statistically significant differences were found at the 24 or 48 hr time points. *Post hoc* pairwise comparisons showed significantly lower Ca^{2+} ion concentration in the media of the pure Mg sample when compared with 0.5Zn, 1Zn, glass reference, cells-only positive control, and DMEM blank reference; significantly lower Ca^{2+} ion concentration was also found in the media of the 4Zn sample when compared with the 1Zn sample. During all prescribed time intervals, the measured values of the media cultured with glass reference, cells-only positive control, and DMEM blank reference were in close agreement with literature values for Ca^{2+} ion concentration in DMEM [30].

Overall degradation results of Mg-xZn-0.5Ca alloy and pure Mg during the 72 hr period are summarized in Figure 3.15. The total Mg^{2+} ion amount shown in Figure 3.15a was calculated by first multiplying the Mg^{2+} ion concentration measured at each prescribed time interval (from ICP-OES measurements shown in Figure 3.14a) by the incubation volume of media (3 mL) and then combining the total amount of Mg^{2+} ion collected at 24, 48, and 72 hr time points. ANOVA was

used to confirm statistically significant differences in the total Mg^{2+} ion amount after 72 hr incubation [F (4, 10) = 6.6498, p = $7.057x10^{-3}$]; specifically, *post hoc* pairwise comparisons showed significantly higher total Mg amount contained in the media of the 4Zn sample when compared with 1Zn, 2Zn, and pure Mg groups. Furthermore, the total amount of Mg^{2+} ion per group was normalized by the initial exposed surface area of each sample to obtain a degradation rate based on initial geometry of the sample. Due to the dynamic nature of the degradable samples, the surface area changed at each time interval and only the initial surface area was fully characterized. The degradation rates of each alloy and pure Mg (given as a mass loss rate per unit area per day) are summarized in Figure 3.15b. ANOVA was used to confirm statistically significant differences in the degradation rates measured during BMSC culture [F (4, 10) = 6.2698, p = $8.612x10^{-3}$]. Specifically, *post hoc* pairwise comparisons showed a significantly higher degradation rate for the 4Zn alloy when compared with all other Mg-xZn-0.5Ca alloy compositions and pure Mg control.

3.3.7. Effects of media alkalinity and Mg^{2+} ion concentration on BMSC viability and morphology

Figure 3.16 shows the results for BMSC viability and morphology after 24 hr of incubation with the culture media intentionally adjusted to pH values of 7.4, 8.1, 8.5, 9.0, and 9.5. The lower end of pH 8.1 was selected because the degradation of the Mg-xZn-0.5Ca alloys caused an increase in pH up to 8.1 (Figure 3.13a)

without reducing cell viability. The higher end of pH 9.5 was selected because a previous study showed an increase of media pH up to 9.5 after culturing with a Mg alloy with 4 wt. % yttrium (Y) [5]. Although the metabolic activities of cells produce acidic metabolites that cause an acidic shift in media pH, this study focused on investigating the effects of alkaline media conditions induced by Mg degradation. Therefore, BMSC behaviors in media with pH values below the physiological pH of 7.4 were not investigated. Fluorescence images of BMSCs after 24 hr of culture with alkaline media are shown in Figure 3.16a. Attached and viable cells were observed in all alkaline media conditions and the cells in all groups showed isotropic spreading. Results of pH measurements of the collected media after 24 hr of incubation with BMSCs are summarized in Figure 3.16b. The pH of all the adjusted culture media decreased after 24 hr of cultures with BMSCs due to the pH buffering effect of DMEM and possible acidic metabolites produced by viable BMSCs. Specifically, the media initially adjusted at 8.1 changed to 8.01, 8.5 changed to 8.07, 9.0 changed to 8.10, and 9.5 changed to 8.18. In contrast, the blank media adjusted at 7.4 and incubated without cells (blank reference) showed a mean pH value of 8.11 after 24 hr of incubation. The difference between the pH values before incubation and after 24 hr indicated that the $NaHCO_3$ buffering system of DMEM in 5-10% CO_2 was most efficient in the 7.4-9.0 range tested. Results of BMSC adhesion density after 24 hr of culture in alkaline media with increased initial pH values are summarized in Figure 3.16c. Statistically significant differences in the mean cell density were confirmed by ANOVA [F (4, 10) = 3.3688,

p = 0.04528]. However, a general decrease in mean cell adhesion density on the culture plates was observed with increasing initial pH. *Post hoc* pairwise comparison showed a significantly lower BMSC adhesion density for the media adjusted to pH 9.5 compared with media at pH 7.4 ($1.60x10^4$ and $2.78x10^4$ cells cm^{-2}, respectively). Figure 3.16d summarizes the size of attached BMSCs as indicated by F-actin area per adhered nucleus. No statistically significant differences were detected in the cell size as a function of increasing initial pH of culture media. Similarly, Figure 3.16e summarizes the shape of adhered BMSCs as indicated by the cell diameter aspect ratio. No statistically significant differences were detected in the cell aspect ratio as a function of increasing initial pH of culture media.

The results of BMSC viability and morphology after 24 hr of incubation in culture media supplemented with 0, 1.3, 2.6, 6.7, 13.1, 21.1, and 27.6 mM of Mg^{2+} ions are shown in Figure 3.17. Figure 3.17a shows fluorescence images of BMSCs attached onto the culture plates after 24 hr of incubation in culture media supplemented with Mg^{2+} ions. Attached and viable cells were observed in all growth media conditions. The morphology of these cells indicated normal growth and isotropic spreading. Figure 3.17b summarizes the Mg^{2+} ion concentration of the culture media analyzed after 24 hr culture with BMSCs. An increasing trend of Mg^{2+} ion concentration in the post culture media of the experimental groups was confirmed. Culture media without supplemental Mg^{2+} ions and incubated for 24 hr without cells (blank reference) had a Mg^{2+} ion concentration of 0.87 mM, which is

in close agreement with literature values [30]. Furthermore, an increasing trend of Mg^{2+} ion concentration in the supplemented culture media was confirmed after 24 hr. Figure 3.17c summarizes the results of BMSC adhesion density after 24 hr of incubation with the culture media supplemented with increasing Mg^{2+} ion concentration. Statistically significant differences in the mean adhesion density were confirmed by ANOVA [F (6, 14) = 3.0721, p = 0.03916]. Interestingly, the only statistically significant difference in adhesion density, confirmed through *post hoc* analysis, was between the cells grown in media supplemented with 13.1 mM and 21.1 mM, which had adhesion densities of $2.04x10^4$ and $3.02x10^4$ cells cm^{-2}, respectively. Figures 3.17d and 3.17e show results of attached cell size and shape, respectively. After 24 hr of culture in the media supplemented with Mg^{2+} ions, the attached cells showed no statistically significant differences in the mean size as indicated by the F-actin area per nucleus (Figure 3.17d). Likewise, the cell shape (i.e. aspect ratio) showed no statistically significant differences as a function of increase in Mg^{2+} ion concentration in the culture media.

3.4. Discussion

As-cast Mg-Zn-Ca alloys were evaluated on their degradation and potential bioactive properties for musculoskeletal implant applications. We cultured BMSCs directly on the surface of Mg-xZn-0.5Ca (x = 0.5, 1.0, 2.0, or 4.0 wt. % Ca) alloys to investigate the *in vitro* degradation of the alloys and, for the first time, study possible modulatory effects on cell responses at the cell/Mg-xZn-0.5Ca alloy

interface. We also examined the BMSCs on the culture plates surrounding the Mg-based samples in the same direct culture to understand BMSC behaviors in direct culture but indirect contact with the Mg-based samples. Additional mechanism studies were conducted to isolate specific effects of degradation and determine which degradation product(s) dominate(s) the modulatory effects on cell responses.

3.4.1. Microstructure and properties of Mg-xZn-0.5Ca alloys

The addition of up to 4 wt. % Zn to the as-cast Mg-xZn-0.5Ca alloy caused changes in the composition, crystallinity, and dispersion of the second phases formed at the grain boundaries. Previous studies on ternary Mg-Zn-Ca crystalline alloys indicated that the second phase composition and crystallinity at the grain boundaries relied most heavily on the Zn/Ca at. % ratio in the alloy composition. According to the Mg-Zn-Ca ternary phase diagram and experimental verification, the eutectic (α-Mg + Mg_2Ca + $Ca_2Mg_6Zn_3$) phase formed when Zn/Ca atomic ratio was less than 1.0-1.2 while the eutectic (α-Mg + $Ca_2Mg_6Zn_3$) phase precipitated when Zn/Ca atomic ratio was more than 1.2 [12, 15, 26, 33]. Additional studies indicated that a Zn-enriched Mg_2Ca phase (which was isomorphous with Mg_2Ca but had slightly different lattice parameters) might also form when the Zn/Ca at. % ratio is < 1.2 [14, 17, 20, 23]. Although the upper-boundary of Zn/Ca at. % has not been clearly defined, previous investigations showed that a Zn/Ca at. % ratio < ~5 will cause precipitation of eutectic (α-Mg + $Ca_2Mg_6Zn_3$ + Mg_xZn_y) phases and a

ratio > ~5 will cause formation of (α-Mg + Mg_xZn_y) phases [8, 9, 11, 12, 20, 25, 26]. Detailed descriptions of dendrite formation and microstructure evolution during the solidification of Mg-xZn-0.5Ca alloys can be found in literature [12, 22, 26]. Therefore, our EDS point analyses and XRD results of the phases identified in the 0.5Zn, 1Zn, 2Zn, and 4Zn alloys (Zn/Ca at. % ratios of 0.61, 1.23, 2.45, and 4.90, respectively) were in agreement with previous reports on second phase formation in Mg-Zn-Ca alloys. Specifically, we confirmed the presence of an α-Mg matrix in all samples, a Mg_2Ca phase for low Zn content (0.5Zn), a $Ca_2Mg_6Zn_3$ phase in all four alloys, and formation of a MgZn phase at high Zn content (4Zn). Additionally, the dispersion of second phases in the Mg-xZn-0.5Ca alloys studied was specific to the predominant phase present. Previous studies reported the formation of continuous networks of lamellar eutectic phases in Mg-xZn-0.5Ca (up to x = 9 wt. %) alloys where the widest grain boundary was observed for the Mg-9.0Zn-0.5Ca alloy [12, 15, 26]. Other studies observed the formation of coarse granular second phases agglomerated at the grain boundaries in the Mg-4.0Zn-0.5Ca alloy (Zn/Ca at. % ratio of 4.90) [8, 24]. Although little information is available in literature for volume fraction of intermetallic phases as a function of increasing Zn content, it has been suggested that the volume fraction of the $Ca_2Mg_6Zn_3$ phase increases with increasing Zn content in Mg-xZn-0.5Ca up to 6 wt. % Zn [12]. Our results indicated that the microstructure of the Mg-xZn-0.5Ca alloys investigated was in agreement with previous studies. Specifically, the formation of continuous networks of lamellar eutectic phases in the 0.5Zn, formation of fine granular

precipitates in 1Zn and 2Zn, and the formation of coarse granular precipitates in the 4Zn alloy (Figure 3.1a-d).

The difference in degradation (i.e. corrosion) resistance of the as-cast Mg-xZn-0.5Ca alloys was due to the varying electrochemical behavior between the α-Mg matrix and second phase precipitates (composition and dispersion) [34]. Values for the standard electrode potential were reported previously for α-Mg (-1.58 V_{SHE}) and Mg_2Ca (-1.87 V_{SHE}) [14]. Although a standard electrode potential is not available for $Ca_2Mg_6Zn_3$, previous studies showed that $Ca_2Mg_6Zn_3$ was more cathodic than α-Mg and Mg_2Ca ($Ca_2Mg_6Zn_3$ > α-Mg > Mg_2Ca) [12, 14, 33]. Furthermore, the MgZn was regarded as the most anodic phase compared with other Mg-Zn-Ca second phases [8, 12]. Sparse literature is available on the potential of the Mg_2Ca(Zn) phase; however, Cha et al. indicated that addition of Zn caused a cathodic shift in the corrosion potential of the Mg_2Ca phase [14]. In terms of the electrochemical interactions between phases, when the $Ca_2Mg_6Zn_3$ phase was present, it formed a galvanic circuit with the α-Mg matrix, which acted as the anode; in such cases, corrosion was directed towards the grains. When the MgZn precipitated, the α-Mg matrix acted as the cathode in the galvanic circuit and corrosion was directed towards the grain boundaries. Additionally, the dispersion of the second phases also influenced the bulk corrosion behavior of the alloys. Specifically, continuous networks or coarse granular precipitates of anodic phases tend to accelerate corrosion compared with dispersed fine granular cathodic phases; cathodic and anodic relative to the potential of the matrix. Bakhsheshi-

Rad et al. indicated that the formation of the more cathodic $Ca_2Mg_6Zn_3$ phase interrupted the formation of continuous networks of anodic Mg_2Ca phase, thereby increasing the bulk corrosion resistance of Mg-xZn-0.5Ca alloys with increasing Zn content (< 3 wt. %, thereafter Mg_xZn_y precipitated and accelerated corrosion) [12]. Several investigations on the degradation of as-cast ternary Mg-Zn-Ca crystalline alloys reported the best corrosion resistance when Zn content < 2.0 wt. % and Ca content < 1.0 wt. %; degradation resistance was reduced when Zn content was increased up to 20 wt. % with fixed Ca [7, 9, 12]. Tafel extrapolation results from our PDP measurements (Figure 3.4) indicated that the polished 2Zn alloy showed the most cathodic E_{corr} and therefore highest degradation resistance compared with 0.5Zn, 2Zn, 4Zn and Mg. The significant improvement in corrosion resistance of the 2Zn alloy was attributed to the presence of the finely dispersed $Ca_2Mg_6Zn_3$ phase. Although the polished 1Zn alloy showed a significantly lower J_{corr} value compared with 4Zn and Mg, it must be noted that PDP measurements only estimate corrosion behavior at narrow transient intervals. Thus, long-term immersion studies are necessary to complement PDP measurements for biomedical applications [35, 36]. The 72 hr immersion tests in cell culture media and analysis of Mg^{2+} ion concentration of the media (Figure 3.14a) provided long-term degradation information under a physiologically relevant condition. Firstly, these results indicated that Mg^{2+} ion release from the 0.5Zn, 1Zn, 2Zn, and Mg samples was highest during the first 24 hr of incubation (all groups were significantly higher compared with the blank media only at 24 hr). These results

were in agreement with gradual decrease in pH of the media during the 72 hr incubation (Figure 3.13b). It is generally accepted that the Mg-based alloys would be passivated in media and the formation of oxide layers should slow down degradation to some degree [34]. Secondly, these results indicated that the significantly higher cumulative Mg^{2+} ion release and higher average degradation rate observed for the 4Zn alloy throughout the 72 hr study (Figure 3.14a and 3.15) was attributed to the accelerated corrosion at the grain boundaries caused by the formation of galvanic couples between the coarse granules of anodic MgZn phase and the α-Mg matrix. This explanation is also supported by the aggressive change in microstructure of the 4Zn alloy observed at 48 and 72 hr of culture with BMSCs in DMEM (Figures 3.6d and 3.7d). In contrast, the lower degradation rate of 0.5Zn, 1Zn, 2Zn, and Mg compared with 4Zn (Figure 3.15b) was attributed to the prevalence of the cathodic $Ca_2Mg_6Zn_3$ phase, which directed the corrosion towards the α-Mg matrix. As a result, the surfaces of the 0.5Zn, 1Zn, 2Zn, and Mg samples remained relatively intact during the 72 hr of culture with BMSCs in DMEM (Figures 3.5, 3.6, and 3.7). The degradation rates (mass loss rate) in Figure 3.15b provide a useful design guideline for Mg-based bioresorbable implants. The implant degradation rate can be estimated based on initial exposed surface area of implants.

Understanding how second phases affect mechanical properties is critical for the design of load-bearing biomedical implants. Thus, although mechanical properties of the as-cast Mg-xZn-0.5Ca (x = 0.5, 1.0, 2.0, or 4.0 wt. %) alloys were

not measured in the present study, previous studies have reported a strong dependence on the second phases present in the alloys and are briefly discussed in the following paragraph. Continuous networks of the brittle Mg_2Ca phase produced cracks that led to brittle failure [15] and the Mg_2Ca(Zn) [20] and $Ca_2Mg_6Zn_3$ [21] phases improved the precipitation hardening of as-cast Mg-Zn-Ca alloys. Zhang et al. reported an increase in yield strength (YS), ultimate tensile strength (UTS), elongation (EL%), and elastic modulus (E) with increasing Zn content up to 4.0 wt. % in a Mg-xZn-1.0Ca alloy; addition of more than 4.0 wt. % Zn caused a decrease in UTS and EL% [9]. In another study Zheng et al. found that for a fixed 4 wt. % Zn content, addition of Ca content up to 2.0 wt. % increased the YS, but decreased the UTS and EL% [8]. Previous studies indicated that the as-cast Mg-4.0Zn-0.5Ca wt. % alloy had a YS of 70±3.0 MPa, UTS of 180-211 MPa, and EL% of 12.3-17% [8, 24]. Geng et al. proposed that the high plasticity of the Mg-Zn-Ca alloys was caused by the activation of prismatic planes and twinning; in contrast, the plasticity of pure Mg is determined only by basal plane deformation [24]. The mechanical properties of as-cast Mg were reported as: YS of 21 MPa [37], UTS of 85 MPa, and EL% of 5.8% [38]. Although our 4Zn would be expected to have similar mechanical properties to the Mg-4.0Zn-0.5Ca alloys reported previously, the significantly faster corrosion of this alloy limits its potential in medical applications. The 0.5Zn, 1Zn, and 2Zn alloys would be expected to have lower YS, UTS, and EL% compared with 4Zn due to lower Zn content. Specifically, based on values reported in [9] and linear extrapolation, the 0.5Zn would have

approximately: YS ~ 47 MPa, UTS ~ 113-133 MPa, and EL% ~ 6-9%, all of which are still greater than as-cast Mg. Furthermore, several studies have reported remarkable improvements in both corrosion resistance and mechanical properties of Mg-Zn-Ca alloys after hot/cold working and heat treatments [17, 19-22, 24, 25]. Thus, the 0.5Zn, 1Zn, and 2Zn alloys with hot/cold deformation and heat treatments are expected to provide better mechanical properties and slower degradation rate than their respective as-cast counterparts and as-rolled commercially pure Mg, and will be the focus of further studies due to their promise for load-bearing orthopedic/spinal applications. Figure 3.18 summarizes the degradation rates measured for the Mg-xZn-0.5Ca (x = 0.5, 1.0, 2.0, or 4.0 wt. %) alloys in this study, the trend of mechanical properties as a function of increasing Zn content reported in literature [8, 9, 24], and the factors that affect degradation and mechanical properties of Mg-Zn-Ca alloys. Specifically, Zn/Ca at. % ratios are the critical factors for the formation of each phase; the phases present and second phase morphology at each Zn content of Mg-xZn-0.5Ca alloys are the key factors affecting degradation and mechanical properties.

3.4.2. BMSCs in the direct culture but indirect contact with the Mg-xZn-0.5Ca alloys

Mg^{2+} ion concentrations from the degradation of the Mg-xZn-0.5Ca (x = 0.5, 1.0, 2.0, or 4.0 wt. %) alloys did not affect cell viability, F-actin area per attached nucleus, or aspect ratio of BMSCs attached on the culture plates surrounding the

samples (indirect contact) after 72 hr of direct culture. The significant differences observed in the adhesion density of the plate at 48 hr (Figure 3.10b), F-actin area per nucleus at 24 and 48 hr (Figure 3.11b), and cell D_{max} at 24 hr (Figure 3.12b) was attributed to the initial rapid degradation of certain alloys. However, at 72 hr, the cells recovered and, despite the higher Mg^{2+} ion concentration of 4Zn (3-4 mM compared with ~2-3 mM for 0.5Zn, 1Zn, 2Zn, and Mg, and 0.8-1.0 mM for glass, cells and DMEM), no statistically significant differences were found on cell responses. Moreover, these results were confirmed through BMSCs cultured in the media supplemented with Mg^{2+} ions, which showed no significantly impaired BMSC adhesion or morphology change for the Mg^{2+} ion concentration of up to 27.6 mM (Figure 3.17). Collectively, these results indicated that adhesion and morphology (size and shape) of BMSCs around the samples (i.e., not in direct contact with the metal substrates) were not affected by Mg^{2+} ions released from the sample degradation. Our results were in agreement with other investigations that reported normal BMSC viability at 72 hr in response to incubation with extracts from Mg, AZ91D, NZ30K, and other Mg alloys containing Al, Zn, Neodymium, and Yttrium [39, 40]. Studies investigating long-term BMSC functions showed that Mg^{2+} ion concentrations up 10 mM (maximum tested) did not suppress osteogenic differentiation [39]. Li et al. proposed that Mg^{2+} ions influence BMSC osteogenic differentiation via SMAD-dependent signaling pathway activated by transforming growth factor- β (TGF-β1) while decreasing adipogenic differentiation via downregulation of tumor necrosis factor (TNF-α) [41]. Although the BMSC-based

model has been used in literature to test the cytocompatibility of Mg-based materials [2, 4, 5, 16, 27, 39, 40, 42, 43], the maximum tolerance level of these cells to Mg^{2+} ion concentrations remains elusive. Our results showed for the first time that BMSCs remained viable and continued to proliferate without any noticeable change in morphology when the media were supplemented with up to 27.6 mM Mg^{2+} ions.

Our results confirmed that the effects of Mg^{2+} ions on cell behaviors are dependent on cell type. For example, Nguyen et al. showed that a Mg^{2+} ion concentration of 10 mM caused changes in the morphology of human embryonic stem cell (hESC) colonies and reduced viability; however, pluripotency was maintained at 40 mM (maximum tested) [30]. We also reported a Mg^{2+} ion LD50 of ~18 mM for hESCs [29], which contrasts an LD50 of ~50-73 mM for RAW, MG63, and HUCPV cells reported by Feyerabend et al. [44]. Cha et al. reported reduced viability for HeLa and L-929 cells for Mg^{2+} ion concentrations exceeding 30 mM [14]. Some studies even reported that mouse embryo fibroblasts could tolerate a Mg^{2+} ion concentration of up to 250 mM without a change in viability or morphology [45]. The effects of Zn^{2+} ion concentration on cell behaviors were not investigated since no significant difference in Zn content was found between the media of the 0.5Zn, 1Zn, and 2Zn alloys as compared with the blank media (< 4 µM; Figure 3.14b). Only the 4Zn alloy showed a significantly higher Zn concentration; however, despite the high YS, UTS, and EL% of the Mg-4.0Zn-0.5Ca alloy, it degraded faster than the other samples studied, which is undesirable for

musculoskeletal implant applications. Similarly, the Ca^{2+} ion concentration was not investigated since no significant increase was found in the Ca^{2+} concentration in the media cultured with the alloys compared to the blank media (Figure 3.14c). In both cases, measured Zn^{2+} and Ca^{2+} ion concentrations (including 4Zn) were well below cytotoxic values reported in literature; the cytotoxicity of Zn and Ca ions using HeLa and L-929 cells was reported as 60 µM for Zn and 30 mM for Ca [14]. Most importantly, all of the concentrations measured were well below therapeutic values recommended for Mg (24-40 mM), Zn (900 µM)[29], and Ca (1-3 g/dL = 250-750 mM) [46, 47].

Even though the increase in alkalinity of the culture media, which resulted from the degradation of Mg-xZn-0.5Ca alloys, only reached a maximum pH of 8.1 and did not cause adverse effects in BMSC viability or morphology, a media pH of 9.5 did reduce the number of BMSCs attached on the tissue culture plates. The culture media experienced an increase in both Mg^{2+} ion concentration and alkalinity as a result of continuous alloy degradation. Since the results showed no adverse effects even at Mg^{2+} ion concentrations much greater than those released into the media due to alloy degradation, we hypothesized that the significant differences observed on the cell behaviors surrounding the different alloy samples were possibly modulated by the continuous alkaline shift in the culture media. The faster degradation of the alloys and Mg during the initial 48 hr (higher Mg^{2+} ion concentration and pH) was correlated with the significant differences detected; thereafter, the Mg-based materials were passivated and degradation was

stabilized. Results from our media alkalinity experiments showed a significantly lower adhesion density for cells incubated in media adjusted to pH 9.5 (Figure 3.16c). However, the size and shape of these cells was not significantly affected as compared with the other conditions tested, indicating that a highly alkaline environment modulated viability but not morphology. Our results indicated that the $NaHCO_3/CO_2$ buffering effect of DMEM contributed to the reduction of sharp pH increases. Lelong et al. indicated that DMEM could neutralize sharp changes in pH in as little as 15-30 min [32]. This could potentially suggest that the effective incubation time in the adjusted alkaline media was only 15-30 min; however, this short incubation period was enough to reduce cell viability at pH 9.5. Additionally, the highest pH of the post-incubation culture media from the metallic samples was measured to be pH 8.1. The pH of the post-incubation culture media originally adjusted to 9.0 was also approximately 8.1, it is reasonable to speculate that the pH of the media in the vicinity of the sample (i.e. interface between cells and Mg/Mg alloy) could reach pH values of 9.0 but not exceed 9.5. It must also be highlighted that the sample degradation process is continuous and therefore the increase in alkalinity is continuous rather than transient. Our experiments with pH-adjusted media represented transient media alkalinity, whereas the direct culture method with direct contact represented continuous media alkalinity. Exposure of BMSCs to continuous media alkalinity, despite the buffering effect of DMEM, presented a harsher, yet more physiologically relevant model, compared with the transient model. Possible implications from localized high pH, specifically at the interface,

will be discussed in detail in the next section. Previous studies indicated that, indeed, an increase in alkalinity of the culture media tends to have a more dramatic effect on cellular functions than high Mg^{2+} ion concentrations. For example, Yang et al. concluded that culture media with a pH of 8.4-8.6 suppressed osteogenic differentiation in BMSCs after 6 and 12 days of incubation (the culture media was replaced every other day) [39]. Similarly, Grillo et al. reported that the culture media with pH 8.6 – 9.1decreased UMR-106 rat osteosarcoma cell viability [48]. Nguyen et al. reported that culture media with pH 8.1 had no adverse effects on the viability, morphology, and pluripotency of hESCs up to 72 hr of culture [30]. Taken together, these results indicated that the reduced BMSC adhesion density in the direct culture but not in direct contact with the metal substrates at 48 hr was most likely due to the local pH increase rather than the released Mg^{2+} ions. In contrast, the absence of significant differences from the analysis of morphology (size and shape) of adhered cells on the culture plate surrounding the sample indicated that incubation in alkaline media for up to 72 hr did not affect cell morphology. These results from the cell morphology analysis indicated that the cells with the ability of surviving higher media alkalinity showed early signs of normal function; however, gene expression analyses are required to validate this hypothesis and will be included in future research.

3.4.3. BMSC/Mg-xZn-0.5Ca alloy interface (BMSCs in the direct culture and direct contact with the Mg-xZn-0.5Ca alloys)

The elevated Mg^{2+} ion concentration and alkalinity localized at the cell/substrate interface did not cause any observable adverse effects on cellular responses. The cell/substrate interface is characterized by elevated Mg^{2+} ion and hydroxide (OH^-) ion concentrations/fluxes, release of hydrogen gas, along with a changing surface topography [3]. The continuous generation of these degradation products at the surface differs greatly from the average concentrations typically measured by extract-based culture or non-contact based methods. The study of BMSCs incubated with either elevated Mg^{2+} ion concentrations or pH did not account for the dynamic flux gradient at the interface. However, these conditions represented maximum static concentrations that are meaningful to understand their respective effects on cells. On one hand, previous studies suggested that active transport of Mg^{2+} ions across the cell membrane were tightly regulated in order to maintain intracellular concentrations within a narrow range, irrespective of extracellular concentration [49]. As a result, passive diffusion of Mg^{2+} ions across cell membrane is limited. Therefore, it is reasonable to speculate that the Mg^{2+} ion flux at the cell/substrate interface would have very little impact on the Mg^{2+} ion influx across the cell membrane; thus, normal viability and morphology of BMSCs were observed on the Mg-xZn-0.5Ca alloys. On the other hand, the local increase in alkalinity at the interface, which resulted from the substrate degradation, could very well reach pH 9.0 (see above). In fact, previous studies suggested that the

local pH at the metal surface always exceeds pH 10 [50]. However, our results showed that the cells at the interface of all samples remained largely viable for up to 72 hr of incubation (Figure 3.10a), indicating that the pH values at the cell/Mg-xZn-0.5Ca alloy interface were unlikely to exceed pH 9.5 (even for as-rolled commercially pure Mg) since a significantly reduced viability was observed at pH 9.5. Within this range of increase in pH (pH < 9.0), the bicarbonate buffering system of DMEM (which is analogous to the buffering system in the human body) can effectively reduce the alkalinity to normal conditions for cell growth. Finally, hydrogen gas is another major byproduct from the degradation of Mg (one H_2 gas molecule produced for each Mg atom dissolved [34]); thus, it is generally accepted that the formation of hydrogen-induced cavities observed *in vivo* [37, 51] can be mitigated by controlling the degradation rate of the Mg-based implant. We consider that cellular responses to elevated Mg^{2+} and OH^- ions are the most important indicators to consider when designing bioresorbable Mg-based implants. Nevertheless, the role of hydrogen gas flux on cell functions at the cell/substrate interface needs to be investigated in order to understand the direct effects of all major degradation products on cellular functions *in vitro*.

Although the BMSCs directly attached onto the surface of the degradable Mg-xZn-0.5Ca alloys did not show any significant reduction in cell viability, signs of anisotropic cell spreading were observed at 24, 48, and 72 hr of incubation. Our results supported the conclusion that elevated Mg^{2+} ion concentration and/or media alkalinity (i.e., supplemented media and/or media with adjusted pH) did not

change BMSC morphology, i.e., F-actin area and aspect ratio (Figure 3.16 and 3.17). Thus, we speculated that the change in surface topography, which resulted from substrate degradation, played an important role in modulating cell size, i.e., F-actin area per adhered BMSC (Figure 3.11a). Cell shape, i.e., aspect ratio, however, was largely unaffected by surface topography (Figure 3.12c). Dublin-Thaler et al. observed two distinct states of cell spreading (namely isotropic and anisotropic spreading) for mouse embryonic fibroblasts *in vitro* due to surface and culture medium conditions [31]. Similarly, Cavalcanti-Adam et al. reported a change in cell area (i.e. size) in response to a change in rationally-designed underlying surface topography [52]. Our results indicated that the 0.5Zn alloy showed significantly lower F-actin area per BMCS nucleus at 48 and 72 hr compared with the glass reference (Figure 3.11a). These observations were in agreement with SEM results from 24, 48, and 72 hr (Figures 3.5, 3.6 and 3.7, respectively). Interestingly, the surface of the 4Zn alloy did not induce any significant difference in the cell F-actin area as compared with the glass reference, which was supposed be lower based on the aggressive change in topography observed. Nevertheless, the lower mean adhesion density of BMSCs on the surface of the 4Zn alloy, although not statistically significant, correlated with the aggressive change in topography observed at the 24, 48, and 72 hr time points. Similarly, the 2Zn alloy, which showed signs of slower degradation and conservation of a relatively intact surface, showed a higher mean BMSC adhesion density. Additionally, our EDS results (Figure 3.8) showed no correlation between

BMSC adhesion and surface elemental distribution, thereby reassuring the potential implications of surface topography in directing cellular functions. Interestingly, our results indicated a co-deposition of Ca and P within the oxygen-rich degradation areas of the Mg-xZn-0.5Ca alloys, especially on areas of aggressive corrosion, which could potentially benefit the mineralization processes at the implant/tissue interface. Cell adhesion and spreading on surface are critical for cell proliferation, long-term functions, and subsequent organization of tissues [31], and therefore need to be further studied to understand the complex dynamics at the tissue-implant interface to further optimize Mg-based materials for potential clinical translation.

Figure 3.19 summarizes all the media conditions used for evaluating BMSC viability and morphology. The x-axis indicates Mg^{2+} ion concentration normalized by Mg^{2+} ion concentration found in DMEM (approximately 0.8 mM), and the y-axis indicates change in pH normalized by the change in pH of blank DMEM (correction for pH drift induced by measurements in absence of 5% CO_2). The effects of different media conditions and surface topography on BMSC adhesion and morphology are also included. Our results showed that the change of BMSC behaviors were modulated mostly by the increase in media alkalinity and/or change in surface topography rather than the elevated Mg^{2+} ion concentrations from alloy degradation. Collectively, our results agree with previous studies investigating the cytocompatibility of Mg-Zn-Ca alloys [8, 9, 15]. Additionally, we provided a thorough mechanistic evaluation using a clinically relevant *in vitro*

model. Furthermore, our results provided the first evidence for altered cellular responses which may be responsible to explain the downstream change of osteoblastic activity and subsequent heterogeneous mineralization as observed by Zhang et al. at the Mg-4.0Zn-0.2Ca (wt. %) implant-tissue interface. Future studies will focus on investigating long-term functions of BMSC, such as osteogenic differentiation, and gene expression, at the cell-substrate interface to realize the full potential of Mg-Zn-Ca alloys for musculoskeletal implant applications. Future studies will also focus on identifying whether implants or scaffolds made from Mg-Zn-Ca alloys are able to induce *in vitro* osteogenic differentiation of BMSCs prior to implantation, or if they are better suited to recruit BMSCs *in situ* post-implantation and improve osseointegration *in vivo*.

3.5. Conclusions

This article reports behaviors of bone marrow mesenchymal stem cells interfacing with four biodegradable Mg-xZn-0.5Ca (x = 0.5, 1.0, 2.0, or 4.0 wt. %) alloys and possible factors and mechanisms that affect cell adhesion, viability, and morphology. The following major conclusions were drawn from the present study:

1. Addition of 0.5 wt. % Zn to the as-cast Mg-xZn-0.5Ca alloy (i.e. 0.5Zn alloy) caused formation of the α-Mg matrix and continuous networks of Mg_2Ca and $Ca_2Mg_6Zn_3$ phases; addition of 1-2 wt. % Zn (1Zn and 2Zn alloys, respectively) caused formation of the α-Mg matrix and finely dispersed granular $Ca_2Mg_6Zn_3$ phases; addition of 4 wt. % Zn (4Zn alloy) caused formation of the α-Mg matrix,

and coarse granules of $Ca_2Mg_6Zn_3$, and MgZn phases. The second phases in each alloy played pivotal roles in the degradation properties of the alloy. The as-cast 4Zn alloy degraded significantly faster than all the other alloy samples. The as-cast 0.5Zn, 1Zn, and 2Zn alloys provided a degradation rate similar to commercially pure as-rolled Mg, and are expected to provide better mechanical properties and slower degradation rate after hot/cold deformation and heat treatments than their respective as-cast counterparts and as-rolled pure Mg.

2. The direct culture method was established to probe cell behaviors at the dynamic interface of bioresorbable Mg alloys, including the cells in direct contact with the samples and the cells surrounding the samples (indirect contact with the samples) in the same culture. The direct culture method provides a more comprehensive *in vitro* method for examining bioresorbable materials compared with the extract-based cell cultures (i.e., ISO 10993), thus promising to be standardized as an *in vitro* culture model for screening bioresorbable materials.

3. The *in vitro* evaluation confirmed the cytocompatibility of Mg-xZn-0.5Ca alloys. BMSC adhesion density directly on the degradable Mg-xZn-0.5Ca alloys was comparable to the cells-only positive controls at 24, 48, and 72 hr culture, and no statistically significant differences were detected. Anisotropic spreading of BMSCs on the alloy surface was observed at 24, 48, and 72 hr of incubation in contrast to isotropic spreading on the glass reference and culture plates. We

speculated that the change in surface topography, as opposed to Mg^{2+} or OH^- ions, which resulted from substrate degradation, played an important role in modulating F-actin per adhered BMSC. Moreover, BMSCs adhered on the culture plates surrounding the alloy samples (i.e., direct culture but indirect contact with the samples) at 72 hr did not show any detectable changes in cell adhesion density, F-actin area, cell diameter and aspect ratio as compared to the cells-only positive control. Additionally, the BMSCs cultured in alkaline media with a pH up to 9 did not induce any detectable changes in cell adhesion density, F-actin area, and cell aspect ratio; however, media pH of 9.5 significantly reduced the adhesion density of BMSCs. The BMSC culture with the Mg-xZn-0.5Ca alloys only reached a maximum pH of 8.1 and thus did not cause adverse effects in BMSC adhesion or morphology. The media supplemented with up to 27.6 mM Mg^{2+} ion concentration did not induce significant adverse effects on BMSC adhesion, size, and morphology.

4. The results of this study supported the promising potential of bioresorbable Mg-Zn-Ca crystalline alloys for musculoskeletal implant applications, and provided design guidelines regarding alloy compositions (mainly Zn content), degradation rates, mechanical properties, and BMSC responses to fine tune Mg-Zn-Ca alloys for specific implant applications. Future directions include optimization of Mg-Zn-Ca alloy processing, *in vitro* studies on long-term functions of BMSCs (e.g., osteogenic differentiation, gene expression, etc.) in

response to Mg-Zn-Ca alloys, and *in vivo* studies, all of which are necessary for clinical translation.

3.6. Figures and tables

Figure 3.1: SEM micrographs of Mg-xZn-0.5Ca alloys with Zn content (wt. %): (a) 0.5, (b) 1.0, (c) 2.0, (d) 4.0, and (e) commercially pure Mg control.
Scale bar = 50 µm for all images. Original magnification: 600x. Insets in (a) – (d) are high magnification (5000x). SEM micrographs of the second phases respective to each alloy. Scale bar = 10 µm for all insets. (f) Alloy surface elemental composition (wt. %) quantified through EDS area analysis on (a-e) at 600x magnification.

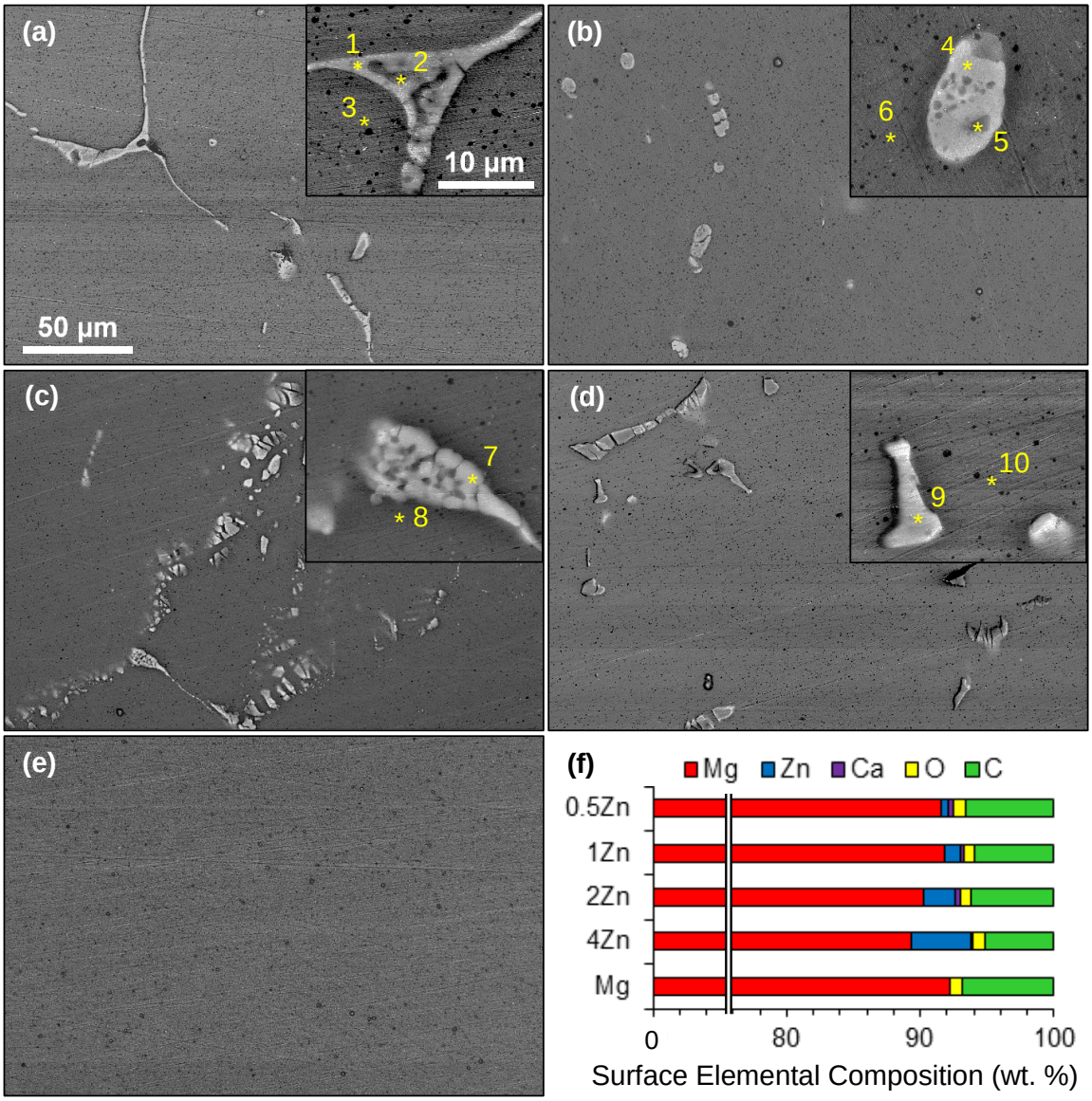

Figure 3.2: EDS analysis of Mg-xZn-0.5Ca alloys, including (a,c,e,g) EDS spectra and (b,d,f,h) quantification of elemental composition (at. %).
(a) and (b): points 1, 2, and 3 in 0.5Zn, respectively; (c) and (d): points 4, 5, and 6 in 1Zn, respectively; (e) and (f): points 7 and 8 in 2Zn, respectively; and (g) and (h): points 9 and 10 in 4Zn, respectively.

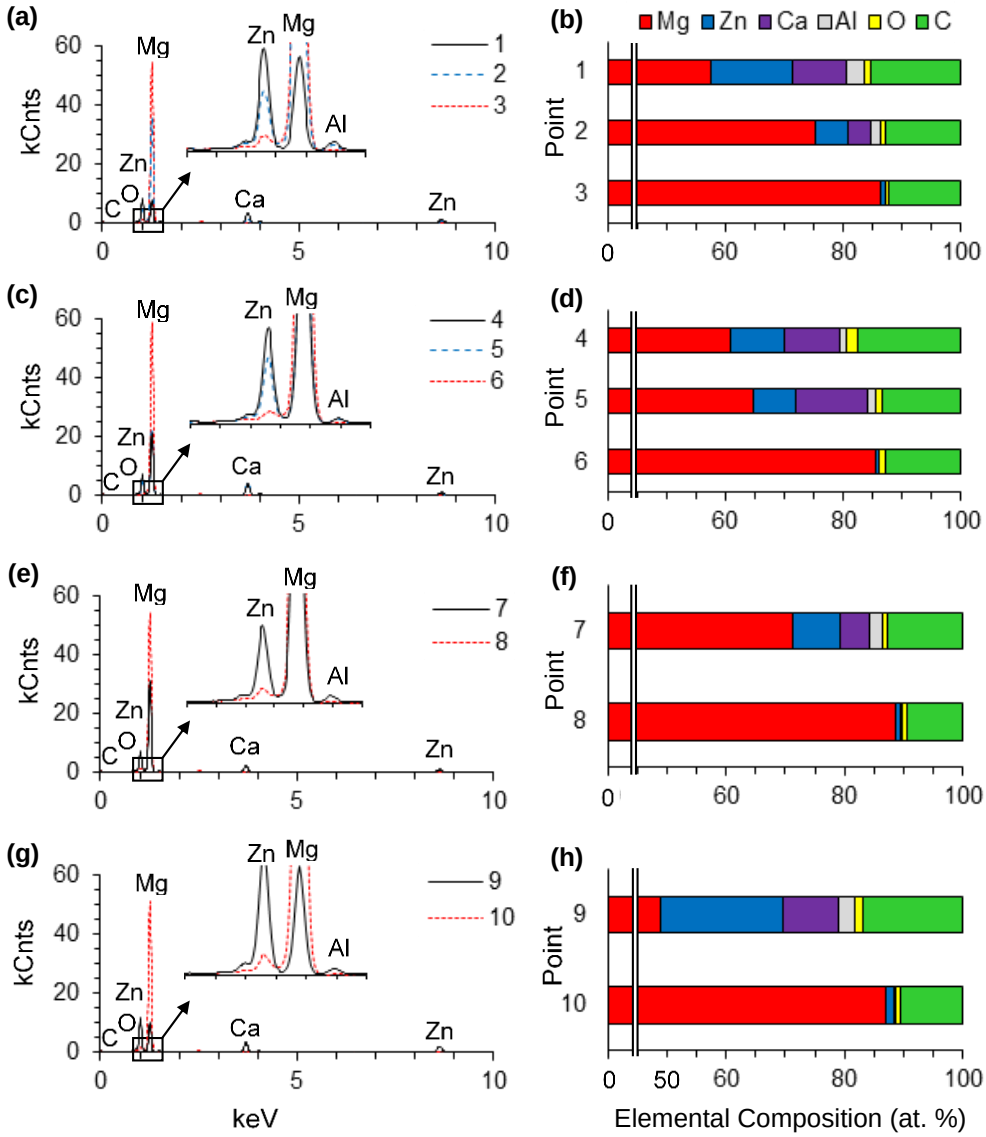

Figure 3.3: X-ray diffraction patterns of Mg-xZn-0.5Ca alloys with Zn content (wt. %) of (a) 0.5, (b) 1.0, (c) 2.0, and (d) 4.0.
Mg ICSD pattern 01-071-6543, Mg_2Ca ICSD pattern 01-073-4526, $Ca_2Mg_6Zn_3$ ICSD pattern 00-012-0266, and MgZn ICSD pattern 01-074-7069.

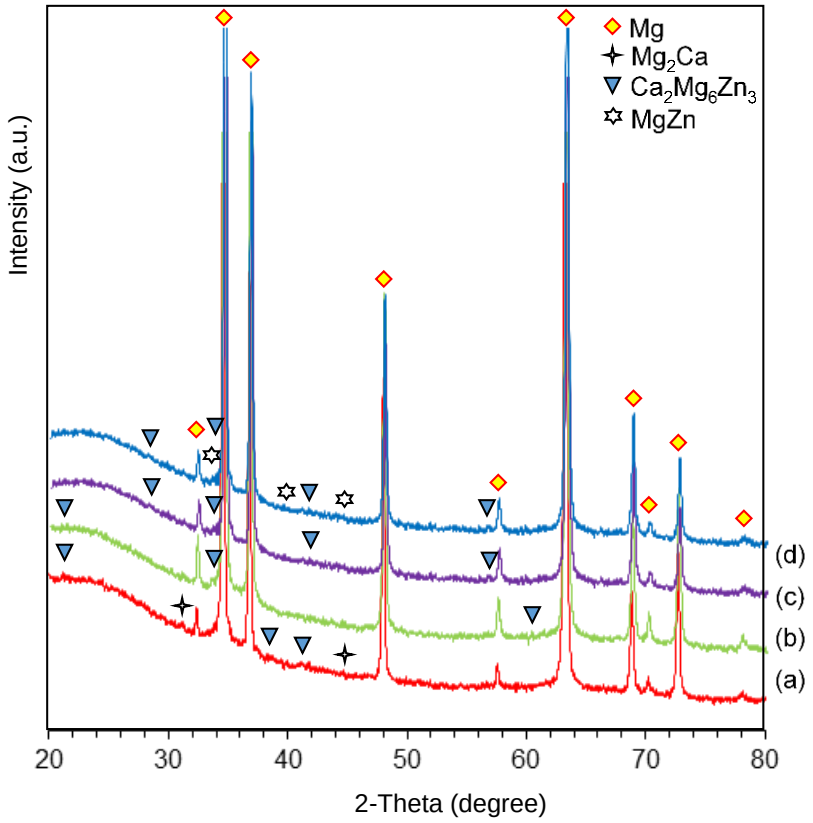

Figure 3.4: Electrochemical polarization testing results of Mg-xZn-0.5Ca alloys (x = 0.5, 1, 2, 4 wt. %) and pure Mg control.
(a) potentiodynamic polarization response of polished metallic samples using r-SBF at 37°C as the electrolyte; and (b) corrosion potential and corrosion current density of Mg-xZn-0.5Ca alloys and pure Mg obtained from Tafel extrapolation (ASTM G102-89) of potentiodynamic polarization curves; values are mean ± SD, n = 3, *p < 0.05, **p < 0.01, ***p < 0.001.

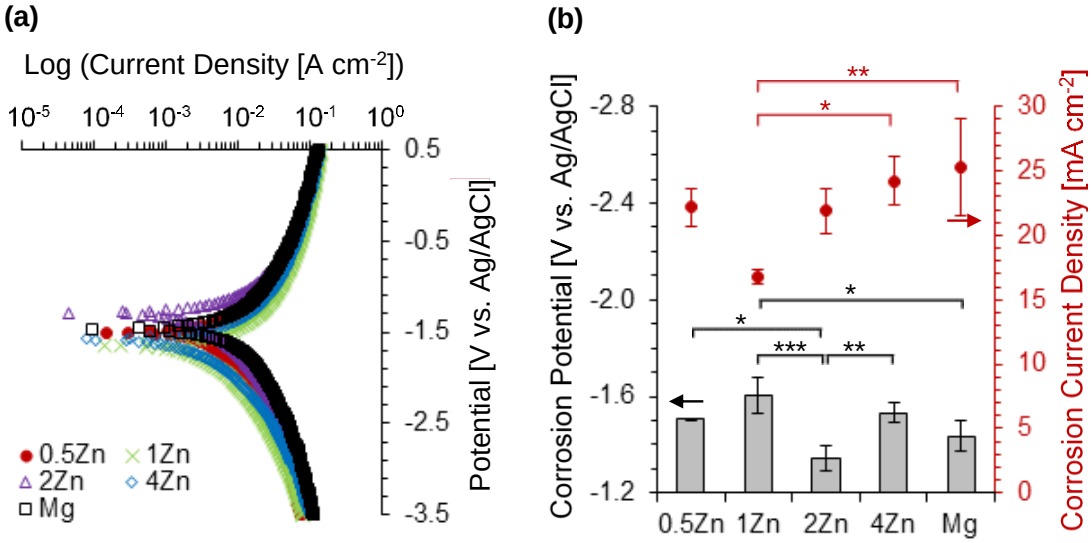

Figure 3.5: Surface characterization of Mg-xZn-0.5Ca alloys (x = 0.5, 1, 2, 4 wt. %), pure Mg control, and glass reference after 24 hr direct culture with BMSCs in DMEM. (a-f) scanning electron micrographs of 0.5Zn, 1Zn, 2Zn, 4Zn, Mg, and glass, respectively, at 150x original magnification with scale bar = 100 µm for all images. Insets were taken at 4,000x original magnification with scale bar = 5 µm for all images. The color mapping in each image represents surface elemental distribution measured by EDS (red = Mg, green = C, yellow = O, white = Si, pink = K, Na, orange = P, purple = Ca, blue = Zn). The color key in (a) is the same for all metallic samples (a-e). White arrows indicate large surface cracks and circles delineate surface degradation products. (g) Surface elemental composition (wt. %) based on EDS quantification on 150x images.

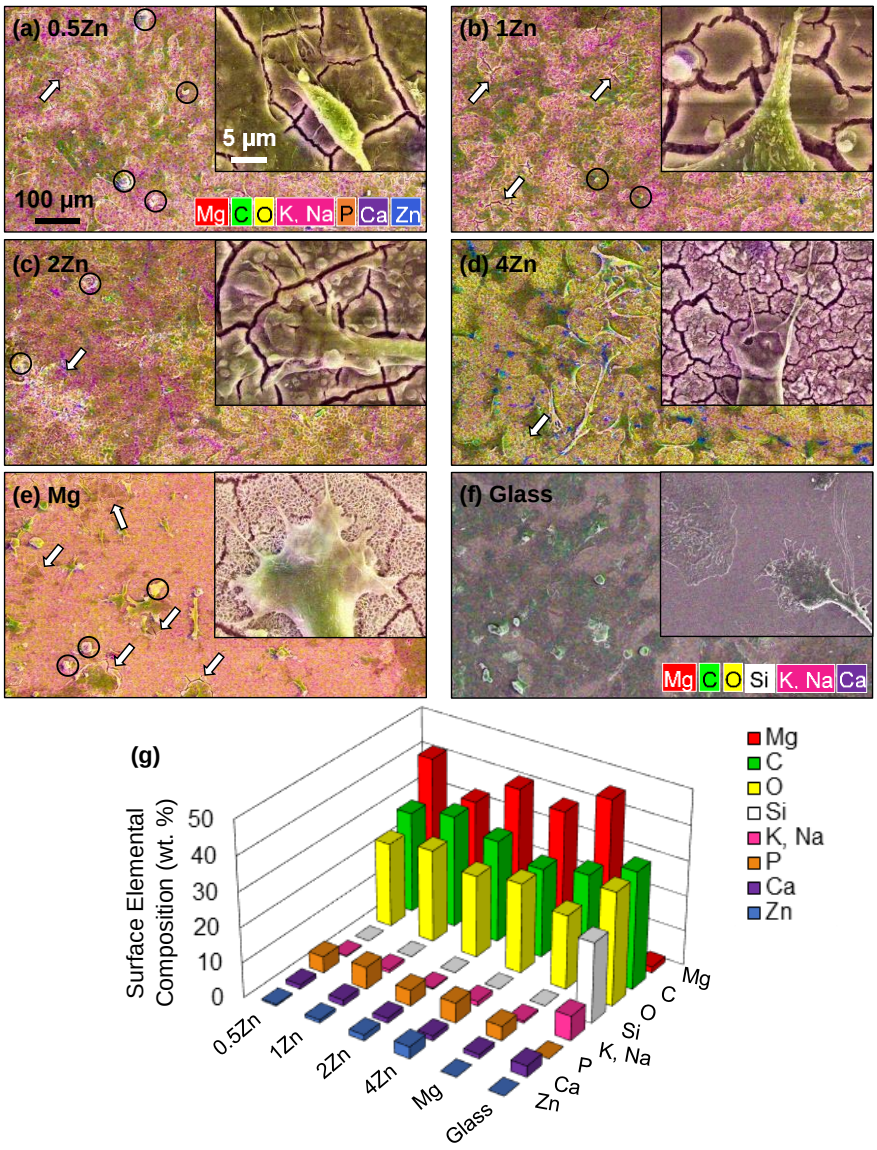

Figure 3.6: Surface characterization of Mg-xZn-0.5Ca alloys (x = 0.5, 1, 2, 4 wt. %), pure Mg control, and glass reference after 48 hr direct culture with BMSCs in DMEM. (a-f) scanning electron micrographs of 0.5Zn, 1Zn, 2Zn, 4Zn, Mg, and glass, respectively, at 150x original magnification with scale bar = 100 µm for all images. Insets were taken at 2,500x original magnification with scale bar = 10 µm for all images. The color mapping in each image represents surface elemental distribution measured by EDS (red = Mg, green = C, yellow = O, white = Si, pink = K, Na, orange = P, purple = Ca, blue = Zn). The color key in (a) is the same for all metallic samples (a-e). White arrows indicate large surface cracks and circles delineate surface degradation products. (g) Surface elemental composition (wt. %) based on EDS quantification on 150x images.

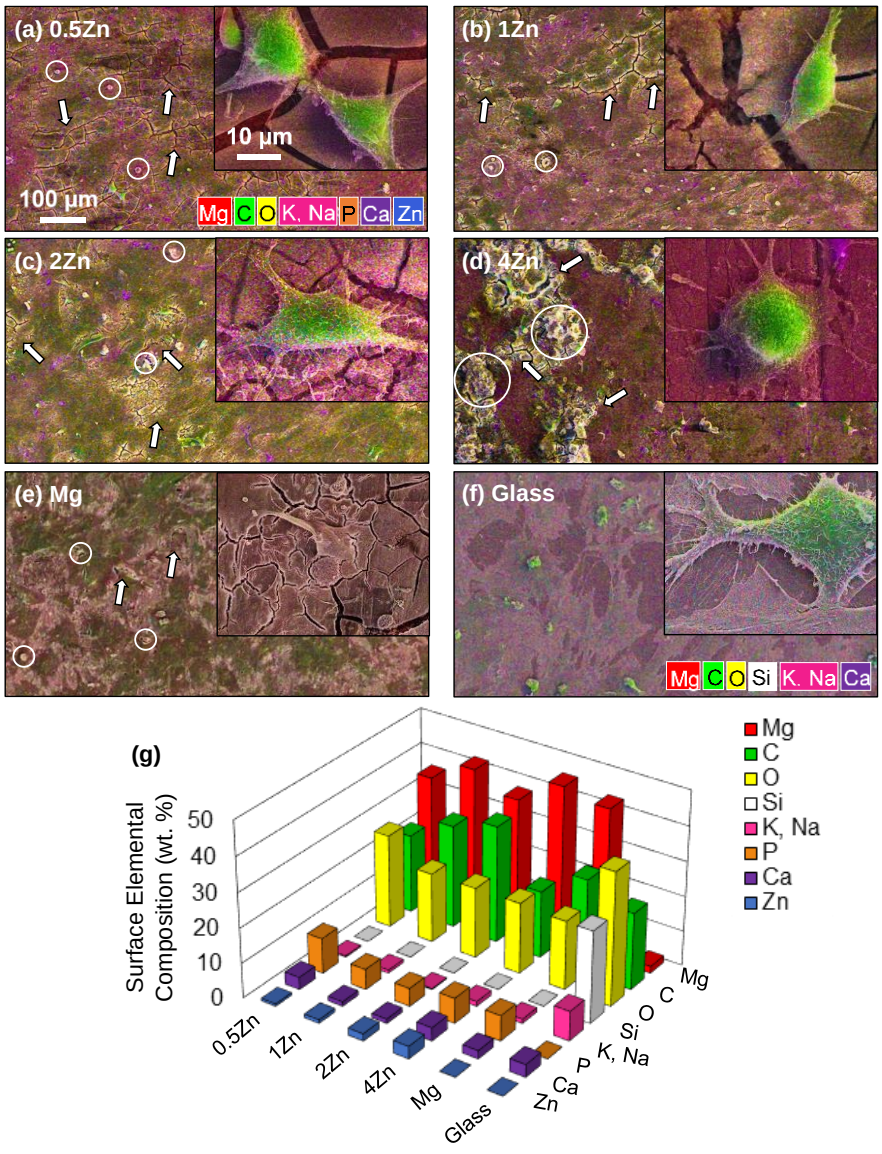

Figure 3.7: Surface characterization of Mg-xZn-0.5Ca alloys (x = 0.5, 1, 2, 4 wt. %), pure Mg control, and glass reference after 72 hr direct culture with BMSCs in DMEM. (a-f) scanning electron micrographs of 0.5Zn, 1Zn, 2Zn, 4Zn, Mg, and glass, respectively, at 150x original magnification with scale bar = 100 µm for all images. Insets were taken at 2,500x original magnification with scale bar = 10 µm for all images. The color mapping in each image represents surface elemental distribution measured by EDS (red = Mg, green = C, yellow = O, white = Si, pink = K, Na, orange = P, purple = Ca, blue = Zn). The color key in (a) is the same for all metallic samples (a-e). White arrows indicate large surface cracks and circles delineate surface degradation products. (g) Surface elemental composition (wt. %) based on EDS quantification on 150x images.

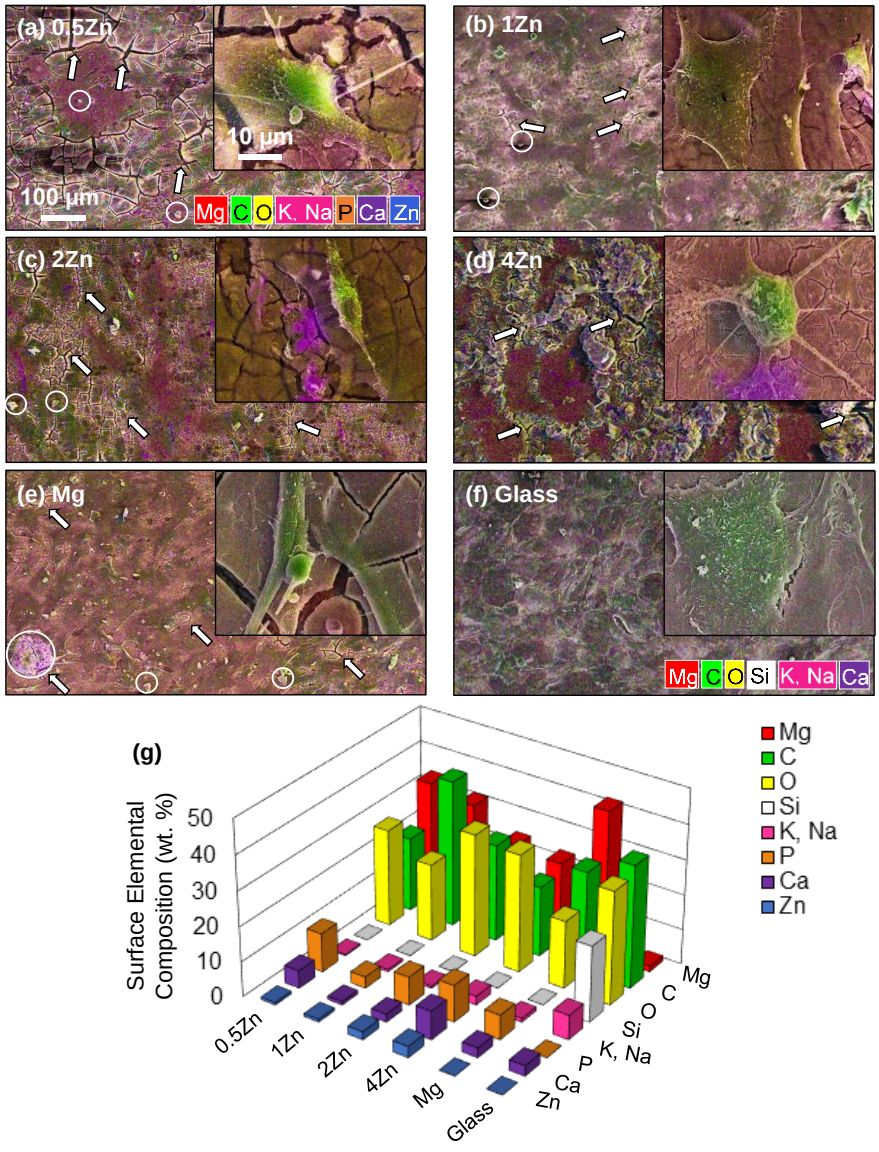

Figure 3.8: EDS elemental distribution maps of Mg-xZn-0.5Ca alloys (x = 0.5, 1, 2, 4 wt. %) and pure Mg control after 72 hr of direct culture with BMSCs in DMEM.
All maps were obtained at 150x original magnification with scale bar = 200 µm for all images. All maps represent Kα1 lines for all elements.

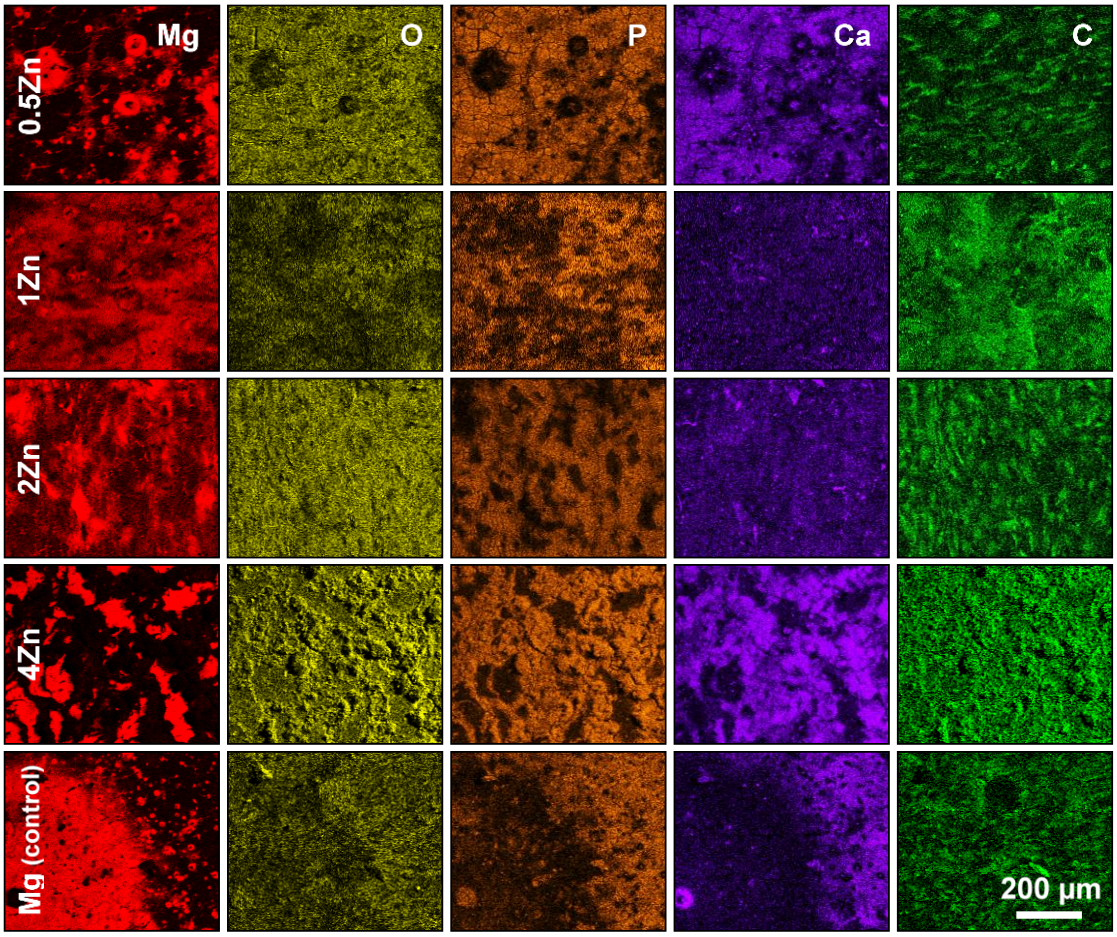

Figure 3.9: Fluorescence images of BMSCs adhered on the surface of Mg-xZn-0.5Ca alloys (x = 0.5, 1, 2, 4 wt. %), pure Mg control, and glass reference (direct contact with the sample) at 24, 48, and 72 hr direct cultures.
Blue color indicates DAPI stained nuclei and green color indicates Alexa Fluor® 488 stained F-actin (cytoskeleton). Scale bar = 200 µm for all images. Original magnification: 10x.

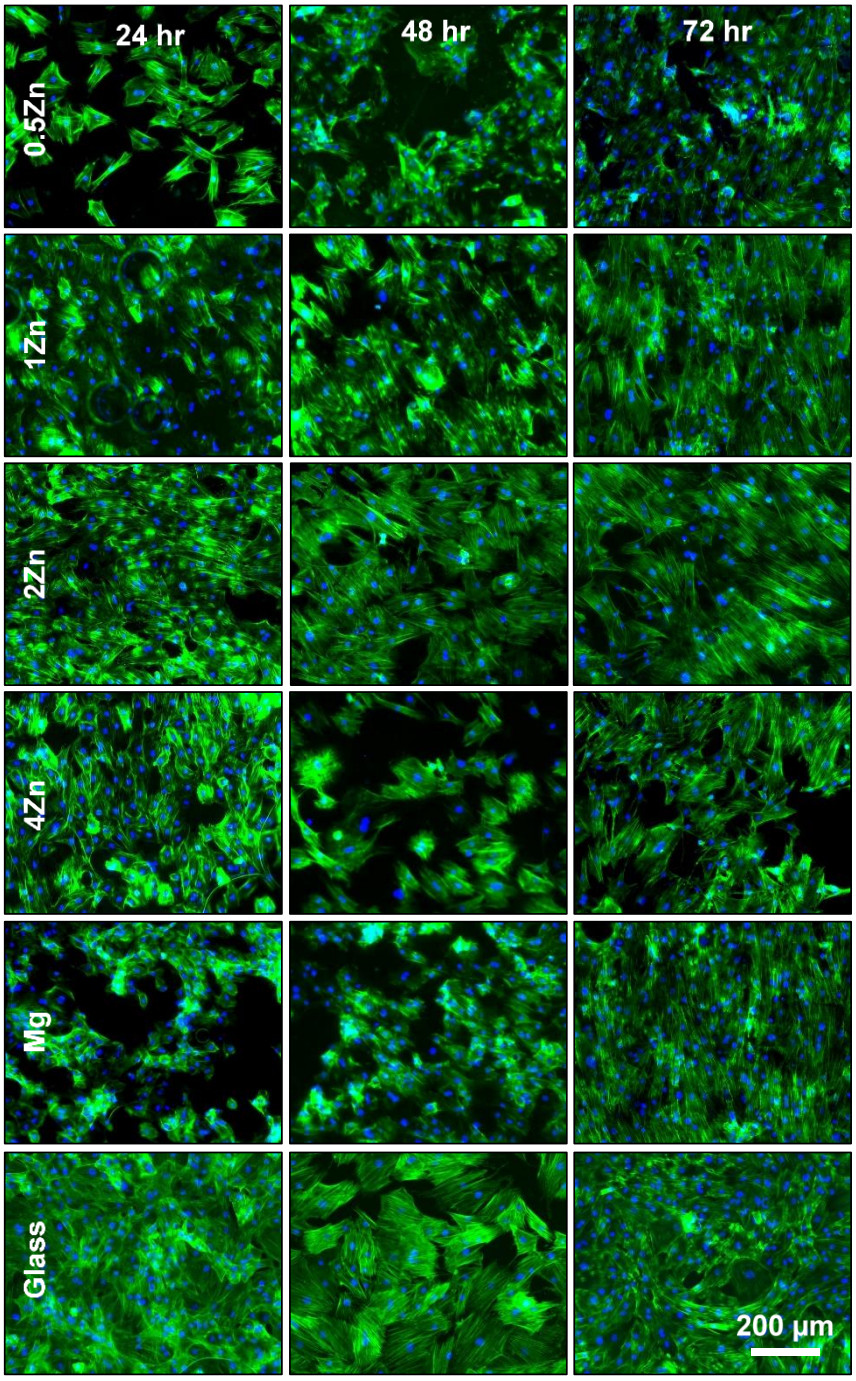

Figure 3.10: BMSC adhesion density at 24, 48, and 72 hr direct cultures on Mg-xZn-0.5Ca alloys (x = 0.5, 1, 2, 4 wt. %), pure Mg control, glass reference, and cells only. BMSC adhesion density on: (a) sample surface (direct contact with the sample), (b) culture plate surrounding each corresponding sample (indirect contact with the sample). Values are mean ± standard error of the means, n = 3; *$p < 0.05$, **$p < 0.01$.

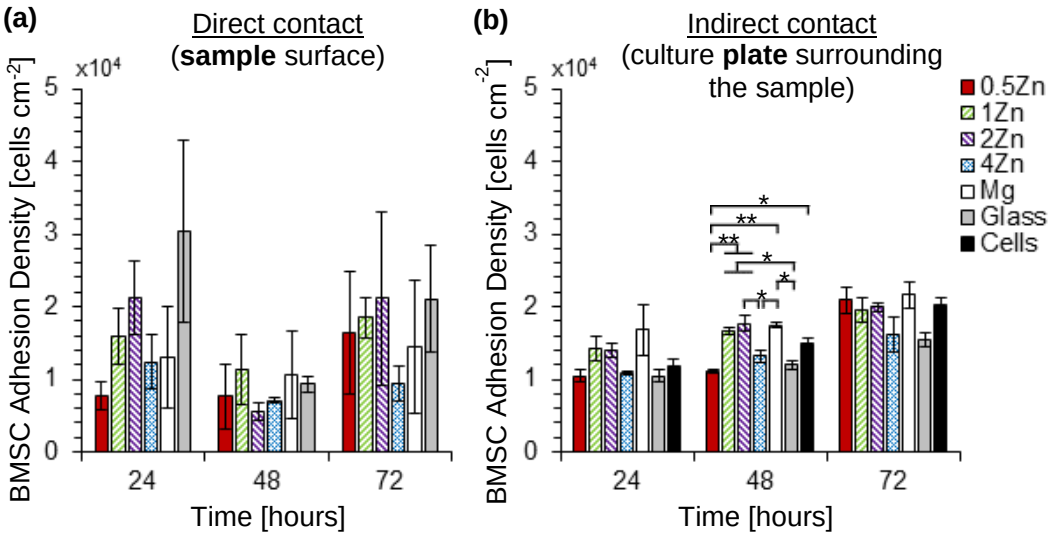

Figure 3.11: F-actin area per BMSC at 24, 48, and 72 hr direct cultures on Mg-xZn-0.5Ca alloys (x = 0.5, 1, 2, 4 wt. %), pure Mg control, glass reference, and cells only. F-actin area per BMSC on: (a) sample surface (direct contact with the sample), (b) culture plate surrounding the corresponding sample (indirect contact with the sample). Values are mean ± standard error of the means, n = 3; **p* < 0.05, ***p* < 0.01, ****p* < 0.001.

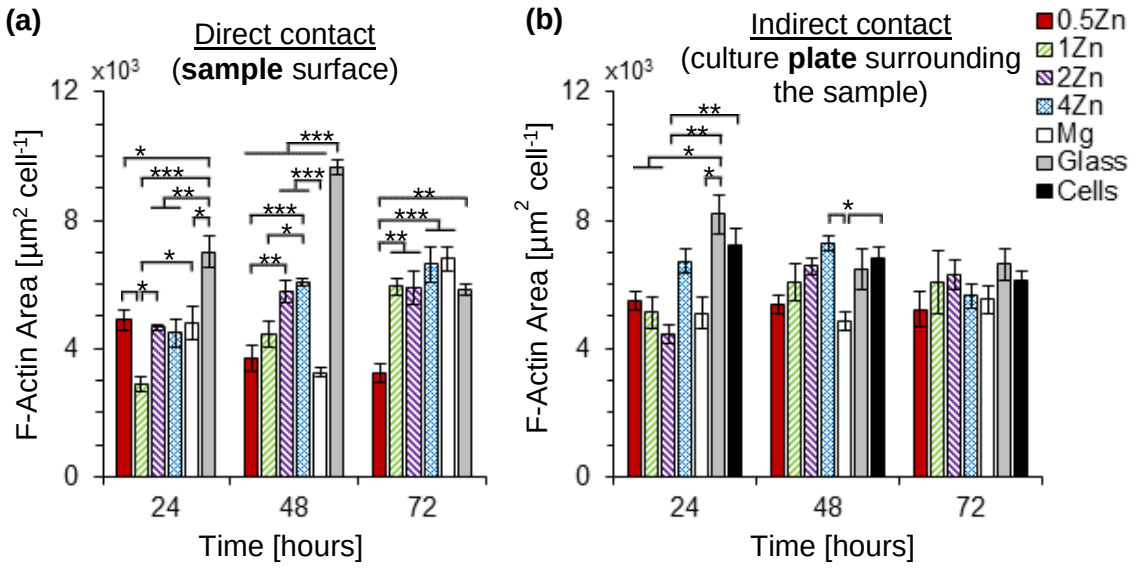

Figure 3.12: Geometrical characterization of BMSCs at 24, 48, and 72 hr direct cultures on Mg-xZn-0.5Ca alloys (x = 0.5, 1, 2, 4 wt. %), pure Mg control, glass reference, and cells only.

Maximum cell diameter on (a) sample surface (direct contact with the sample), and (b) culture plate surrounding the corresponding sample (indirect contact with the sample). Cell diameter aspect ratio (D_{max}/D_{min}) on (c) sample surface, and (d) culture plate surrounding the corresponding sample. Fluorescence images in (d) exemplify cells with distinct aspect ratios. Values are mean ± standard error of the means, n = 3; **p* < 0.05, ***p* < 0.01, ****p* < 0.001.

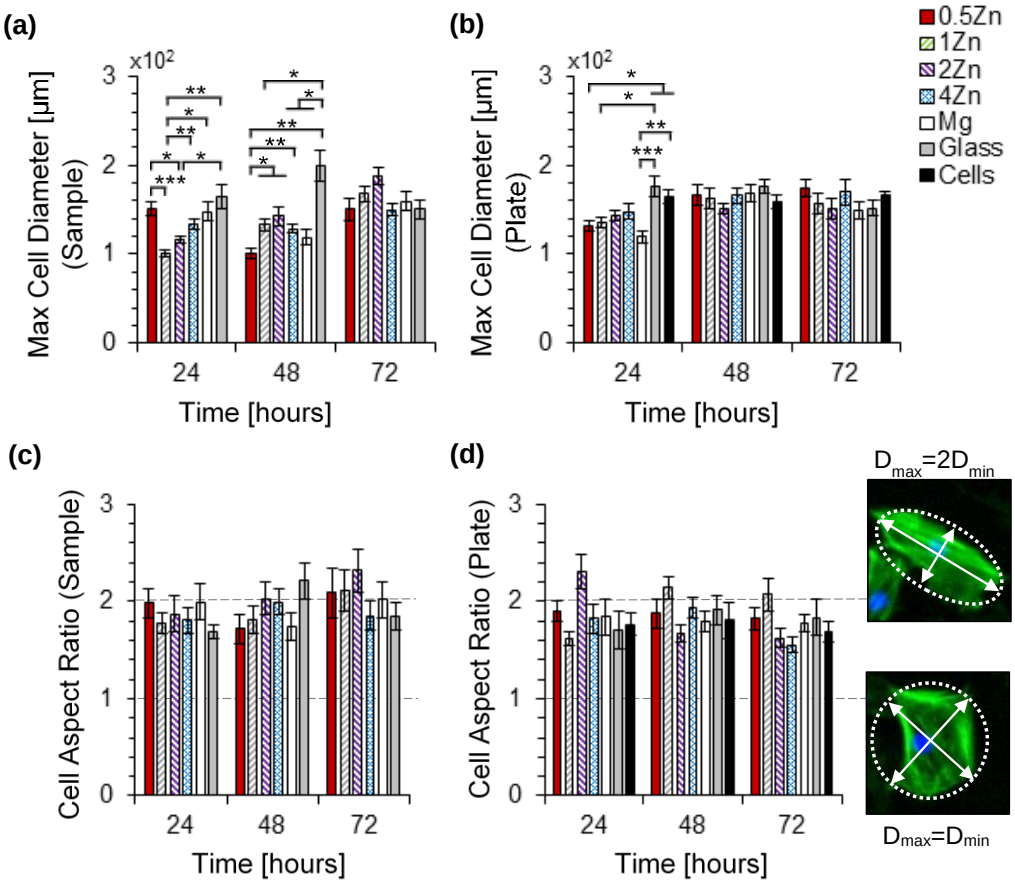

Figure 3.13: pH of the BMSC culture media and change in mass of the samples during the 72 hr incubation.
(a) pH of BMSC culture media incubated with Mg-xZn-0.5Ca alloys (x = 0.5, 1, 2, 4 wt. %), pure Mg control, glass reference, cells only, and DMEM (blank culture media) at 24, 48, and 72 hr. At each time interval, culture media was collected, measured, and replaced with fresh media at pH 7.4; values are mean ± standard deviation (SD), n = 9 at 24 hr, n = 6 at 48 hr, n = 3 at 72 hr. (b) Change in pH of Mg-xZn-0.5Ca alloys, pure Mg, glass, and cells only normalized by the mean change in DMEM at each prescribed interval; the change, relative to the change in blank DMEM, resulted in a net acidic or alkaline shift. (c) Change in mass of the Mg-xZn-0.5Ca alloys and pure Mg samples; M_i/M_o is the sample mass at time i = *24, 48, 72 hr* (M_i) divided by the initial mass (M_o); values are mean ± SD, n = 3. *p < 0.05, **p < 0.01, ***p < 0.001.

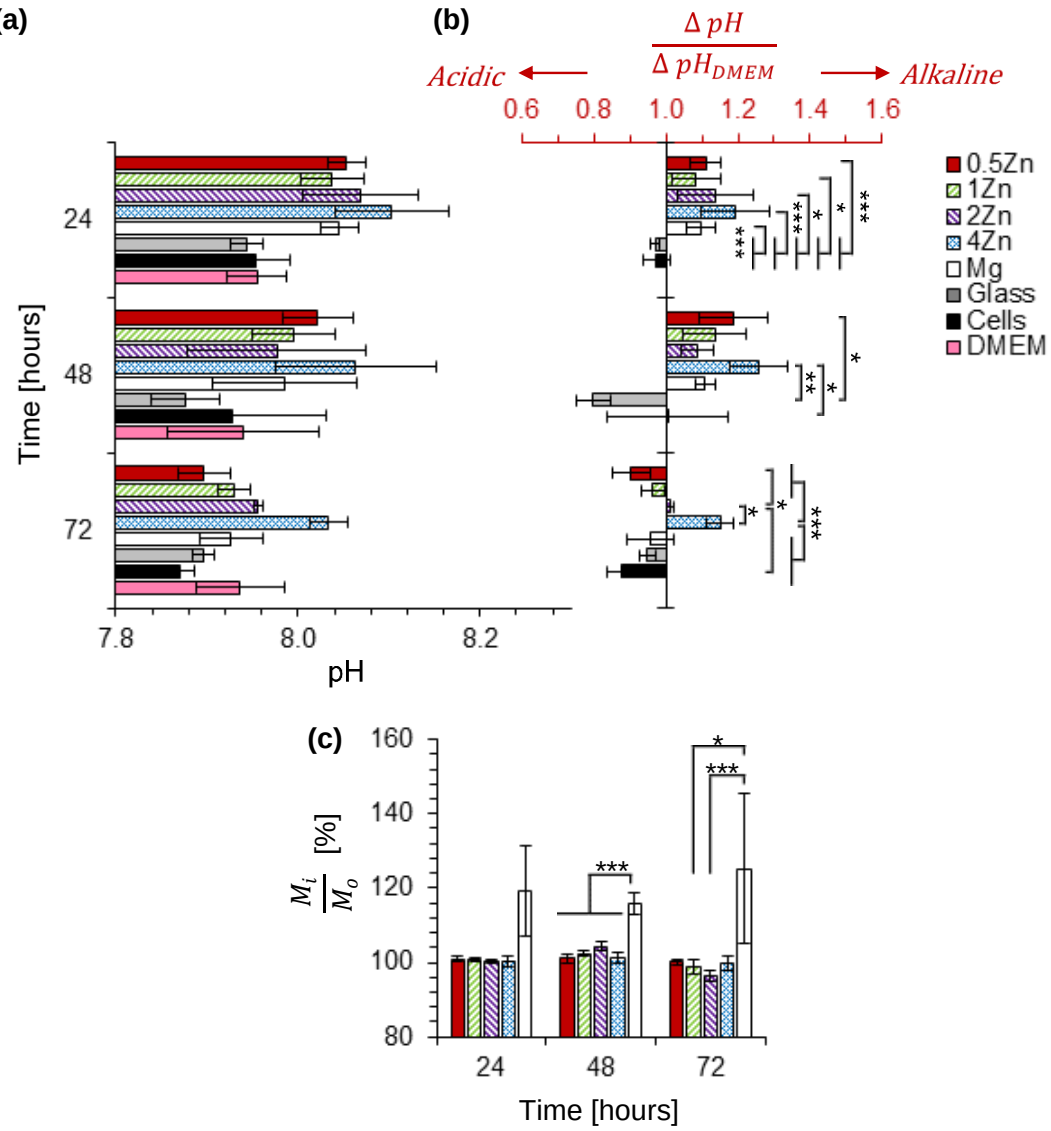

Figure 3.14: Ion concentrations in BMSC culture media incubated with Mg-xZn-0.5Ca alloys (x = 0.5, 1, 2, 4 wt. %), pure Mg, glass, cells only, and DMEM (blank culture media) at 24, 48, and 72 hr.
(a) Mg^{2+} ion concentration, (b) Zn^{2+} ion concentration, (c) Ca^{2+} ion concentration. At each time interval, culture media was collected, measured, and replaced with fresh culture media at pH 7.4. Values are mean ± SD, n = 9 at 24 hr, n = 6 at 48 hr, n = 3 at 72 hr. *p < 0.05, **p < 0.01, ***p < 0.001.

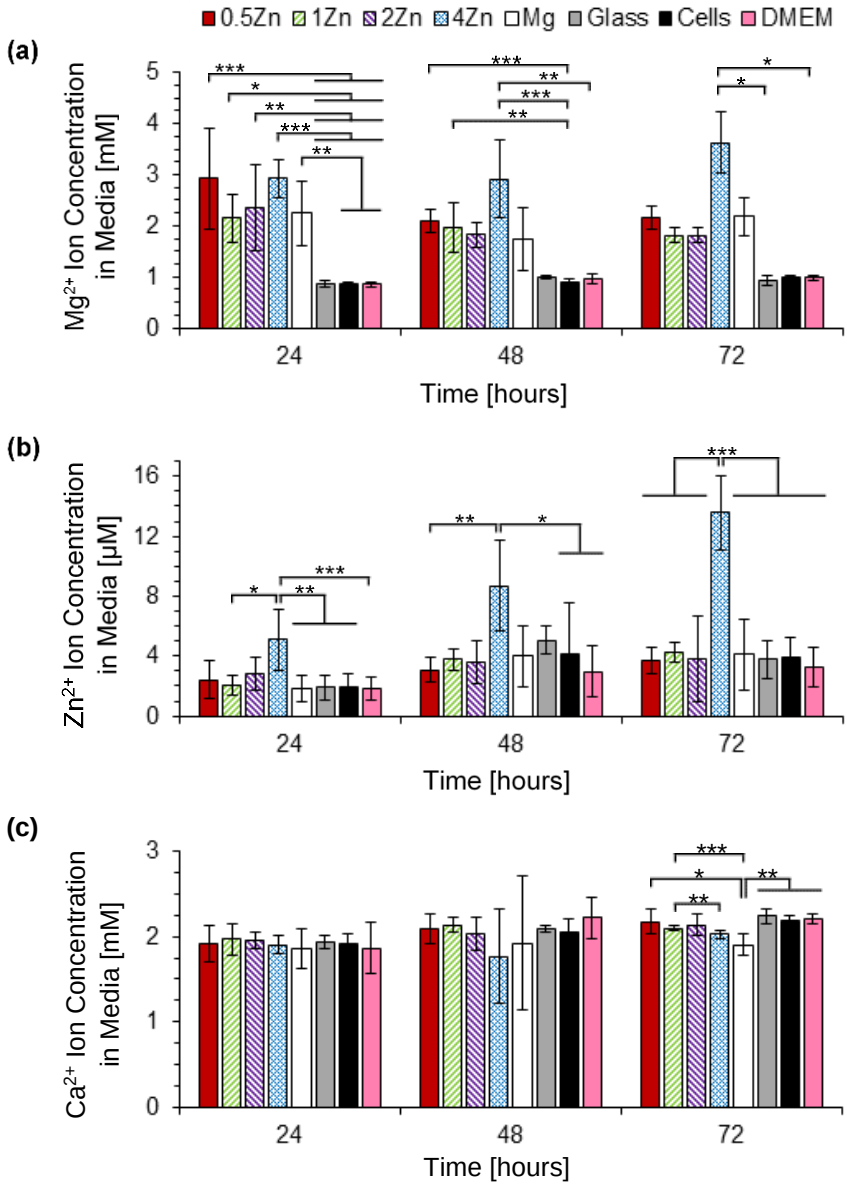

Figure 3.15: Degradation of Mg-xZn-0.5Ca alloys (x = 0.5, 1, 2, 4 wt. %) and pure Mg control in BMSC culture media during 72 hr.
(a) Total Mg^{2+} ion amount in BMSC culture media over 72 hr, and (b) average daily degradation rate (mass loss rate) per unit surface area. Values are mean ± SD, n = 3; *p < 0.05, **p < 0.01.

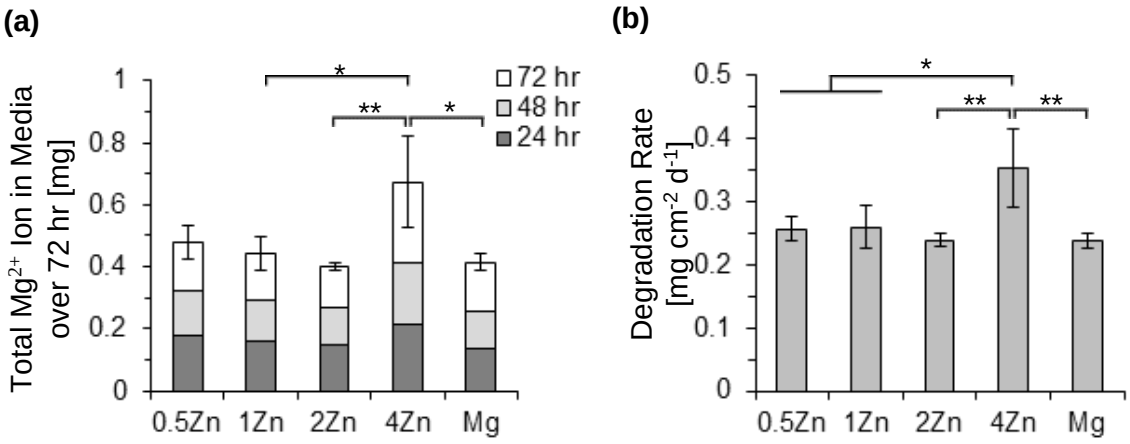

Figure 3.16: BMSC behaviors after 24 hr of incubation in DMEM + 10% FBS + 1% P/S with initial pH values intentionally adjusted to 7.4 – 9.5.
(a) Fluorescence images of BMSCs. Blue color indicates DAPI stained nuclei and green color indicates Alexa Fluor® 488 stained F-actin (cytoskeleton). Scale bar = 200 µm for all images. Original magnification: 10x. (b) Measured pH of culture media after 24 hr incubation with BMSCs. Blank indicates media without cells. (c) BMSC adhesion density on culture plates. (d) F-actin area per adhered BMSC nucleus. (e) Cell diameter aspect ratio (D_{max}/D_{min}). Values in (b) are mean ± SD, and (c) – (e) are mean ± standard error of the means; n = 3 for all measurements; *p < 0.05.

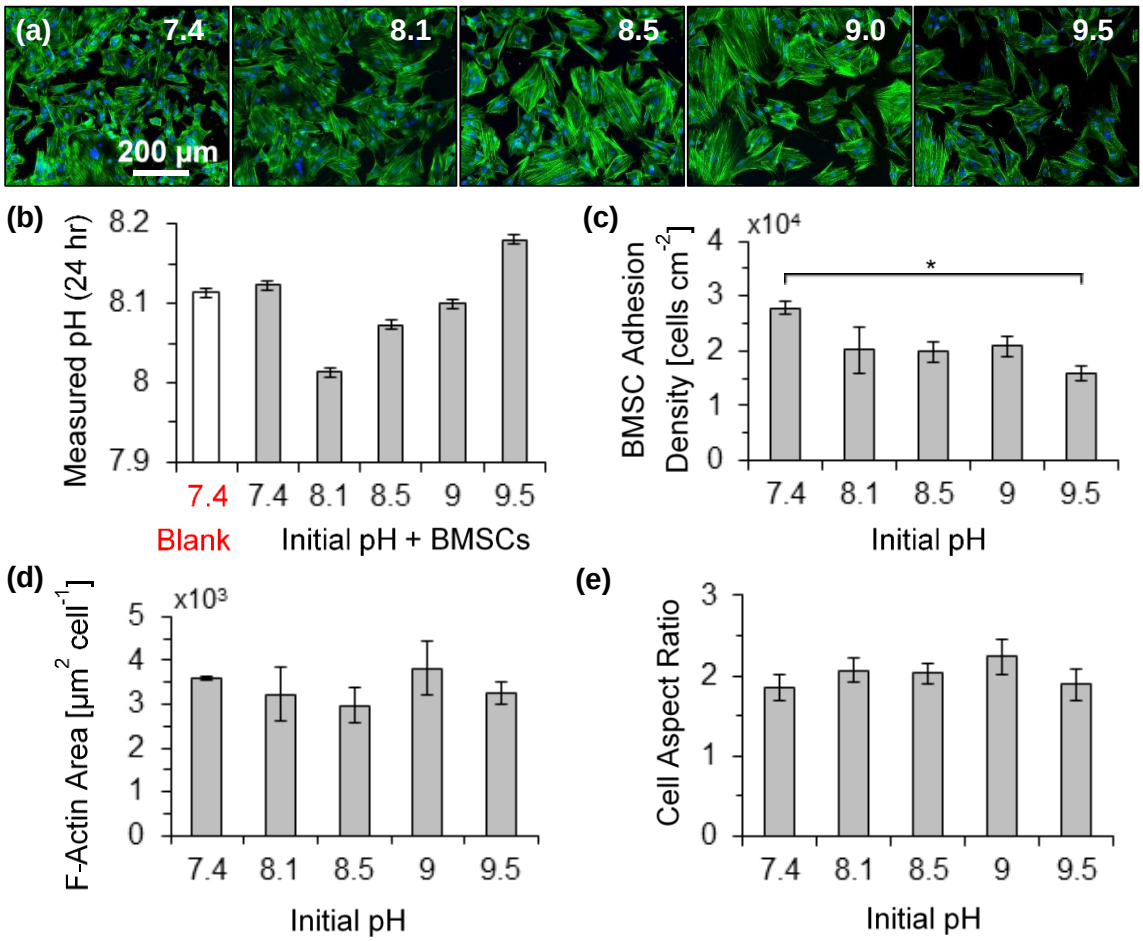

Figure 3.17: BMSC behaviors after 24 hr of incubation in DMEM + 10% FBS + 1% P/S supplemented with Mg^{2+} concentration of 0 - 27.6 mM initially.
(a) Fluorescence images of BMSCs. Blue color indicates DAPI stained nuclei and green color indicates Alexa Fluor® 488 stained F-actin (cytoskeleton). Scale bar = 200 μm for all images. Original magnification: 10x. (b) Measured Mg ion concentration in culture media after 24 hr of incubation with BMSCs. Blank indicates media without cells. (c) BMSC adhesion density on culture plates. (d) F-actin area per adhered BMSC nucleus. (e) Cell diameter aspect ratio (D_{max}/D_{min}). Values in (b) are mean ± SD, and (c) – (e) are mean ± standard error of the means; n = 3 for all measurements; *$p < 0.05$.

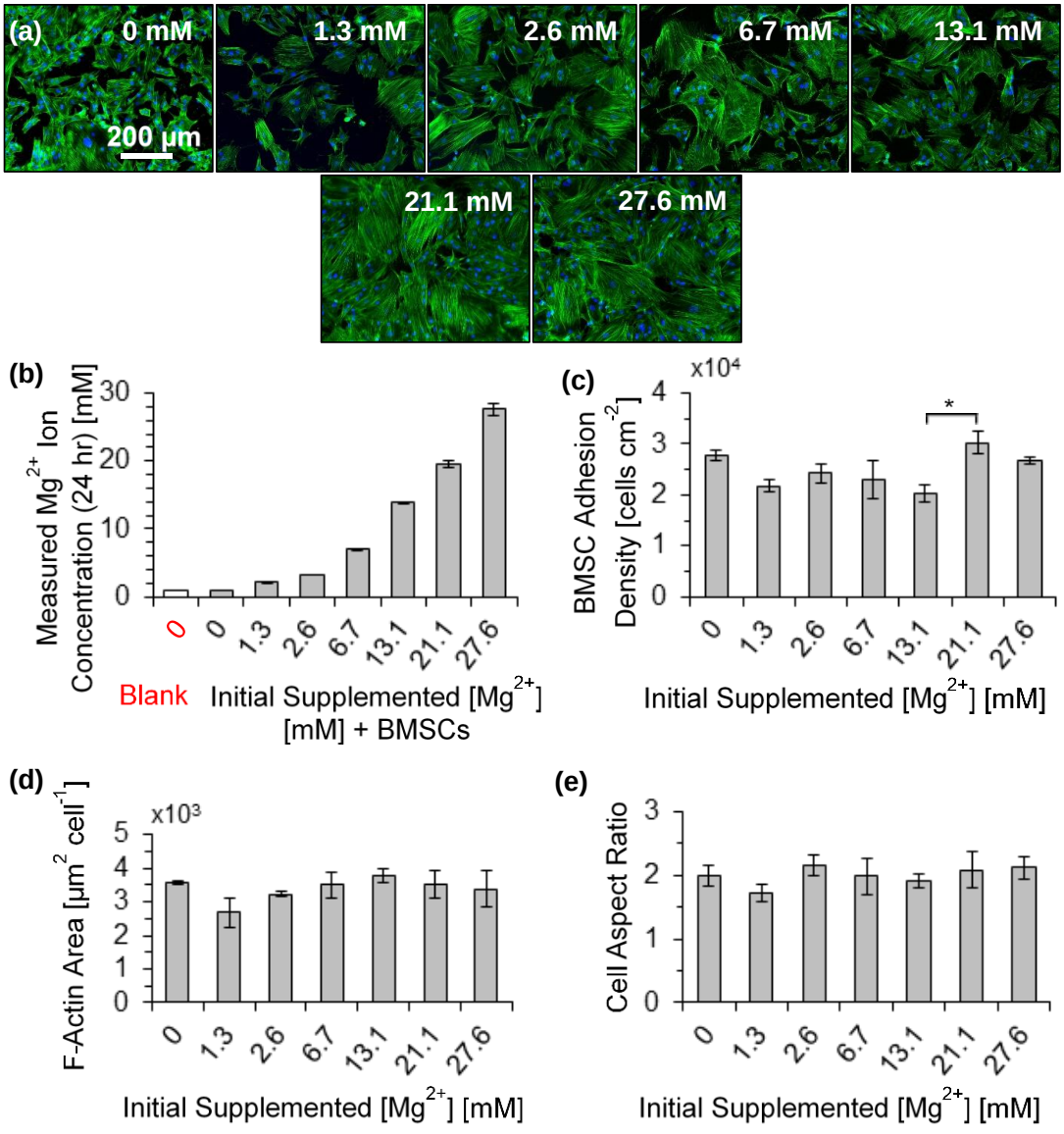

Figure 3.18: Summary of the degradation and mechanical properties of Mg-xZn-0.5Ca (x = 0.5, 1.0, 2.0, or 4.0 wt. %) alloys, critical Zn/Ca ratios that affect phase formation, and major phase composition and second phase morphology formed (which affect mechanical and corrosion properties).
The mechanical properties for the Mg-4.0Zn-0.5Ca alloy were obtained from Refs. [8, 24]. The mechanical properties for the Mg-0.5Zn-0.5Ca alloy were extrapolated based on values in Ref. [9].

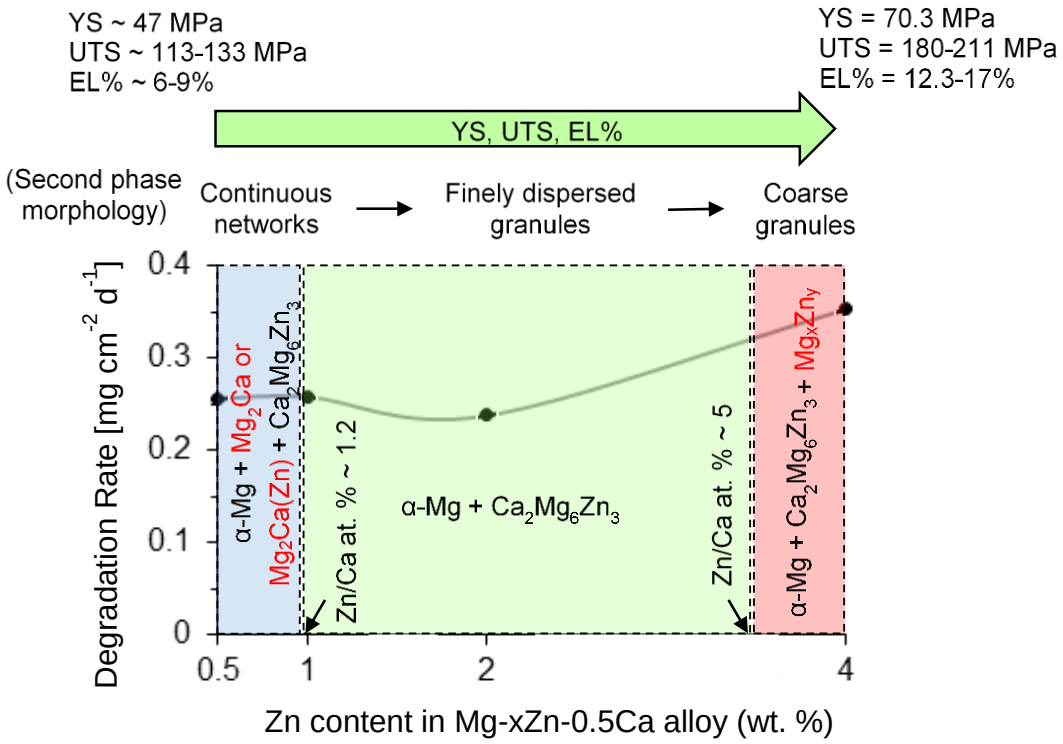

Figure 3.19: Summary of the cell culture conditions generated by the degradation of the Mg-xZn-0.5Ca alloys (x = 0.5, 1, 2, 4 wt. %) and pure Mg control compared with glass reference and cells-only positive control.
Change in pH is normalized by change in pH of cell culture media only (DMEM). Mg^{2+} ion concentration is normalized by the Mg^{2+} ion concentration in cell culture media only (DMEM). Values are mean.

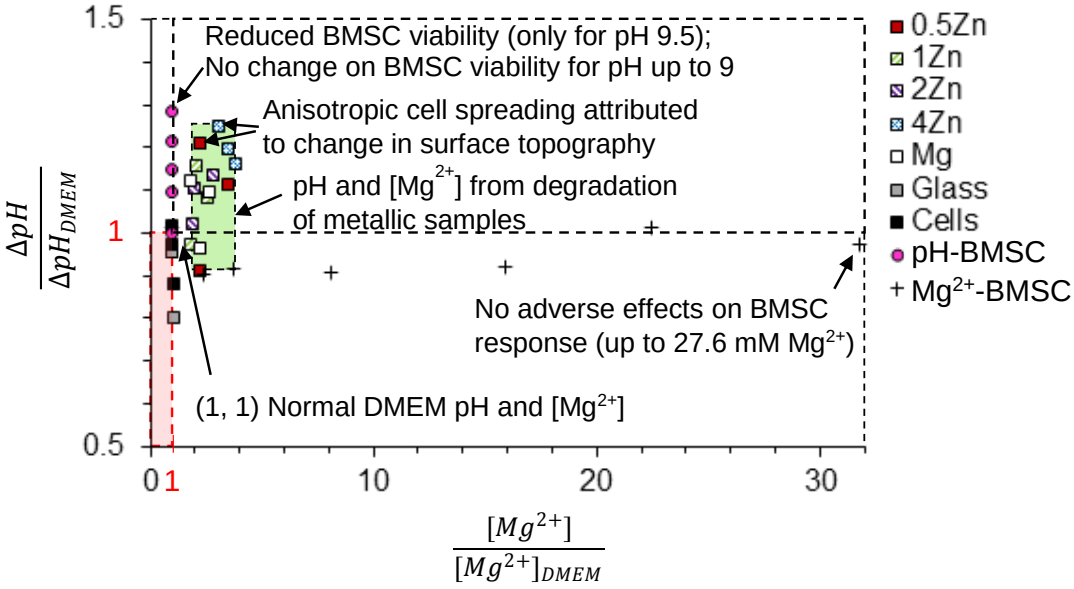

Table 3.1: Timeline of the development of as-cast crystalline Mg-Zn-Ca ternary alloys up-to-date.
Remarks summarize the key information of interest from the reported literature. Note: "Alloy design" articles typically included microstructure, crystallinity, and/or results on mechanical properties. "Bio-corrosion" articles typically included alloy design, and electrochemical/immersion results; "Cytocompatibility" articles typically included alloy design, bio-corrosion, and cell culture results; and "*In vivo*" articles typically included alloy design, bio-corrosion, cytocompatibility, and results from *in vivo* implantation. Values obtained from Refs. [6-26].

Year	Ref	Zn content (wt. %)	Ca content (wt. %)	Zn/Ca at. % ratio	Type of Article	Remarks
1997	[17]	1.0	1.0	0.61	Alloy design	First report of cast Mg-Zn-Ca crystalline ternary alloys
2004	[18]	3.0, 6.0, 9.0	1.5	1.23, 2.45, 4.09	Alloy design	Second phase formation
2005	[19]	1.0	1.0	0.61	Alloy design	Precipitation hardening
2005	[20]	0.80, 4.69	0.5	1.0, 6.0	Alloy design	TEM and 3DAP Characterization of age-hardening
2006	[21]	0.2, 1.05, 1.2, 1.9	0.3, 0.5, 1.2	0.25, 0.61, 1.29, 3.88	Alloy design	Precipitation hardening
2006	[22]	3.2	1.6	1.23	Alloy design	Solidification, solution treatment, and age-hardening
2007	[23]	1.0	1.0	0.61	Alloy design	Analysis of precipitation using positron annihilation
2009	[24]	4.0	0.5	4.90	Alloy design	Microstructure and mechanical properties
2009	[25]	0.80, 1.6, 4.2	0.5	1.0, 2.0, 5.33	Alloy design	Age-hardening response
2010	[6]	2.0	0.2	6.13	Bio-corrosion	Electrochemical tests in Ringer's solution
2011	[7]	6.0, 10, 20	1.0	3.68, 6.13, 12.26	Bio-corrosion	Electrochemical tests in phosphate buffered saline
2011	[9]	1.0, 2.0, 3.0, 4.0, 5.0, 6.0	1.0	0.61, 1.23, 1.84, 2.45, 3.07, 3.68	Cytocompatibility	L-929 fibroblasts and extract method
2011	[8]	4.0	0.2, 0.5, 1.0, 1.5, 2.0	0.61, 1.23, 1.84, 2.45, 3.07, 3.68	*In vivo*	3 months in New Zealand white rabbit
2011	[10]	2.0	3.0	0.41	Bio-corrosion	Electrochemical tests and immersion for 9 days in Hank's solution
2011	[11]	2.0	0.24	5.11	Bio-corrosion	Electrochemical tests and immersion for 2 days in Kokubo's simulated body fluid
2012	[26]	0.50, 1.0, 3.0, 4.5, 9.0	0.5	0.61, 1.23, 3.68, 5.52, 11.03	Alloy design	Thermal analysis and macroscopical characterization
2012	[12]	0.5, 1.0, 3.0, 4.5, 6.0, 9.0	0.5	0.61, 1.23, 3.68, 5.52, 7.36, 11.03	Bio-corrosion	Electrochemical tests and immersion for 14 days in Kokubo's simulated body fluid; thermal analysis of secondary phase formation
2012	[13]	4.0	0.2	12.26	Cytocompatibility	L-929 fibroblasts and extract method
2013	[14]	0.5, 1.0, 1.5, 3.0, 5.0	5.0	0.06, 0.12, 0.18, 0.36, 0.61	*In vivo*	12 weeks in Sprague-Dawley rats; 24 weeks in New Zealand white rabbit
2013	[15]	5.0, 6.0	1.0, 2.0, 3.0	1.02, 1.53, 3.07, 3.68	Cytocompatibility	L-929 fibroblasts and extract method
2013	[16]	4.0, 9.0	1.0	2.45, 5.52	Cytocompatibility	BMSCs in co-culture with Mg-Zn-Ca alloys
2014	This study	0.5 ,1.0, 2.0, 4.0	0.5	0.61, 1.23, 2.45, 4.90	Cytocompatibility	BMSCs in direct culture with Mg-Zn-Ca alloys; the first report of *in vitro* cell responses at the dynamic interface and mechanisms

3.7. References

[1] Rickard DJ, Sullivan TA, Shenker BJ, Leboy PS, Kazhdan I. Induction of Rapid Osteoblast Differentiation in Rat Bone Marrow Stromal Cell Cultures by Dexamethasone and BMP-2. Dev Bio. 1994;161:218-28.

[2] Fischer J, Pröfrock D, Hort N, Willumeit R, Feyerabend F. Reprint of: Improved cytotoxicity testing of magnesium materials. Mater Sci Eng, B. 2011;176:1773-7.

[3] Xin Y, Hu T, Chu PK. In vitro studies of biomedical magnesium alloys in a simulated physiological environment: A review. Acta Biomater. 2011;7:1452-9.

[4] Liu H. The effects of surface and biomolecules on magnesium degradation and mesenchymal stem cell adhesion. J Biomed Mater Res A. 2011;99:249-60.

[5] Johnson I, Perchy D, Liu H. In vitro evaluation of the surface effects on magnesium-yttrium alloy degradation and mesenchymal stem cell adhesion. J Biomed Mater Res A. 2011;100A:477–85.

[6] Rosalbino F, Negri S, Saccone A, Angelini E, Delfino S. Bio-corrosion characterization of Mg–Zn–X (X = Ca, Mn, Si) alloys for biomedical applications. J Mater Sci Mater Med. 2010;21:1091-8.

[7] Xu Z, Smith C, Chen S, Sankar J. Development and microstructural characterizations of Mg–Zn–Ca alloys for biomedical applications. Mater Sci Eng, B. 2011;176:1660-5.

[8] Zhang BP, Wang Y, Geng L. Research on Mg-Zn-Ca Alloy as Degradable Biomaterial. In: Pignatello R, editor. Biomaterials - Physics and Chemistry. Rijeka, Croatia: InTech; 2011. p. 183-204.

[9] Zhang B, Hou Y, Wang X, Wang Y, Geng L. Mechanical properties, degradation performance and cytotoxicity of Mg–Zn–Ca biomedical alloys with different compositions. Mater Sci Eng, C. 2011;31:1667-73.

[10] Du H, Wei Z, Liu X, Zhang E. Effects of Zn on the microstructure, mechanical property and bio-corrosion property of Mg–3Ca alloys for biomedical application. Mater Chem Phys. 2011;125:568-75.

[11] Gao JH, Guan SK, Ren ZW, Sun YF, Zhu SJ, Wang B. Homogeneous corrosion of high pressure torsion treated Mg–Zn–Ca alloy in simulated body fluid. Mater Lett. 2011;65:691-3.

[12] Bakhsheshi-Rad HR, Abdul-Kadir MR, Idris MH, Farahany S. Relationship between the corrosion behavior and the thermal characteristics and microstructure of Mg–0.5Ca–xZn alloys. Corros Sci. 2012;64:184-97.

[13] Sun Y, Zhang B, Wang Y, Geng L, Jiao X. Preparation and characterization of a new biomedical Mg–Zn–Ca alloy. Mater Design. 2012;34:58-64.

[14] Cha P-R, Han H-S, Yang G-F, Kim Y-C, Hong K-H, Lee S-C, et al. Biodegradability engineering of biodegradable Mg alloys: Tailoring the electrochemical properties and microstructure of constituent phases. Sci Rep. 2013;3.

[15] Yin P, Li N, Lei T, Liu L, Ouyang C. Effects of Ca on microstructure, mechanical and corrosion properties and biocompatibility of Mg–Zn–Ca alloys. J Mater Sci Mater Med. 2013;24:1365-73.

[16] Cipriano AF, Miller CT, Liu H. Cytocompatibility of Magnesium-Zinc-Calcium Alloys with Bone Marrow Derived Mesenchymal Stem Cells. In: B. Mishra MIaTC, editor. Advanced Materials Research, THERMEC 2013 Supplement. Las Vegas, NV: Trans Tech Publ; 2014. p. 1-6.

[17] Nie JF, Muddle BC. Precipitation hardening of Mg-Ca(-Zn) alloys. Scr Mater. 1997;37:1475-81.

[18] Jardim PM, Solórzano G, Sande JBV. Second phase formation in melt-spun Mg–Ca–Zn alloys. Mater Sci Eng, A. 2004;381:196-205.

[19] Gao X, Zhu SM, Muddle BC, Nie JF. Precipitation-hardened Mg–Ca–Zn alloys with superior creep resistance. Scr Mater. 2005;53:1321-6.

[20] Oh JC, Ohkubo T, Mukai T, Hono K. TEM and 3DAP characterization of an age-hardened Mg–Ca–Zn alloy. Scr Mater. 2005;53:675-9.

[21] Bamberger M, Levi G, Sande JB. Precipitation hardening in Mg-Ca-Zn alloys. Metall and Mat Trans A. 2006;37:481-7.

[22] Levi G, Avraham S, Zilberov A, Bamberger M. Solidification, solution treatment and age hardening of a Mg–1.6 wt.% Ca–3.2 wt.% Zn alloy. Acta Materialia. 2006;54:523-30.

[23] Ortega Y, Monge MA, Pareja R. The precipitation process in Mg–Ca–(Zn) alloys investigated by positron annihilation spectroscopy. J Alloy Compd. 2008;463:62-6.

[24] Geng L, Zhang BP, Li AB, Dong CC. Microstructure and mechanical properties of Mg–4.0Zn–0.5Ca alloy. Mater Lett. 2009;63:557-9.

[25] Oh-ishi K, Watanabe R, Mendis CL, Hono K. Age-hardening response of Mg–0.3 at.%Ca alloys with different Zn contents. Mater Sci Eng, A. 2009;526:177-84.

[26] Farahany S, Bakhsheshi-Rad HR, Idris MH, Abdul Kadir MR, Lotfabadi AF, Ourdjini A. In-situ thermal analysis and macroscopical characterization of Mg–xCa and Mg–0.5Ca–xZn alloy systems. Thermochim Acta. 2012;527:180-9.

[27] Iskandar ME, Aslani A, Liu H. The effects of nanostructured hydroxyapatite coating on the biodegradation and cytocompatibility of magnesium implants. J Biomed Mater Res, A. 2013;101A:2340-54.

[28] Cipriano AF, De Howitt N, Gott SC, Miller CT, Rao MP, Liu H. Bone Marrow Stromal Cell Adhesion and Morphology on Micro- and Sub-Micropatterned Titanium. J Biomed Nanotechnol. 2014;10:660-8.

[29] Cipriano AF, Zhao T, Johnson I, Guan R-G, Garcia S, Liu H. In vitro degradation of four magnesium–zinc–strontium alloys and their cytocompatibility with human embryonic stem cells. J Mater Sci Mater Med. 2013;24:989-1003.

[30] Nguyen TY, Liew CG, Liu H. An In Vitro Mechanism Study on the Proliferation and Pluripotency of Human Embryonic Stems Cells in Response to Magnesium Degradation. PLoS ONE. 2013;8:e76547.

[31] Dubin-Thaler BJ, Giannone G, Döbereiner H-G, Sheetz MP. Nanometer Analysis of Cell Spreading on Matrix-Coated Surfaces Reveals Two Distinct Cell States and STEPs. Biophys J. 2004;86:1794-806.

[32] Lelong IH, Rebel G. ph drift of “physiological buffers” and culture media used for cell incubation during in vitro studies. J Pharmacol Toxicol Methods. 1998;39:203-10.

[33] Zhang E, Yang L. Microstructure, mechanical properties and bio-corrosion properties of Mg–Zn–Mn–Ca alloy for biomedical application. Mater Sci Eng, A. 2008;497:111-8.

[34] Song G, Atrens A. Understanding Magnesium Corrosion—A Framework for Improved Alloy Performance. Adv Eng Mater. 2003;5:837-58.

[35] Ian J, Khalid A, Huinan L. Nanostructured hydroxyapatite/poly(lactic- co - glycolic acid) composite coating for controlling magnesium degradation in simulated body fluid. Nanotechnology. 2013;24:375103.

[36] Kirkland NT, Birbilis N, Staiger MP. Assessing the corrosion of biodegradable magnesium implants: A critical review of current methodologies and their limitations. Acta Biomater. 2012;8:925-36.

[37] Zheng YF, Gu XN, Witte F. Biodegradable metals. Mater Sci Eng, R. 2014;77:1-34.

[38] Liu H, Chen Y, Tang Y, Wei S, Niu G. The microstructure, tensile properties, and creep behavior of as-cast Mg–(1–10)%Sn alloys. J Alloy Compd. 2007;440:122-6.

[39] Yang C, Yuan G, Zhang J, Tang Z, Zhang X, Dai K. Effects of magnesium alloys extracts on adult human bone marrow-derived stromal cell viability and osteogenic differentiation. Biomed Mater. 2010;5:045005.

[40] Niederlaender J, Walter M, Krajewski S, Schweizer E, Post M, Schille C, et al. Cytocompatibility evaluation of different biodegradable magnesium alloys with human mesenchymal stem cells. J Mater Sci Mater Med. 2014;25:835-43.

[41] Li RW, Kirkland NT, Truong J, Wang J, Smith PN, Birbilis N, et al. The influence of biodegradable magnesium alloys on the osteogenic differentiation of human mesenchymal stem cells. J Biomed Mater Res, A. 2014:n/a-n/a.

[42] Li L, Gao J, Wang Y. Evaluation of cyto-toxicity and corrosion behavior of alkali-heat-treated magnesium in simulated body fluid. Surf Coat Tech. 2004;185:92-8.

[43] Lock J, Nguyen T, Liu H. Nanophase hydroxyapatite and poly(lactide-co-glycolide) composites promote human mesenchymal stem cell adhesion and osteogenic differentiation in vitro. J Mater Sci Mater Med. 2012;23:2543-52.

[44] Feyerabend F, Fischer J, Holtz J, Witte F, Willumeit R, Drücker H, et al. Evaluation of short-term effects of rare earth and other elements used in magnesium alloys on primary cells and cell lines. Acta Biomater. 2010;6:1834-42.

[45] Miki H, Kasprzak KS, Kenney S, Heine UI. Inhibition of intercellular communication by nickel(II): antagonistic effect of magnesium. Carcinogenesis. 1987;8:1757-60.

[46] Sheikh MS, Santa Ana CA, Nicar MJ, Schiller LR, Fordtran JS. Gastrointestinal Absorption of Calcium from Milk and Calcium Salts. New Engl J Med. 1987;317:532-6.

[47] Roh J-L, Park CI. Routine oral calcium and vitamin D supplements for prevention of hypocalcemia after total thyroidectomy. Am J Surg. 2006;192:675-8.

[48] Grillo CA, Alvarez F, Fernández Lorenzo de Mele MA. Biological effects of magnesium particles degradation on UMR-106 cell line: Influence of fluoride treatments. Colloids Surf, B. 2011;88:471-6.

[49] Romani A. Regulation of magnesium homeostasis and transport in mammalian cells. Arch Biochem Biophys. 2007;458:90-102.

[50] Song G. Control of biodegradation of biocompatable magnesium alloys. Corros Sci. 2007;49:1696-701.

[51] Staiger MP, Pietak AM, Huadmai J, Dias G. Magnesium and its alloys as orthopedic biomaterials: A review. Biomaterials. 2006;27:1728-34.

[52] Cavalcanti-Adam EA, Volberg T, Micoulet A, Kessler H, Geiger B, Spatz JP. Cell Spreading and Focal Adhesion Dynamics Are Regulated by Spacing of Integrin Ligands. Biophys J. 2007;92:2964-74.

Chapter 4 – A comparative study on the degradation of Mg-4Zn-xSr alloys and their cytocompatibility using the direct culture method

4.1. Background

The first objective of this study was to utilize the cell-based direct *in vitro* culture method to investigate the degradation and cytocompatibility of four Mg-4Zn-xSr alloys (x = 0.15, 0.5, 1.0, 1.5 wt. %; designated as ZSr41A, B, C, and D respectively) with bone marrow derived mesenchymal stem cells (BMSCs). The direct *in vitro* culture method was used to mimic *in vivo* physiological conditions and evaluate cell responses at the cell-biomaterial interface (*direct contact*) and on the culture plate (*indirect contact*; exposure to solubilized degradation products) surrounding the Mg-based biomaterial [1]. The use of BMSCs for this *in vitro* study was motivated by their important roles in early implant osseointegration and bone regeneration *in vivo* [2]. Other research groups have also supported the applicability of BMSCs for testing the cytocompatibility of Mg-based materials for orthopedic applications [3]. It has also been suggested that the degradation of Mg-based materials in Dulbecco's Modified Eagle Medium (DMEM) resembled *in vivo* conditions more closely due to the presence of physiologically relevant ions and proteins [4-6]. Additionally, a systematic comparison on the degradation of the ZSr41 alloys in the direct culture with multiple cell types in their respective media [7, 8] along with the biological performance compared with other Mg alloys [1] was included in this study. The objective of the systematic comparison was to: (i)

identify key aspects in distinct cell-based direct *in vitro* cultures that affect the degradation of Mg-based biomaterials, (ii) rate ZSr41 alloy performance compared to other Mg-based biomaterials screened with the same experimental methodology, and (iii) identify the capabilities of different cell lines in detecting cytotoxic effects induced by the degradation of Mg-based biomaterials. To our knowledge, this is the first comprehensive report to focus on BMSC interactions at the cell-ZSr41 interface along with a comprehensive evaluation of factors within the direct *in vitro* culture method that will help design screening tests designed specifically for Mg-based biomaterials.

4.2. Materials and methods

4.2.1. Preparation of ZSr41 alloy and Mg control

The ZSr41 alloys in this study had a nominal composition of 4 wt. % Zn with 0.15, 0.5, 1.0, or 1.5 wt. % Sr; these alloys were designated as ZSr41A, ZSr41B, ZSr41C, and ZSr41D accordingly with increasing Sr content. Details pertaining to the metallurgical process and heat treatment used for alloy preparation are given elsewhere [7, 9]. The heat-treated sheets of ZSr41 alloys had a nominal thickness of 1 mm and were cut into 5 x 5 mm squares. Likewise, commercially pure Mg sheets (99.9%, as-rolled, 1.0 mm thick, Cat# 40604; Alfa Aesar, Ward Hill, MA, USA) and non-culture treated glass slides (1.0 mm thick, Cat#12-544-1; Fisher Scientific, Hampton, NH, USA) were cut into 5 x 5 mm squares and used as a control and reference, respectively, in this study. Prior to cell culture experiments,

all metallic samples were ground with SiC abrasive paper up to 1200 grit, ultrasonically cleaned for 15 min in separate baths of acetone and ethanol, individually weighed (M_0), and sterilized under ultraviolet (UV) radiation for 4 hr on each side. The glass samples were cleaned in acetone and ethanol, and sterilized under UV radiation following the same procedure.

4.2.2. BMSC responses and *in vitro* degradation of ZSr41 alloys

4.2.2.1. Preparation of BMSC culture

Following a protocol approved by the University of California at Riverside (UCR) Institutional Animal Care and Use Committee (IACUC), BMSCs were harvested from the marrow cavity of the femur and tibia of three-week-old female Sprague Dawley rat weanlings after euthanasia by CO_2. Specific details regarding BMSC extraction, isolation and culture are described previously [10]. Briefly, the distal and proximal ends of the bones were dissected and the bone marrow was flushed out of the bone cavity and collected using DMEM (Sigma Aldrich, St. Louis, MO, USA) supplemented with 10% fetal bovine serum (FBS; HyClone, Logan, UT, USA) and 1% penicillin/streptomycin (P/S; Invitrogen, Grand Island, NY, USA). Hereafter, DMEM + 10% FBS + 1% P/S is referred to as DMEM. The collected cells were then filtered through a 70-μm nylon strainer to remove cell aggregates and tissue debris. The filtered BMSCs were cultured in DMEM under standard cell culture conditions (i.e., 37ºC, 5%/95% CO_2/air, humidified sterile environment) to 90-95% confluency. Subsequently, BMSCs were detached using Trypsin

(Invitrogen) and passaged up to the second passage (P2) for culture with ZSr41 alloys.

4.2.2.2. Direct culture of BMSCs with ZSr41 alloys

All the samples were placed in standard 12-well cell culture treated plates and rinsed with 2 mL of DMEM to calibrate the osmotic pressure. Subsequently, BMSCs (P2) were seeded directly onto the surfaces of the samples at a density of $4x10^4$ cells cm^{-2} and incubated in 3 mL of DMEM under standard cell culture conditions for 72 hr. A positive control, designated as "cells" group, consisted of BMSCs cultured only with DMEM in the wells, i.e. without any samples. DMEM alone was also used as a blank reference and designated as “DMEM” group. In order to more closely mimic *in vivo* conditions where the circulation system regularly takes away soluble degradation products from the local site of implantation [7], the cell culture media was collected for analysis and replenished with 3 mL of fresh media at every 24 hr interval.

4.2.2.3. Characterization of the BMSCs in *direct* contact with ZSr41 alloys

The interface between the BMSC culture and ZSr41 alloys, Mg control, and glass reference was characterized using a scanning electron microscope (SEM; Nova NanoSEM 450, FEI Co., Hillsboro, OR, USA) following the 72 hr *in vitro* cultures. Additionally, corresponding surface elemental composition, and Mg Kα1 and C Kα1 elemental distribution maps were acquired with energy dispersive x-ray

spectroscopy (EDS) using a Nova NanoSEM 450 equipped with an X-Max50 detector and AZtecEnergy software (Oxford Instruments, Abingdon, Oxfordshire, UK). In preparation for SEM and EDS, the samples were removed from the culture wells and dip-rinsed in phosphate buffered saline (PBS) to remove non-adherent cells. Adherent cells were fixed with 3% glutaraldehyde in 0.1 M potassium phosphate buffer for 1 hr. After fixation, the samples were again dip-rinsed in PBS followed by a serial dehydration in increasing ethanol concentration (50%, 75%, 90%, 2x100%; 10 min each). The samples were then critical-point dried (Autosamdri-815, Tousimis Research Corp., Rockville, MD, USA) and sputter coated (Model 108, Cressington Scientific Instruments Ltd., Watford, UK) with platinum/palladium at 20 mA and 40 sec sputter time. An accelerating voltage of 20 kV was used to obtain SEM images and perform EDS analysis.

4.2.2.4. Quantification of BMSC adhesion and morphology under *direct* versus *indirect* contact conditions

BMSC adhesion and morphology on the surface of the samples (*direct contact* with the sample) and on culture plate surrounding the respective samples (*indirect contact* with the sample) was evaluated at 72 hr of incubation through fluorescence microscopy. The results from the culture plates were grouped separately and designated as “plate”. The samples in direct contact with BMSCs were removed from the wells and dip-rinsed in PBS to remove non-adherent cells. The corresponding wells were washed separately with PBS to remove non-adherent

cells. Adherent cells, both on the sample surface and on the plates, were separately fixed with 4% formaldehyde (10% neutral buffered formalin; VWR, Radnor, PA, USA) and stained with 4',6-diamidino-2-phenylindole dilactate (DAPI; Invitrogen) nucleic acid stain and Alexa Flour® 488-phalloidin F-actin stain for fluorescence imaging. Adherent cells on the sample surface and on the culture plate surrounding the sample were visualized using a fluorescence microscope (Eclipse Ti and NIS software, Nikon, Melville, NY, USA) with a 10x objective lens at the same exposure condition and analyzed using Image J (NIH, Bethesda, MD, USA). Cell adhesion per group was quantified by counting the DAPI-stained cell nuclei at five random locations on the sample surface and at nine random locations on the culture plate. Cell adhesion density was calculated as the number of adherent cells per unit area.

4.2.2.5. *In vitro* degradation of ZSr41 alloys in the BMSC culture

At each prescribed incubation interval, the *in vitro* degradation of the ZSr41 alloys and Mg was evaluated through measurements of pH and ionic concentrations of the collected media. The pH of the media at each incubation interval was measured immediately after collection using a calibrated pH meter (Model SB70P, VWR). The concentration of Mg^{2+}, Zn^{2+}, and Sr^{2+} ions in the collected media was measured using inductively coupled plasma optical emission spectroscopy (ICP-OES; Optima 8000, Perkin Elmer, Waltham, MA, USA). In order to minimize matrix effects in ICP-OES, the collected DMEM aliquots were diluted

to 1:100 solutions in DI water. Ionic concentrations were then obtained from calibration curves generated using Mg, Zn, and Sr standards (Perkin Elmer) diluted to ranges of 0.5-5.0, 0.1-1.0, and 0.1-1.0 mg/L respectively.

4.2.3. Statistical analyses

Cell adhesion through fluorescence and *in vitro* degradation experiments were run in triplicate. All data sets were tested for normal distribution and homogeneous variance. Parametric data sets were analyzed using one-way analysis of variance (ANOVA) followed by the Tukey HSD *post hoc* test. Data sets with normal distribution but heterogeneous variance were analyzed using one-way ANOVA (homogeneous variance not assumed) followed by the Games-Howell *post hoc* test. Non-parametric data sets were analyzed using the Kruskal-Wallis test followed by the Nemenyi *post hoc* test. Statistical significance was considered at $p < 0.05$.

4.3. Results

4.3.1. BMSCs in *direct* contact with ZSr41 alloys

A qualitative analysis of the BMSC-substrate interface showed changes in surface topography for the ZSr41 alloys compared with the Mg control and glass reference after 72 hrs of incubation. Figure 4.1 shows SEM micrographs of the cell-substrate interface for the materials investigated at an original magnification of 150x (insets were obtained at 1,000x) after 72 hr of direct culture and *direct*

contact with the samples. Degradation-induced surface cracks and secondary phases (indicated with black arrows) were observed on the surfaces of all ZSr41 alloys. As expected, the presence of secondary phases increased with increasing Sr content, as shown in previous characterization of the ZSr41 alloys [8]. All ZSr41 alloys showed similar characteristics in terms of the size and distribution of degradation cracks and debris. In contrast, surface cracks and severe localized degradation were more prevalent on the Mg control samples. Additionally, adhered BMSCs (indicated with white arrows) were observed on the surface of all ZSr41 alloy and Mg control samples. In all cases, the cells showed a high degree of isotropic spreading [1, 11] but the confluence was visibly lower compared with the glass reference which showed complete confluency after the 72 hr incubation period.

Furthermore, qualitative and semi-quantitative assessment of the elemental distribution and composition after the 72 hrs of incubation gave further evidence of changes in structural integrity and mineral deposition at the BMSC-substrate interface. Figure 4.2 shows elemental distribution maps of Mg and carbon (C; Kα1 lines for both) and a summary of elemental composition (in wt. %) results obtained from EDS analyses at 150x magnification of the samples after the 72 hr incubation. The Mg distribution maps (Figure 4.2a) of ZSr41 alloys compared with the Mg control showed that the surface of ZSr41 alloys remained more intact and gave indication of similar degradation mode for the ZSr41 alloys up to 72 hrs. Additionally, the C distribution maps (Figure 4.2a) of all metallic samples confirmed

the adhesion of BMSCs (brighter regions) along with other organic components (most likely protein and extracellular matrix adsorption). The stacked histogram shown in Figure 4.2b summarizes the elemental composition (in wt. %) results obtained from EDS analyses at 150x magnification. A Zn content comparable to the nominal 4% was detected on the surfaces of alloys ZSr41A, B, C, and D (3.81%, 4.46%, 3.04%, and 4.92%, respectively); Zn was not detected on the Mg control or glass reference. Additionally, increasing Sr content was also detected on alloys ZSr41B, C, and D (0.08, 0.34, and 0.84%, respectively); Sr was not detected on the surface of ZSr41A alloy, Mg control, or glass reference. Interestingly, all Mg-based materials showed co-localization of calcium (Ca), phosphorus (P), and oxygen (O) which indicated that Mg degradation possibly attracted mineral deposition. The deposition of Ca, P, and O was approximately equal and exclusive for all Mg-based materials and is consistent with prior published work [1, 8]. In contrast, the glass reference did not show deposition of Ca and P; the Ca and O content reported in glass closely matched the composition of soda lime glass characterized before cell culture [1]. Lastly, all samples showed sodium (Na) and potassium (K) content which was attributed to deposited salts from solubilized ions in the culture media.

4.3.2. BMSC adhesion under *direct* and *indirect* contact conditions

Figure 4.3 summarizes results from BMSC adhesion directly onto the sample surface (*direct* contact) and on the culture plate (*indirect* contact) after 72 hr direct

culture with the ZSr41 alloys, Mg control, and glass reference. Figure 4.3a shows representative fluorescence images of BMSCs attached to the culture plates (*indirect* contact) at 72 hrs post-incubation; similar images were obtained for the 72 hr *direct* contact (not shown). The representative fluorescence images showed that BMSCs under *indirect* contact grew to confluency during the 72 hr incubation with the samples. The DAPI-stained nuclei were used to quantify cell adhesion density and results are plotted in the histograms shown in Figure 4.3b. ANOVA was used to confirm statistically significant differences in the mean cell adhesion density on the sample surface (*direct* contact) [F (5, 12) = 3.985, p = 2.312x10^{-2}]. Specifically, *post hoc* pairwise comparisons showed that the cell adhesion density on the surface of ZSr41A (0.28±0.14x10^4 cells cm^{-2}) and ZSr41B (0.13±0.08x10^4 cells cm^{-2}) was significantly lower (p < 0.05) when compared with the glass reference (2.97±0.70x10^4 cells cm^{-2}). Results from cell adhesion density on the culture plate (*indirect* contact) showed no statistically significant differences.

4.3.3. *In vitro* degradation of ZSr41 alloys in the BMSC culture

Results from the analysis of the DMEM culture media during the 72 hrs of incubation (in 24 hr intervals) are summarized in the histograms shown in Figure 4.4. Media pH and Mg^{2+} ion concentration ([Mg^{2+}]) are both important indicators of the degradation of Mg-based materials [12]; in addition the Zn^{2+} and Sr^{2+} ion concentrations ([Zn^{2+}] and [Sr^{2+}], respectively) were also measured to ensure concentrations remained below reported cytotoxic levels.

ANOVA was used to confirm statistically significant differences in the mean pH of the collected culture media at 24 hrs [F (7, 16) = 4.5647, p = 5.685x10^{-3}], 48 hrs [F (7, 16) = 7.7447, p = 3.672x10^{-4}], and 72 hrs [F (7, 16) = 13.21, p = 1.40x10^{-5}] (Figure 4.4a). Specifically, *post hoc* pairwise comparisons at 24 hrs showed that the pH of Mg culture media (8.13±0.01) was significantly higher (p < 0.05) compared with ZSr41A (8.06±0.02) and the glass reference (8.06±0.01). At 48 hrs, *post hoc* pairwise comparisons showed that pH of the glass reference (7.95±0.01) and BMSC-only positive control (7.96±0.02) culture media were significantly lower (p < 0.01 and p < 0.05, respectively) when compared with ZSr41C (8.03±0.04), ZSr41D (8.04±0.02), and DMEM-only blank reference (7.95±0.01). At 72 hrs, *post hoc* tests showed that the pH of the culture media of ZSr41B (8.07±0.05) was significantly higher (p < 0.05) compared with the Mg control (7.98±0.03) and glass reference (7.94±0.02). Likewise, the pH of the ZSr41C (8.15±0.05) culture media was significantly higher (p < 0.05) compared with ZSr41A (8.02±0.05); both ZSr41C and ZSr41D (8.11±0.02) were significantly higher (p < 0.001 and p < 0.05, respectively) compared with the Mg control, glass reference, and BMSC-only positive control (7.99±0.02). Furthermore, the pH of the DMEM blank reference (8.07±0.02) was significantly higher (p < 0.05) compared with the glass reference.

The Kruskal-Wallis for non-parametric data was used to confirm statistically significant differences in the mean [Mg^{2+}] of the collected culture media at 24 hrs [X^2 (7, N = 24) = 19.2267, p = 7.506x10^{-3}] and 48 hrs [X^2 (7, N = 24) = 18.8267, p = 8.748x10^{-3}]; likewise, ANOVA confirmed statistically significant differences at 72

hrs [F (7, 16) = 33.958, p = 1.92x10^{-8}] (Figure 4.4b). At 24 hrs, *post hoc* pairwise comparisons showed that the [Mg^{2+}] in the culture media of ZSr41A (3.15±0.73 mM) and ZSr41B (2.72±0.18 mM) were significantly higher (p < 0.05) when compared with the BMSC-only positive control (0.59±0.10 mM) and DMEM blank reference (0.59±0.13 mM). At 48 hrs, *post hoc* pairwise comparisons showed that the [Mg^{2+}] in the culture media of ZSr41A (2.72±0.33 mM) was significantly higher (p < 0.05) when compared with the glass (0.60±0.08 mM) and DMEM blank (0.63±0.08 mM) references. Additionally, both ZSr41B (2.56±0.19 mM) and ZSr41C (2.54±0.07 mM) were significantly higher (p < 0.05) when compared with the glass reference. At 72 hrs, *post hoc* pairwise comparisons showed that the [Mg^{2+}] in the culture media of all ZSr41 alloys was significantly higher (p < 0.001) when compared with the non-metallic groups. That is, ZSr41A (2.65±0.40 mM), ZSr41B (2.48±0.22 mM), ZSr41C (2.37±0.11 mM), and ZSr41D (2.39±0.19 mM) were all significantly higher compared with the glass reference (0.68±0.05 mM), BMSC-only positive control (0.61±0.06 mM), and DMEM-only blank reference (0.77±0.21 mM). Likewise, the Mg control (1.77±0.50 mM) was significantly higher compared with the glass, BMSC, and DMEM groups. The only significant difference (p < 0.05) between metallic groups was confirmed between ZSr41A and the Mg control. In general, as expected, all of the Mg-based samples caused an increase in the [Mg^{2+}] of the cell culture media.

Figures 4.4c and 4.4d show [Zn^{2+}] and [Sr^{2+}], respectively, in the cell culture media after 72 hrs of incubation. No statistically significant differences were

confirmed for either $[Zn^{2+}]$ or $[Sr^{2+}]$. Despite the absence of significant differences, in general, the $[Zn^{2+}]$ and $[Sr^{2+}]$ in the culture media were near the single-digit μM range.

The degradation rates of each ZSr41 alloy and pure Mg control (given as a mass loss rate per unit area per day) are summarized in Figure 4.5. These values were calculated according to the following equation (Eq. 4.1):

$$(Eq.\,4.1) \qquad Deg.Rate = \frac{\left([Mg^{2+}]_{i,tot} - [Mg^{2+}]_{DMEM,tot}\right) * V}{SA_i * t}$$

Where $[Mg^{2+}]_{i,tot}$ represents the total $[Mg^{2+}]$ in the culture media (in mg/L) from all three 24-hr incubation periods for each sample in each group "*i*" (*i* = ZSr41A, B, C, D, and Mg), $[Mg^{2+}]_{DMEM,tot}$ represents the total $[Mg^{2+}]$ in the culture media from all three 24-hr incubation periods for the DMEM-only reference (i.e. basal media correction), *V* represents the media incubation volume (0.003 L), *SAi* represents the initial surface area (cm^2) of each sample in group "*i*", and *t* is the total incubation time (in days). The degradation rate obtained is based on the initial geometry of the sample and is given in [mg cm^{-2} day^{-1}]. ANOVA confirmed statistically significant differences in the normalized degradation rates during the 72 hr incubation period [F (4, 10) = 5.8336, p = 1.09×10^{-2}]. *Post hoc* pairwise comparisons showed that the degradation rates of ZSr41A (0.308±0.047 mg cm^{-2} day^{-1}) and ZSr41B (0.306±0.038 mg cm-2 day-1) were significantly higher (p < 0.05) when compared with the Mg control (0.174±0.058 mg cm^{-2} day^{-1}).

4.3.4. *In vitro* degradation of ZSr41 alloys in the direct culture with multiple culture media and respective cells

The degradation rate obtained in this study using the direct culture of ZSr41 alloys with BMSCs in DMEM and Eq. 4.1 was compared with previous published literature from our group in which we reported on the degradation rate of ZSr41 alloys with human embryonic stem cells (hESCs) in mTeSR®1 culture media [7] and with human umbilical vein endothelial cells (HUVECs) in EGM™-2 culture media [8]. Additionally the degradation rates of ZSr41 from this study were also compared with the degradation rates of Mg-xZn-0.5Ca alloys (x = 0.5, 1.0, 2.0, and 4.0 wt. %) under identical culture conditions (i.e. 72 hrs, direct culture with BMSCs) [1], to rate alloy performance. The degradation rates from previous published work [1, 7] were re-evaluated from the original data according to Eq. 4.1. It is important to mention that Mg controls for all four degradation (and cytocompatibility) experiments consisted of 99.9% pure, as-rolled sheets with the following thickness: ZSr41-hESC/mTeSR®1, 250 µm thick (Goodfellow Co.); ZSr41-HUVEC/EGM™-2 and ZSr41-BMSC/DMEM, 1 mm thick (Alpha Aesar); and Mg-xZn-0.5Ca-BMSC/DMEM, 500 µm (Goodfellow Co.).

Results for the degradation rate comparison of ZSr41 in hESC/mTeSR®1, HUVEC/EGM™-2, and BMSC/DMEM, along with the comparison with Mg-xZn-0.5Ca in BMSC/DMEM are summarized in the histograms shown in Figure 4.6. For ease of visualization, the results from this study are represented by the red striped

columns in all panels. Figure 4.6a shows the normalized degradation rates of ZSr41 alloys and Mg control (1 mm thick; Alfa Aesar) over a 24 hr incubation in different cell culture media with corresponding cell types. The Mg control group in mTeSR®1 was deliberately excluded for ease of comparison since it was geometrically distinct from the Mg control in DMEM and EGM™-2. ANOVA was used to confirm statistically significant differences in the mean degradation rates of ZSr41 [F (2, 6) = 72.715, p = 6.22×10^{-5}], ZSr41C [F (2, 6) = 14.289, p = 5.23×10^{-3}], and Mg [F (1, 4) = 288.92, p = 7.03×10^{-5}], while the Kruskal-Wallis test was used to confirm differences for ZSr41B [X^2 (2, N = 9) = 7.2, p = 2.732×10^{-2}] and ZSr41D [X^2 (2, N = 9) = 7.2, p = 2.732×10^{-2}] (Figure 4.6a). *Post hoc* pairwise comparisons for ZSr41A showed that the degradation rate in BMSC/DMEM (0.36±0.07 mg cm^{-2} day^{-1}) was significantly lower (p < 0.01) compared with HUVEC/EGM™-2 (0.93±0.03 mg cm^{-2} day^{-1}) and hESC/mTeSR®1 (0.69±0.07 mg cm^{-2} day^{-1}); likewise, the degradation rate of ZSr41A in hESC/mTeSR®1 was significantly lower (p < 0.01) compared with HUVEC/EGM™-2. Additionally, *post hoc* pairwise comparisons for ZSr41B showed that the degradation rate in BMSC/DMEM (0.34±0.06 mg cm^{-2} day^{-1}) was significantly lower (p < 0.05) compared with HUVEC/EGM™-2 (1.63±0.54 mg cm^{-2} day^{-1}) and hESC/mTeSR®1 (0.56±0.03 mg cm^{-2} day^{-1}); likewise, the degradation rate of ZSr41B in hESC/mTeSR®1 was significantly lower (p < 0.05) compared with HUVEC/EGM™-2. Furthermore, *post hoc* pairwise comparisons for ZSr41C showed that the degradation rate in BMSC/DMEM (0.25±0.03 mg cm^{-2} day^{-1}) was significantly lower (p < 0.01)

compared with HUVEC/EGM™-2 (0.70±0.18 mg cm^{-2} day^{-1}) and hESC/mTeSR®1 (0.65±0.07 mg cm^{-2} day^{-1}). Moreover, *post hoc* pairwise comparisons for ZSr41D showed that the degradation rate in BMSC/DMEM (0.27±0.04 mg cm^{-2} day^{-1}) was significantly lower ($p < 0.05$) compared with HUVEC/EGM™-2 (1.67±0.52 mg cm^{-2} day^{-1}) and hESC/mTeSR®1 (0.51±0.06 mg cm^{-2} day^{-1}); likewise, the degradation rate of ZSr41B in hESC/mTeSR®1 was significantly lower ($p < 0.05$) compared with HUVEC/EGM™-2. In addition, *post hoc* pairwise comparisons for Mg control showed that the degradation rate in BMSC/DMEM (0.23±0.01 mg cm^{-2} day^{-1}) was significantly lower ($p < 0.001$) compared with HUVEC/EGM™-2 (0.72±0.05 mg cm^{-2} day^{-1}). Additionally, Figure 4.6b shows a comparison of the normalized daily degradation rates of ZSr41 alloys, Mg-xZn-0.5Ca alloys, and their respective Mg controls over a 72 hr incubation in BMSC/DMEM culture media. These results showed that the degradation rates of the Mg-xZn-0.5Ca alloys were superior compared with the ZSr41 alloys. Specifically, the Mg-xZn-0.5Ca alloys with x = 0.5, 1.0, and 2.0 wt. % stand out as superior candidates based on degradation rate [1].

4.3.5. Cytocompatibility of ZSr41 alloys in the direct culture with multiple cell lines in their respective culture media

Cytocompatibility results from the direct culture of ZSr41 alloys with BMSCs (this study) were compared with previous published literature from our group in which we reported on the cytocompatibility of ZSr41 alloys with hESCs [7] and HUVECs [8], and the cytocompatibility of Mg-xZn-0.5Ca alloys with BMSCs [1].

This multiple-point comparative analysis allowed the identification of cytotoxic differences between different cell types (hESC, HUVEC, and BMSC) using the same ZSr41 alloys, and also identification of cytotoxic differences between different Mg alloys (ZSr41 and Mg-xZn-0.5Ca) while using the same cell type (BMSC). To facilitate comparison, the viability of each cell type was represented as percent cell viability and was calculated as follows: percent viability of hESCs was determined by calculating the area of viable hESC colonies in the experimental groups and normalizing by the positive control at either 72 or 24 hrs [7]; percent viability of HUVECs [8] and BMSCs ([1] and this study) was determined by calculating the adhesion density of DAPI-stained cell nuclei and normalizing by the positive control at each time point (i.e., 72 hrs for BMSCs and 24 hrs for HUVECs). It is important to mention that while all four *in vitro* experiments used the *direct* culture method, the ZSr41-hESC experiment used transwell inserts thus only providing cytocompatibility results under *indirect* contact. Tian *et al.* reported similar results when evaluating the viability of urothelial cells under *indirect* contact when using the direct culture method with either transwell inserts or direct placement of the samples (*unpublished results*), thereby validating the comparison presented in this study.

Results for the cytocompatibility comparison with hESCs, HUVECs, and BMSCs with ZSr41 and Mg-xZn-0.5Ca alloys are summarized in the histograms shown in Figure 4.7. For ease of visualization, the results from this study are represented by the red striped columns in all panels. Figure 4.7a shows the

percent cell viability of BMSCs and hESCs in the direct culture and under *indirect* contact with ZSr41 alloys after 72 hrs of incubation. These results showed that after 72 hrs of incubation with ZSr41 alloys and Mg control, the percent viability of BMSCs was much higher when compared with hESCs. Furthermore, Figure 4.7b shows the percent cell viability of hESCs and HUVECs in the direct culture and under *indirect* contact with ZSr41 alloys after 24 hrs of incubation. These results showed that the percent viability of HUVECs in response to the degradation products of ZSr41 alloys and Mg control was higher when compared with the viability of hESCs. Furthermore, the percent viability of BMSCs using the direct culture method under both *direct* and *indirect* contact with ZSr41 alloys and Mg-xZn-0.5Ca alloys after 72 hrs of incubation was also plotted for comparison and results are shown in Figures 4.7c and 4.7d, respectively. Comparison of the *direct* contact evaluation (Figure 4.7c) showed that, in general, the BMSC-substrate interface of the Mg-xZn-0.5Ca alloys was more favorable for the adhesion and continued viability of BMSCs when compared with ZSr41 alloys. In contrast, comparison of the *indirect* contact evaluation (Figure 4.7d) showed that BMSCs growing on the culture plate remained largely unaffected by the degradation rate (and concomitant solubilized degradation products) of Mg-based biomaterials after 72 hrs of incubation.

4.4. Discussion

The degradation of four heat-treated ZSr41 crystalline Mg alloys and their cytocompatibility with BMSCs was investigated using the direct *in vitro* culture method to model and study possible cellular modulatory effects at the BMSC/ZSr41 alloy interface. We also examined the BMSCs on the culture plates surrounding the Mg-based samples in the same direct culture to understand BMSC behaviors in direct culture but *indirect* contact with the Mg-based samples. Furthermore, the results from this study were compared with published literature to systematically compare the degradation and cytocompatibility of the ZSr41 alloys with other cell lines in their respective culture media.

4.4.1. *In vitro* degradation of ZSr41 alloys in direct culture

Alloys ZSr41A and ZSr41B showed a significantly faster *in vitro* degradation rate compared with the Mg control in this study after 72 hrs of incubation in DMEM media with BMSCs. The degradation rate data (Figure 4.5) was qualitatively supported by the relatively heterogeneous surface integrity of ZSr41A and ZSr41B compared with the more homogeneous surfaces of ZSr41C and ZSr41D indicated by the post-incubation SEM images (Figure 4.1) and Mg Kα1 maps (Figure 4.2a). Interestingly, the Mg control showed the slowest degradation rate but also the most heterogeneous surface integrity of all the Mg-based materials investigated in this study. Results from pH measurements taken during the 24-hr intervals (Figure 4.4a) showed that although the degradation of all Mg-based materials induced an

alkaline shift in the culture media, the CO_2/HCO_3^- buffer system in DMEM was effective in maintain media pH well below pH 9.5 which is cytotoxic for BMSC [1]. Additionally, results from [Mg^{2+}] in the culture media during the 24-hr intervals (Figure 4.4b) showed a nearly constant Mg^{2+} ion release by the degradation of all ZSr41 alloys during the 72 hr incubation. In contrast, the mean Mg^{2+} ion release by the degradation of the Mg control showed a continuously decreasing trend in degradation rate during the 72 hr incubation with the lowest mean value measured during the last 24-hr interval. In a previous investigation, we demonstrated that the differences in *in vitro* degradation rates of ZSr41 alloys could be potentially correlated with specific Zn/Sr at. % ratio in the β-phase of these alloys and the corresponding micro-galvanic corrosion formed with the α-matrix [8]. Moreover, the solubilized [Mg^{2+}], [Zn^{2+}], and [Sr^{2+}] in the culture media during the repeated 24-hr intervals resulting from the degradation of the ZSr41 alloys were all below therapeutic daily doses and LD50 concentrations reported for all three ions with multiple mammalian cell types [7, 8].

The results from this study and comparison with previous literature showed that the *in vitro* degradation rates of ZSr41 alloys in distinct culture media increased as follows: BMSC/DMEM < hESC/mTeSR®1 < HUVEC/EGM™-2. In all cases, the degradation rates of all ZSr41 alloys and Mg control in DMEM were significantly lower when compared with their corresponding counterparts in mTeSR®1 and EGM™-2. Furthermore, although less conclusive (i.e. not significantly different in all cases), the degradation rate of ZSr41 in mTeSR®1 appeared to be slower when

compared with EGM™-2. Interestingly, in terms of degradation rate, alloys ZSr41C and ZSr41D performed better in BMSC/DMEM compared with alloys ZSr41A and ZSr41B during the 72 hr incubation reported in this study. In contrast, ZSr41A and ZSr41C showed a slower degradation rate compared with ZSr41B and ZSr41D when incubated for 72 hrs in hESC/mTeSR®1. The degradation of ZSr41 alloys was also studied in whole blood, blood plasma after fractionation, and fibroblast culture media; however, the experimental setup was different from parameters used in this study and was not included in the comparison [13]. Despite the distinct degradation rates observed in the various culture media tested, ZSr41C stands out as a candidate with consistently lower degradation rates compared with ZSr41A, B, and D.

The comparative evaluation presented in this study showed that the *in vitro* degradation rates of ZSr41 in BMSC/DMEM, hESC/mTeSR®1, and HUVEC/EGM™-2 were likely independent of the following media aspects: chloride ion concentration ($[Cl^-]$), osmolality, and/or ionic strength. Table 4.1 summarizes the ionic concentrations from the inorganic salts, ionic strength, D-glucose, and osmolality of DMEM [14], MCDB 131 (non-commercial analog of EGM™-2) [15], mTeSR®1 [16], r-SBF [14], and human blood plasma [16]. D-glucose and osmolality values for DMEM, EGM™-2, and mTeSR®1 were obtained from technical specification sheets from the vendors, while values for human blood plasma were obtained from [17] and [18], respectively. The presence of chloride ions (Cl^-) in physiological fluids has been extensively argued to play a dramatic

role in the degradation of Mg-based materials [19-21], especially when the [Cl^-] > 30 mM [20]. However, the degradation rates of ZSr41 alloys in distinct culture media with corresponding [Cl^-] (i.e. DMEM = 118.48 mM, MCDB 131/EGM™-2 = 117.2 mM, and mTeSR®1 = 100.96 mM; Table 4.1) appear to be largely influenced by other factors. For example, a significantly faster degradation rate of ZSr41 was observed for culture media with lower [Cl^-] (i.e. mTeSR®1 had lower [Cl^-] but induced a faster degradation rate compared with DMEM). Similarly, the significantly faster degradation rate of ZSr41 alloys in EGM™-2 occurred despite a mid-range [Cl^-] relative to the concentration in DMEM and mTeSR®1. Additionally, our results showed that the significantly faster degradation rate observed for the ZSr41 alloys in EGM™-2 appeared to be independent of media osmolality and ionic strength since: (i) DMEM had the highest nominal media osmolality, yet induced the slowest degradation rate, and (ii) the degradation rate in DMEM was slowest despite DMEM having a mid-range ionic strength relative to MCDB 131/EGM™-2 and mTeSR®1. Specific values for osmolality and ionic strength are listed in Table 4.1.

Our comparative evaluation showed that buffer capacity (i.e. HCO_3^- concentration) of DMEM, mTeSR®1, and MCDB 131/EGM™-2, and to a lesser extent, D-glucose concentration, were likely responsible for the range of degradation rates of ZSr41 and Mg control. Previous *in vitro* studies extensively showed that the degradation of Mg-based materials is influenced by environmental factors including CO_2, buffers, proteins, and other components [5, 22, 23].

However, many of these studies focused on evaluating the effects of these components in incubation media without cells. For example, Walker *et al.* demonstrated that the buffer type ($NaHCO_3$ or HEPES) mediated the degradation rate of several Mg-based materials after a 7 day incubation, with a faster rate observed for incubation in HEPES [22]. They concluded that for degradation testing purposes, incubation in Earle's balanced salt solution (EBSS) buffered with $NaHCO_3$ provided a close approximation to subcutaneous degradation in a rat model [22]. Similarly, Willumeit *et al.* utilized artificial neural networks (ANNs) to analyze the correlation between measured degradation rates (incubation media only without cells) and the following parameters: FBS (0%, 10% and 20% v/v); temperature (20 °C and 37 °C); CO_2 (0%, 2.5% and 5%); O_2 (5% and 21%); and media composition, which experimentally included glucose (0–4.5 g L^{-1}) and NaCl concentration, and computationally included $NaHCO_3$, $CaCl_2$, and $MgSO_4$ [23]. Following two distinct simulations, they demonstrated that CO_2 and NaCl played the strongest influence on degradation rate, followed by both temperature and $NaHCO_3$, and finally by glucose. Interestingly, proteins (i.e. FBS) played the least important role in one scenario but ranked mid-importance in the second simulation, which agrees with the experimental discrepancy on the role of proteins [23]. Collectively, despite the absence of cells in their studies, the results provided by Walker *et al.* and Willumeit *et al.* identified important parameters to consider when using *in vitro* cell-based methods such as the direct culture method utilized in this study. The cell-based direct culture method introduces the advantages of

predicting degradation rates, testing cytocompatibility with solubilized degradation products, and probing cellular responses at the cell-substrate interface, all in a single platform [1]. A dissection of the factors identified by Willumeit *et al.* showed that only concentrations of NaCl, $NaHCO_3$, and glucose are most relevant to cell-based *in vitro* incubations since conventional cell culture methods fix O_2/CO_2 content and temperature (i.e. 95/5% and 37 °C, respectively). Specifically, in the comparison presented in this study between BMSC/DMEM, hESC/mTeSR®1, and HUVEC/EGM™-2, we demonstrated that [Cl^-] was not likely responsible for the different degradation rates of ZSr41 alloys and the Mg control. However, HCO_3^- and D-glucose concentrations in the culture media decreased as follows: DMEM < mTeSR®1 < MCDB 131/EGM™-2. This trend was directly related to the degradation rates of the ZSr41 alloys and Mg controls obtained from the comparative study and highlights the importance, based on the studies by Walker *et al.* and Willumeit *et al.*, of HCO_3^- concentration in modulating *in vitro* degradation of Mg-based materials when using cell-based methods. In fact, Kirkland et al. suggested that the corrosion of Mg-based materials was mediated by a precipitated calcium phosphate layer which was modulated through HCO_3^- concentration [24]. Further experiments are needed to verify the individual contributions of HCO_3^- concentration and D-glucose, in that order, while maintaining all other concentrations constant. Likewise, further experiments using the direct culture method are necessary to elucidate possible roles of cell attachment at the cell-substrate interface on *in vitro* degradation rate.

In terms of Mg-alloy performance, our comparative assessment showed that the degradation rates of the Mg-xZn-0.5Ca alloys were superior compared with the ZSr41 alloys when using the direct culture with BMSC during a 72-hr incubation. Comparison of the mean degradation rates with their respective controls, showed that ZSr41A, ZSr41B, and Mg-4Zn-0.5Ca degraded significantly faster. Furthermore, the degradation rates of Mg-xZn-0.5Ca (x = 0.5, 1.0, and 2.0 wt. %) were approximately half of ZSr41C and ZSr41D; however, statistical differences were not confirmed for these alloys compared with their respective Mg controls. Detailed explanations on the degradation mechanism and participation of second phases in the ZSr41 alloys and Mg-xZn-0.5Ca alloys are given in [8] and [1], respectively. From this comparative screening, the Mg-2Zn-0.5Ca alloy stands out as a promising candidate for further testing in regards to orthopedic implant applications.

4.4.2. Cytocompatibility of ZSr41 alloys in direct culture

The direct culture method used in this study to show that BMSCs adhered and remained viable under *direct* contact at the cell-ZSr41 alloy interface; likewise, BMSCs under *indirect* contact with the samples (i.e. adherent to the culture plate surrounding the sample) were largely unaffected by the solubilized degradation products from the ZSr41 alloys during a 72 hr incubation. Although adherent and viable BMSCs were observed at the cell-ZSr41 interface (Figure 4.1; Figure 4.2a, C Kα1 maps) for all four ZSr41 alloys, the significantly lower adhesion on ZSr41A

and ZSr41B compared with the glass reference (Figure 4.3b, sample) could have been induced by the significantly faster degradation rate of these two alloys (Figure 4.5). Most importantly, the significantly lower adhesion at the cell-substrate interface was most likely caused by the sharper increase in local pH and heterogeneous surface topography (Figure 4.2a, Mg Kα1 maps) induced by rapid degradation, rather than by the local increase in [Mg^{2+}] [1]. The effects of pH and supplemented [Mg^{2+}] on BMSC viability and morphology showed that transient media alkalinity played a more important role than [Mg^{2+}] concentration in the media. Thus, it was expected that the degradation of ZSr41 alloys in DMEM (which was significantly lower compared to EGM™-2 and mTeSR®1, as discussed in the previous section) and concomitant change in pH and Mg^{2+} ion release, would have negligible effects on the viability of BMSCs *indirectly* in contact with the ZSr41 alloy samples (Figure 4.3b, plate).

Results from comparing the cytocompatibility of hESCs, HUVECs, and BMSCs showed that the sensitivity to Mg-based degradation products for each cell type (in their respective culture media) increased as follows: BMSC < HUVEC < hESC. Previously, we introduced an *in vitro* cytocompatibility study based on H9 hESCs to assess subtle cellular effects (e.g. adhesion, proliferation, and differentiation) induced by the degradation of Mg-based biomaterials [7]. The H9 hESC model was used to potentially screen subtle cytotoxic effects due to the greater sensitivity of hESCs to known toxicants [25, 26]. The higher percent viability of BMSCs compared with hESCs (Figure 4.7a) gave evidence that indeed the viability

threshold to environmental changes was much higher for BMSCs. Thus, the results from this study pointed towards the higher sensitivity of hESCs to the degradation products of Mg-based biomaterials. Further evidence for the increased sensitivity of hESCs, compared with primary cell lines, for the purpose of screening subtle environmental changes is obtained when comparing the viability of hESCs and HUVECs in the direct culture and under *indirect* contact with ZSr41 alloys after 24 hrs of incubation (Figure 4.7b). These results showed that the percent viability of HUVECs in response to the degradation products of ZSr41 alloys and Mg control was higher when compared with the viability of hESCs. In fact, stand-alone experiments on the individual effects of adjusted media alkalinity and Mg^{2+} ion supplementation on the viability of hESCs, HUVECs, and BMSCs showed that indeed hESC viability was reduced at supplemented [Mg^{2+}] > 10 mM, but HUVECs and BMSCs were not [1, 7, 8]. Additionally, adjusting the culture media to pH 9.5 followed by a 24-hr incubation significantly reduced the viability of HUVECs and BMSCs; however, the same study needs to be carried out to study the sensitivity of hESCs to highly alkaline culture media. It should also be highlighted that the faster degradation rate of ZSr41 alloys and Mg in mTeSR®1 and EGM™-2 compared with DMEM (and cultured with hESCs, HUVECs, and BMSCs, respectively), and concomitant increase in concentration of solubilized degradation products, could also play a role in the percent cell viability when comparing different cell-based culture methods. However, each of these cell types necessitates specific culture media formulations (i.e. mTeSR®1, EGM™-2, DMEM,

etc.) and the respective degradation rate becomes an intrinsic aspect of utilizing each cell culture method. In the case of biodegradable Mg-based biomaterials, whose degradation rate depends on cell culture media composition, the selection of a relevant *in vitro* model to investigate degradation and cytocompatibility becomes a critical aspect that should be carefully assessed to narrow the mismatch gap between *in vitro* and *in vivo* results. Collectively, our results not only confirmed the higher sensitivity of hESCs to the degradation products of Mg-based materials, but also pointed towards the need of carefully-selected cytocompatibility studies with durations longer than 24 hrs to obtain a comprehensive representation of *in vitro* cellular responses.

Though not statistically significant, our comparative study showed an inverse relationship between mean percent BMSC viability at the cell-substrate interface and alloy degradation rate (i.e. normalized mass loss rate). Specifically, the percent BMSC viability under *direct* contact (Figure 4.7c) followed an inverse trend compared with the degradation rates of ZSr41 and Mg-xZn-0.5Ca alloys (Figure 4.6b), suggesting a close relationship between BMSC viability at the cell-substrate interface and Mg-based biomaterial degradation rate (Figure 4.8). In general, the trend showed that the degradation rate of Mg-xZn-0.5Ca alloys (x = 0.5, 1.0, and 2.0 wt. %) allowed for BMSC adhesion, growth, and proliferation at the cell-substrate interface up to 72 hrs of incubation. In contrast, the faster degrading Mg-4Zn-0.5Ca alloy and all ZSr41 alloys showed a truncated percent BMSC viability which could have been attributed in part to the significantly faster degradation rate

of this alloy [1]. In the case of the ZSr41 alloys, the statistically lower viability of BMSCs at the cell-substrate interface with alloys ZSr41A and ZSr41B could correlate with the statistically significant faster degradation rate of these two alloys compared with the Mg control in this study. Since the degradation process induces a highly dynamic environment at the cell-substrate interface, further studies using the direct culture method are needed to elucidate which component(s) of the degradation process have the most impact on BMSC adhesion and viability.

4.5. Conclusions

This article reports behaviors of BMSCs interfacing with four biodegradable Mg-4Zn-xSr alloys (x = 0.15, 0.5, 1.0, or 1.5 wt. %; designated as ZSr41A, B, C, and D, respectively). Additionally, a comparative assessment of the cell-based direct culture method between: ZSr41/BMSC/DMEM, ZSr41/HUVEC/EGM™-2, ZSr41/hESC/mTeSR®1, and Mg-xZn-0.5Ca/BMSC/DMEM, was used to identify parameters of interest when utilizing the direct culture method for screening Mg-based materials. The following major conclusions were drawn from the present study:

1. In this study, alloys ZSr41A and ZSr41B showed a significantly faster *in vitro* degradation rate compared with the Mg control after 72 hrs of incubation in DMEM media with BMSCs. The direct culture method was used to show that BMSCs adhered and remained viable under *direct* contact at the cell-ZSr41 alloy interface; likewise, BMSCs under *indirect* contact with the samples (i.e.

adherent to the culture plate surrounding the sample) were largely unaffected by the solubilized degradation products from the ZSr41 alloys.

2. In terms of Mg-alloy performance, our comparative assessment showed that the degradation rates of the Mg-xZn-0.5Ca alloys were superior compared with the ZSr41 alloys when using the direct culture with BMSC/DMEM during a 72-hr incubation.

3. A comparison with published literature showed that the *in vitro* degradation rates of ZSr41 alloys in distinct culture media increased as follows: BMSC/DMEM < hESC/mTeSR®1 < HUVEC/EGM™-2. The differences in *in vitro* degradation rates were likely independent of media: chloride ion concentration ($[Cl^-]$), osmolality, and/or ionic strength. In contrast, the differences could have been caused by buffer capacity (i.e. HCO_3^- concentration), and to a lesser extent, D-glucose concentration.

4. A comprehensive comparison of the cytocompatibility of ZSr41 with hESCs, HUVECs, and BMSCs showed that the sensitivity to Mg-based degradation products for each cell type (in their respective culture media) increased as follows: BMSC < HUVEC < hESC. Additionally, though not statistically significant, our comparative study showed an inverse relationship between mean percent BMSC viability at the cell-substrate interface and alloy degradation rate (i.e. normalized mass loss rate). Specifically, the degradation rate of Mg-xZn-0.5Ca alloys (x = 0.5, 1.0, and 2.0 wt. %) allowed for higher

BMSC adhesion, growth, and proliferation at the cell-substrate interface up to 72 hrs of incubation when compared with the ZSr41 alloys.

4.6. Figures and tables

Figure 4.1: BMSCs in direct contact with ZSr41 alloy surface after 72 hrs of direct culture in DMEM culture media.
SEM micrographs of ZSr41 alloys, pure Mg (control), and glass reference. Original magnification: 150x; scale bar = 250 µm for all images. Insets were taken at 1,000x original magnification with scale bar = 50 µm for all images. Black arrows indicate secondary phases and white arrows indicate adhered and spread BMSCs.

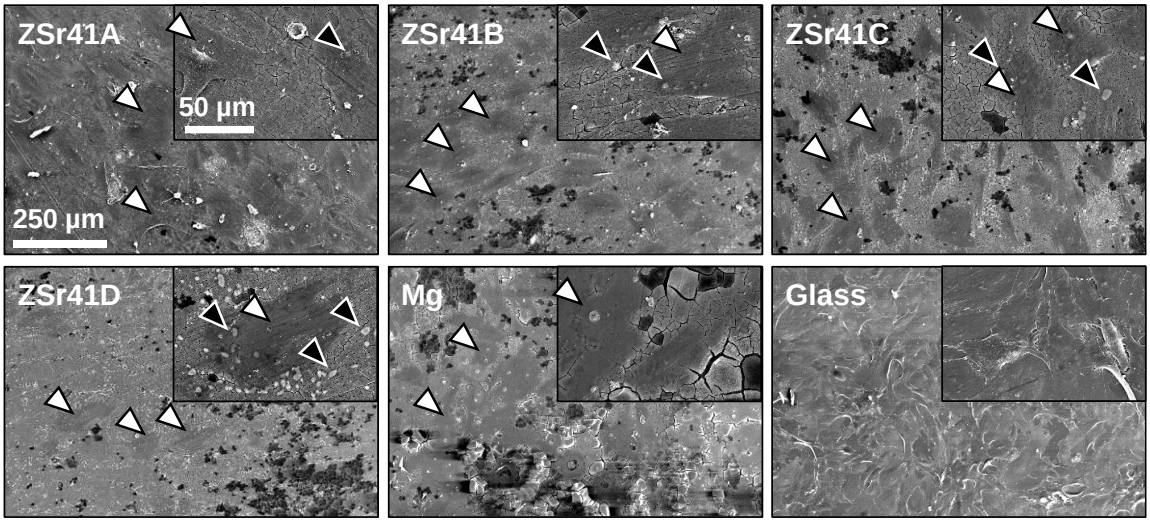

Figure 4.2: Surface characterization of Mg-based materials after 72 hrs of direct culture in DMEM culture media.
(a) EDS elemental distribution maps of Mg and C Kα1 lines of ZSr41 alloys (A-D) and pure Mg (control) after 72 hr direct culture with BMSCs in DMEM media. Original magnification: 150x; scale bar = 250 μm for all images. (b) Surface elemental composition (wt. %) based on EDS quantification on 150x images.

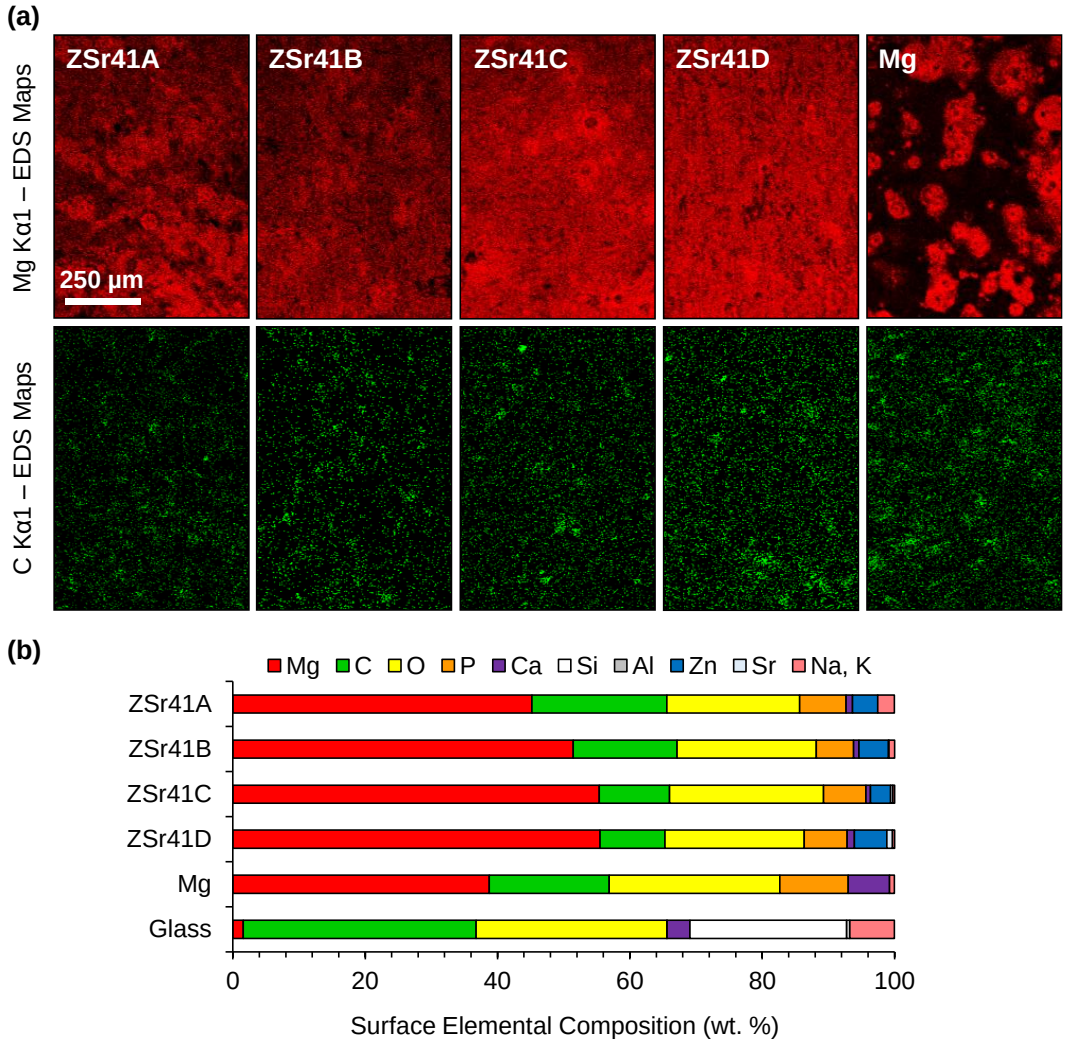

Figure 4.3: BMSC adhesion at 72 hr direct culture on ZSr41 alloys (A-D), pure Mg control, glass reference, and cells-only positive control.
(a) Representative fluorescence images of adhered BMSCs at 72 hr on the tissue culture plates, (b) adhesion density on the sample surface (*direct* contact with the sample) and on the culture plate surrounding each corresponding sample (*indirect* contact with the sample). Values are mean ± standard error of the means, n = 3; **p* < 0.05.

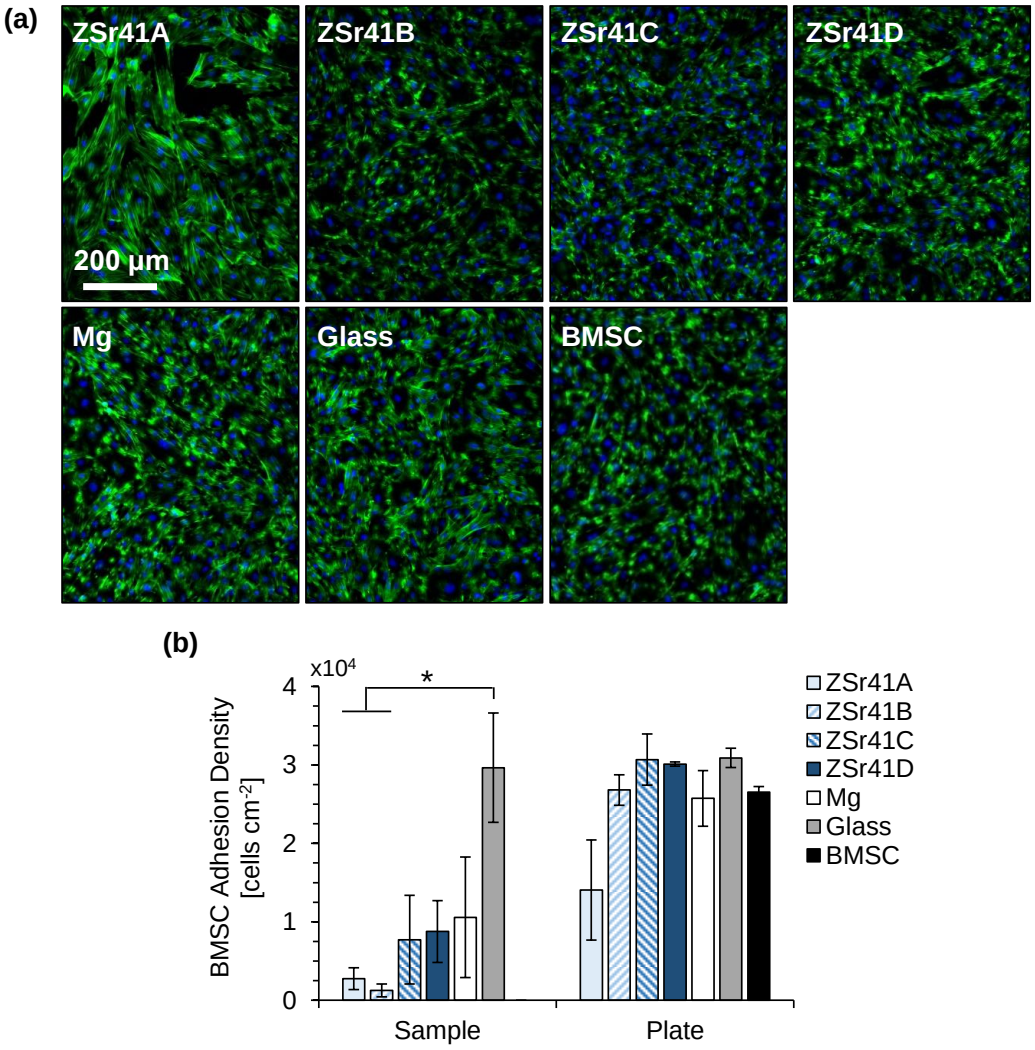

Figure 4.4: Analysis of solubilized degradation products in culture media at 24, 48 and 72 hr direct culture with ZSr41 alloys (A-D), pure Mg control, glass reference, cells-only positive control, and blank DMEM media.
(a) pH of media, (b) Mg^{2+} ion concentration, (c) Zn^{2+} ion concentration, and (d) Sr^{2+} ion concentration. Values are mean ± SD, n = 3 at all time points. *p < 0.05, **p < 0.01, ***p < 0.001.

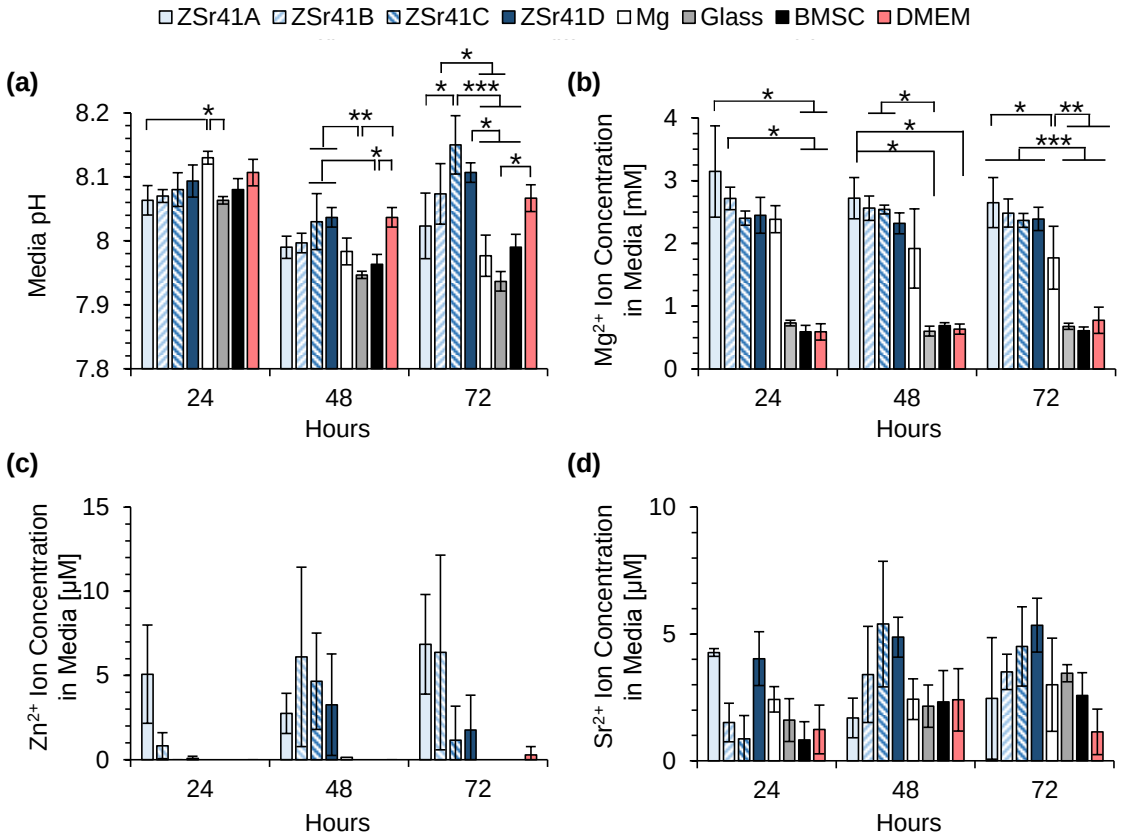

Figure 4.5: Average daily degradation rate (mass loss rate) per unit surface area of ZSr41 alloys and pure Mg in DMEM culture media during 72 hrs of incubation with BMSCs.
Values are mean ± SD, n = 3; *p < 0.05.

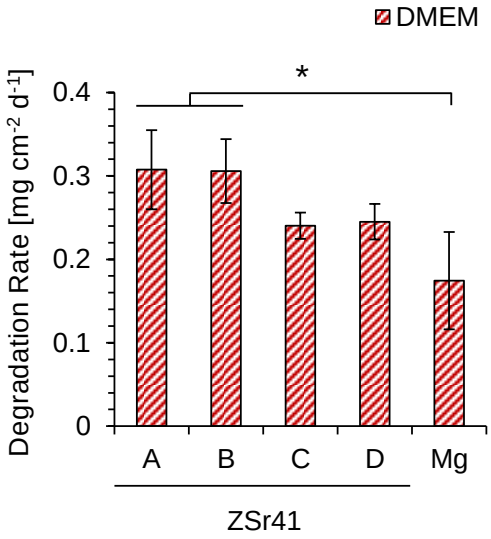

Figure 4.6: Comparison of daily degradation rates of ZSr41 alloys in distinct cell culture media, or with Mg-xZn-0.5Ca alloys.
(a) ZSr41 alloys in DMEM [this study], EGM™-2 [8], and mTeSR®1 [7] culture media during 24 hrs of incubation with respective cells; and (b) ZSr41 alloys and Mg-xZn-0.5Ca (x = 0.5, 1.0, 2.0, and 4.0 wt. %) alloys [1] in DMEM during 72 hrs of incubation with BMSCs. All Mg controls were 99.9% pure, as-rolled with the following thickness: ZSr41-hESC/mTeSR®1, 250 µm thick (Goodfellow Co.), ZSr41-HUVEC/EGM™-2 and ZSr41-BMSC/DMEM, 1 mm thick (Alpha Aesar), and Mg-xZn-0.5Ca-BMSC/DMEM, 500 µm (Goodfellow Co.). Values are mean ± SD, n = 3; *$p < 0.05$, **$p < 0.01$, ***$p < 0.001$.

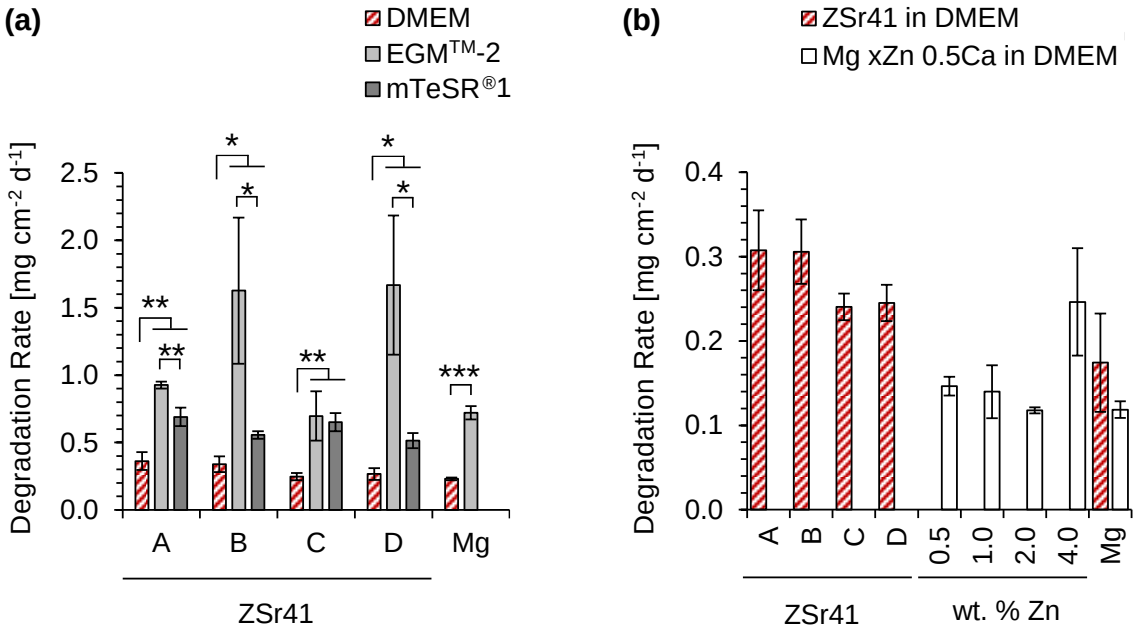

Figure 4.7: Comparison of cell viability percentage with ZSr41 alloys relative to a cells-only positive control in the direct culture method.
(a) BMSC compared with hESC viability, in their respective culture media, at 72 hrs under *indirect* contact; (b) hESC compared with HUVEC viability, in their respective culture media, at 24 hrs under *indirect* contact; (c) BMSC viability with ZSr41 alloys compared with Mg-xZn-0.5Ca (x = 0.5, 1.0, 2.0, and 4.0 wt. %) alloys at 72 hrs under *direct* contact; and, (d) BMSC viability with ZSr41 alloys compared with Mg-xZn-0.5Ca (x = 0.5, 1.0, 2.0, and 4.0 wt. %) alloys at 72 hrs under *indirect* contact. Percent viability of hESCs was determined by calculating the area of viable hESC colonies in the experimental groups and normalizing by the positive control at each time point (i.e., 24 and 72 hrs) [7]. Percent viability of HUVECs [8] and BMSCs [1] was determined by calculating the adhesion density of DAPI-stained cell nuclei and normalizing by the positive control at each time point (i.e., 24 hrs for HUVECs and 72 hrs for BMSCs). All Mg controls were 99.9% pure, as-rolled with the following thickness: ZSr41-hESC/ mTeSR®1, 250 µm thick (Goodfellow Co.), ZSr41-HUVEC/EGM™-2 and ZSr41-BMSC/DMEM, 1 mm thick (Alpha Aesar), and Mg-xZn-0.5Ca-BMSC/DMEM, 500 µm (Goodfellow Co.).

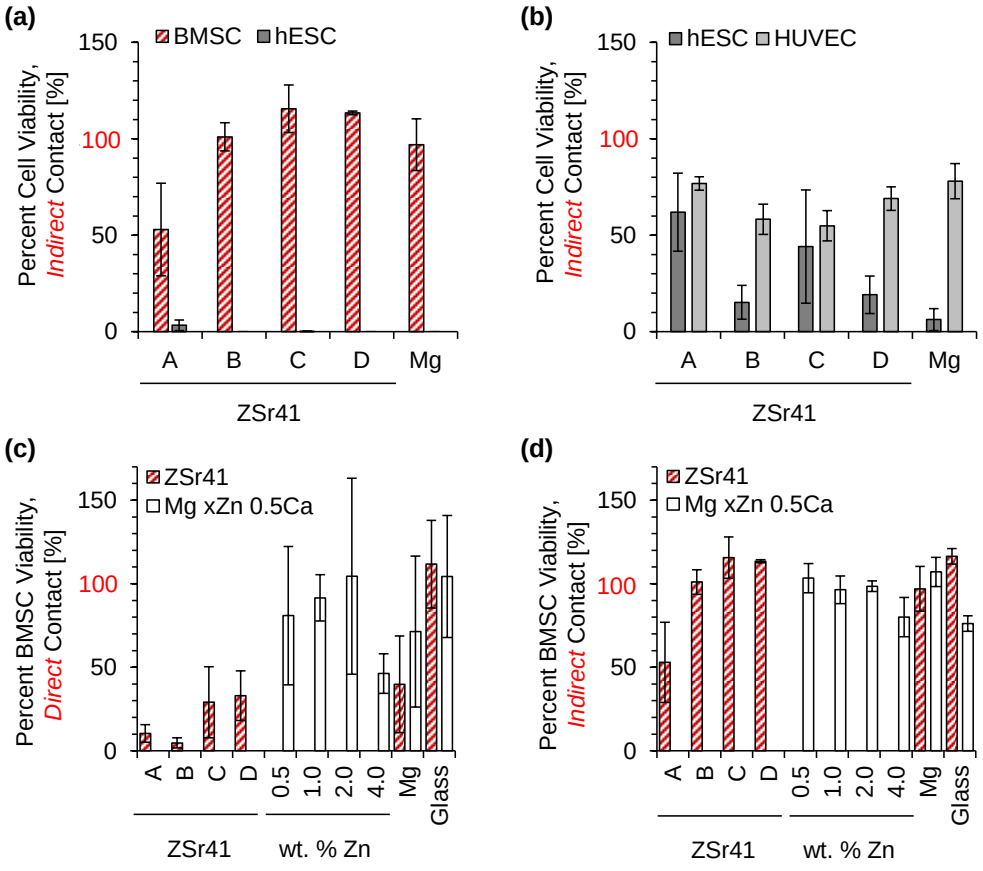

Figure 4.8: Inverse relationship of daily degradation rates of ZSr41 alloys and Mg-xZn-0.5Ca (x = 0.5, 1.0, 2.0, and 4.0 wt. %) alloys compared with percent BMSC viability under *direct* contact at the cell-substrate interface after 72 hrs of incubation in DMEM.

Data for Mg-xZn-0.5Ca alloys obtained from [1]. Percent BMSC viability is relative to a cells-only positive control. Degradation rates are mean ± SD and percent BMSC viabilities are mean ± standard error of the means; n = 3.

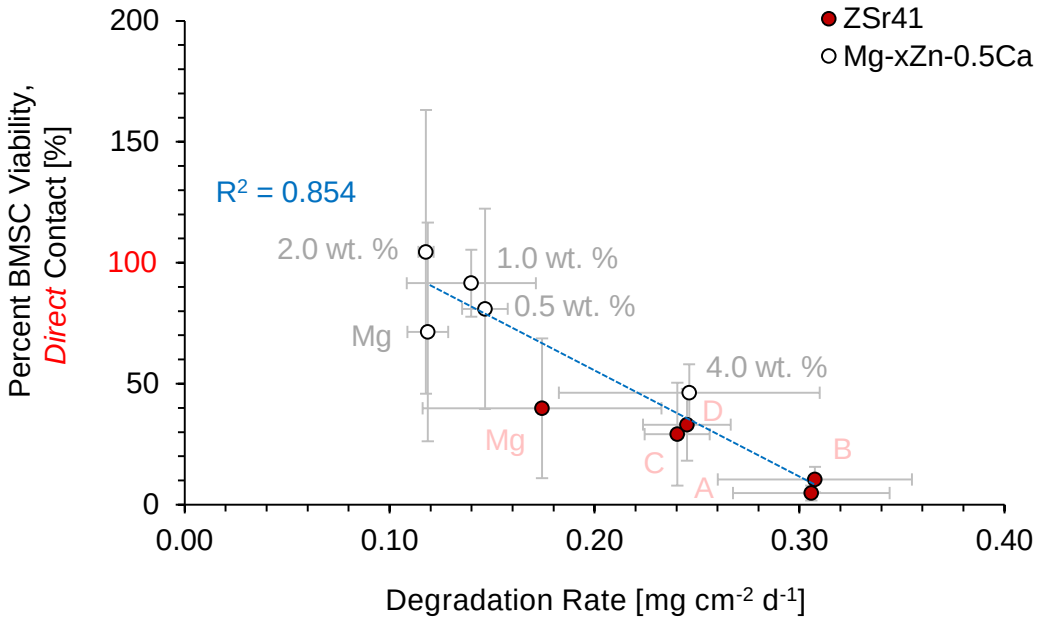

Table 4.1: Ionic concentrations (mM) from inorganic salts in DMEM, MCDB 131 (non-commercial analog of EGM™-2), mTeSR®1, and r-SBF in comparison with human blood plasma.

Compiled from Refs. [14-18].

[a] Osmolality values reported with the presence of organic species and buffers.

[b] Osmolality for DMEM media from technical specification sheet. Corning Cat# 50-013.

[c] Osmolality for EGM™-2 media from technical specification sheet. Lonza Cat# CC-3162.

[d] Osmolality for mTeSR®1 media from technical specification sheet. Stem Cell Tech, Cat# 85850.

	DMEM	MCDB 131	mTeSR®1	r-SBF	Plasma
Na^+	156.46	124.5	113.74	142	142
K^+	5.37	4	3.26	5	5
Mg^{2+}	0.81	10	0.56	1.5	1.5
Li^{2+}	-	-	0.98	-	-
Ca^{2+}	1.80	1.6	0.82	2.5	2.5
Fe^{3+}	0.0002	0.001	-	-	-
Cl^-	118.48	117.2	100.96	103	103
HCO_3^-	44.04	14	18	27	27
$H_2PO_4^-$	0.0007	0.5	0.36	-	-
HPO_4^{2-}	0.91	-	0.39	1	1
SO_4^{2-}	-	10	0.32	0.5	0.5
Ionic Strength	0.168	0.173	0.123	0.150	0.150
D-glucose	24.98	5.55	13.75	-	5
Osmolality (mOsm/kg H_2O)[a]	335±30[b]	275±15[c]	240±10[d]		290

4.7. References

[1] Cipriano AF, Sallee A, Guan R-G, Zhao Z-Y, Tayoba M, Sanchez J, et al. Investigation of magnesium–zinc–calcium alloys and bone marrow derived mesenchymal stem cell response in direct culture. Acta Biomater. 2015;12:298-321.

[2] Rickard DJ, Sullivan TA, Shenker BJ, Leboy PS, Kazhdan I. Induction of Rapid Osteoblast Differentiation in Rat Bone Marrow Stromal Cell Cultures by Dexamethasone and BMP-2. Dev Bio. 1994;161:218-28.

[3] Fischer J, Pröfrock D, Hort N, Willumeit R, Feyerabend F. Reprint of: Improved cytotoxicity testing of magnesium materials. Mater Sci Eng, B. 2011;176:1773-7.

[4] Xin Y, Hu T, Chu PK. In vitro studies of biomedical magnesium alloys in a simulated physiological environment: A review. Acta Biomater. 2011;7:1452-9.

[5] Liu H. The effects of surface and biomolecules on magnesium degradation and mesenchymal stem cell adhesion. J Biomed Mater Res A. 2011;99:249-60.

[6] Johnson I, Perchy D, Liu H. In vitro evaluation of the surface effects on magnesium-yttrium alloy degradation and mesenchymal stem cell adhesion. J Biomed Mater Res A. 2011;100A:477–85.

[7] Cipriano AF, Zhao T, Johnson I, Guan R-G, Garcia S, Liu H. In vitro degradation of four magnesium–zinc–strontium alloys and their cytocompatibility with human embryonic stem cells. J Mater Sci Mater Med. 2013;24:989-1003.

[8] Cipriano AF, Sallee A, Guan R-G, Zhan-Yong Z, Tayoba M, Cortez MC, et al. Cytocompatibility and Early Inflammatory Response of Human Endothelial Cells in Direct Culture with Mg-Zn-Sr Alloys. Submitted to Biomaterials. 2015.

[9] Guan RG, Cipriano AF, Zhao ZY, Lock J, Tie D, Zhao T, et al. Development and Evaluation of a Magnesium-Zinc-Strontium Alloy for Biomedical Applications – Alloy Processing, Microstructure, Mechanical Properties, and Biodegradation. Mater Sci Eng, C. 2013;33:3661-9.

[10] Cipriano AF, De Howitt N, Gott SC, Miller CT, Rao MP, Liu H. Bone Marrow Stromal Cell Adhesion and Morphology on Micro- and Sub-Micropatterned Titanium. J Biomed Nanotechnol. 2014;10:660-8.

[11] Dubin-Thaler BJ, Giannone G, Döbereiner H-G, Sheetz MP. Nanometer Analysis of Cell Spreading on Matrix-Coated Surfaces Reveals Two Distinct Cell States and STEPs. Biophys J. 2004;86:1794-806.

[12] Kirkland NT, Birbilis N, Staiger MP. Assessing the corrosion of biodegradable magnesium implants: A critical review of current methodologies and their limitations. Acta Biomater. 2012;8:925-36.

[13] Nguyen TY, Cipriano AF, Guan RG, Zhao ZY, Liu H. In vitro interactions of blood, platelet, and fibroblast with biodegradable Magnesium-Zinc-Strontium alloys. J Biomed Mater Res, A. 2015;103:2974–86.

[14] Iskandar ME, Aslani A, Liu H. The effects of nanostructured hydroxyapatite coating on the biodegradation and cytocompatibility of magnesium implants. J Biomed Mater Res, A. 2013;101A:2340-54.

[15] Knedler A, Ham R. Optimized medium for clonal growth of human microvascular endothelial cells with minimal serum. In Vitro Cell Dev Biol. 1987;23:481-91.

[16] Nguyen TY, Liew CG, Liu H. An In Vitro Mechanism Study on the Proliferation and Pluripotency of Human Embryonic Stems Cells in Response to Magnesium Degradation. PLoS ONE. 2013;8:e76547.

[17] Rusin O, Alpturk O, He M, Escobedo J, Jiang S, Dawan F, et al. Macrocycle-Derived Functional Xanthenes and Progress Towards Concurrent Detection of Glucose and Fructose. J Fluoresc. 2004;14:611-5.

[18] Sands JM, Layton HE. The Physiology of Urinary Concentration: an Update. Sem Nephrol. 2009;29:178-95.

[19] Staiger MP, Pietak AM, Huadmai J, Dias G. Magnesium and its alloys as orthopedic biomaterials: A review. Biomaterials. 2006;27:1728-34.

[20] Witte F, Hort N, Vogt C, Cohen S, Kainer KU, Willumeit R, et al. Degradable biomaterials based on magnesium corrosion. Curr Opin Solid State Mater Sci. 2008;12:63-72.

[21] Zheng YF, Gu XN, Witte F. Biodegradable metals. Mater Sci Eng, R. 2014;77:1-34.

[22] Walker J, Shadanbaz S, Kirkland NT, Stace E, Woodfield T, Staiger MP, et al. Magnesium alloys: Predicting in vivo corrosion with in vitro immersion testing. J Biomed Mater Res, B. 2012;100B:1134-41.

[23] Willumeit R, Feyerabend F, Huber N. Magnesium degradation as determined by artificial neural networks. Acta Biomater. 2013;9:8722-9.

[24] Kirkland N, Waterman J, Birbilis N, Dias G, Woodfield TF, Hartshorn R, et al. Buffer-regulated biocorrosion of pure magnesium. J Mater Sci Mater Med. 2012;23:283-91.

[25] Laschinski G, Vogel R, Spielmann H. Cytotoxicity test using blastocyst-derived euploid embryonal stem cells: A new approach to in vitro teratogenesis screening. Reprod Toxicol. 1991;5:57-64.

[26] Talbot P, Lin S. Mouse and Human Embryonic Stem Cells: Can They Improve Human Health by Preventing Disease? Curr Top Med Chem. 2011;11:1638-52.

Chapter 5 - Cytocompatibility and early inflammatory response of human endothelial cells in direct culture with Mg-Zn-Sr alloys

5.1. Background

As Mg alloys continue to be investigated for biomedical applications, it is necessary to understand whether Mg-based materials or the alloying elements have the intrinsic ability to direct an immune response to improve implant integration while avoiding cell-biomaterial interactions leading to chronic inflammation and/or foreign body reactions [1, 2]. In contrast, previous studies have shown that conventional permanent metallic implants, and associated wear debris, can trigger chronic inflammatory responses, result in tissue loss, and are prone to infection [3-5].

In general, the initial (acute) inflammatory response (i.e. innate immunity) to biomaterials is activated by the reaction of vascularized connective tissue to injury caused either by trauma or implantation [6, 7]. The physiological response of inflammation consists of a complex series of meticulously controlled responses which cannot possibly be summarized in a few sentences; however, the informed reader is referred to excellent reviews on the inflammatory response to biomaterials [2, 7]. Endothelial cells (EC) play an important role in the regulation of immune and inflammatory local responses by expressing, among other things, cell adhesion molecules (CAM) [8, 9]. CAM expression in activated ECs (type II activation) can be induced by pro-inflammatory cytokines, e.g. tumor necrosis

factor α (TNFα) [8, 9], released by inflammatory cells activated on contact with adsorbed proteins on the implanted biomaterial [2, 7, 10]. In turn, these adhesion molecules help recruit leukocytes from circulating blood and facilitate transendothelial migration to the site of injury to initiate the acute inflammation response [2, 7-10]. Additionally, previous *in vitro* studies showed that CAM expression in ECs was activated by elevated concentrations of metallic ions typically found in permanent metallic implants [1, 11-19]. Vascular cell adhesion molecule-1 (VCAM-1) is an immunoglobulin superfamily-specific receptor that provides high-affinity interactions between ECs and integrins on the leukocyte surface and facilitates transendothelial migration [6, 9, 10]. Moreover, VCAM-1 binds with monocytes, but not neutrophils, and it is the first CAM expressed in chronic inflammation such as atherosclerosis (before atherosclerotic plaque development) [9, 10, 20] and restenosis following coronary stent implantation [21]. Thus, VCAM-1 can be used as an indicator of *in vitro* EC activation during the early stages of inflammation. Furthermore, previous studies support the applicability of human umbilical vein endothelial cells (HUVEC) to model and investigate components of the inflammatory response, such as CAM expression [1, 13].

Previously, we reported on the development of Mg-Zinc-Strontium (Mg-Zn-Sr) ternary alloys and the evaluation of their biological performance for biomedical applications [22-24]. Furthermore, we reported on the *in vitro* direct culture method to mimic *in vivo* physiological conditions and evaluate cell responses at the cell-biomaterial interface (*direct contact*) and on the culture plate (*indirect contact*;

exposure to solubilized degradation products) surrounding the Mg-based biomaterial [25]. Thus, the first objective of this study was to investigate the degradation and cytocompatibility of four Mg-4Zn-xSr alloys (x = 0.15, 0.5, 1.0, 1.5 wt. %; designated as ZSr41A, B, C, and D respectively) in the direct culture with HUVECs *in vitro*. The second objective was to investigate the induction of an inflammatory response in HUVECs as indicated by the expression of VCAM-1 activated by the degradation products of the ZSr41 alloys. While several recent *in vivo* studies reported on adequate immunological response during the foreign body reaction or fibrosis stages following implantation of Mg-based materials [26-30], sparse literature is found on the early-stage inflammatory response. Specifically, to the authors' knowledge, early-stage inflammatory induction by the degradation of Mg-based materials has only been investigated *in vitro* with primary murine and human macrophages [31] and with dendritic cells [32]. In both cases, the Mg-based materials and the respective degradation products were not found to have detrimental immunomodulatory effects. This study reported for the first time on the *in vitro* transient inflammatory activation of ECs induced by the degradation products of Zn-containing Mg alloys.

5.2. Materials and methods

5.2.1. Preparation of ZSr41 alloys, Mg control, and reference materials

The ZSr41 alloys in this study had a nominal composition of 4 wt. % Zn with 0.15, 0.5, 1.0, or 1.5 wt. % Sr; these alloys were designated as ZSr41A, ZSr41B,

ZSr41C, and ZSr41D accordingly with increasing Sr content. Details pertaining to the metallurgical process and heat treatment used for alloy preparation are described elsewhere [22, 23]. The heat-treated 1.0 mm thick sheets of ZSr41 alloys were cut into 5 x 5 mm squares. Likewise, commercially pure Mg sheets (99.9%, As-rolled, 1.0 mm thick, Cat# 40604; Alfa Aesar, Ward Hill, MA, USA) were cut into 5 x 5 mm squares and used as a control in this study. Commercially available AZ31 (1.0 mm thick, Cat# 44009; Alfa Aesar) and Nitinol (NiTi; 0.25 mm thick, Cat# 44953; Alfa Aesar) sheets were cut into 5 x 5 mm squares and used as metallic reference materials in this study. AZ31 was included in this study since it has been used previously as a reference material for the investigation of Mg-based materials [33-35]; likewise, NiTi was included due to the widespread use for cardiovascular stents [36]. Additionally, 90:10 polylactic-co-glycolic acid (PLGA) was included in this study as a non-metallic reference material due to the use of PLGA-based coatings to control the degradation of Mg-based materials for cardiovascular stents [36, 37]. The PLGA samples were prepared by cutting non-tissue culture treated glass (Cat# 12-544-1; Fisher Scientific, Hampton, NH, USA) into 5 x 5 mm squares followed by rough polishing with 240 grit SiC paper to improve the glass-PLGA adhesion. The 90:10 PLGA (Cat# AP49; Polyscitech, West Lafayette, IN, USA) was dissolved in chloroform at 10 wt./vol. % and sonicated for 1 hr at 40 °C. Subsequently, 50 µL of the dissolved PLGA was spin coated (SC100; Smart Coater Co., Saint Louis, MO, USA) onto the rough-polished

glass substrates at 1300 RPM for 60 sec. The PLGA coatings had a thickness of 64.0 ± 12.6 µm.

5.2.2. Microstructure characterization

Prior to degradation and cell experiments, the microstructure of the ZSr41 alloys, pure Mg control, and AZ31 reference was characterized using a scanning electron microscope (SEM; Nova NanoSEM 450, FEI Co., Hillsboro, OR, USA). For microstructure characterization, the samples were ground with SiC abrasive paper (Ted Pella Inc., Redding, CA, USA) up to 1200 grit, and fine polished up to 0.25 µm with polycrystalline diamond paste (Physical Test Solutions, Culver City, CA, USA). Surface elemental composition and distribution were analyzed with energy dispersive x-ray spectroscopy (EDS) using a Nova NanoSEM 450 equipped with an X-Max50 detector and AZtecEnergy software (Oxford Instruments, Abingdon, Oxfordshire, UK). An accelerating voltage of 20 kV was used to obtain SEM images and perform EDS analyses.

5.2.3. Electrochemical testing

Potentiodynamic polarization (PDP) curves were obtained using a three-electrode cell configuration connected to a potentiostat (Model 273A, Princeton Applied Research, Oak Ridge, TN, USA) and acquired with PowerSuite 2.50.0 software (Princeton Applied Research). Specific details pertaining to preparation of the working electrode are given elsewhere [25]. Briefly, the ZSr41 alloys, Mg

control, and AZ31 reference samples were embedded in epoxy resin as the working electrode (0.5 cm^2 area exposed). Platinum foil was used as the counter electrode, and a silver/silver chloride (Ag/AgCl) electrode was used as a reference. Prior to electrochemical experiments, the working electrode was ground with SiC abrasive paper up to 1200 grit and ultrasonically cleaned in acetone and ethanol. Revised simulated body fluid (r-SBF; pH 7.4, 37.5°C) was used as the electrolyte for PDP scans (no equilibration, 0.5 to -3.5 V, 20 mV s^{-1}) since the ionic composition of r-SBF is the same as human blood plasma [38]. Values for corrosion potential (E_{corr}) and corrosion current density (J_{corr}) were extrapolated from the PDP curves according to ASTM G102-89 standard. All potentials are in reference to Ag/AgCl electrode.

5.2.4. HUVEC responses and *in vitro* degradation of ZSr41 alloys

5.2.4.1. Preparation of HUVEC culture

Human umbilical vein endothelial cells (HUVECs; Cat# C2519A; Lonza Walkersville Inc., Walkersville, MD, USA) were cultured according to the manufacturer's recommended culture protocol to passage 5 in complete Endothelial Cell Growth Medium-2 (EGM™-2) media (Cat# CC-3162; Lonza Walkersville Inc.) in standard cell culture conditions (37°C, 5%/95% CO_2/air, sterile, humidified environment). Cell morphology was observed at each passage using an optical microscope to ensure HUVECs were normal and healthy.

5.2.4.2. Direct culture of HUVECs with ZSr41 alloys

Prior to cell culture experiments, all metallic samples were ground with SiC abrasive paper up to 1200 grit, ultrasonically cleaned for 15 min in separate baths of acetone and ethanol, and sterilized under ultraviolet (UV) radiation for 4 hrs on each side. The as-coated PLGA samples were disinfected by immersing in 70% ethanol for 20 min. Additionally, non-tissue culture treated glass slides (non-coated with PLGA) were cut into 5 x 5 mm squares, cleaned in acetone and ethanol, disinfected under UV radiation, and used as a reference material for cell culture experiments. All the samples were placed in standard 12-well cell culture treated plates and rinsed with 3 mL of phosphate buffered saline (PBS) to calibrate the osmotic pressure. Subsequently, HUVECs (P5) were seeded directly onto the surfaces of the samples at a density of $6x10^3$ cells cm^{-2} and incubated in 3 mL of EGM™-2 under standard cell culture conditions for 4 and 24 hrs. HUVECs cultured in EGM™-2 media supplemented with 10 ng/mL of tumor necrosis factor α (TNFα; Cat# PHC3015; Life Technologies, Carlsbad, CA, USA) was used as a positive control for VCAM-1 expression experiments; this group was designated as “HUVEC+TNFα”. A positive control for HUVEC adhesion and negative control for VCAM-1 expression, designated as "HUVEC" group, consisted of HUVECs cultured only with EGM™-2 in the wells, i.e. without any samples or TNFα stimulation. EGM™-2 alone was also used as a blank reference and designated as “EGM-2” group. Separate sets of samples were used for the 4 and 24 hr adhesion experiments, and for the 4 and 24 hr inflammation experiments.

5.2.4.3. Characterization of the HUVECs in *direct* contact with ZSr41 alloys

The interface between the HUVEC culture and ZSr41 alloys, and all other reference materials was characterized using SEM following the 4 and 24 hr *in vitro* cultures. Additionally, corresponding surface elemental composition and Mg Kα1 elemental distribution maps were acquired with EDS. The samples used for SEM and EDS analysis were removed from the wells and dip-rinsed in PBS to remove non-adherent cells. Adherent cells were fixed with 3% glutaraldehyde in 0.1 M potassium phosphate buffer for 1 hr. After fixation, the samples were again dip-rinsed in PBS followed by a serial dehydration in increasing ethanol concentration (50%, 75%, 90%, 2x100%; 10 min each). The samples were then critical-point dried (Autosamdri-815, Tousimis Research Corp., Rockville, MD, USA) and sputter coated (Model 108, Cressington Scientific Instruments Ltd., Watford, UK) with platinum/palladium at 20 mA and 40 sec sputter time.

5.2.4.4. Quantification of HUVEC adhesion under *direct* versus *indirect* contact conditions

HUVEC adhesion on the surface of the samples (i.e. *direct* contact with the sample) and on culture plate surrounding the respective samples (*indirect* contact with the sample) following the 24 hr *in vitro* culture was evaluated using fluorescence microscopy. The results from the culture plates were grouped separately and designated as “plate”. The samples in *direct* contact with HUVECs were removed from the wells and dip-rinsed in PBS to remove non-adherent cells.

The corresponding wells were washed separately with PBS to remove non-adherent cells. Adherent cells, both on the sample surface and on the plates, were separately fixed with 4% formaldehyde (10% neutral buffered formalin; VWR, Radnor, PA, USA) for 20 min, followed by incubation in Alexa Fluor 488® phalloidin (Cat# A12379; Life Technologies) for 20 minutes and 4',6-diamidino-2-phenylindole dilactate (DAPI; Cat# D1306; Invitrogen™, Life Technologies) for 5 minutes to fluorescently label cellular F-actin and nucleus, respectively. Adherent cells on the sample surface and on the culture plate surrounding the sample were visualized using a fluorescence microscope (Eclipse Ti and NIS software, Nikon, Melville, NY, USA) with a 10x objective lens at the same exposure condition and analyzed using Image J (NIH, Bethesda, MD, USA). Cell adhesion per group was quantified by counting the DAPI-stained cell nuclei at five random locations on the sample surface and at nine random locations on the culture plate at each prescribed incubation interval. Cell adhesion density was calculated as the number of adherent cells per unit area.

5.2.4.5. Quantification of HUVEC inflammatory response to the degradation of ZSr41 alloys in *indirect* contact

The inflammatory response of HUVECs to the degradation of ZSr41 alloys was evaluated using immunofluorescence of VCAM-1 and were carried out only for the cells in *indirect* contact with the samples (i.e. adhered to the tissue culture plates). The cells adhered to the culture plates were fixed with 4% formaldehyde for 20

min, incubated with 5% goat serum in PBS during 1 hr for blocking, incubated with 10 µg/mL VCAM-1 (Cat# SC-13160; Santa Cruz Biotechnology Inc., Dallas, TX, USA) mouse anti-human primary IgG overnight at 4 °C, and incubated with 10 µg/mL goat anti-mouse secondary IgG-FITC (Cat# SC-2010; Santa Cruz Biotechnology Inc.) at room temperature for 1 hr. The nuclei were subsequently stained with DAPI nucleic acid stain for 5 min. Five FITC images (640x512 pixel digital resolution, 16-bit depth, and 4 s exposure) per well per group were captured using a Nikon Eclipse T*i* fluorescent microscope. A mean fluorescence intensity signal per pixel was calculated using ImageJ and the method described by Patapova *et al.* [39].

5.2.4.6. *In vitro* degradation of ZSr41 alloys in the HUVEC culture

The *in vitro* degradation of the ZSr41 alloys, Mg, and AZ31 after the 4 and 24 hr cultures was evaluated through measurements of pH and ionic concentrations of the collected media. The pH of the media was measured immediately after collection using a calibrated pH meter (Model SB70P, VWR). The concentration of Mg^{2+}, Zn^{2+}, and Sr^{2+} ions in the collected media was measured using inductively coupled plasma optical emission spectrometry (ICP-OES; Optima 8000, Perkin Elmer, Waltham, MA, USA). In order to minimize matrix effects in ICP-OES, the collected EGM^{TM}-2 aliquots were diluted to 1:100 solutions in DI water to measure the concentrations of Mg^{2+} and Sr^{2+}. Ionic concentrations were then obtained from calibration curves generated using Mg and Sr standards (Perkin Elmer) diluted to

ranges of 0.5-5.0 and 0.1-1.0 mg/L, respectively. The concentrations of Zn^{2+} in the EGM™-2 at 4 and 24 hrs were measured by diluting the collected aliquots to 1:7 solutions in DI water and then obtained using a calibration curve generated using a Zn standard (Perkin Elmer) diluted to a range of 10-1000 µg/L.

5.2.5. Effects of media alkalinity and Mg^{2+} ion concentration on HUVEC viability and morphology

To identify which factor(s) modulated HUVEC viability or morphology, separate experiments evaluating the effects of increasing Mg^{2+} ion concentration and increase in pH in the cell culture media were carried out. HUVECs (P5) were seeded in standard 12-well cell culture treated plates at a density of $6x10^3$ cells cm^{-2} and incubated in 3 mL of EGM™-2 under standard cell culture conditions for 24 hrs. The cell density after this initial 24 hr stabilization period was designated as “EGM-2 (t = 0).” Subsequently, the media was removed and replenished with 3 mL of (i) EGM™-2 with pH values intentionally adjusted to 8.1, 8.5, 9.0, and 9.5, or (ii) EMG-2 supplemented with respective Mg^{2+} ion concentrations of 1.3, 2.6, 6.7, 13.1, 21.2, and 27.6 mM. EGM™-2 media without pH adjustment and without supplemented Mg^{2+} ions was used as a control in the pH and Mg^{2+} ion experiments, respectively. EGM™-2 incubated without cells was used as a blank reference. HUVECs were then incubated under standard cell culture conditions with the adjusted media conditions for another 24 hrs. Specific details used for adjusting pH and instructions for supplementing Mg ions using $MgCl_2•6H_2O$ are

described elsewhere [25, 40]. After 24 hrs, adhered cells were fixed and stained, and viability was analyzed and quantified using the same method described above. Cell morphology was quantified by manually outlining twenty cells per image per group (on the cell culture plate) in ImageJ and obtaining values for average F-actin area per HUVEC nucleus, and Feret diameter aspect ratio of cells (D_{max}/D_{min}). D_{min} is the minimum Feret diameter. The culture media was also collected and analyzed for changes in pH and Mg^{2+} ion concentration as described above.

5.2.6. Statistical analyses

All experiments described above were done in triplicate. All data sets were tested for normal distribution and homogeneous variance. Parametric data sets were analyzed using one-way analysis of variance (ANOVA) followed by the Tukey HSD *post hoc* test. Data sets with normal distribution but heterogeneous variance were analyzed using one-way ANOVA (homogeneous variance not assumed) followed by the Games-Howell *post hoc* test. Non-parametric data sets were analyzed using the Kruskal-Wallis test followed by the Nemenyi *post hoc* test. Statistical significance was considered at $p < 0.05$.

5.3. Results

5.3.1. Microstructure of ZSr41 alloys

Figure 5.1 shows the surface microstructures and elemental compositions of the ZSr41 alloys, pure Mg control, and AZ31 reference. SEM images at a low

magnification of 600x (Figures 5.1a) confirmed an increase in intermetallic β-phase with increasing Sr content in the ZSr41A-D alloys, respectively. As expected, the pure Mg control showed a surface free of secondary phases, and the AZ31 reference showed the presence of an intermetallic β-phase. SEM images at a high magnification of 5000x (Figures 5.1a, insets) showed that the intermetallic β-phase of ZSr41A had a morphology of finely dispersed precipitates whereas coarse precipitates were observed on ZSr41B-D. Figure 5.1b shows the quantification of surface elemental composition of the ZSr41 alloys, Mg, and AZ31 samples using EDS area analysis at a 600x magnification. Increasing Sr content was detected for each of the ZSr41 alloys; specifically (in wt. %), 0.16 for A, 0.21 for B, 0.43 for C, and 1.18 for D. Additionally, a Zn content in close agreement to the nominal 4 wt. % and 1 wt.% was measured for the ZSr41 alloys and AZ31, respectively. Furthermore, all samples had a predominant Mg content (> 86.7 wt. %), as well as Carbon (C) content (~ 7.0 wt. %), and Oxygen (O) content (~ 1 wt. %). AZ31 was confirmed to contain 3.27% Aluminum (Al) and traces of Manganese (Mn).

The composition of the α-matrices and β-phases (in at. %) of the ZSr41 alloys was determined through EDS point analyses (Figure 5.2) at the Points 1-8 shown in Figure 5.1a. Comparison of the composition of the α-matrices of each ZSr41 alloy at the Points 1, 3, 5, 7 showed a largely similar elemental content irrespective of nominal Sr content in the alloy (Figures 5.2a-b). Specifically, the α-matrices of all four ZSr41 alloys showed a Zn content of ~1.5 (i.e. ~4 wt. %), O content of ~1%, and C content of ~10%; these results are presented graphically in the histogram

shown in Figure 5.2b. In contrast, comparison of the composition of the intermetallic β-phases of each ZSr41 alloys at the Points 2, 4, 6, 8 (Figure 5.2c) showed that the β-phases in the ZSr41B alloy (Point 4) and ZSr41D (Point 8) alloy had a higher Zn content than the ZSr41A (Point 2) and ZSr41C (Point 6). However, the Sr content was ~4 at. % in the β-phases of all four ZSr41 alloys, irrespective of the alloy. Additionally, a higher O content of 11.7% was found in the β-phase of ZSr41A compared with the other three ZSr41 alloys (~1.3%). A trace amount of Calcium (Ca) was also detected in the β-phases of all ZSr41 alloys. The composition of the β-phases of the ZSr41 alloys is shown graphically in the stacked histogram in Figure 5.2d. The Zn/Sr atomic ratio was calculated for the β-phases of the four ZSr41 alloys and is shown in Table 5.1. Comparison of the Zn/Sr atomic ratio showed that ZSr41B and ZSr41D had Zn/Sr ratios of ~1.6 and 1.7, respectively, while ZSr41A and ZSr41C had Zn/Sr ratios of 0.4 and 0.9, respectively.

5.3.2. Corrosion properties of ZSr41 alloys based on electrochemical testing

PDP curves obtained for the polished samples showed that the initial corrosion (or degradation) behavior of the ZSr41 alloys, pure Mg control, and AZ31 reference were similar (Figure 5.3). The median PDP trace with the most representative corrosion potential (E_{corr}) and corrosion current density (J_{corr}) for each sample type was plotted in Figure 5.3a. A qualitative assessment of the PDP curves indicated

that the as-polished AZ31 reference showed the most cathodic behavior when compared to all other Mg-based materials tested, all of which showed similar behavior. Furthermore, assessment of the linear anodic (b_a) and cathodic (b_c) portions of the PDP curves gave indication that AZ31 and Mg had similar half-reaction characteristics in contrast to those for all ZSr41 alloys. ANOVA was used to confirm statistically significant differences in the E_{corr} [F (5, 12) = 18.114, p = 3.209x10^{-5}] and J_{corr} [F (5, 12) = 6.7707, p = 3.22x10^{-3}] values calculated by Tafel extrapolation from the PDP curves (Figure 5.3b). *Post hoc* pairwise comparisons confirmed that the E_{corr} of AZ31 (-1.42±0.01 V) was significantly more cathodic (p < 0.001) when compared with ZSr41A (-1.52±0.01 V), ZSr41B (-1.51±0.01 V), ZSr41C (-1.55±0.02 V), ZSr41D (-1.51±0.02 V), and Mg (-1.57±0.03 V). In contrast, Mg was significantly more anodic (p < 0.01) when compared with ZSr41A, ZSr41B, and ZSr41D. In addition, *post hoc* pairwise comparisons also confirmed a statistically significant higher J_{corr} (p < 0.001) for AZ31 (67.51±5.47 mA cm^{-2}) when compared with ZSr41A (39.99±5.68 mA cm^{-2}) and ZSr41B (40.07±6.47 mA cm^{-2}).

5.3.3. HUVECs in *direct* contact with ZSr41 alloys

A qualitative analysis of the HUVEC-substrate interface showed changes in surface topography and elemental composition for the ZSr41 alloys compared with the Mg control and reference materials as early as 4 hrs after incubation. Figure 5.4a shows SEM micrographs of the cell-substrate interface for the materials

investigated at an original magnification of 150x (Figure 4a) and 1,000x (Figure 5.4a, insets) after 4 hr of direct culture and *direct* contact with the samples. Adhered cells were observed on the surfaces of all samples; however, the cells attached on all the Mg-based materials (i.e. ZSr41 alloys, Mg, and AZ31) showed relatively compact cell bodies compared with the highly spread cells observed on the NiTi, PLGA, and glass samples. These two distinct cell morphologies were referred to as anisotropic and isotropic spreading, respectively [25, 41]. Furthermore, comparison of cell attachment on the non-Mg-based samples showed that cells on both NiTi and glass were isotropically-spread almost completely flat on the surface of the samples whereas cells on the PLGA were isotropically-spread but not completely flat on the surface. Additionally, all Mg-based samples showed similar distribution of degradation-induced surface cracks indicating similar degradation characteristics after 4 hrs of incubation in EGM^{TM}-2 media. Figure 5.4b shows composite images of SEM micrographs with EDS elemental distribution maps (red = Mg, green = C, yellow = O, pink = Potassium (K) and Sodium (Na), orange = Phosphorus (P), purple = Ca, blue = Zn, white = Sr). The SEM-EDS composite images allowed visualization of the cell-biomaterial interface and confirmed cell adhesion directly on the surface of all Mg-based materials after 4 hrs of incubation. Interestingly, all Mg-based materials showed co-localization of Ca, P, and O which indicated that Mg degradation possibly attracted mineral deposition [25]. Figure 5.5 shows elemental distribution maps of Mg (Kα1 lines) and a summary of elemental composition (in wt. %) results obtained

from EDS analyses at 150x magnification of the samples after the 4 hr incubation. All Mg-based materials showed a similar surface distribution of Mg (Figure 5.5a), giving further indication of similar degradation characteristics after 4 hrs of incubation. The stacked histogram shown in Figure 5.5b summarizes the elemental composition (in wt. %) results obtained from EDS analyses at 150x magnification. A Zn content comparable to the nominal 4% was detected on the surfaces of alloys ZSr41A, B, C, and D (4.47%, 4.28%, 3.01%, and 4.68%, respectively); Zn was also detected on AZ31 (0.96%) but not on the Mg control or any of the other reference materials. Additionally, increasing Sr content was also detected on alloys ZSr41B, C, and D (0.03, 0.31, and 0.66%, respectively); Sr was not detected on the surface of ZSr41A alloy, Mg control, or any of the reference materials. The deposition of Ca, P, and O was approximately equal and exclusive for all Mg-based materials. In contrast, none of the Mg-based materials (i.e. NiTi, PLGA, glass) showed deposition of Ca and P. Additionally, as expected, content in NiTi was predominantly Nickel (Ni) and Titanium (Ti), PLGA was predominantly C and O, and the glass sample had typical composition of soda-lime glass [25]. Lastly, all samples showed C content (attributed to adhered cells, proteins, and extracellular matrix produced by cells), and Na and K content (attributed to solubilized ions from salts in the culture media).

Similarly, SEM and EDS analyses of the HUVEC-substrate interface after 24 hrs of incubation showed further changes in surface topography and elemental composition of the biomaterials investigated. Figure 5.6 shows SEM micrographs

of the cell-substrate interface at an original magnification of 150x and 1,000x (Figure 5.6, insets) after 24 hr of direct culture and *direct* contact with the samples. In contrast to the 4 hr samples, adhered cells were not observed on the surface of any of the ZSr41 alloys or Mg control. Some cell attachment was observed on the AZ31 sample but these HUVECs showed abnormal/unhealthy morphology. Additionally, isotropically-attached cells were observed on the surfaces of NiTi, PLGA, and glass reference materials. Similar to the 4 hr time point, the cells attached on the surface of NiTi and glass continued to spread almost completely flat while the cells on PLGA sample did not appear to spread completely flat. At the 24 hr time point, the cell monolayer on the glass sample was approximately 80-90% confluent. Furthermore, comparison of the surface morphology and degradation-induced crack distribution showed that all of the ZSr41 alloy and AZ31 samples had similar characteristics after the 24 hr incubation in EGM^{TM}-2 media. In contrast, the Mg control sample showed much larger cracks compared with the other Mg-based materials. Figure 5.7 shows elemental distribution maps of Mg (Kα1 lines) and a summary of elemental composition (in wt. %) results obtained from EDS analyses at 150x magnification of the samples after the 24 hr incubation. Surface distribution of Mg (Figure 5.7a) showed heterogeneous distribution likely indicative of localized corrosion; the bright spots in each image corresponds to regions of higher Mg content (most evident in Figure 5.7a, Mg). These images showed the varying degree of surface integrity of all of the Mg-based materials after 24 hrs of culture in EGM^{TM}-2 media, with AZ31 showing the most

homogeneous surface. The stacked histogram shown in Figure 5.7b summarizes the elemental composition (in wt. %) results obtained from EDS analyses at 150x magnification. Similar to the 4 hr time point, a Zn content comparable to the nominal 4% was detected on the surfaces of ZSr41 alloys and AZ31 but not on the Mg control or any of the other reference materials. Additionally, increasing Sr content was also detected on alloys ZSr41B, C, and D but not on ZSr41A alloy, Mg control, or any of the reference materials. All Mg-based samples continued to show similar content and co-localization of Ca, P, and O; however, the Ca content was slightly higher and the P content was slightly lower for all samples compared to their 4 hr counterparts. The NiTi, PLGA, and glass samples showed very similar surface compositions compared with their 4 hr counterparts and continued to showed a lack of deposition of Ca and P. Lastly, all samples showed C, and Na and K content.

5.3.4. HUVEC adhesion under *direct* and *indirect* contact conditions

HUVEC adhesion directly onto the sample (*direct* contact) and on the culture plate (indirect contact) was evaluated at 4 and 24 hr after direct culture with the ZSr41 alloys, Mg control, and reference materials, and results are summarized in Figure 5.8. Figure 5.8a shows fluorescence images of HUVECs attached to the culture plates at 24 hrs post-incubation; similar images were obtained for the 4 hr culture on both direct and *indirect* contact, and for the 24 hr *direct* contact. The DAPI-stained nuclei were used to quantify cell adhesion density at the 4 and 24 hr

time points and results are plotted in the histograms shown in Figure 5.8b for HUVECs adhered to the culture plates and Figure 5.8c for HUVECs adhered directly onto the samples. Results from cell adhesion density on the culture plate at 4 and 24 hrs (Figure 5.8b) showed no statistically significant differences among all the groups evaluated. A comparison between cell adhesion densities at 24 hr with their respective counterparts at 4 hr on the culture plates showed an increasing trend for almost all the samples indicating possible early signs of proliferation. In all cases, the mean adhesion density at 24 hr was within the range of error of the 4 hr values. Results from cell adhesion density directly on the sample surface at 4 hrs (Figure 5.8c) showed no statistically significant differences; in contrast, the Kruskal-Wallis test showed a statistically significant difference in the mean adhesion density at the 24 hr time point [X^2 (8, N = 27) = 19.676, p = 0.017]. *Post hoc* pairwise comparisons showed a significantly lower adhesion density on both ZSr41A ($0.32\pm0.20\times10^3$ cells cm^{-2}) and ZSr41D ($0.30\pm0.22\times10^3$ cells cm^{-2}) compared with the glass reference ($3.81\pm0.89\times10^3$ cells cm^{-2}; $p < 0.05$). A comparison between cell adhesion densities at 24 hr with their respective counterparts at 4 hr on the sample surface showed a large decrease for all groups except for the glass reference indicating detrimental conditions for prolonged HUVEC adhesion and viability.

5.3.5. HUVEC inflammatory response under *indirect* contact

Results from the inflammatory response, as indicated by the immunofluorescence expression of surface marker VCAM-1, are summarized in Figure 5.9. The inflammatory response was only measured on HUVECs under *indirect* contact since adhesion density for *direct* contact was greatly reduced (nearly non-existent) after 24 hrs of incubation. Figure 5.9a shows immunofluorescence images of VCAM-1 expression (with DAPI-stained nuclei) of HUVECs attached to the culture plates at 4 hrs post-incubation; similar images were obtained for the 24 hr time point. The mean VCAM-1 fluorescence intensity signal per pixel at the 4 and 24 hr time points are plotted in the histograms shown in Figures 5.9b and 5.9c, respectively. ANOVA (without homogeneous variance) was used to show statistically significant differences in the mean VCAM-1 expression at 4 hrs post incubation (Figure 5.9b) [F (10, 9) = 22.715, p = 5.191×10^{-5}]. *Post hoc* pairwise comparisons showed a significantly lower fluorescence intensity for the ZSr41A (159.9±4.2 A.U.) and HUVEC (negative control; 136.2±10.9 A. U.) groups compared with both the ZSr41D (267.4±5.7 A. U.) and HUVEC+TNFα (positive control; 322.7±11.3 A. U.) groups. Analysis of VCAM-1 intensity at the 24 hr time point (Figure 5.9c) showed no statistically significant differences. Interestingly, despite the lack of significant differences, a trend of increasing VCAM-1 fluorescence intensity was observed with increasing Sr content in the ZSr41 alloys.

5.3.6. *In vitro* degradation of ZSr41 alloys in the HUVEC culture

Results from the analysis of the culture media at the 4 hr time point are summarized in the histograms shown in Figure 5.10. Media pH and Mg^{2+} ion concentration ([Mg^{2+}]) are both important indicators of the degradation of Mg-based materials [42]; in addition the Zn^{2+} and Sr^{2+} ion concentrations ([Zn^{2+}] and [Sr^{2+}], respectively) were also measured to ensure concentrations remained below reported cytotoxic levels. The Kruskal-Wallis test showed statistically significant differences in the mean pH of the culture media at 4 hrs (Figure 5.10a) [X^2 (11, N = 36) = 31.444, $p = 9.36 \times 10^{-4}$]. Specifically, *post hoc* pairwise comparisons showed a significantly higher pH for AZ31 (8.13±0.03) when compared with NiTi (7.82±0.03; $p < 0.05$), PLGA (7.83±0.04; $p < 0.05$), and the EGM-2 blank reference (7.78±0.01; $p < 0.01$). Similarly a significantly more alkaline media was measured for ZSr41A (8.01±0.08) when compared with the EGM-2 blank reference ($p < 0.05$). In general, as expected, all of the Mg-based samples caused an increase in alkalinity of the media. Furthermore, ANOVA was used to confirm a statistically significant difference in the mean [Mg^{2+}] in the culture media (Figure 5.10b) [F (11, 24) = 12.535, $p = 1.99 \times 10^{-7}$]. Specifically, *post hoc* pairwise comparisons showed that the concentrations of ZSr41A (9.69±0.15 mM) and ZSr41B (9.69±0.34 mM) were both significantly higher ($p < 0.05$) compared with PLGA (8.92±0.12 mM) and glass (8.78±0.26 mM); ZSr41B was also significantly higher ($p < 0.05$) compared with the HUVEC cells-only control (8.93±0.05 mM). Similarly, the [Mg^{2+}] in the culture media of ZSr41C (10.02±0.11 mM), ZSr41D (10.09±0.37 mM), and AZ31

(10.20±0.15 mM) were all significantly higher ($p < 0.01$, $p < 0.001$, and $p < 0.001$, respectively) when compared with NiTi (8.98±0.12 mM), PLGA, glass, HUVEC+TNFα (8.99±0.17 mM), HUVEC, and EGM-2 blank reference (9.16±0.58 mM). *Post hoc* pairwise comparisons also showed a significantly higher [Mg^{2+}] in the culture media of the pure Mg control (9.80±0.16 mM; $p < 0.05$) when compared with NiTi, PLGA, glass, HUVEC+TNFα, and HUVEC cells-only control. Figures 5.10c and 5.10d show [Zn^{2+}] and [Sr^{2+}], respectively, in the cell culture media after 4 hrs. ANOVA confirmed statistically significant differences in the mean [Zn^{2+}] in the media [F (11, 24) = 4.0052, $p = 2.17 \times 10^{-3}$]. *Post hoc* pairwise comparisons showed that the [Zn^{2+}] of ZSr41D (1.59±0.34 µM) was significantly higher when compared with the pure Mg control (0.49±0.09 µM; $p < 0.01$), NiTi (0.57±0.22 µM; $p < 0.05$), PLGA (0.78±0.27 µM; $p < 0.05$), glass (0.56±0.03 µM; $p < 0.01$), and EGM-2 blank reference (0.65±0.12 µM; $p < 0.01$). No statistically significant differences were confirmed for [Sr^{2+}] and all values were in the low single-digit µM range.

Results from the analysis of the culture media at the 24 hr time point are summarized in the histograms shown in Figure 5.11. ANOVA was used to confirm statistically significant differences in the mean pH of the culture media at 24 hrs (Figure 5.11a) [F (11, 24) = 69.008, $p = 2.06 \times 10^{-15}$]. *Post hoc* pairwise comparisons showed a significantly more alkaline media for all Mg-based materials compared with the reference materials and controls ($p < 0.001$); however, no statistically significant differences were confirmed when comparing Mg-based materials

amongst each other. Specifically, the culture media of ZSr41A (8.12±0.02), ZSr41B (8.16±0.01), ZSr41C (8.07±0.06), ZSr41D (8.15±0.03), Mg (8.10±0.06), and AZ31 (8.11±0.01) were all significantly more alkaline compared with NiTi (7.79±0.02), PLGA (7.81±0.03), glass (7.85±0.02), HUVEC+TNFα (7.85±0.02), HUVEC (7.87±0.02), and EGM-2 (7.79±0.02). Furthermore, ANOVA showed statistically significant differences in the mean [Mg^{2+}] of the culture media at 24 hrs (Figure 5.11b) [F (11, 24) = 55.126, p = 3.542×10^{-15}]. *Post hoc* pairwise comparisons indicated that the [Mg^{2+}] in the media incubated with all Mg-based materials was significantly higher ($p < 0.001$) when compared with NiTi (9.14±0.29 mM), PLGA (9.48±0.24 mM), glass (9.52±0.24 mM), HUVEC+TNFα (9.37±0.07 mM), HUVEC cells-only control (9.29±0.04 mM), and EGM-2 blank reference (9.22±0.19 mM). Specifically, the [Mg^{2+}] for the Mg-based materials were as follows: ZSr41A (16.19±0.94 mM), ZSr41B (19.53±0.90 mM), ZSr41C (13.92±1.50 mM), ZSr41D (18.12±1.61 mM), Mg (14.18±1.07 mM), and AZ31 (13.63±0.28 mM). The following significant differences in [Mg^{2+}] were also confirmed: ZSr41B and ZSr41D were both significantly higher ($p < 0.001$) compared with ZSr41C, Mg, and AZ31; and ZSr41A was significantly lower ($p < 0.01$) compared with ZSr41B, but significantly higher ($p < 0.05$) compared with AZ31. Figures 5.11c and 5.11d show [Zn^{2+}] and [Sr^{2+}], respectively, in the cell culture media after 24 hrs. ANOVA confirmed statistically significant differences in the mean [Zn^{2+}] (Figure 5.11c) [F (11, 24) = 55.126, p = 2.697×10^{-14}]. *Post hoc* pairwise comparisons showed that the [Zn^{2+}] in the media incubated with ZSr41A (47.91±2.84 μM), ZSr41B

(32.87±6.34 μM), and ZSr41D (40.65±12.39 μM) were all significantly higher (p < 0.001) when compared with Mg (0.65±0.31 μM), AZ31 (2.13±0.32 μM), NiTi (1.09±0.35 μM), PLGA (1.09±0.20 μM), glass (1.06±0.39 μM), HUVEC+TNFα (0.86±0.40 μM), HUVEC cells-only control (0.52±0.06 μM), and EGM-2 blank reference (0.68±0.08 μM). Similarly, ZSr41C (8.24±2.58 μM) was significantly lower (p < 0.001) compared with ZSr41A, ZSr41B, and ZSr41D; likewise, ZSr41A was significantly higher (p < 0.01) compared with ZSr41B. ANOVA also confirmed statistically significant differences in the mean [Sr^{2+}] (Figure 5.11d) [F (11, 24) = 35.955, p = $3.29x10^{-12}$]. Specifically, *post hoc* pairwise comparisons showed a significantly higher [Sr^{2+}] (p < 0.001) in the media of ZSr41B (16.42±7.34 μM) and ZSr41D (38.22±4.91 μM) when compared with Mg (4.01±1.37 μM), AZ31 (3.22±1.56 μM), NiTi (3.94±0.74 μM), PLGA (4.21±2.46 μM), glass (3.13±2.16 μM), HUVEC+TNFα (2.67±1.76 μM), HUVEC cells-only control (4.91±0.64 μM), and EGM-2 blank reference (4.04±0.59 μM). Likewise, ZSr41D was also significantly higher (p < 0.001) when compared with ZSr41A (6.16±1.87 μM), ZSr41B, and ZSr41C (8.76±1.48 μM), and ZSr41B was significantly higher (p < 0.05) compared with ZSr41A. Compared with their 4 hr counterparts, the [Zn^{2+}] and [Sr^{2+}] measured at 24 hrs represented a ten-fold increase.

The degradation rates of each ZSr41 alloy, pure Mg control, and AZ31 reference (given as a mass loss rate per unit area per day) are summarized in Figure 5.12. These values were calculated by multiplying the [Mg^{2+}] of each group at 24 hrs (ICP-OES results shown Figure 5.11b) by the incubation volume of media

(3 mL) and then dividing by the initial exposed surface area of each sample to obtain a degradation rate based on initial geometry of the sample. ANOVA confirmed statistically significant differences in the normalized degradation rates during the 24 hr incubation period [F (5, 12) = 7.628, p = 1.954x10^{-3}]. *Post hoc* pairwise comparisons showed that the degradation rates of ZSr41B (1.63±0.54 mg cm^{-2} day^{-1}) and ZSr41D (1.67±0.52 mg cm^{-2} day^{-1}) were both significantly higher (p < 0.05) when compared with ZSr41C (0.70±0.18 mg cm^{-2} day^{-1}), Mg (0.72±0.05 mg cm^{-2} day^{-1}), and AZ31 (0.49±0.05 mg cm^{-2} day^{-1}).

5.3.7. Effects of media alkalinity and Mg^{2+} ion concentration on HUVEC viability and morphology

Figure 5.13 shows the results for HUVEC viability and morphology after 24 hr of incubation with the culture media intentionally adjusted to pH values of 8.1, 8.5, 9.0, and 9.5 and non-adjusted media (EGM-2). The lower end of pH 8.1 was selected because the degradation of the Mg-based materials in this study caused an increase in pH up to approximately 8.1 (Figures 5.10a and 5.11a) without reducing cell viability (Figure 5.8b). In contrast, the higher end of pH 9.5 was selected based on previous results that showed significantly reduce cell viability at pH 9.5 [25]. Fluorescence images of HUVECs after 24 hr of culture in non-adjusted media and alkaline media conditions (Figure 5.13a) showed attached and viable, and isotropically-spread cells. Figure 5.13b summarizes results of pH measurements of the collected media after 24 hrs of incubation with HUVECs

("blank" designates EGM-2 media incubated without HUVECs). It was observed that the pH of all the adjusted culture media decreased compared with their nominally-adjusted value due to the pH buffering effect of EGM-2 and possible acidic metabolites produced by viable HUVECs. Specifically, the media adjusted to 8.1, 8.5, 9.0, and 9.5 changed to 7.74±0.01, 7.82±0.05, 7.89±0.02, and 8.01±0.02, respectively. The blank reference (without HUVECs) and non-adjusted media (EGM-2) had pH values of 7.79±0.03 and 7.78±0.02, respectively. Results of HUVEC adhesion density in the adjusted media conditions after the 24 hr culture are summarized in Figure 5.13c. Statistically significant differences in the mean cell adhesion density were confirmed by ANOVA [F (4, 10) = 5.723, p = 0.01163]. *Post hoc* pairwise comparisons showed a significantly lower cell adhesion density ($p < 0.05$) for cells cultured in the media adjusted to pH 9.5 ($2.92\pm0.15 \times 10^3$ cells cm^{-2}) compared with cells cultured in media adjusted to pH 8.1 ($6.34\pm0.62 \times 10^3$ cells cm^{-2}), pH 8.5 ($6.86\pm0.58 \times 10^3$ cells cm^{-2}), and pH 9.0 ($7.04\pm0.90 \times 10^3$ cells cm^{-2}). The HUVEC adhesion density after the 24 hr stabilization period and before the 24 hr culture with the adjusted media (EGM-2 (t = 0)) was $3.86\pm0.09 \times 10^3$ cells cm^{-2}. The HUVEC adhesion density after the stabilization period and 24 hr incubation in EGM-2 was $4.59\pm1.33 \times 10^3$ cells cm^{-2}. Interestingly, although no statistically significant differences were confirmed, a general trend of increasing cell adhesion density with increasing transient media alkalinity up to pH 9.0 was observed. Figures 5.13d and 5.13e summarize the size and shape of adhered HUVECs as indicated by F-actin area per adhered nucleus and cell diameter aspect ratio,

respectively. No statistically significant differences were confirmed for either measurement as a function of increasing initial pH of culture media. However, the F-actin area of adhered HUVECs cultured in media adjusted to pH 9.5 had a lower mean indicating a possible correlation between reduced cell viability and size.

Figure 5.14 shows the results for HUVEC viability and morphology after 24 hr of incubation with the culture media supplemented with [Mg^{2+}] of 0 (EGM-2), 1.3, 2.6, 6.7, 13.1, 21.1, and 27.6 mM. Fluorescence images of HUVECs in all supplemented [Mg^{2+}] conditions (Figure 5.14a) showed attached and viable, and isotropically-spread cells. Figure 5.14b summarizes the [Mg^{2+}] of the culture media analyzed after 24 hr culture with HUVECs. An increasing trend of [Mg^{2+}] in the supplemented culture media was confirmed after 24 hr. Culture media without supplemental Mg^{2+} ions and incubated for 24 hr without cells (blank reference) had a [Mg^{2+}] of 10.56±0.18 mM, which is in close agreement with literature values for MCDB 131 media [43]. The formulation for EGM^{TM}-2 is proprietary, however, per the vendor, it is based on the formulation of the classical MCDB 131 media. Results of HUVEC adhesion density in the media supplemented with increasing [Mg^{2+}] after the 24 hr culture are summarized in Figure 5.14c. ANOVA was used to confirm statistically significant differences in the mean adhesion density [$F(6, 14) = 5.406$, $p = 4.427 \times 10^{-3}$). *Post hoc* pairwise comparisons did not confirm a significant reduction in adhesion density for any of the supplemented [Mg^{2+}] conditions tested. However, a significantly higher cell adhesion density was observed in the media supplemented with 2.6 mM [Mg^{2+}] ($11.45 \pm 0.78 \times 10^3$ cells

cm^{-2}) when compared with the non-supplemented media (EGM-2; $5.03\pm1.35x10^3$ cells cm^{-2}; $p < 0.001$), media supplemented with 1.3 mM [Mg^{2+}] ($5.83\pm1.13x10^3$ cells cm^{-2}; $p < 0.001$), and media supplemented with 27.6 mM [Mg^{2+}] ($6.40\pm0.78x10^3$ cells cm^{-2}; $p < 0.01$). The HUVEC adhesion density after the 24 hr stabilization period and before the 24 hr culture with the adjusted media (EGM-2 (t = 0)) was $4.91\pm1.15x10^3$ cells cm^{-2}. Figures 5.14d and 5.14e summarize the size (F-actin area per adhered nucleus) and shape (cell diameter aspect ratio) of adhered HUVECs, respectively, as a function of increasing supplemented [Mg^{2+}]. No statistically significant differences were confirmed for either measurement; however, a wider distribution of size was observed for HUVECs grown in the media supplemented with 2.6 mM [Mg^{2+}].

5.4. Discussion

The degradation of four heat-treated ZSr41 crystalline Mg alloys and their interaction with HUVECs was investigated using the direct *in vitro* culture method to model and study possible cellular modulatory effects at the HUVEC/ZSr41 alloy interface. We also examined HUVECs on the culture plate surrounding the ZSr41 alloy samples to understand modulatory effects of solubilized degradation products. Our results showed for the first time that the degradation products of Zn-containing Mg-alloys can induce an expression of VCAM-1 in cultured ECs, thus providing evidence of a transient inflammatory activation of ECs representative of the early-stages of inflammation.

5.4.1. Microstructure and degradation of ZSr41 alloys

The incremental addition of Sr to the ZSr41 alloy resulted in distinctive β-phase composition and morphology. Our results are in agreement with previous studies for age-hardened Mg-Zn-Sr alloys that showed the segregation of Zn and Sr predominantly in the precipitated phases accompanied by an α-matrix with ~4 wt. % Zn [22, 44, 45]. Brar *et al.* suggested that the intermetallic β-phases in the Mg-4Zn-0.5Sr alloy were ternary compounds of the form $Mg_xZn_ySr_z$ [44]. In contrast, Li *et al.* showed through transmission electron microscopy (TEM) analysis for the Mg-1Zn-0.8Sr alloy the presence of two distinct β-phases, namely $Mg_{17}Sr_2$ and $MgZn_2$ [45]. Similarly, previous results from our group also confirmed the presence of $Mg_{17}Sr_2$ and $MgZn_2$ in the Mg-4Zn-1Sr (ZSr41C) alloy through EDS and x-ray diffraction (XRD) analysis. Li *et al.* also suggested that the formation of the $Mg_xZn_ySr_z$ was strongly related to the Zn content in the Mg-Zn-Sr alloys. Collectively, results from these independent studies suggest a transition in β-phase composition and morphology that might be correlated to the Zn/Sr at. % from the nominal composition of the Mg-Zn-Sr alloys (e.g. 10.9 Zn/Sr at. % ratio for Mg-4Zn-0.5Sr; 1.7 Zn/Sr at. % ratio for Mg-1Zn-0.8Sr; 5.3 Zn/Sr at. % ratio for Mg-4Zn-1Sr). Critical Zn/X at. % ratios that control second phase composition have been described in detail for the Mg-Zn-Ca alloy system [25]. Although a detailed TEM analysis is required to accurately identify the composition of the β-phases in the ZSr41A-D alloys presented in this study, it is reasonable to speculate that the high Zn/Sr at. % ratio in the secondary phases of the ZSr41B and ZSr41D alloys

could correspond to the $MgZn_2$ phase while the Zn/Sr at. % close to unity observed for ZSr41A and ZSr41C could correspond to the $Mg_xZn_ySr_z$ and/or $Mg_{17}Sr_2$ phase. Detailed discussions on the evolution of the microstructure during solidification, grain size, and mechanical properties of the Mg-Zn-Sr alloy system can be found in Refs. [22, 44, 45], and a thermodynamic evaluation with phase diagrams are presented in Ref. [46].

Furthermore, an increasing β-phase volume fraction with increasing Sr content was observed for the ZSr41A-D alloys and is consistent with previous reports in literature [23]. In this systematic study, the samples were polished up to 0.25 μm polycrystalline diamond paste to show in detail that the morphology of the second phases. Our results showed that β-phase morphology transitions from finely dispersed oxygen-rich precipitates with the addition of 0.15 wt. % Sr to coarse particulates with increased volume fraction corresponding to the addition of 0.5-1.5 wt. % Sr. Previous studies investigating Mg-Zn-Sr alloys for biomedical applications pointed out that the mechanical enhancement induced by solid-solution strengthening resulting from the increasing volume fraction of the β-phases must be carefully balanced by the detrimental effects of secondary phases on corrosion resistance [44, 45]. Specifically, although the secondary phase volume fraction is generally reduced by a lower content of alloying elements, the Zn/Sr at. % ratio could play a critical role in dictating mechanical and corrosion properties of the Mg-Zn-Sr alloys. For example, Brar *et al.* and Li *et al.* showed that both yield strength (YS) and ultimate tensile strength (UTS) of Mg-Zn-Sr alloys

increased with decreasing Zn/Sr at. % ratio; Brar *et al.* observed this trend for increasing Zn content [44] while Li *et al.* observed the trend for increasing Sr content [45]. Additionally, in this study, the Zn/Sr at. % ratio also dictated composition and morphology of the distinctive β-phases, both of which are critical factors for micro-galvanic corrosion (i.e. corrosion resistance of the alloy). In fact, Brar *et al.* reported a decrease in corrosion resistance with increasing Zn/Sr at. % ratio in Hank's solution for heat-treated Mg-xZn-0.5Sr alloys [44]; likewise, Cui et al. reported an improved corrosion resistance in SBF for heat treated Mg-4Zn-xSr alloys with decreasing Zn/Sr at. % ratio [47]; and, Xia *et al.* recently reported improved corrosion resistance in 0.1 M NaCl for heat-treated Mg-1Zn-xSr alloys with decreasing Zn/Sr at. % ratio [48]. This critical ratio effect is also observed in the Mg-4Zn-xCa alloy system, where optimal mechanical (i.e. YS, UTS, elongation) and corrosion properties were achieved for Mg-Zn-Ca alloys when ~1.2 < Zn/Ca at. % < ~5 [25]. Other ternary polycrystalline Mg-Zn-X alloys investigated for biomedical applications that exhibit solution strengthening and β-phase-mediated corrosion include X = Al [33, 49-51], Ca [25, 52, 53], Yttrium [54], Zirconium [55], Mn [56, 57], Si [57], and Selenium and Copper (Cu) [58]. To highlight the significance and novelty of this study in comparison with the state-of-the-art, a thorough review on the history and current development of as-cast crystalline Mg-Zn-Sr ternary alloys is summarized in Table 5.2 [22-24, 44-48, 59].

The significantly faster *in vitro* degradation rate of ZSr41B and ZSr41D in EGM^{TM}-2 media after 24 hrs of incubation could potentially be correlated with the

high Zn/Sr at. % ratio in the β-phase of these alloys compared with ratio in the second phases of ZSr41A and ZSr41C, and the corresponding micro-galvanic corrosion formed with the α-matrix. Figure 5.15 shows a summary of the average daily degradation rate (mass loss rate) per unit area of the ZSr41 alloys in this study as a function of Zn/Sr at. %, O content, and morphology of each respective β-phase. Results from PDP measurements and Tafel extrapolation (Figure 5.3) showed that the initial corrosion response of all as-polished ZSr41 alloys in this study had similar characteristics, i.e. similar E_{corr} values and J_{corr} in the same order of magnitude for all ZSr41 alloys. Furthermore, collective results from the 4 hr time point (SEM-based qualitative assessment of the surface integrity of the samples, Figure 5.4; the surface distribution of Mg acquired through EDS, Figure 5.5; pH measurements of the media, Figure 5.10a; and [$Mg2^{+}$] in the media, Figure 5.10b) supported the conclusion that all Mg-based materials had a similar initial corrosion behavior when incubated in complete EGM^{TM}-2 media. Additionally, the pH and [Mg^{2+}] measurements indicated that the degradation of all the Mg-based materials investigated induced significant changes in the media as early as 4 hrs of incubation. Previous studies confirmed that the degradation of Mg-based materials in buffered static media caused a sharp increase in the pH after only hours of incubation [60, 61]. Analysis of the 24 hr results showed differences in surface crack density and Mg surface distribution (Figures 5.6 and 5.7) which could be the first signs of different long-term degradation behavior. Moreover, the differences in the degradation profiles at 24 hrs was observed through the linearly-correlated pH

and [Mg^{2+}] measured in the media (Figures 5.11a and 5.11b). Specifically, the significant increase in both indicators induced by the degradation of alloys ZSr41B and ZSr41D, along with the normalized results shown in Figure 5.12 are direct evidence of the faster degradation of these alloys. These results are in close agreement with a previous 72-hr evaluation of the *in vitro* degradation of ZSr41 alloys with human embryonic stem cells (hESC) in mTeSR®1 media showing both higher pH and [Mg^{2+}] for alloys ZSr41B and ZSr41D compared with ZSr41A and ZSr41C [23]. Additionally, the 24-hr degradation rates per unit surface area of the ZSr41 alloys in EGM™-2 media was in close agreement with the degradation rate per unit surface area measured during the first 24 hr interval in mTeSR®1 media despite the differences in media composition (osmolality 260-290 mOsm/kg H_2O for EGM™-2 and 330-350 mOsm/kg H_2O for mTeSR®1). Table 5.3 summarizes the ionic concentrations from the inorganic salts, ionic strength, and osmolality of MCDB 131 (non-commercial analog of EGM™-2) [43], mTeSR®1 [40], r-SBF [38], and human blood plasma [40]. Osmolality values for EGM™-2 and mTeSR®1 were obtained from technical specification sheets from the vendors, while values for human blood plasma were obtained from [62].

The solubilized [Mg^{2+}], [Zn^{2+}], and [Sr^{2+}] in the media as a result from the degradation of the ZSr41 alloys during the 24 hr incubation were below the therapeutic daily dosages (TDD) and LD50 reported in literature. The TDD and LD50 for Mg^{2+}, Zn^{2+}, and Sr^{2+} are summarized in Ref. [23]. The largest change in [Mg^{2+}] in the culture media induced by the degradation of the ZSr41 alloys in this

study was observed for ZSr41B at 24 hr (10.31 mM above the blank reference), which was well below the TDD of 24-40 mM and LD50 of 50-73 mM (multiple mammalian cell types) Specifically for ECs, Zhao *et al.* indicated that the Mg^{2+} LD50 was 30 mM [63]. Likewise, the largest change in $[Zn^{2+}]$ and $[Sr^{2+}]$ in this study were both measured at 24 hrs for ZSr41A (47.22 µM $[Zn^{2+}]$ above the blank reference) and ZSr41D (34.44 µM $[Sr^{2+}]$ above the blank reference). Thus, the $[Zn^{2+}]$ and $[Sr^{2+}]$ concentrations measured in this study at 24 hr were lower when compared with the $[Zn^{2+}]$ TDD of 900 µM and LD50 of 3.7 mM, and $[Sr^{2+}]$ TDD of 5.9 mM and LD50 of 33.8 mM.

5.4.2. HUVECs in *indirect* contact with ZSr41 alloys: viability and early inflammatory response

HUVEC adhesion density on the culture plate (*indirect* contact) up to 24 hrs was largely unaffected by the solubilized degradation products of the ZSr41 alloys indicating adequate cytocompatibility. The absence of significant differences in the adhesion densities on the culture plates surrounding the ZSr41 samples compared with each other at 4 hrs and then at 24 hrs (Figure 5.8b) indicated that HUVEC viability was unaffected by the varying degradation rates (and concomitant solubilized degradation products) of the Mg-based materials. Specifically, at 24 hrs, HUVEC adhesion density was unaffected by the significantly higher degradation rates of ZSr41B and ZSr41D. Furthermore, our results from the effects of media alkalinity and $[Mg^{2+}]$ on HUVEC viability and morphology confirmed

unaltered HUVEC responses in media “transiently-adjusted” to pH 9.0 (Figure 5.13) or supplemented with [Mg^{2+}] = 27.6 mM (Figure 5.14). It is important to highlight that in our alkalinity experiments the media was “transiently-adjusted” to pH 8.1-9.5 because the $NaHCO_3$/5% CO_2 buffer system in EGM™-2 media (and other mammalian cell culture media) can effectively buffer sharp increases in pH within minutes [64]. In the direct culture, however, the change in pH induced by the degradation of Mg-based materials is continuous and explains why the pH of the EMG™-2 media after 24 hrs of incubation with Mg-based materials (pH 8.07-8.16) is higher compared with the media “transiently-adjusted” to pH 9.5 (8.01). Taken together, these results indicated that continuous slightly-alkaline media does not seem to affect HUVEC viability or morphology as much as sharp transient alkaline changes (i.e. pH 9.5). In contrast, [Mg^{2+}] in the media from the degradation of the Mg-based materials (4.41-10.31 mM) and from the supplemented media experiment (27.6 mM) above the baseline (~10 mM) were confirmed to have no significantly detrimental effects on HUVEC viability or morphology mainly because active transport of Mg^{2+} ions across the cell membrane is tightly regulated [65]. Interestingly, in our experiments, supplementing the EGM™-2 media with a [Mg^{2+}] = 2.6 mM led to a significant increase in cell adhesion density. Zhao *et al.* also showed beneficial EC *in vitro* responses with a total 13 mM [Mg^{2+}] in the culture media (3 mM basal + 10 mM supplemented). Specifically, they reported enhanced human coronary aorta EC (HCAEC) proliferation rate for 13 mM followed by a gradual decrease up to 33 mM tested [63]. Conversely, previous *in vitro* studies

showed that Mg^{2+} ion deficiency (lower than 10 mM found in basal EGM™-2 media) inhibited HUVEC proliferation and migration [66, 67]; taken together, these *in vitro* results indicate the biphasic effects of [Mg^{2+}] in the culture media. Clinically, Mg^{2+} ion deficiency has been associated with cardiovascular conditions including atherosclerosis, hypertension and thrombosis [66, 67]. However, the *in vitro* effects of Mg^{2+} ions on cell behavior are dependent on cell type [25]; therefore, the degradation rate should be carefully engineered to maximize the benefits for each end-goal application. Collectively, results from this study that indicate more dramatic effects on cellular function induced by media alkalinity compared with [Mg^{2+}] from the degradation of Mg-based materials were in agreement with previous studies for bone marrow derived mesenchymal stromal cells (BMSCs) [25, 68], UMR-106 rat osteosarcoma [69], and hESCs [40]. Furthermore, overall cytocompatibility results of Mg-Zn-Sr alloys with HUVECs reported in this study were within acceptable agreement with previous *in vitro* studies with hESCs [23] and fibroblasts [24, 45, 59].

Transient type II EC inflammatory activation, characterized by significantly enhanced VCAM-1 expression, can be induced by solubilized heavy metal ions in the culture media. We investigated the *in vitro* induction of VCAM-1 expression in HUVECs at 4 and 24 hrs based on published literature showing that *in vitro* CAM induction by TNFα in ECs peaks 4-6 hrs after stimulation and declines to basal levels by 24 hr (refractory period) [70-72]. Previous studies showed that the transient expression of CAMs including E-selectin, intercellular adhesion

molecule-1 (ICAM-1), and VCAM-1 in cultured ECs could be induced by the exposure to non-cytotoxic concentrations of heavy metal ions. *In vitro* experiments with Ni^{2+} and Co^{2+} ion concentrations (in the form of $NiCl_2$, $NiSO_4$, $CoCl_2$, or $CoSO_4$) ranging from 0.1 to 2 mM were reported to induce the expression of all three CAMs at the mRNA and protein levels in a dose-dependent and transient manner; CAM induction by heavy metal ions was comparable to the induction by pro-inflammatory mediators such as TNFα, interleukin 1 (IL-1), and bacterial lipopolysaccharide (LPS) [1, 11-17]. Additionally, Klein *et al.* observed CAM induction by Ni^{2+} and Co^{2+} ion concentrations in the mM and nM but not µM range, suggesting a possible biphasic CAM induction response to heavy metal ions [13]. Interestingly, other Period 4 transition metal ions such as Cr^{3+} (up to 1 mM) [1, 15], Fe^{3+} [14], Mn^{2+}, and Cu^{2+} (both up to 2 mM) [12, 14] did not induce CAM expression in cultured ECs. Previous studies showed that Ni^{2+} or Co^{2+} ions activated the autoregulatory mechanism of the nuclear factor-κB/inhibitor of κB (NF-κB/IκB) system [12, 14-16], up-regulated transcription factor activator protein-1 (AP-1) [15, 16], but did not initiate a pro-inflammatory cytokine-induced autocrine stimulation [12, 14]. The ubiquitous transcription factor NF-κB, and AP-1, are key regulators of cytokine-induced pro-inflammatory proteins such as endothelial CAMs, cytokines, and growth factors among others [8, 15]. Further mechanistic studies identified the involvement of phosphorylation events of different protein kinases of two or more signaling pathways leading to the translocation of NF-κB and subsequent CAM expression [14, 16]. It was suggested that Ni^{2+} and Co^{2+}-induced

CAM expression could be a result from metal ion attachment to proteins presented to the cultured ECs [16], due to the involvement of oxygen radicals [14, 73], or due to the inhibition of the biological activity of nitric oxide [73]. More recent studies focused on the culture of ECs with bulk permanent implant materials and reported: no significant CAM expression after culture with NiTi, CoCrNi, or NiCr [17]; significant ICAM-1 and VCAM-1 expression induced by the ion release of Ti-6Al-4V alloy [18]; and significant E-selectin expression induced by the ion release of NiTi wires [19].

Early-stage inflammatory activation in HUVECs was most likely induced by the solubilized Zn^{2+} ions from the fast-degrading ZSr41D alloy, giving first *in vitro* evidence of an early-stage inflammatory response to the degradation of Zn-containing Mg-based biomaterials. Our results showed that a [Mg^{2+}] of 0.9 mM above baseline (pure Mg control; Figure 5.10b) did not induce a significant VCAM-1 expression on the cultured HUVECs at 4 hr (Figure 5.9b). Although a [Mg^{2+}] of ~1.2 mM was measured for ZSr41D and AZ31, these alloys contained other alloying elements and the effects of Mg^{2+} ions could not be deconvoluted. Since the [Mg^{2+}] released into the culture media was in a similar range compared with Ni^{2+} and Co^{2+} (µM to mM range), and since no significant VCAM-1 expression was observed at either 4 or 24 hr, it is reasonable to conclude that Mg^{2+} ions in the µM to mM range (above baseline, i.e. ~10 mM) do not transiently induce the expression of VCAM-1 on cultured HUVECs. However, previous *in vitro* studies showed that Mg^{2+} ion deficiency (i.e. below 10 mM) can induce the expression of

VCAM-1 in cultured HUVECs [66, 67]. Previous studies also showed that a supplemented [Mg^{2+}] higher than 40 mM caused discontinuities within the intercellular cell-to-cell junctions in cultured ECs [63], indicating possible mediation of EC inflammation. In fact, other studies showed that Mg^{2+} ions could attenuate the NF-κB signaling pathway [74, 75], thereby participating in multiple NF-κB-related cellular responses. Furthermore, Zn^{2+}, another Period 4 transition metal ion, released at 4 hrs (Figure 5.10c) could have been involved in the induction of VCAM-1 on HUVECs (Figure 5.9b). Previous studies showed that Zn^{2+} ions (in the form of $ZnCl_2$) induced the following responses in cultured ECs: at [Zn^{2+}] of 1-10 nM significantly increased the expression of both E-selectin and ICAM-1 after a 5 hr incubation [13]; at [Zn^{2+}] of 1 μM and 1 mM weakly induced the expression of NF-κB p65 mRNA after an 8 hr incubation [15]; and at [Zn^{2+}] of 1 mM increased the expression of E-selectin after a 5 hr incubation [13] and ICAM-1 after a 4 hr incubation [16]. Similar to Ni^{2+} and Co^{2+} ions, one mechanistic study provided evidence for the involvement of phosphorylation events of different protein kinases involved in the translocation of NF-κB and concomitant ICAM-1 induction by Zn^{2+} ions [16]. In fact, previous studies demonstrated the active role of Zn in the phosphorylation of IκB leading to the translocation of NF-κB in HUT-78 cells [76, 77]. However, other CAM-related studies also reported the inability of Zn^{2+} ions to induce the expression E-selectin, ICAM-1, or VCAM-1 after a 6 hr incubation with a [Zn^{2+}] of 2 mM [12] and no E-selectin induction by a [Zn^{2+}] of 1 mM after a 4 hr incubation [16] or 5 hr incubation [15]. A possible explanation for these seemingly

contradictory results at [Zn^{2+}] in the mM range could be due to the close proximity to the TDD and LD50 for Zn^{2+} ions. In fact, Wagner *et al.* observed that HUVEC morphology at [Zn^{2+}] of 1 mM was strongly damaged [16]. Additionally, time-dependent CAM induction [12] to Zn^{2+} ions could also lead to some of the discrepancies in published literature and should be systematically evaluated to identify distinct effects on the expression of E-selectin, ICAM-1, and VCAM-1 in cultured ECs. Although Zn^{2+} does not directly induce the formation of reactive oxygen intermediates via Fenton reaction (in contrast with Ni^{2+} and Co^{2+} [78]), varying [Zn^{2+}] has been shown to have an active role in the production of nitric oxide (NO) [79, 80] and on the activity of Zn/Cu-superoxide dismutase (SOD) [81]; both NO and Zn/Cu-SOD have also been shown to have an effect on CAM expression in cultured ECs [82, 83]. Moreover, to our knowledge, a systematic evaluation of CAM induction by Sr^{2+} ions has not been reported in literature; thus, direct effects of Sr^{2+} ions are unknown. The absence of statistically significant differences in the [Sr^{2+}] of the culture media at 4 hrs presented in this study (Figure 5.10d) indicated that the [Sr^{2+}] in the media of all groups was comparable. Specifically, the [Sr^{2+}] in the media of the negative control group for VCAM-1 expression (HUVEC group; 1.50±1.31 µM) did not show an induction of VCAM-1 expression. Therefore, it is likely that Sr^{2+} ions in the low µM range do not induce EC activation through CAM expression. Our results from VCAM-1 expression at 4 hrs indicated a significantly higher response to ZSr41D most likely due to the significantly faster degradation of ZSr41D (compared with ZSr41A and ZSr41C)

and concomitantly higher [Zn^{2+}] in the media. In terms of clinical translation, an engineered activation of ECs (and concomitant CAM expression) could help control the activation of macrophages during the distinct phases of the inflammatory response leading to dampened inflammation throughout the foreign body response and resolution stages (biological response) or the degradation of the Mg-based materials (biomaterial response) [2, 7]. Heavy metal ions including Zn^{2+}, Ni^{2+}, Co^{2+}, and Cr^{3+} were also shown to increase the activity of immune cells, e.g. polymorphonuclear neutrophil granulocytes (PMNs) [84], macrophages [85], and lymphocytes [86]. Interestingly, low concentrations of Zn^{2+} ions activated the secretion of pro-inflammatory mediators from PMNs and increased PMN-EC binding [84]. In contrast, Mg^{2+} ions did not induce detrimental immunomodulatory effects on cultured macrophages or dendritic cells [31, 32] but modulated EC/macrophage adhesion via CAM expression [66, 67]. Future studies will continue exploring the effects of Zn-containing Mg-alloys and their role in the activation of cells involved in inflammation, cardiovascular, and orthopedic applications to improve alloys design for these applications.

5.4.3. HUVECs in *direct* contact with ZSr41 alloys: cell-biomaterial interface

The dynamic interface between the degrading ZSr41 alloys and HUVECs cultured directly onto the sample surface showed signs of reduced *in vitro* cell adhesion after 24 hrs. The observed decrease in cell adhesion density for all Mg-based materials (24 hr compared with 4 hr; Figure 5.8c) gave evidence of reduced

EC growth directly on the sample surface. Our results from the effects of [Mg^{2+}] on HUVEC viability and morphology supported the conclusion that the solubilized Mg^{2+} ions were unlikely involved in the reduction of cell adhesion observed. However, the results presented in this study were unable to determine if the reduction of cell adhesion between the 4 and 24 hr intervals was due to a local increase in alkalinity, to the changing surface topography, and/or the surface composition at the cell-biomaterial interface. While a sharp increase in local alkalinity at the interface would be sufficient to reduce cell adhesion (Figure 5.13c), the drastic change in surface topography between 4 hrs and 24 hrs could have also participated in reducing cell adhesion. Comparison between the corrosion-induced cracks and elemental Mg distribution at 4 hrs (Figures 5.4a and 5.5a) and 24 hrs (Figures 5.6 and 5.7a) showed a drastic change in the surface topography. Additionally, the surface elemental composition of this *in vitro* study closely resembled the post-implantation surface reported previously for an *in vivo* study in a murine artery [87]. Previous *in vitro* studies using HUVECs and polymer-based substrates reported on the ability of surface topography in the nm [88] and μm [89] ranges to accelerate cell adhesion, and to modulate proliferation [90]. In a previous study, in which we investigated the dynamic interface between Mg-Zn-Ca alloys and BMSCs, we suggested that the changing surface topography of Mg-based materials could be heavily involved in mediating cellular responses [25]. In the Mg-Zn-Ca/BMSC study, BMSCs proliferated on the sample surface up to 72 hr. In contrast, HUVEC viability was nearly truncated on the surface of the Mg-Zn-Sr

alloys after only 24 hrs. Taken together, these observations could be indicative of: the sensitivity of HUVECs compared with BMSCs; the effect of alloying elements on cellular responses when cultured directly onto the sample surface; and/or, of the distinct alloy degradation profile in distinct cell culture media. Cardiovascular biomaterials, including Mg-based materials, for stent applications are idealized to be hemocompatible (i.e. thromboresistant and reduce platelet adhesion), promote endothelialization, reduce neointimal hyperplasia, and not have pro-inflammatory properties [91, 92]. The truncated HUVEC viability and increased platelet adhesion [24] at the cell-ZSr41 alloy interface indicated that the ZSr41 alloys (especially ZSr41D) need to be studied further to verify the applicability for cardiovascular stent applications. Previous *in vivo* and pre-clinical studies of cardiovascular stents showed the potential of Mg-based materials [91]; however, evidence of undesired neointimal hyperplasia and a desire to further reduce the degradation rate was reported in most cases. The *direct* culture method used in this study could therefore be a valuable tool in studying the *in vitro* endothelialization, smooth muscle cell responses leading to neointimal hyperplasia, and immunomodulation in order to engineer solutions for current shortcomings of Mg-based materials for cardiovascular applications.

5.5. Conclusions

This article reported on the cytocompatibility and early-stage inflammatory induction of human umbilical vein endothelial cells in response to the degradation

of four Mg-4Zn-xSr alloys (x = 0.15, 0.5, 1.0, 1.5 wt. %; designated as ZSr41A, B, C, and D respectively) in the direct culture *in vitro*. Possible factors and mechanisms that affect cellular responses were also investigated. The following major conclusions were drawn from the present study:

1. Addition of 0.5 or 1.5 wt. % Sr to the heat-treated Mg-4Zn-xSr alloys resulted in a Zn-enriched coarse β-phase (Zn/Sr at. % ~1.5). In contrast, addition of 0.15 or 1.0 wt. % resulted in a β-phase with a Zn/Sr at. % < 1; however, the β-phase morphology in the Mg-4Zn-0.15Sr alloy consisted of finely dispersed precipitates while the Mg-4Zn-1.0Sr alloy had coarse precipitates. Furthermore, an increasing β-phase volume fraction with increasing Sr content was observed. Given that the *in vitro* degradation of the Mg-4Zn-0.5Sr and Mg-4Zn-1.5Sr alloys was significantly higher compared with the other two Mg-4Zn-xSr alloys in this study, it was suggested that the Zn/Sr at. % ratio could play a critical role in dictating corrosion, and perhaps mechanical, properties of the Mg-Zn-Sr alloys.

2. HUVEC adhesion density on the culture plate (*indirect* contact) up to 24 hrs was largely unaffected by the solubilized degradation products of the Mg-4Zn-xSr alloys indicating adequate cytocompatibility. Results from this study also indicated that HUVEC viability is not negatively impacted when cultured in media with pH up to 9.0 or in media with supplemented [Mg^{2+}] up to 27.6 mM (maximum tested for [Mg^{2+}]).

3. Solubilized Zn^{2+} ions (in a non-cytotoxic range) resulting from the significantly faster degradation of Mg-4Zn-1.5Sr alloy likely induced a significantly higher VCAM-1 expression on HUVECs in *indirect* contact with the samples. Effects on VCAM-1 induction were comparable to the effects of pro-inflammatory cytokine TNFα, thereby providing first evidence of an early-stage inflammatory response to the degradation of Zn-containing Mg-based biomaterials.

4. The dynamic interface between the degrading Mg-4Zn-xSr alloys and HUVECs cultured *directly* onto the sample surface showed reduced *in vitro* cell adhesion after 24 hrs. However, the results presented in this study were unable to determine if the reduction of cell adhesion was due to a local increase in alkalinity, to the changing surface topography, and/or the surface composition at the cell-biomaterial interface.

5. The *direct* culture method used in this study is proposed as a valuable tool in studying *in vitro* design aspects of Mg-based cardiovascular biomaterials such as: endothelialization, smooth muscle cell responses leading to neointimal hyperplasia, and immunomodulation in order to engineer solutions for current shortcomings of Mg-based materials for cardiovascular applications.

5.6. Figures and tables

Figure 5.1: Microstructural analyses of ZSr41 alloys.
(a) SEM images of ZSr41A-D alloys, commercial pure Mg (control), and commercial AZ31 alloy (reference). Scale bar = 50 µm for all images. Original magnification: 600x. Insets in (a) are SEM images of the secondary phases respective to each alloy at a high magnification of 5,000x. Scale bar = 10 µm for all insets. (b) Surface elemental composition (wt. %) quantified through EDS area analysis on (a) at 600x magnification. Points 1-8 represent locations for the EDS point analyses for which results are shown in Figure 2.

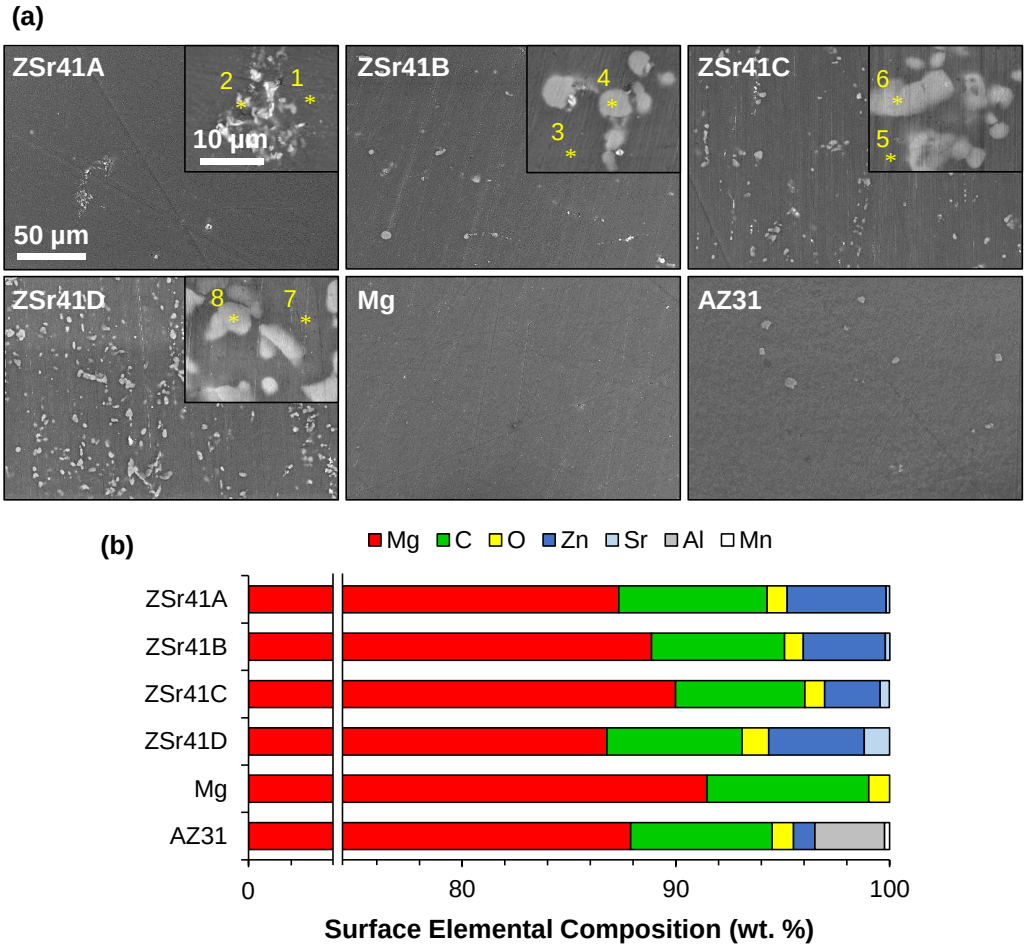

Figure 5.2: EDS analyses of the primary and secondary phases of ZSr41 alloys, including (a,c) EDS spectra and (b,d) quantification of elemental composition (at. %).

(a) and (b): EDS analyses of points 1, 3, 5, and 7 at the α-matrices of ZSr41A-D in Figure 1a; (c) and (d): EDS analyses of points 2, 4, 6, and 8 at the intermetallic β-phases in ZSr41A-D in Figure 1a.

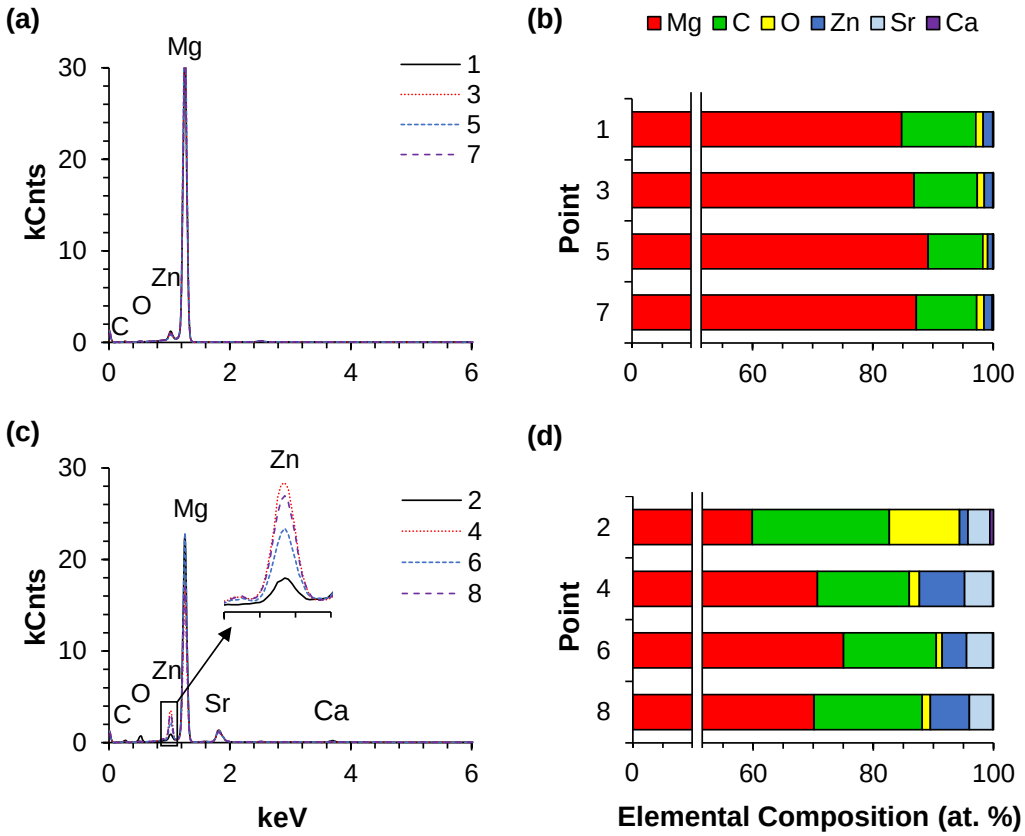

Figure 5.3: Electrochemical testing results of ZSr41 alloys, pure Mg control, and AZ31 reference.
(a) potentiodynamic polarization curves of the polished Mg-based samples at 37°C using r-SBF as the electrolyte; and (b) corrosion potential and corrosion current density of ZSr41 alloys, pure Mg, and AZ31 obtained from Tafel extrapolation (ASTM G102-89) of potentiodynamic polarization curves; values are mean ± SD, n = 3, $^{**}p < 0.01$, $^{***}p < 0.001$.

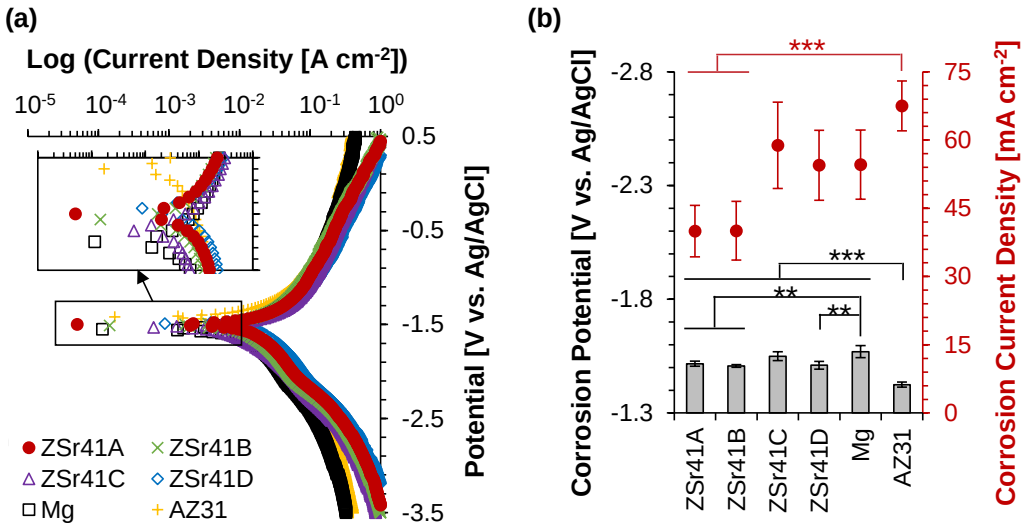

Figure 5.4: Human umbilical vein endothelial cells (HUVECs) in direct contact with ZSr41 alloy surface after 4 hrs of direct culture in EGM™-2 media.
(a) SEM micrographs of ZSr41 alloys, pure Mg (control), and reference materials (AZ31 alloy, NiTi, PLGA, and glass, respectively). Original magnification: 150x; scale bar = 200 μm for all images. Insets in (a) were taken at 1,000x original magnification with scale bar = 20 μm for all images. (b) SEM-EDS composite image of the ZSr41 alloys, Mg control, and AZ31 reference at 1,000x magnification. The color mapping in each image represents surface elemental distribution measured by EDS (red = Mg, green = C, yellow = O, pink = K, Na, orange = P, purple = Ca, blue = Zn, white = Sr). Scale bar = 25 μm for all images.

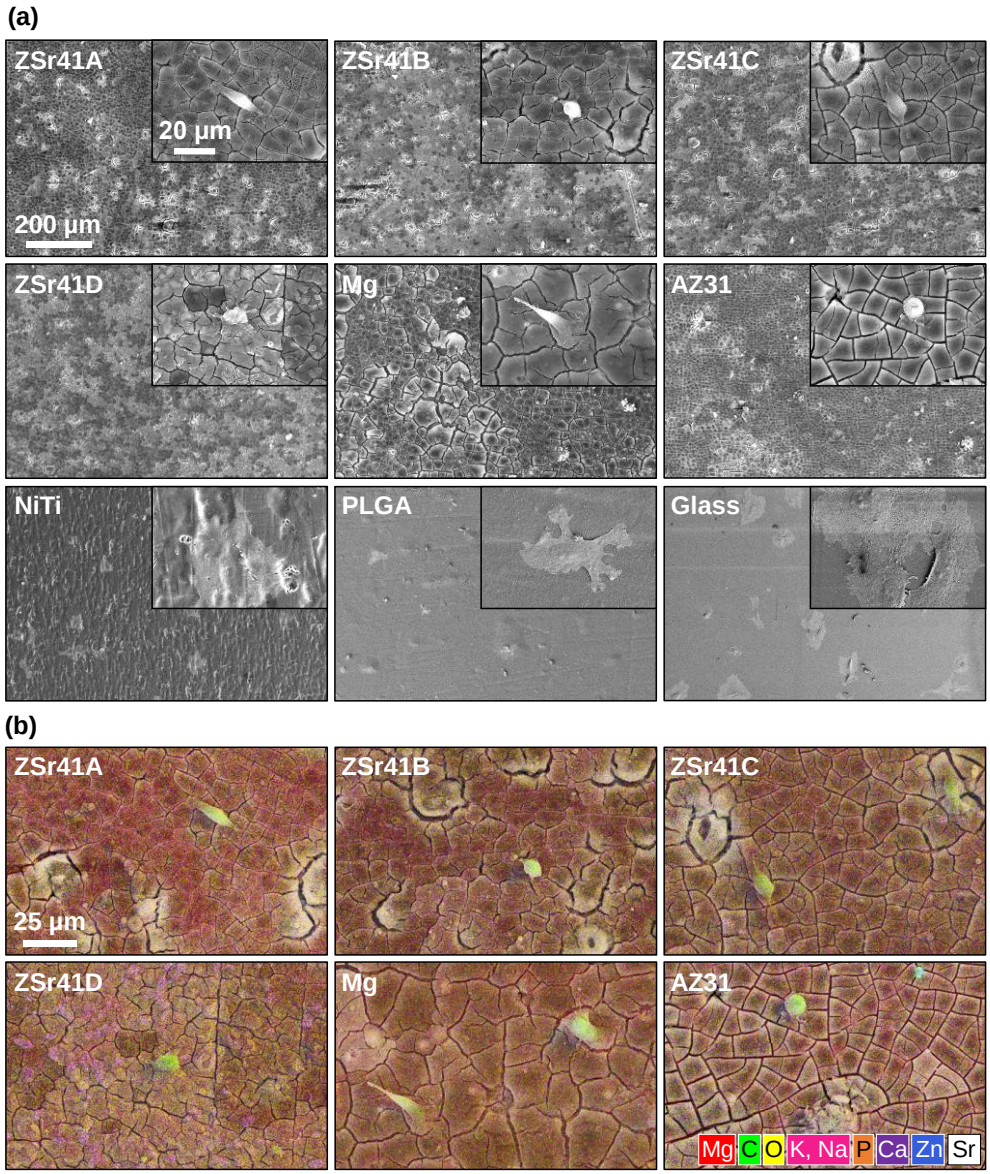

Figure 5.5: Surface characterization of Mg-based materials: (a) EDS elemental distribution map of Mg Kα1 lines of ZSr41 alloys (A-D), pure Mg (control), and AZ31 alloy (reference), respectively, after 4 hr direct culture with HUVECs in EGM™-2 media.

Original magnification: 150x; scale bar = 200 μm for all images. (b) Surface elemental composition (wt. %) based on EDS quantification on 150x images of Mg-based materials, NiTi, PLGA, and glass.

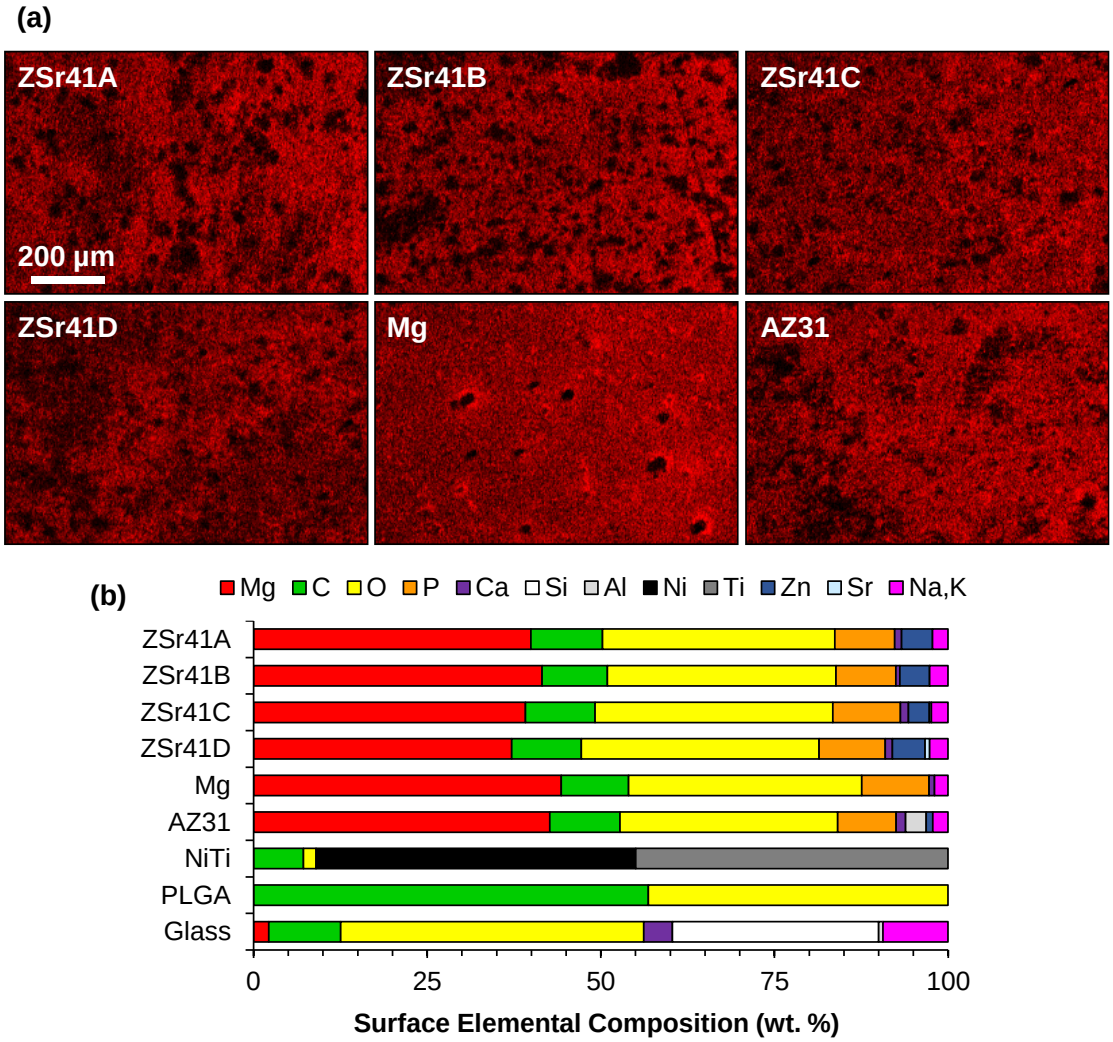

Figure 5.6: HUVECs in direct contact with ZSr41 alloy surface after 24 hrs of direct culture in EGM™-2 media.

SEM micrographs of ZSr41 alloys, pure Mg (control), and reference materials (AZ31 alloy, NiTi, PLGA, and glass, respectively). Original magnification: 150x; scale bar = 200 μm for all images. Insets in were taken at 1,000x original magnification with scale bar = 20 μm for all images.

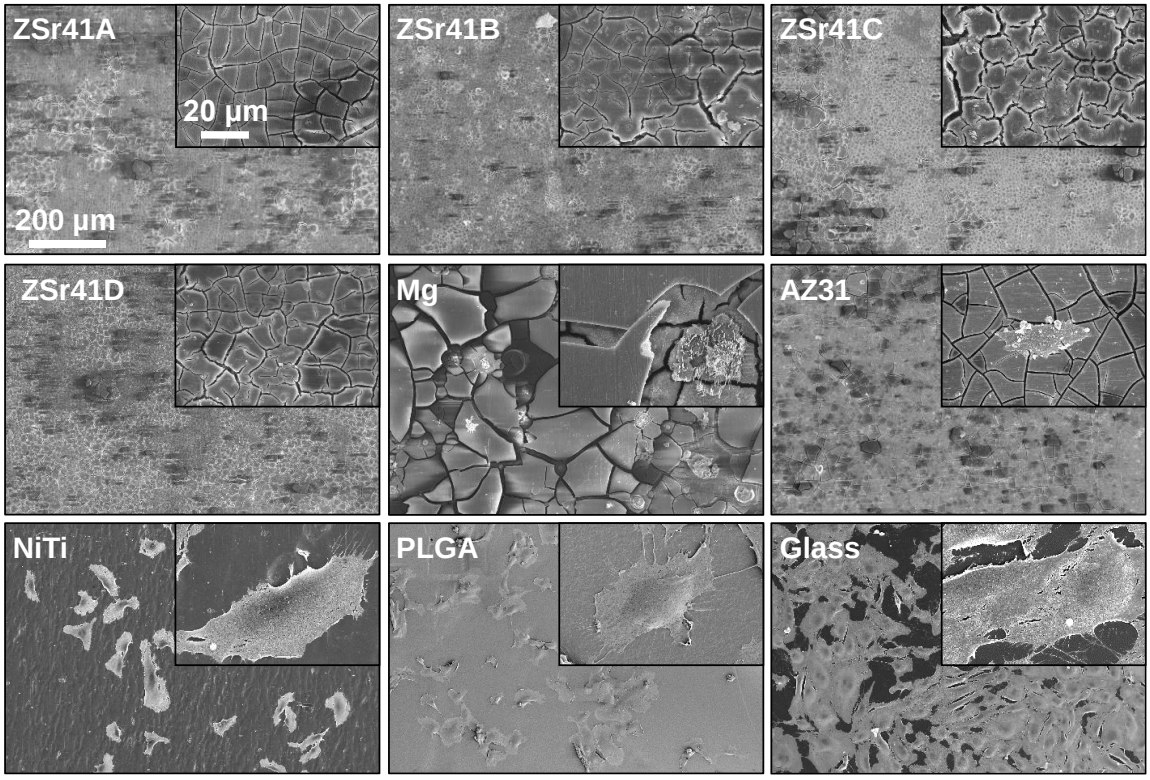

Figure 5.7: Surface characterization of Mg-based materials: (a) EDS elemental distribution map of Mg Kα1 lines of ZSr41 alloys (A-D), pure Mg (control), and AZ31 alloy (reference), respectively, after 24 hr direct culture with HUVECs in EGM™-2 media.

Original magnification: 150x; scale bar = 200 μm for all images. (b) Surface elemental composition (wt. %) based on EDS quantification on 150x images of Mg-based materials, NiTi, PLGA, and glass.

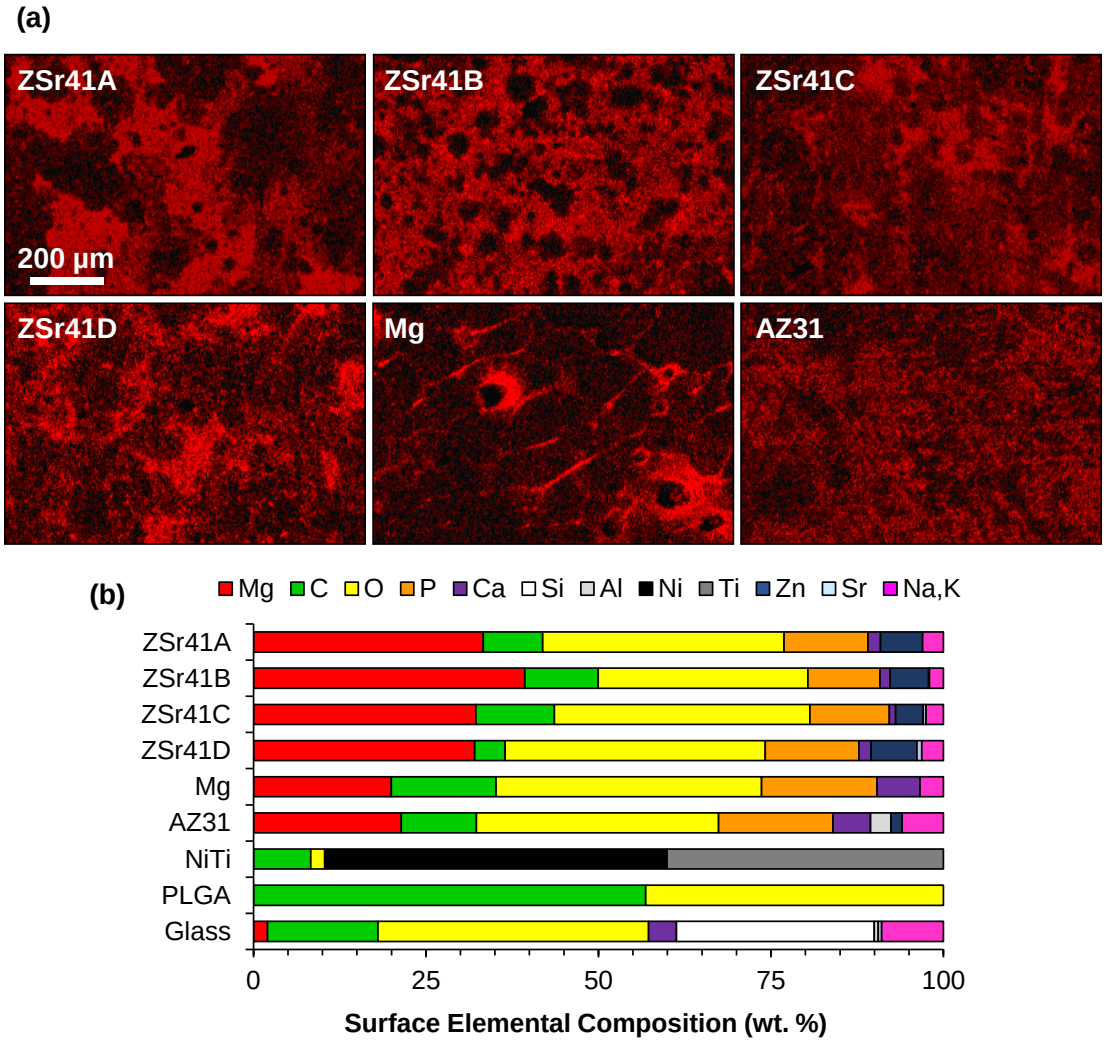

Figure 5.8: HUVEC adhesion at 4 and 24 hr direct culture on ZSr41 alloys (A-D), pure Mg control, reference materials (AZ31 alloy, NiTi, PLGA, and glass), cells only supplemented with 10 ng/mL TNFα, and cells only control.
(a) representative fluorescence images of adhered HUVECs at 24 hr on the tissue culture plates, (b) adhesion density on the culture plate surrounding each corresponding sample (indirect contact with the sample), and (c) adhesion density on the sample surface (direct contact with the sample). Values are mean ± standard error of the means, n = 3; *$p < 0.05$.

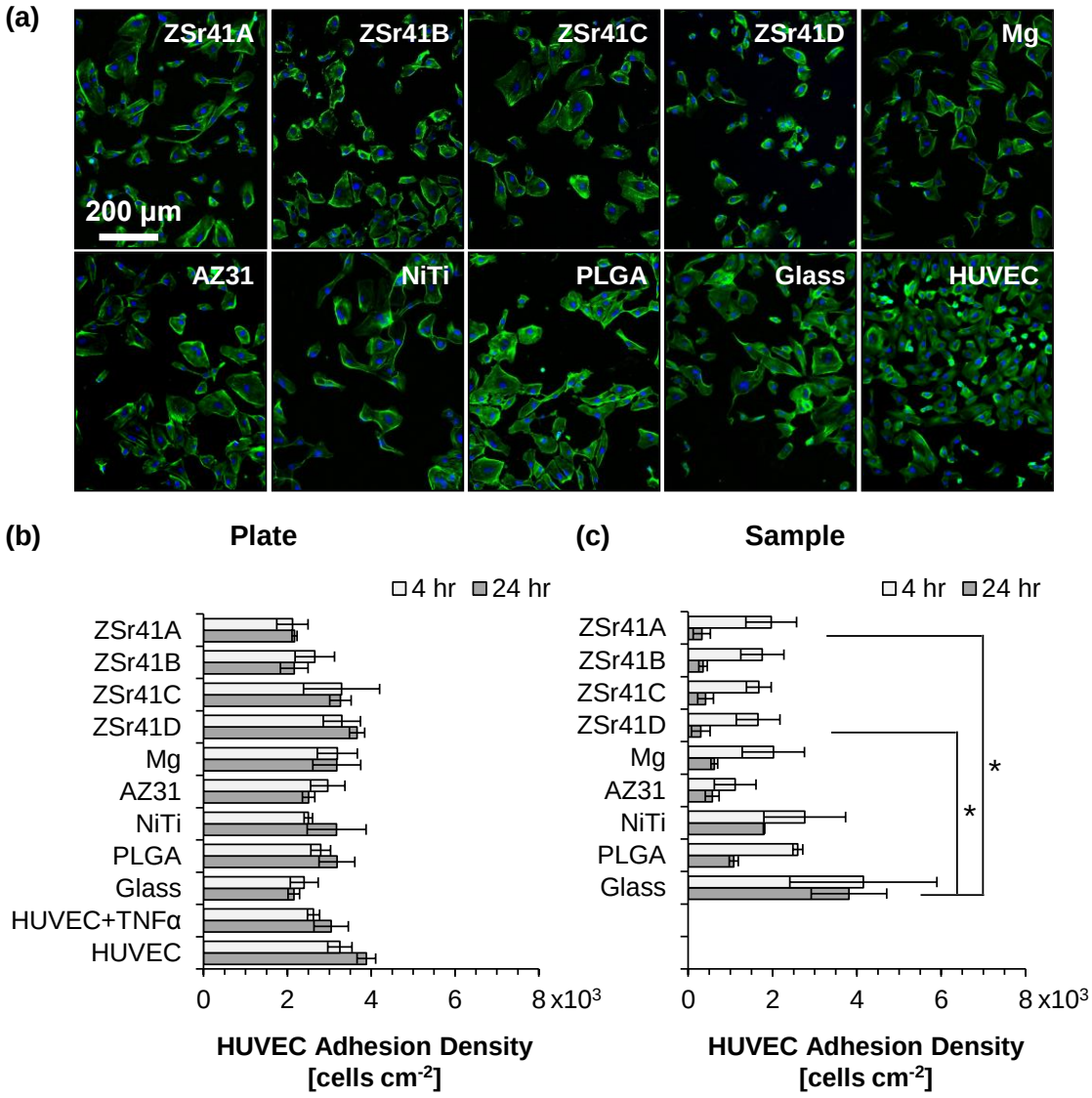

Figure 5.9: HUVEC responses at 4 and 24 hr direct cultures with ZSr41 alloys (A-D), pure Mg control, reference materials (AZ31 alloy, NiTi, PLGA, and glass), cells only supplemented with 10 ng/mL TNFα (positive control), and cells only (negative control).

(a) Fluorescence images of adhered HUVECs at 4 hr culture. Blue color indicates DAPI stained nuclei and green color indicates FITC-labeled VCAM-1. Scale bar = 50 μm for all images. (b) Quantification of VCAM-1 mean fluorescence intensity signal per pixel at 4 hr culture. (c) Quantification of VCAM-1 mean fluorescence intensity signal per pixel at 24 hr culture. All results only for cells adhered on the culture plate surrounding the samples. Values are mean ± SEM, n = 3, *$p < 0.05$ and **$p < 0.01$.

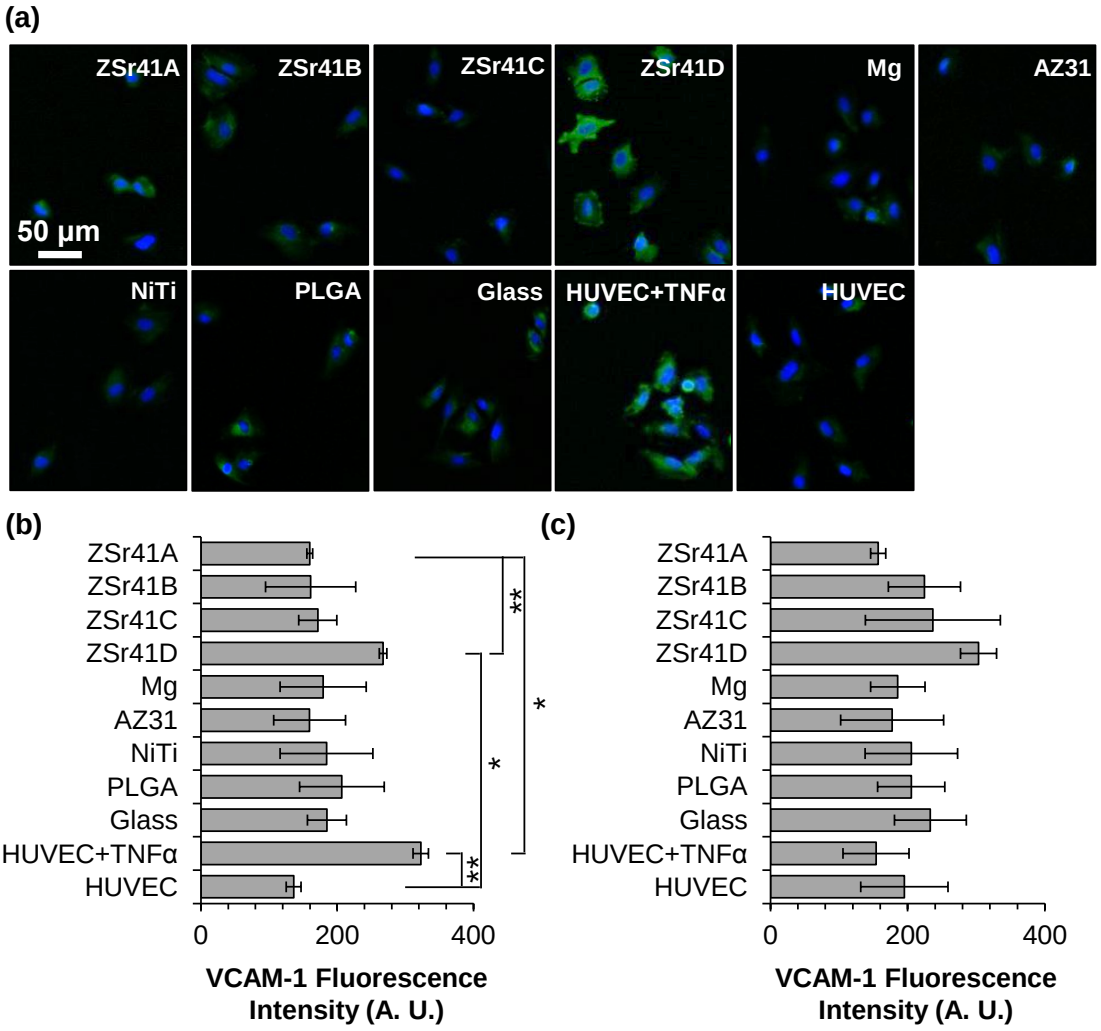

Figure 5.10: Analysis of solubilized degradation products in culture media at 4 hr direct culture with ZSr41 alloys (A-D), pure Mg control, reference materials (AZ31 alloy, NiTi, PLGA, and glass), cells only supplemented with 10 ng/mL TNFα, cells only, and blank EGM™-2 media.

(a) pH of media, (b) Mg^{2+} ion concentration, (c) Zn^{2+} ion concentration, and (d) Sr^{2+} ion concentration. Values are mean ± SD, n = 3. *p < 0.05, **p < 0.01, ***p < 0.001.

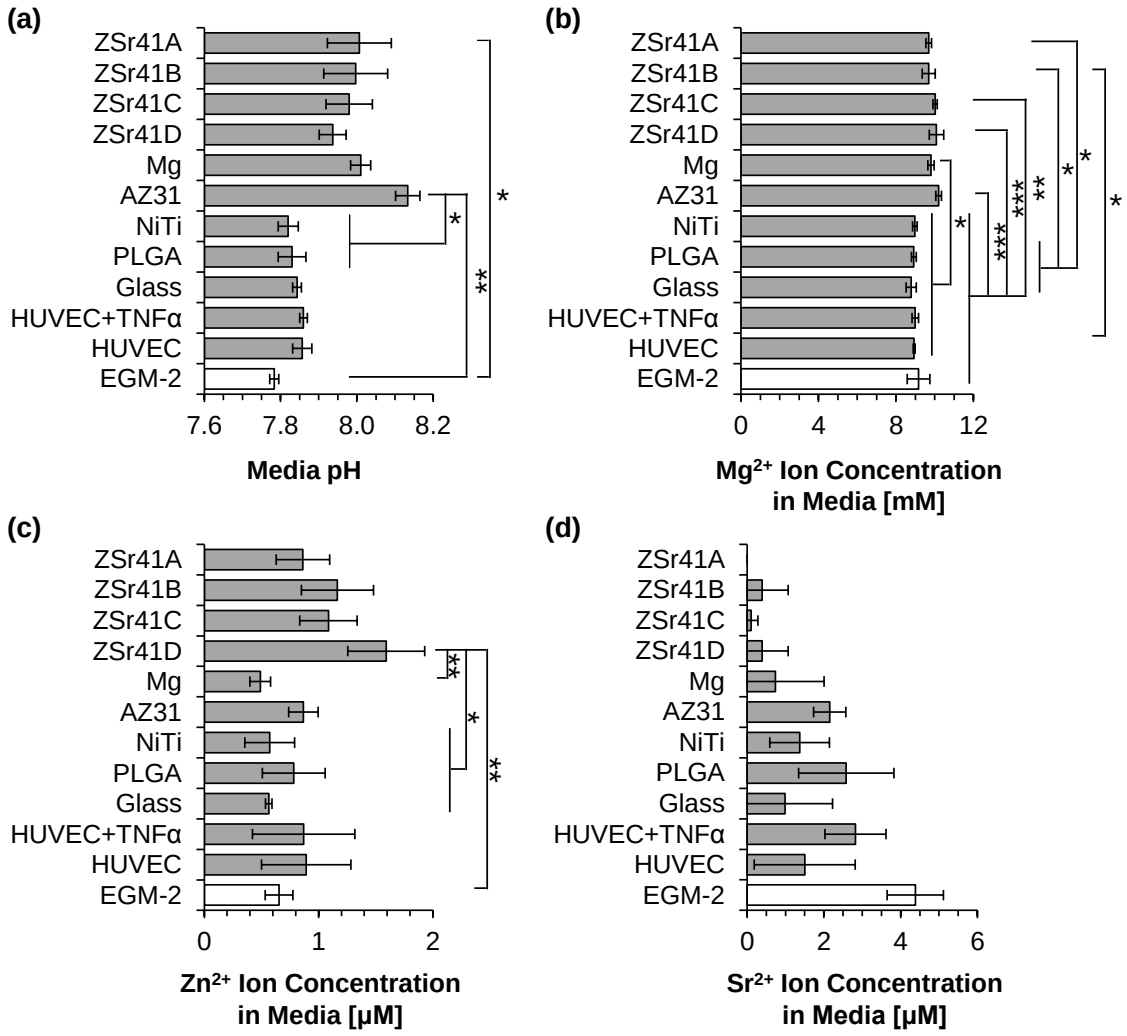

Figure 5.11: Analysis of solubilized degradation products in culture media at 24 hr direct culture with ZSr41 alloys (A-D), pure Mg control, reference materials (AZ31 alloy, NiTi, PLGA, and glass), cells only supplemented with 10 ng/mL TNFα, cells only, and blank EGM™-2 media.

(a) pH of media, (b) Mg^{2+} ion concentration, (c) Zn^{2+} ion concentration, and (d) Sr^{2+} ion concentration. Values are mean ± SD, n = 3. *$p < 0.05$, **$p < 0.01$, ***$p < 0.001$.

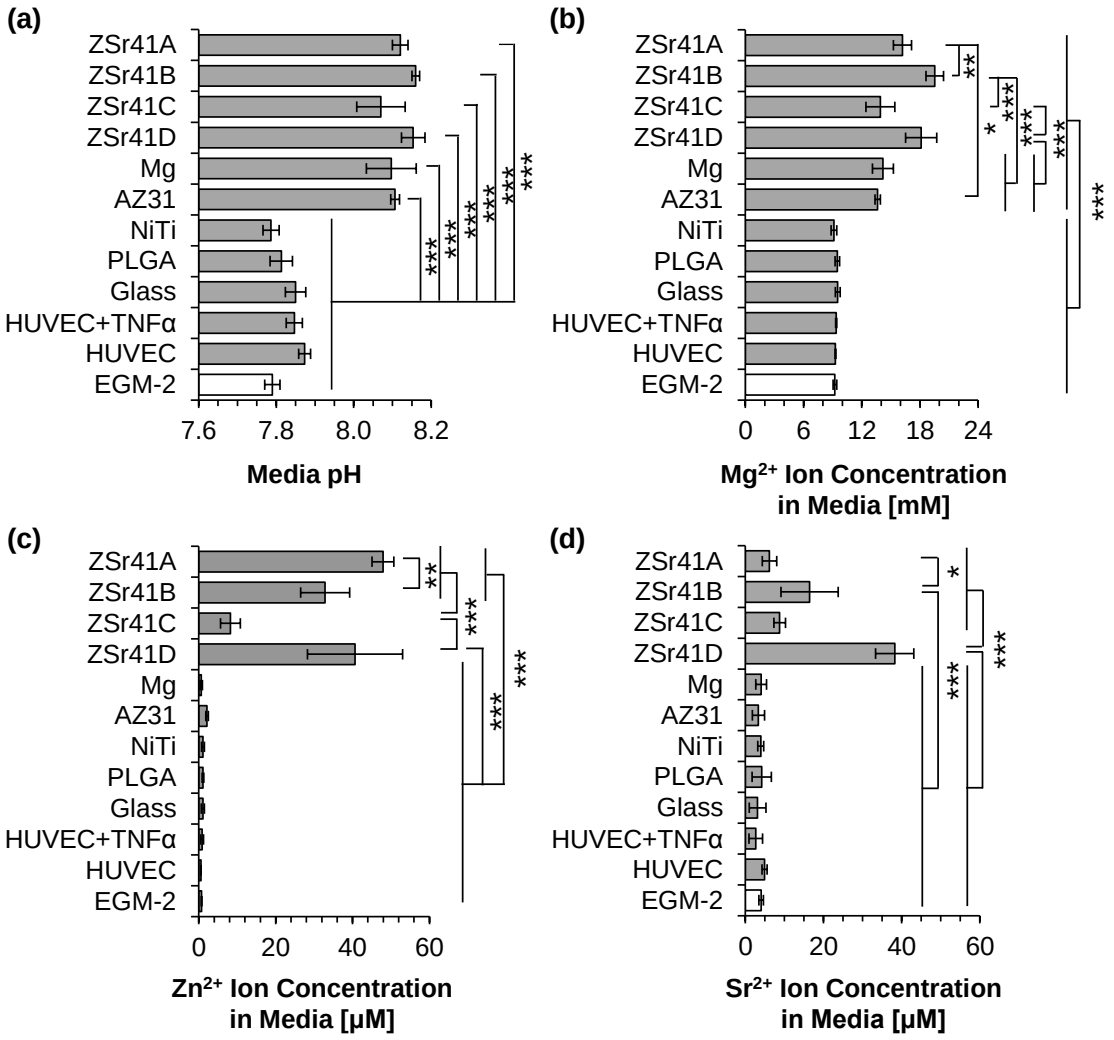

Figure 5.12: Average daily degradation rate (mass loss rate) per unit surface area of ZSr41 alloys, pure Mg control, and AZ31 reference in EGM^{TM}-2 culture media during 24 hrs of incubation.
Values are mean ± SD, n = 3; *p < 0.05.

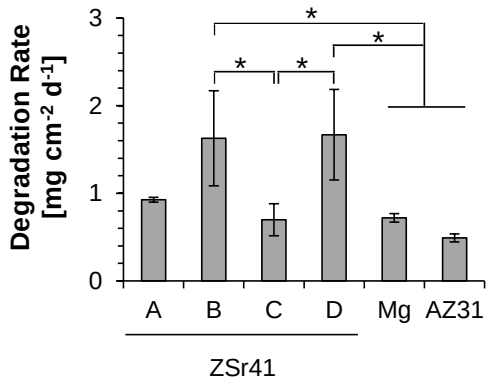

Figure 5.13: HUVEC behaviors after 24 hr of incubation in complete EGM™-2 media with initial pH values intentionally adjusted to 8.1 – 9.5.
(a) Fluorescence images of HUVECs. Blue color indicates DAPI stained nuclei and green color indicates Alexa Fluor® 488 stained F-actin (cytoskeleton). Scale bar = 200 µm for all images. Original magnification: 10x. (b) Measured pH of culture media after 24 hr incubation with HUVECs. Blank indicates media without cells. EGM-2 indicates non-adjusted media. (c) HUVEC adhesion density on culture plates. EGM-2 (t=0) represents HUVEC adhesion density after 24 hr pre-incubation for cell stabilization prior to incubation with alkaline media. (d) F-actin area per adhered HUVEC nucleus. (e) Cell diameter aspect ratio (D_{max}/D_{min}). Values in (b) are mean ± SD, and (c) – (e) are mean ± standard error of the means; n = 3 for all measurements; **p* < 0.05.

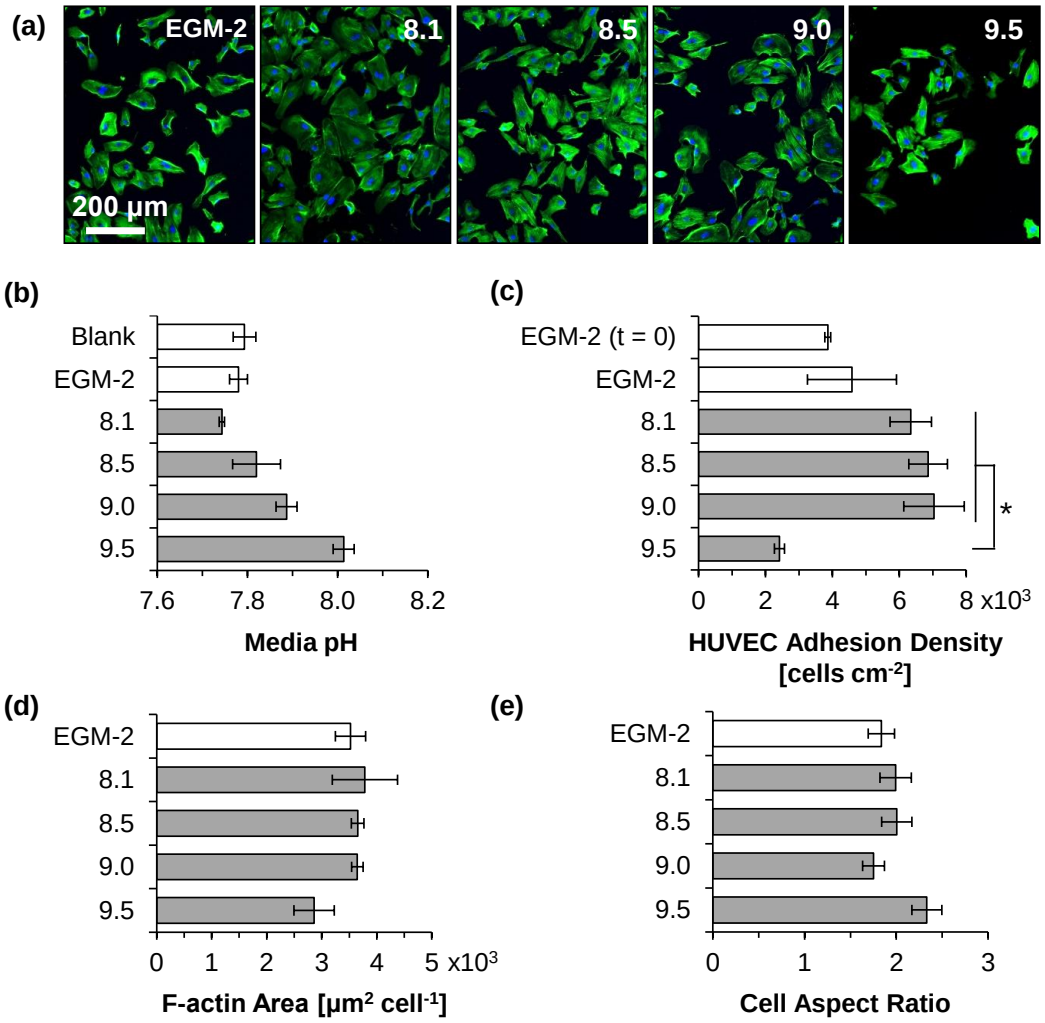

Figure 5.14: HUVEC behaviors after 24 hr of incubation in complete EGM™-2 media supplemented with Mg^{2+} concentration of 0 - 27.6 mM initially.
(a) Fluorescence images of HUVECs. Blue color indicates DAPI stained nuclei and green color indicates Alexa Fluor® 488 stained F-actin (cytoskeleton). Scale bar = 200 µm for all images. Original magnification: 10x. (b) Measured Mg^{2+} ion concentration in culture media after 24 hr of incubation with HUVECs. Blank indicates media without cells. EGM-2 indicates non-adjusted media. (c) HUVEC adhesion density on culture plates. EGM-2 (t=0) represents HUVEC adhesion density after 24 hr pre-incubation for cell stabilization prior to incubation with alkaline media. (d) F-actin area per adhered HUVEC nucleus. (e) Cell diameter aspect ratio (D_{max}/D_{min}). Values in (b) are mean ± SD, and (c) – (e) are mean ± standard error of the means; n = 3 for all measurements; *$p < 0.05$, ***$p < 0.001$.

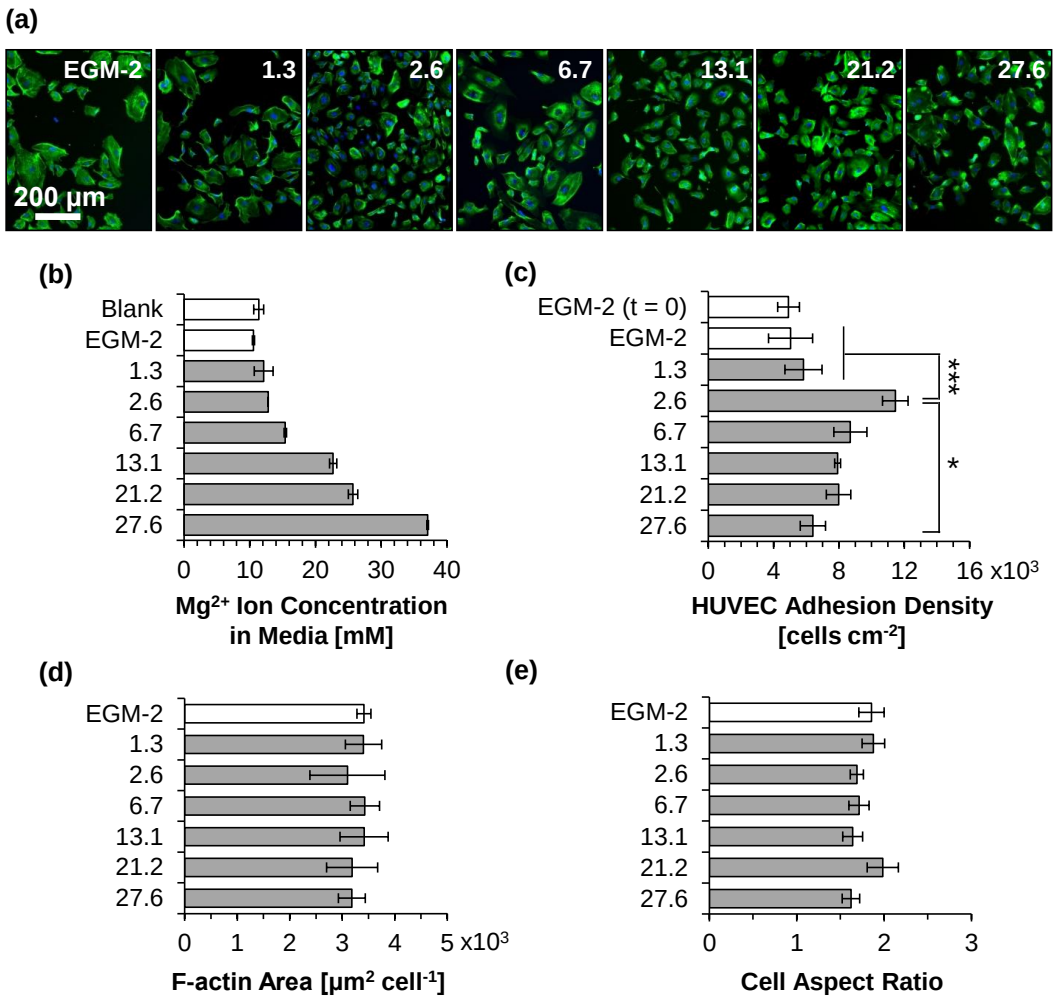

Figure 5.15: Summary of the average daily degradation rate (mass loss rate) per unit surface area in EGM™-2 media of the Mg-based materials in this study and critical Zn/Sr at. % ratios that affect β-phase formation and corrosion resistance of ZSr41 alloys.

Scale bar in SEM micrographs = 10 µm. Numbers in parenthesis indicate elemental O content (at. %) in the β-phase of each ZSr41 alloy. Degradation values are mean ± SD, n = 3; *p < 0.05.

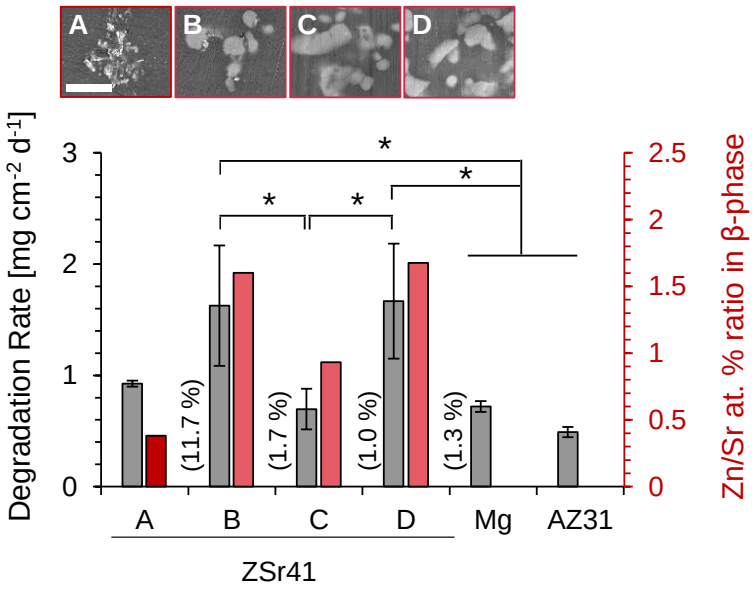

Table 5.1: Quantification of surface elemental composition (at. %) from EDS analysis of points 1, 3, 5, and 7 (i.e., intermetallic phases in ZSr41A-D, respectively) and corresponding Zn/Sr at. % ratio.

Point (Alloy)	Mg	C	O	Zn	Sr	Ca	Zn/Sr
1 (ZSr41A)	59.9	22.8	11.7	1.4	3.6	0.6	0.4
3 (ZSr41B)	70.7	15.3	1.7	7.5	4.7	0.1	1.6
5 (ZSr41C)	75.1	15.4	1.0	4.1	4.4	0.1	0.9
7 (ZSr41D)	70.2	18.0	1.3	6.5	3.9	0.1	1.7

Table 5.2: Timeline of the development of as-cast crystalline Mg-Zn-Sr ternary alloys up-to-date.
Remarks summarize the key information of interest from the reported literature. Note: "Alloy design" articles typically included microstructure, crystallinity, and/or results on mechanical properties. "Bio-corrosion/Corrosion" articles typically included alloy design, and electrochemical/immersion results; and "Cell Studies" articles typically included alloy design, bio-corrosion, and cell culture results. Values obtained from Refs. [22-24, 44-48, 59].

Year	Ref	Zn Content (wt. %)	Sr Content (wt. %)	Zn/Sr at. % ratio	Type of Article	*In vitro* cellular assays	Remarks
2007	[46]	All	All	All	Alloy design	-	First to provide a thermodynamic assessment and phase diagram.
2012	[44]	2	0.5	5.36	Bio-Corrosion	-	First to systematically assess the bio-corrosion properties *in vitro* (Hank's solution for 8 days).
		4	0.5	10.72			
		6	0.5	16.08			
2013	[22]	4	1	5.36	Bio-Corrosion	-	First to report bio-corrosion properties *in vitro* in simulated body fluid (SBF for 15 days).
2013	[47]	4	0.5	10.72	Bio-Corrosion	-	First to report systematic evaluation of bio-corrosion properties *in vitro* in simulated body fluid (SBF for 17 days).
		4	1.5	3.57			
2013	[23]	4	0.15	35.74	Cell Studies	Cytocompatibility	First to evaluate Mg-Zn-Sr alloy cytocompatibility which was evaluated using the direct culture with human embryonic stem cells.
		4	0.5	10.72			
		4	1	5.36			
		4	1.5	3.57			
2014	[45]	1	0.2	6.70	Cell Studies	Cytocompatibility	First to process alloys via zone purification and backward extrusion. Cytocompatibility was assessed using the extract-based method with L929 fibroblasts.
		1	0.5	2.68			
		1	0.8	1.68			
		1	1	1.34			
2014	[48]	0.4	0.05	10.72	Corrosion	-	First to provide optimization of alloy corrosion resistance for structural applications.
		1	0.05	26.80			
		1	0.1	13.40			
2014	[59]	N/A	N/A	N/A	Cell Studies	Cytocompatibility Hemocompatibility Anti-bacterial	First to evaluate alloy hemocompatibility and anti-bacterial efficacy.
2015	[24]	4	0.15	35.74	Cell Studies	Cytocompatibility Hemocompatibility	First to evaluate and compare alloy degradation in whole blood vs. plasma fraction of blood.
		4	0.5	10.72			
		4	1	5.36			
		4	1.5	3.57			
2015	Present Study	4	0.15	35.74	Cell Studies	Cytocompatibility Inflammatory response	First to evaluate cytocompatibility with HUVECs in the direct culture and in vitro inflammatory response via VCAM-1 expression.
		4	0.5	10.72			
		4	1	5.36			
		4	1.5	3.57			

Table 5.3: Ionic concentrations (mM) from inorganic salts in MCDB 131 (non-commercial analog of EGM™-2), mTeSR®1, and r-SBF in comparison with human blood plasma.
Compiled from Refs. [38, 40, 43, 62].
[a] Osmolality values reported with the presence of organic species and buffers.
[b] Osmolality for EGM™-2 media from technical specification sheet. Lonza Cat# CC-3162.
[c] Osmolality for mTeSR®1 media from technical specification sheet. Stem Cell Tech, Cat# 85850.

	MCDB 131	mTeSR®1	r-SBF	Plasma
Na^+	124.5	113.74	142	142
K^+	4	3.26	5	5
Mg^{2+}	10	0.56	1.5	1.5
Li^{2+}	-	0.98	-	-
Ca^{2+}	1.6	0.82	2.5	2.5
Fe^{3+}	0.001	-	-	-
Cl^-	117.2	100.96	103	103
HCO_3^-	14	18	27	27
$H_2PO_4^-$	0.5	0.36	-	-
HPO_4^{2-}	-	0.39	1	1
SO_4^{2-}	10	0.32	0.5	0.5
Ionic Strength	0.173	0.123	0.150	0.150
Osmolality (mOsm/kg H_2O)[a]	260-290[b]	330-350[c]		290

5.7. References

[1] Kirkpatrick CJ, Krump-Konvalinkova V, Unger RE, Bittinger F, Otto M, Peters K. Tissue response and biomaterial integration: the efficacy of in vitro methods. Biomol Eng. 2002;19:211-7.

[2] Franz S, Rammelt S, Scharnweber D, Simon JC. Immune responses to implants – A review of the implications for the design of immunomodulatory biomaterials. Biomaterials. 2011;32:6692-709.

[3] Staiger MP, Pietak AM, Huadmai J, Dias G. Magnesium and its alloys as orthopedic biomaterials: A review. Biomaterials. 2006;27:1728-34.

[4] Belt Hvd, Neut D, Schenk W, Horn JRv, Mei HCvd, Busscher HJ. Infection of orthopedic implants and the use of antibiotic-loaded bone cements: A review. Acta Orthop. 2001;72:557-71.

[5] Jiang Y, Jia T, Wooley PH, Yang S-Y. Current research in the pathogenesis of aseptic implant loosening associated with particulate wear debris. Acta Orthop Belg. 2013;79:1-9.

[6] Anderson JM. Chapter 4 Mechanisms of inflammation and infection with implanted devices. Cardiovasc Pathol. 1993;2:33-41.

[7] Anderson JM, Rodriguez A, Chang DT. Foreign body reaction to biomaterials. Semin Immunol. 2008;20:86-100.

[8] Pober JS, Sessa WC. Evolving functions of endothelial cells in inflammation. Nat Rev Immunol. 2007;7:803-15.

[9] Cook-Mills JM, Marchese ME, Abdala-Valencia H. Vascular Cell Adhesion Molecule-1 Expression and Signaling During Disease: Regulation by Reactive Oxygen Species and Antioxidants. Antioxid Redox Sign. 2010;15:1607-38.

[10] Sobieszczanska B, Wawrzynska M, BiaLy D. Chapter 12 Immunological Response of Electrostatic Charge at the Surface of Biomaterials. In: Tofail S, editor. Biological Interactions with Surface Charge in Biomaterials. London: The Royal Society of Chemistry; 2012. p. 161-71.

[11] Wildner O, Lipkow T, Knop J. Increased expression of ICAM-1, E-selectin, and VCAM-1 by cultured human endothelial cells upon exposure to haptens. Exp Dermatol. 1992;1:191-8.

[12] Goebeler M, Meinardus-Hager G, Roth J, Goerdt S, Sorg C. Nickel Chloride and Cobalt Chloride, Two Common Contact Sensitizers, Directly Induce Expression of Intercellular Adhesion Molecule-1 (ICAM-1), Vascular Cell Adhesion Molecule-1 (VCAM-1), and Endothelial Leukocyte Adhesion Molecule (ELAM-1) by Endothelial Cells. J Investig Dermatol. 1993;100:759-65.

[13] Klein CL, Nieder P, Wagner M, Köhler H, Bittinger F, Kirkpatrick CJ, et al. The role of metal corrosion in inflammatory processes: induction of adhesion molecules by heavy metal ions. J Mater Sci Mater Med. 1994;5:798-807.

[14] Goebeler M, Roth J, Bröcker EB, Sorg C, Schulze-Osthoff K. Activation of nuclear factor-kappa B and gene expression in human endothelial cells by the common haptens nickel and cobalt. J Immunol. 1995;155:2459-67.

[15] Wagner M, Klein CL, Kleinert H, Euchenhofer C, Förstermann U, Kirkpatrick CJ. Heavy Metal Ion Induction of Adhesion Molecules and Cytokines in Human Endothelial Cells: The Role of NF-κB, IκB-α and AP-1. Pathobiology. 1997;65:241-52.

[16] Wagner M, Klein CL, van Kooten TG, Kirkpatrick CJ. Mechanisms of cell activation by heavy metal ions. J Biomed Mater Res. 1998;42:443-52.

[17] Messer RLW, Wataha JC, Lewis JB, Lockwood PE, Caughman GB, Tseng W-Y. Effect of Vascular Stent Alloys on Expression of Cellular Adhesion Molecules by Endothelial Cells. J Long Term Eff Med Implants. 2005;15:39-48.

[18] Martinesi M, Bruni S, Stio M, Treves C, Borgioli F. In vitro interaction between surface-treated Ti-6Al-4V titanium alloy and human peripheral blood mononuclear cells. J Biomed Mater Res, A. 2005;74A:197-207.

[19] McLucas E, Rochev Y, Carroll WM, Smith TJ. Analysis of the effects of surface treatments on nickel release from nitinol wires and their impact on candidate gene expression in endothelial cells. J Mater Sci Mater Med. 2008;19:975-80.

[20] Cybulsky MI, Iiyama K, Li H, Zhu S, Chen M, Iiyama M, et al. A major role for VCAM-1, but not ICAM-1, in early atherosclerosis. J Clin Invest. 2001;107:1255-62.

[21] Bayata S, Arikan E, Yesil M, Postaci N, Tas A, Koseoglu M. An important role for VCAM-1, but not for ICAM-1 in restenosis following coronary implantation. Anadolu Kardiyol Derg. 2010;10:405-9.

[22] Guan RG, Cipriano AF, Zhao ZY, Lock J, Tie D, Zhao T, et al. Development and Evaluation of a Magnesium-Zinc-Strontium Alloy for Biomedical Applications – Alloy Processing, Microstructure, Mechanical Properties, and Biodegradation. Mater Sci Eng, C. 2013;33:3661-9.

[23] Cipriano AF, Zhao T, Johnson I, Guan R-G, Garcia S, Liu H. In vitro degradation of four magnesium–zinc–strontium alloys and their cytocompatibility with human embryonic stem cells. J Mater Sci Mater Med. 2013;24:989-1003.

[24] Nguyen TY, Cipriano AF, Guan RG, Zhao ZY, Liu H. In vitro interactions of blood, platelet, and fibroblast with biodegradable Magnesium-Zinc-Strontium alloys. J Biomed Mater Res, A. 2015;103:2974–86.

[25] Cipriano AF, Sallee A, Guan R-G, Zhao Z-Y, Tayoba M, Sanchez J, et al. Investigation of magnesium–zinc–calcium alloys and bone marrow derived mesenchymal stem cell response in direct culture. Acta Biomater. 2015;12:298-321.

[26] Witte F, Ulrich H, Rudert M, Willbold E. Biodegradable magnesium scaffolds: Part 1: Appropriate inflammatory response. J Biomed Mater Res, A. 2007;81A:748-56.

[27] Willbold E, Kaya AA, Kaya RA, Beckmann F, Witte F. Corrosion of magnesium alloy AZ31 screws is dependent on the implantation site. Mater Sci Eng, B. 2011;176:1835-40.

[28] Bondarenko A, Hewicker-Trautwein M, Erdmann N, Angrisani N, Reifenrath J, Meyer-Lindenberg A. Comparison of morphological changes in efferent lymph nodes after implantation of resorbable and non-resorbable implants in rabbits. Biomed Eng Online. 2011;10:1-15.

[29] Kraus T, Fischerauer SF, Hänzi AC, Uggowitzer PJ, Löffler JF, Weinberg AM. Magnesium alloys for temporary implants in osteosynthesis: In vivo studies of their degradation and interaction with bone. Acta Biomater. 2012;8:1230-8.

[30] Badar M, Lünsdorf H, Evertz F, Rahim MI, Glasmacher B, Hauser H, et al. The formation of an organic coat and the release of corrosion microparticles from metallic magnesium implants. Acta Biomater. 2013;9:7580-9.

[31] Roth I, Schumacher S, Basler T, Baumert K, Seitz J-M, Evertz F, et al. Magnesium corrosion particles do not interfere with the immune function of primary human and murine macrophages. Prog Biomater. 2014:1-10.

[32] Feser K, Kietzmann M, Bäumer W, Krause C, Bach FW. Effects of Degradable Mg-Ca Alloys on Dendritic Cell Function. J Biomater Appl. 2011;25:685-97.

[33] Witte F, Kaese V, Haferkamp H, Switzer E, Meyer-Lindenberg A, Wirth CJ, et al. In vivo corrosion of four magnesium alloys and the associated bone response. Biomaterials. 2005;26:3557-63.

[34] Gu XN, Zheng YF, Chen LJ. Influence of artificial biological fluid composition on the biocorrosion of potential orthopedic Mg?Ca, AZ31, AZ91 alloys. Biomed Mater. 2009;4:065011.

[35] Zhang X, Yuan G, Mao L, Niu J, Ding W. Biocorrosion properties of as-extruded Mg–Nd–Zn–Zr alloy compared with commercial AZ31 and WE43 alloys. Mater Lett. 2012;66:209-11.

[36] Mani G, Feldman MD, Patel D, Agrawal CM. Coronary stents: A materials perspective. Biomaterials. 2007;28:1689-710.

[37] Moravej M, Mantovani D. Biodegradable metals for cardiovascular stent application: interests and new opportunities. Int J Mol Sci. 2011;12:4250-70.

[38] Iskandar ME, Aslani A, Liu H. The effects of nanostructured hydroxyapatite coating on the biodegradation and cytocompatibility of magnesium implants. J Biomed Mater Res, A. 2013;101A:2340-54.

[39] Potapova TA, Sivakumar S, Flynn JN, Li R, Gorbsky GJ. Mitotic progression becomes irreversible in prometaphase and collapses when Wee1 and Cdc25 are inhibited. Mol Biol Cell. 2011;22:1191-206.

[40] Nguyen TY, Liew CG, Liu H. An In Vitro Mechanism Study on the Proliferation and Pluripotency of Human Embryonic Stems Cells in Response to Magnesium Degradation. PLoS ONE. 2013;8:e76547.

[41] Dubin-Thaler BJ, Giannone G, Döbereiner H-G, Sheetz MP. Nanometer Analysis of Cell Spreading on Matrix-Coated Surfaces Reveals Two Distinct Cell States and STEPs. Biophys J. 2004;86:1794-806.

[42] Kirkland NT, Birbilis N, Staiger MP. Assessing the corrosion of biodegradable magnesium implants: A critical review of current methodologies and their limitations. Acta Biomater. 2012;8:925-36.

[43] Knedler A, Ham R. Optimized medium for clonal growth of human microvascular endothelial cells with minimal serum. In Vitro Cell Dev Biol. 1987;23:481-91.

[44] Brar HS, Wong J, Manuel MV. Investigation of the mechanical and degradation properties of Mg–Sr and Mg–Zn–Sr alloys for use as potential biodegradable implant materials. J Mech Behav Biomed Mater. 2012;7:87-95.

[45] Li H, Peng Q, Li X, Li K, Han Z, Fang D. Microstructures, mechanical and cytocompatibility of degradable Mg–Zn based orthopedic biomaterials. Mater Design. 2014;58:43-51.

[46] Aljarrah M, Aghaulor U, Medraj M. Thermodynamic assessment of the Mg–Zn–Sr system. Intermetallics. 2007;15:93-7.

[47] Cui T, Guan R-G, Qin H-M. The Microstructure and the Degradation Behaviour of a Novel Biomaterial Mg-Zn-Sr Alloy Sheet in Simulated Body Fluid (SBF). Adv Sci Lett. 2013;19:1082-5.

[48] Xia X, Davies CHJ, Nie JF, Birbilis N. Influence of Composition and Processing on the Corrosion of Magnesium Alloys Containing Binary and Ternary Additions of Zinc and Strontium. Corrosion. 2014;71:38-49.

[49] Niinomi M. Recent metallic materials for biomedical applications. Metall and Mat Trans A. 2002;33:477-86.

[50] Alvarez-Lopez M, Pereda MD, del Valle JA, Fernandez-Lorenzo M, Garcia-Alonso MC, Ruano OA, et al. Corrosion behaviour of AZ31 magnesium alloy with different grain sizes in simulated biological fluids. Acta Biomater. 2010;6:1763-71.

[51] Haiwei L, Ke X, Ke Y, Jing L, Binchun Z, Yonghui X, et al. The degradation performance of AZ31 bioabsorbable magnesium alloy stent implanted in the abdominal aorta of rabbits. J Interv Radiol China. 2010;19:315-7.

[52] Zhang BP, Wang Y, Geng L. Research on Mg-Zn-Ca Alloy as Degradable Biomaterial. In: Pignatello R, editor. Biomaterials - Physics and Chemistry. Rijeka, Croatia: InTech; 2011. p. 183-204.

[53] Cha P-R, Han H-S, Yang G-F, Kim Y-C, Hong K-H, Lee S-C, et al. Biodegradability engineering of biodegradable Mg alloys: Tailoring the electrochemical properties and microstructure of constituent phases. Sci Rep. 2013;3.

[54] Hänzi AC, Gerber I, Schinhammer M, Löffler JF, Uggowitzer PJ. On the in vitro and in vivo degradation performance and biological response of new biodegradable Mg–Y–Zn alloys. Acta Biomater. 2010;6:1824-33.

[55] Huan ZG, Leeflang MA, Zhou J, Fratila-Apachitei LE, Duszczyk J. In vitro degradation behavior and cytocompatibility of Mg–Zn–Zr alloys. J Mater Sci Mater Med. 2010;21:2623-35.

[56] Zhang E, Yin D, Xu L, Yang L, Yang K. Microstructure, mechanical and corrosion properties and biocompatibility of Mg–Zn–Mn alloys for biomedical application. Mater Sci Eng, C. 2009;29:987-93.

[57] Rosalbino F, Negri S, Saccone A, Angelini E, Delfino S. Bio-corrosion characterization of Mg–Zn–X (X = Ca, Mn, Si) alloys for biomedical applications. J Mater Sci Mater Med. 2010;21:1091-8.

[58] Persaud-Sharma D, Budiansky N. In Vitro Degradation Behavior of Ternary Mg-Zn-Se and Mg-Zn-Cu Alloys as Biomaterials. Journal of biomimetics, biomaterials, and tissue engineering. 2013;18:10.4172/1662-100X.1000101.

[59] Liu L, Li N, Lei T, Li K, Zhang Y. The in vitro biological properties of Mg-Zn-Sr alloy and superiority for preparation of biodegradable intestinal anastomosis rings. Med Sci Monit. 2014;20:1056-66.

[60] Liu H. The effects of surface and biomolecules on magnesium degradation and mesenchymal stem cell adhesion. J Biomed Mater Res A. 2011;99:249-60.

[61] Johnson I, Perchy D, Liu H. In vitro evaluation of the surface effects on magnesium-yttrium alloy degradation and mesenchymal stem cell adhesion. J Biomed Mater Res A. 2011;100A:477–85.

[62] Sands JM, Layton HE. The Physiology of Urinary Concentration: an Update. Sem Nephrol. 2009;29:178-95.

[63] Zhao N, Zhu D. Endothelial responses of magnesium and other alloying elements in magnesium-based stent materials. Metallomics. 2015;7:118-28.

[64] Lelong IH, Rebel G. ph drift of “physiological buffers” and culture media used for cell incubation during in vitro studies. J Pharmacol Toxicol Methods. 1998;39:203-10.

[65] Romani A. Regulation of magnesium homeostasis and transport in mammalian cells. Arch Biochem Biophys. 2007;458:90-102.

[66] Maier JAM, Bernardini D, Rayssiguier Y, Mazur A. High concentrations of magnesium modulate vascular endothelial cell behaviour in vitro. BBA-Mol Basis Dis. 2004;1689:6-12.

[67] Maier JAM, Malpuech-Brugère C, Zimowska W, Rayssiguier Y, Mazur A. Low magnesium promotes endothelial cell dysfunction: implications for atherosclerosis, inflammation and thrombosis. BBA-Mol Basis Dis. 2004;1689:13-21.

[68] Yang C, Yuan G, Zhang J, Tang Z, Zhang X, Dai K. Effects of magnesium alloys extracts on adult human bone marrow-derived stromal cell viability and osteogenic differentiation. Biomed Mater. 2010;5:045005.

[69] Grillo CA, Alvarez F, Fernández Lorenzo de Mele MA. Biological effects of magnesium particles degradation on UMR-106 cell line: Influence of fluoride treatments. Colloids Surf, B. 2011;88:471-6.

[70] Pober JS, Bevilacqua MP, Mendrick DL, Lapierre LA, Fiers W, Gimbrone MA. Two distinct monokines, interleukin 1 and tumor necrosis factor, each independently induce biosynthesis and transient expression of the same antigen on the surface of cultured human vascular endothelial cells. J Immunol. 1986;136:1680-7.

[71] Pober JS, Gimbrone MA, Lapierre LA, Mendrick DL, Fiers W, Rothlein R, et al. Overlapping patterns of activation of human endothelial cells by interleukin 1, tumor necrosis factor, and immune interferon. J Immunol. 1986;137:1893-6.

[72] Leeuwenberg JF, Smeets EF, Neefjes JJ, Shaffer MA, Cinek T, Jeunhomme TM, et al. E-selectin and intercellular adhesion molecule-1 are released by activated human endothelial cells in vitro. Immunology. 1992;77:543-9.

[73] Zhang W-J, Frei B. Intracellular metal ion chelators inhibit TNFα-induced SP-1 activation and adhesion molecule expression in human aortic endothelial cells. Free Radic Biol Med. 2003;34:674-82.

[74] Rochelson B, Dowling O, Schwartz N, Metz CN. Magnesium sulfate suppresses inflammatory responses by human umbilical vein endothelial cells (HuVECs) through the NFκB pathway. Journal of Reproductive Immunology. 2007;73:101-7.

[75] Zhai Z, Qu X, Li H, Yang K, Wan P, Tan L, et al. The effect of metallic magnesium degradation products on osteoclast-induced osteolysis and attenuation of NF-κB and NFATc1 signaling. Biomaterials. 2014;35:6299-310.

[76] Prasad AS, Bao B, Beck FWJ, Sarkar FH. Zinc activates NF-κB in HUT-78 cells. J Lab Clin Med. 2001;138:250-6.

[77] Bao B, Prasad AS, Beck FWJ, Sarkar FH. Zinc up-regulates NF-κB activation via phosphorylation of IκB in HUT-78 (Th0) cells. Febs Lett. 2007;581:4507-11.

[78] Strlič M, Kolar J, Šelih V-S, Kočar D, Pihlar B. A comparative study of several transition metals in Fenton-like reaction systems at circum-neutral pH. Acta Chim Slov. 2003;50:619-32.

[79] Wilham JM. The role of Zinc and Reactive Oxygen Species in the Regulation of Endothelial Nitric Oxide Synthase: University of Montana; 2007.

[80] Cortese-Krott MM, Kulakov L, Opländer C, Kolb-Bachofen V, Kröncke K-D, Suschek CV. Zinc regulates iNOS-derived nitric oxide formation in endothelial cells. Redox Biol. 2014;2:945-54.

[81] Kocatürk P, Kavas G, Erdeve Ö, Siklar Z. Superoxide dismutase activity and zinc and copper concentrations in growth retardation. Biol Trace Elem Res. 2004;102:51-9.

[82] Khan BV, Harrison DG, Olbrych MT, Alexander RW, Medford RM. Nitric oxide regulates vascular cell adhesion molecule 1 gene expression and redox-sensitive transcriptional events in human vascular endothelial cells. PNAS. 1996;93:9114-9.

[83] Lin S-J, Shyue S-K, Hung Y-Y, Chen Y-H, Ku H-H, Chen J-W, et al. Superoxide Dismutase Inhibits the Expression of Vascular Cell Adhesion Molecule-1 and Intracellular Cell Adhesion Molecule-1 Induced by Tumor Necrosis Factor-α in Human Endothelial Cells Through the JNK/p38 Pathways. Arterioscler Thromb Vasc Biol. 2005;25:334-40.

[84] Klein CL, Köhler H, Kirkpatrick CJ. Increased Adhesion and Activation of Polymorphonuclear Neutrophil Granulocytes to Endothelial Cells under Heavy Metal Exposure in vitro. Pathobiology. 1994;62:90-8.

[85] Arsalane K, Gosset P, Hildebrand HF, Voisin C, Tonnel A-B, Wallaert B. Nickel hydroxy carbonate increases tumour necrosis factor alpha and interleukin 6 secretion by alveolar macrophages. J Appl Toxicol. 1994;14:375-9.

[86] Ninomiya JT, Kuzma SA, Schnettler TJ, Krolikowski JG, Struve JA, Weihrauch D. Metal ions activate vascular endothelial cells and increase lymphocyte chemotaxis and binding. J Orthop Res. 2013;31:1484-91.

[87] Bowen PK, Drelich J, Goldman J. Magnesium in the murine artery: Probing the products of corrosion. Acta Biomater. 2014;10:1475-83.

[88] Chung T-W, Liu D-Z, Wang S-Y, Wang S-S. Enhancement of the growth of human endothelial cells by surface roughness at nanometer scale. Biomaterials. 2003;24:4655-61.

[89] Franco D, Klingauf M, Bednarzik M, Cecchini M, Kurtcuoglu V, Gobrecht J, et al. Control of initial endothelial spreading by topographic activation of focal adhesion kinase. Soft Matter. 2011;7:7313-24.

[90] Liliensiek SJ, Wood JA, Yong J, Auerbach R, Nealey PF, Murphy CJ. Modulation of human vascular endothelial cell behaviors by nanotopographic cues. Biomaterials. 2010;31:5418-26.

[91] Hermawan H, Dubé D, Mantovani D. Developments in metallic biodegradable stents. Acta Biomater. 2010;6:1693-7.

[92] Ruygrok PN, Serruys PW. Intracoronary Stenting: From Concept to Custom. Circulation. 1996;94:882-90.

Chapter 6 – The *in vivo* degradation of as-drawn Mg-4Zn-1Sr intramedullar pins and associated peri-implant bone remodeling in the rat tibia

6.1. Background

Previous work by our lab focused on addressing the rapid degradation of Mg-based materials through the design, development, and evaluation of biological performance of heat-treated Mg-Zinc-Strontium (Mg-Zn-Sr) ternary alloys [1-5]. Crystalline Mg-Zn-Sr ternary alloys consist of elements naturally present in the human body and provide attractive mechanical and biodegradable properties for a variety of biomedical applications [1-5]. Previous results using physiologically relevant *in vitro* models, which are useful for initial rapid screening of cytocompatibility and cytotoxicity of engineered biomaterials [6, 7], converged on the superior performance of Mg-4Zn-1Sr alloy compared with other Mg-4Zn-xSr compositions [2-5]. Since *in vivo* evaluations at a later-stage of alloy development remain imperative for clinical translation, especially due to the gap between *in vitro* and *in vivo* studies [8-10], we aimed to investigate the *in vivo* degradation and biological performance of the Mg-4Zn-1Sr (designated as ZSr41) alloy in a small animal model.

In situ microcomputer tomography (μCT) is a technique of growing popularity to transiently study the volumetric change of Mg-based implants as well as peri-implant bone structure surrounding the implant [11-13]. With better instrumentation, it is now possible to transiently monitor Mg implant degradation *in*

situ [10], thus obtaining quantitative measurements of implant degradation and associated bone structural responses all while minimizing the amount of animals needed since the same animal can be anesthetized and monitored at distinct time points [11-13]. In fact, Martinez Sanchez et al. pointed in a recent review that transient *in situ* μCT measurements provided a reliable method and multiple time points to study the *in vivo* degradation of Mg-based implants in a continuous manner [10]. Likewise, due to the demonstrated ability of μCT to provide quantitative bone morphometric values, this technique can also be used to provide information on bone structure and density [11-16]. Thus, in this study we continuously investigated the *in vivo* performance of the Mg-4Zn-1Sr alloys through *in situ* μCT and results were verified through histological analysis of undecalcified sections.

The first objective of this study was to investigate the *in vitro* degradation and cytocompatibility of as-drawn ZSr41 pins in Dulbecco's Modified Eagle Medium (DMEM) in co-culture with bone marrow derived mesenchymal stem cells (BMSCs). The use of DMEM was motived by previous studies indicating that degradation in this culture medium resembled *in vivo* conditions more closely due to the presence of physiologically relevant ions and proteins [17-19]. Likewise, use of BMSCs was motivated by their important roles in early implant osseointegration and bone regeneration *in vivo* [20], as well as by their demonstrated applicability for testing the cytocompatibility of Mg-based materials for orthopedic applications [7, 21]. The second objective of this study was to investigate for the first time the

in vivo degradation of as-drawn ZSr41 pins and associated host response when implanted in the intramedullar cavities of rat tibiae for 47 days. The methods to measure both *in vitro* degradation (electrochemical and immersion) and *in vivo* degradation (transient *in situ* µCT) were carefully selected based on recent recommendations [10] in order to directly compare results with published literature. In doing so, our results seek to contribute towards community-wide efforts [8-10] geared towards resolving the mismatch between *in vitro* and *in vivo* degradation of Mg-based materials.

We should highlight that the *in vivo* degradation rate of the as-drawn ZSr41 intramedullar pins was drastically faster than any other alloy reported in literature [10]. The drastically fast degradation rate of the ZSr41 alloy allowed us to investigate the host response at the upper threshold related to the degradation of Mg-based implants. In fact, to our knowledge, only Kraus et al. monitored the complete degradation of a rapidly-degrading Mg-alloy implant and reported on the associated host-response [11]. Kraus et al. reported on ion-induced bone formation but also hydrogen-gas-induced damage during the aggressive bone remodeling resulting from the quick degradation of the ZX50 alloy (Mg-5Zn-0.25Ca-0.15Mn, wt. %). However, after complete resorption of the ZX50 implant, near-complete bone homeostasis was recovered after 6 months. In this study we showed that the fast degradation of the ZSr41 implant also induced aggressive peri-implant bone remodeling. However, we showed (for the first time) detrimental effects related to fast Mg-implant degradation which might contribute to altered

long-term peri-implant bone remodeling. These results contribute towards an overall understanding of host-responses to the degradation of Mg-based implants for orthopedic implants.

6.2. Materials and methods

6.2.1. Preparation of ZSr41 alloy and Mg control

The ZSr41 alloy in this study had a nominal composition of 4 wt. % Zn and 1 wt. % Sr in a Mg matrix. The ZSr41 alloy pins were produced by a metallurgical process consisting of melting, casting, aging, and extrusion. Firstly, high-purity commercially available Mg ingots (99.94 wt. %; Boyu, Shenyang, China) were melted at 750 °C using a mild steel crucible under a gas-protected environment consisting of Argon (Ar) and 2% SF_6. Subsequently, commercially available bulk metallic Zn (99.5%; Boyu, Shenyang, China), and a Mg–20 wt. % Sr master alloy (Boyu, Shenyang, China) were added to the melt at 720 °C in nominal amounts. The mixture was stirred (30 min, 200 rpm) and heated for 15 min at 700 °C to homogenize and deslag the melt. The melt was cast as ingots (Ø30 × 150 mm) at 700 °C and solidified in the air. After casting, 25 mm from either end of the ingots (lengthwise) were removed and the middle segmets (100 mm in length) were solid-solution treated at 450 °C for 12 h, followed by quenching in water. Subsequently, the heat-treated trimmed ingots were hot extruded at 250 °C with an extrusion ratio of 56:1 to produce ZSr41 wires with Ø4 mm. Lastly, the hot-extruded wires were drawn through a single pass at 150 °C with a drawing ratio of 1.44:1 to produce

ZSr41 wires with Ø1.1 mm. Likewise, commercially pure Mg wire (P-Mg; 99.9+%, as-drawn, Cat# 679-751-72; Goodfellow Co., Coraopolis, PA, USA) with a nominal Ø1.1 mm (1.05 ± 0.03 measured) was used as a control in this study. The as-drawn ZSr41 alloy and P-Mg wires were cut into 15.08 ± 0.46 mm long pins, ground with SiC abrasive paper (Ted Pella Inc., Redding, CA, USA) up to 1200 grit, ultrasonically cleaned for 15 min in separate baths of acetone and 200-proof ethanol, individually weighed (M_0), and sterilized with an autoclave using a standard gravity cycle (122 °C for 30 min).

6.2.2. Surface characterization of ZSr41 alloys

Prior to electrochemical tests, and *in vitro* and *in vivo* experiments, the surface microstructure of ZSr41 and P-Mg pins, with and without sterilization, were characterized using a scanning electron microscope (SEM; Nova NanoSEM 450, FEI Co., Hillsboro, OR, USA). The samples were designated as either polished or autoclaved (the latter consisted of polishing followed by sterilization through autoclaving). Surface elemental composition and distribution were analyzed with energy dispersive x-ray spectroscopy (EDS) using a Nova NanoSEM 450 equipped with an X-Max50 detector and AZtecEnergy software (Oxford Instruments, Abingdon, Oxfordshire, UK). An accelerating voltage of 20 kV was used to obtain SEM images and perform EDS analysis. Additionally, x-ray diffraction (XRD; Empyrean, PANalytical, Westborough, MA, USA) was used to analyze the crystal structures of the phases present. All XRD spectra were

acquired using Cu Kα radiation (45 kV, 40 mA) at a step size of 0.006 degree, and dwell time of 50 sec using a PIXcel 1D detector (PANalytical). Phase identification was performed using the HighScore software (PANalytical) and were identified according to patterns in the Inorganic Crystal Structure Database (ICSD): 00-004-0770 for Mg, 01-074-6807 for $Mg_{17}Sr_2$, 00-008-0269 for Mg_7Zn_3, 01-077-8619 for MgO, 00-074-2582 for $Mg(OH)_2$, 00-007-9187 for $Mg_2O(OH)_2$, 00-036-1451 for ZnO, 01-075-9745 for $(Zn_{0.85}Mg_{0.15})O$, and 01-074-1227 for SrO.

6.2.3. Electrochemical testing

Potentiodynamic polarization (PDP) curves were obtained using a potentiostat (Model 273A, Princeton Applied Research, Oak Ridge, TN, USA) with a three-electrode cell configuration and acquired with PowerSuite 2.50.0 software (Princeton Applied Research). Specific details pertaining to preparation of the working electrode are given elsewhere [4, 7]. Briefly, the ZSr41 and P-Mg pins were embedded longitudinally in epoxy resin as the working electrode and ground with SiC abrasive paper to expose a rectangular cross section along the length of the wire (0.17 cm^2 exposed). Platinum foil was used as the counter electrode, and a silver/silver chloride (Ag/AgCl) electrode was used as reference. Prior to electrochemical experiments, the working electrode was cleaned as described above but not sterilized. Revised simulated body fluid (r-SBF; pH 7.4, 37.5°C) was used as the electrolyte for PDP scans (no equilibration, 0.5 to -3.5 V, 20 mV s^{-1}) since the ionic composition of r-SBF is the same as human blood plasma . Values

for corrosion potential (E_{corr}) and corrosion current density (J_{corr}) were extrapolated from the PDP curves according to ASTM G102-89 standard. All potentials are in reference to Ag/AgCl electrode.

6.2.4. Cytocompatibility and *in vitro* degradation of ZSr41 pins in co-culture with BMSCs

Following a protocol approved by the University of California, Riverside (UCR) Institutional Animal Care and Use Committee (IACUC), BMSCs were harvested from the femur and tibia of a three-week-old female Sprague Dawley rat weanling after euthanasia by CO_2. Specific details regarding BMSC extraction, isolation and culture are described elsewhere [22]. Briefly, the distal and proximal ends of the bones were dissected and the bone marrow was flushed out of the bone cavity and collected using DMEM (Sigma Aldrich, St. Louis, MO, USA) supplemented with 10% fetal bovine serum (FBS; HyClone, Logan, UT, USA) and 1% penicillin/streptomycin (P/S; Invitrogen, Grand Island, NY, USA). Hereafter, DMEM + 10% FBS + 1% P/S is referred to as DMEM. The collected cells were then filtered through a 70-μm nylon strainer to remove cell aggregates and tissue debris. The filtered BMSCs were cultured in DMEM under standard cell culture conditions (i.e., 37 ºC, 5%/95% CO2/air, humidified sterile environment) to 90-95% confluency.

The direct exposure co-culture method (i.e. cells are co-cultured, but not placed directly in contact with samples) was used to compare with previous *in vitro* cytocompatibility results of ZSr41 [2, 3]. The direct culture method permits for direct

exposure of degradation products without the need for diluting the culture media, like ISO 10993 methods. BMSCs (first passage; P1) were detached using Trypsin (Invitrogen), cultured in 12-well plates at an initial density of 40,000 cells cm^{-2} in DMEM, and incubated in DMEM for an initial period of 1 day under standard cell culture conditions. Subsequently, the DMEM media was removed and replenished with 3 mL of fresh media, and Transwell® inserts (Cat #3460; Corning, Union City, CA) with the sterilized ZSr41 and P-Mg pins at the center were placed into each BMSC-containing well and incubated for 1, 2, and 3 days (D1, D2, D3, respectively). A positive control, designated as "cells" group, consisted of BMSCs cultured only with DMEM in the wells, (i.e. without any samples). DMEM alone was also used as a blank reference and designated as “DMEM” group. In order to closely mimic *in vivo* conditions where the circulation system regularly takes away soluble degradation products from the local site of implantation [2], the cell culture media was collected for analysis and replenished with 3 mL of fresh media at 1 day intervals.

Fluorescence microscopy was used to evaluate BMSC viability and adhesion on the culture plates at D1, D2, and D3 of co-culture with ZSr41 and P-Mg pins. At each time interval, the Transwell® inserts with the ZSr41 and P-Mg pins were removed from the wells and dried in an oven at 37 ºC for 2 days. The corresponding wells were washed with PBS to remove non-adherent cells. Adherent cells on the culture plates, were fixed with 4% formaldehyde (10% neutral buffered formalin; VWR, Radnor, PA, USA) and stained with 4',6-diamidino-2-phenylindole dilactate

(DAPI; Invitrogen) nucleic acid stain and Alexa Flour® 488-phalloidin (Life Technologies, Carlsbad, CA) F-actin stain for fluorescence imaging. Adherent cells on the sample surface and on the culture plate surrounding the sample were visualized using a fluorescence microscope (Eclipse Ti and NIS software, Nikon, Melville, NY, USA) with a 10x objective lens at the same exposure condition and analyzed using Image J (NIH, Bethesda, MD, USA). At least 9 images per well were obtained according to the template and guidelines in [3] o determine BMSC viability in regards to proximity to samples and/or degradation products. Briefly, 1 image was obtained at the center of each well (designated as R_0), 4 images were obtained concentrically at 3.5 mm from the center of each well (designated as R_1), and 4 images were obtained concentrically at 7.0 mm from the center of each well (designated as R_2). Cell adhesion density for each group/location/time was quantified by counting the DAPI-stained cell nuclei in each image and dividing per unit area.

The *in vitro* degradation of the ZSr41 and P-Mg pins at each time point was evaluated through measurements of: mass; pH and ionic concentrations of the collected media; and surface analysis via SEM, EDS, and XRD. The mass of the dried pins from each time point was measured (M_f) and used to determine a percent final mass relative to the initial mass (i.e. M_f/M_0*100; %). The pH of the media was measured immediately after collection using a calibrated pH meter (Model SB70P, VWR). The concentration of Mg^{2+}, Zn^{2+}, and Sr^{2+} ions in the collected media was measured using inductively coupled plasma optical emission

spectroscopy (ICP-OES; Optima 8000, Perkin Elmer, Waltham, MA, USA). In order to minimize matrix effects in ICP-OES, the collected DMEM aliquots were diluted to 1:100 solutions in DI water. Ionic concentrations were then obtained from calibration curves generated using Mg, Zn, and Sr standards (Perkin Elmer) diluted to ranges of 0.5-5.0, 0.1-1.0, and 0.1-1.0 mg/L respectively. Surface topography and elemental composition of the ZSr41 and P-Mg pins after D3 degradation were characterized using SEM and EDS, respectively; likewise, crystal structures of the phases present were analyzed with XRD. Experimental settings for SEM, EDS, and XRD were the same as outlined in section 2.2. XRD phases were identified according to patterns in the ICSD: 00-004-0770 for Mg, 01-077-8619 for MgO, 00-070-9184 for $Mg_5O_4(OH)_2$, 00-033-0879 for $Mg_2PO_4(OH)$, 01-070-6449 for $Ca(OH)_2$, 00-055-0898 for $Ca_3(PO_4)_2$, 00-048-1474 for $Ca_{0.3}Sr_{0.7}O$, 01-075-9526 for hydroxyapatite (HA) $Ca_{10}(PO_4)_6(OH)_2$, and 00-024-1444 for $Zn(OH)_2$.

6.2.5. *In vivo* implantation of ZSr41 intramedullar pins in rat proximal tibia

6.2.5.1. Animal surgery

The *in vivo* degradation and bioactivity of ZSr41 pins was evaluated through intramedullar implantation in the proximal tibia of rats for a period of 47 days. The animal experimental protocol was reviewed and approved by the Loma Linda University IACUC (reference No. 8120020). Eighteen 12-week-old Sprague Dawley rats were randomly assigned to three groups (n = 6). All rats were generally anesthetized in an induction chamber (2% Isoflurane in O_2 at 1.5 L/min).

Subsequently, the animals were transferred to the operative table, an anesthesia nose cone was placed (1.5% Isoflurane in O_2 at 1.5 L/min), and the right knee was prepped with a razor and scrubbed with Clorhexadine in preparation for surgery. A longitudinal peripatellar skin incision was made on the medial side of the right leg followed by direct dissection down to the tibial plateau. A drill bit (1/64 inch diameter) was used to prepare pre-drilled bone tunnels (15 mm in length) in the medullary canal [23]. For the experimental groups, ZSr41 and P-Mg pins were implanted into pre-drilled bone tunnels along the axis of the shaft from the proximal tibia using established surgical and model protocols [24-26]. In the control group (Sham), the pre-drilled tunnel was left empty for comparison. The wounds were then carefully sutured (Monochryl 4-0) and the rats housed in an environmentally controlled animal care laboratory after surgery. Buprenorphine (60 µg/kg) was administered intramuscularly for 2 days as an analgesic. During the surgical procedure, the pre-drilled canal in one animal for both ZSr41 and P-Mg groups was drilled diagonally through the cortical bone of the mid-diaphysis; therefore, the implanted pins were partially in the medullary canal and partially protruded from the diaphysis. These two animals were observed but not used for qualitative analysis. Table 1 indicates the sample sizes and measurements/data obtained from each animal. Postoperatively, the animals were allowed to move freely in their cages without external support and unrestricted weight bearing, and were fed regularly. Likewise, daily observation ensured no signs of compromised health or

significant inflammation. Finally, the animals were sacrificed by CO_2 inhalation followed by cervical dislocation at 47 days post-implantation.

6.2.5.2. Weekly *in situ* monitoring of the degradation of ZSr41 pins: µCT evaluation and blood collection

An *in vivo* µCT set-up (MicroCAT II; Imtek Corp, Oak Ridge, TN USA; 74 kVp, 1 mA, 2s) with a mean voxel size of 63x63x80 μm^3 was used to monitor proximal tibiae of rats at days 3, 7, 12, 28, 39, and 47 post-implantation. A total of 512 transverse two-dimensional (2-D) images (512x512 pixels) were acquired across the length of the implant site in the tibia for each anesthetized animal at each time point. Likewise, blood draws were obtained at days 0, 3, 5, 7, 14, 21, 28, 35, and 42 to evaluate the concentration of Mg^{2+}, Zn^{2+}, and Sr^{2+} ions in the blood serum using ICP-OES. Solutions for ICP-OES were prepared as described in section 6.2.4.

6.2.5.3. Reconstruction, visualization, and quantification of peri-implant bone remodeling and ZSr41 intramedullar pin degradation

Peri-implant bone remodeling and implant degradation were visualized and quantified using scale-corrected three-dimensional (3-D) digital reconstructions of 2-D µCT scans. 3-D structures of implants and peri-implant tissue were reconstructed in IMARIS® (Bitplane AG, Zurich, Switzerland) using the volume of interest (VOI) technique with an optimized intensity-based grayscale distribution

threshold to isolate tissue (muscle, and trabecular and cortical bone) and/or implants from the background [27, 28]. VOIs included: ZSr41 and P-Mg implants (along the entire length of the implant); and, peri-implant muscle, trabecular bone, and cortical bone regions in the proximal tibia (delimited by the tibial tuberosity and 12.82 ± 50 mm distally from tibial plateau). The volume and mean voxel grayscale intensity of each of the 3-D reconstructed VOIs were quantified at days 12, 28, and 47 using the Volume and Mean Intensity functions in IMARIS®, respectively; additionally, the volume of the ZSr41 and P-Mg pins, and Sham pre-drilled cavity were quantified at days 0, 3, 7, 12, 28, 39, and 47. The volume of the pins at each time point (V_i) was used to determine a percent final volume relative to the initial volume (V_i/V_0*100; %).

Values for the weight density (g cm^{-3}) of each VOI were calculated from mean voxel grayscale intensity; note that the weight density does not represent values for bone mineral density (BMD) for trabecular or compact bone VOIs. A calibration curve which converted the µCT mean voxel intensity values of each VOI to weight density was constructed [29] based on the measured mean voxel intensity (36,902.1±217.6 and 35,582.8±56.6 A.U.) and theoretical weight density (1.90 and 1.74 g cm^{-3}) for the ZSr41 and P-Mg pins, respectively. To calculate the weight density of P-Mg we used: hexagonally close packed configuration for Mg; 2 atoms/unit cell; volume of $1.406a^3$ where a = 3.210 Å; and atomic mass of 24.305 g mol^{-1}. The same values were used to calculate the weight density of ZSr41, with

the exception of the atomic mass which was 26.581 g mol^{-1} for 95 wt. % Mg, 4 wt. % Zn, and 1 wt. % Sr.

6.2.5.4. Surface characterization of dissected implant

Surface topography and elemental composition of the ZSr41 and P-Mg intramedullar pins after implantation in rat tibiae during 47 days were characterized using SEM and EDS, respectively. Additionally, elemental distribution maps on the surface of dissected pins were obtained for Mg, Ca, and P (Kα lines). Likewise, crystal structures of the phases present were analyzed with XRD. Experimental settings for SEM, EDS, and XRD were the same as outlined in section 2.2. The right tibia from one Sham specimen was dissected, lyophilized overnight, and pulverized with a mortar and pestle for XRD analysis (reference spectrum). XRD phases were identified according to patterns in the ICSD: 00-004-0770 for Mg, 00-074-2582 for $Mg(OH)_2$, 00-056-1216 for P, and 01-075-9526 for hydroxyapatite (HA) $Ca_{10}(PO_4)_6(OH)_2$.

6.2.5.5. Elemental mapping analysis on transverse cross-sections at the implant-tissue interface

Elemental mapping analysis was used to study the implant-tissue interface, the release and diffusion of alloying elements into peri-implant tissue, and peri-implant bone remodeling and composition in response to the degradation of the ZSr41 and P-Mg intramedullar pins. For elemental mapping analysis, one complete right tibia

from each group was harvested, then the muscle and periosteum was dissected. Subsequently the complete tibia was lyophilized overnight, and embedded in a low viscosity epoxy resin (Cat# ULTRA-3000R-32, Pace Technologies, Tucson, AZ, USA) in vacuum. The embedded complete tibia was sectioned transversely at the mid-diaphysis 5 mm from the tibia plateau using a low speed saw (Model 650; South Bay Technology, Inc., San Clemente, CA, USA) equipped with a diamond wheel (0.305 mm thick, Cat# DWH4122; South Bay Technology, Inc.) to obtain transverse undecalcified sections. Subsequently the sections were sputter coated (Model 108, Cressington Scientific Instruments Ltd., Watford, UK) with platinum/palladium at 20 mA and 40 sec sputter time. Surface topography and elemental distribution maps for Mg, Zn, Sr, Ca, and P (Kα lines) were characterized using SEM and EDS, respectively. EDS point analyses were utilized to semi-quantitatively investigate the Ca/P (at. %/at. %) ratio in the peri-implant cortical bone regions and in the newly formed cortical bone fractions as a measure of bone quality.

6.2.5.6. Histological evaluation

Plastic-embedded undecalcified sections were used for histological evaluation of the implantation site with ZSr41 and P-Mg intramedullar pins. For histological evaluation, two complete right tibiae from each group were harvested and fixed in 10% neutral buffered formalin for 24 hrs. After serial dehydration in increasing ethanol (2x70%, 2x95%, 2x100%; 3 hrs each), the harvested tibiae were

embedded in methyl methacrylate (MMA). Specific details regarding infiltration and embedding solutions, and embedding process are described elsewhere [30]. The resin blocks were cut into thick undecalcified sections (~200 µm thick) using a diamond-embedded wire saw (Model 3241; Well Diamond Wire Saws Inc., Norcross, GA USA). The thick undecalcified sections were re-embedded in MMA and cut into serial 5-10 µm undecalcified proximal saggital sections or transverse thin sections (at mid-diaphysis 6 mm from tibial plateau) using a rotary microtome (Model 5030; Bright Instruments Ltd., Cambridgeshire, UK) equipped with a D-profile tungsten carbide blade (Delaware Diamond Knives, Inc., Wilmington, DE USA). Serial thin sections were stained with Goldner's trichrome stain for analysis of bone structure [31] and with Toluidine blue (0.1% toluidine blue O in 0.1% borax solution for 10 s) for analysis of cell and cartilage distribution. The stained sections were observed by light microscopy.

6.2.6. Degradation rates of ZSr41

ZSr41 and P-Mg pin volume (V_i) from 3-D reconstruction analysis at distinct time points was used to establish a model for the degradation of Mg-based intramedullar pins in the rat tibia. In order to capture the differences in pin volume, the volume of each pin at each time point (V_i) was normalized by its corresponding initial volume (V_0). A linear model with the y-intercept set to unity was used to fit the ratio of V_i/V_0 as a function of time in weeks; the model was used to predict the lifetimes of the ZSr41 and P-Mg intramedullar pins.

In vitro average daily degradation rates (mass loss rates) for the ZSr41 and P-Mg pins were calculated based on measured Mg^{2+} ion concentration in the culture media. The *in vitro* degradation rates, either normalized by initial volume (V_0) or by initial surface area (SA_0), were calculated according to the following equations (Eq. 6.1a and 6.1b, respectively):

$$(Eq.\,6.1a) \quad \frac{Avg.\,Daily\,Deg.\;Rate}{Unit\,Initial\,Vol} = \frac{[\sum_{i=1}^{3}([Mg^{2+}]_i) - [Mg^{2+}]_{DMEM,tot}] \times 0.003\;L}{3\;day \times V_0}$$

$$(Eq.\,6.1b) \quad \frac{Avg.\,Daily\,Deg.\;Rate}{Unit\,Initial\,Surf.Area} = \frac{[\sum_{i=1}^{3}([Mg^{2+}]_i) - [Mg^{2+}]_{DMEM,tot}] \times 0.003\;L}{3\;day \times SA_0}$$

Only data from the 3-day *in vitro* experiments were used in conjunction with Eq. 6.1 since each replicate for the 3-day experiment yielded values at three distinct time points (*i* =1, 2, 3). Furthermore, Eq. 6.1 was first calculated for each wire replicate for each group (ZSr41, P-Mg) and then a mean value was obtained. In Eq. 6.1, $[Mg^{2+}]_{group,i}$ were obtained through ICP-OES measurements in mg/L. The total measured concentration in blank DMEM over the 3 day period, $[Mg^{2+}]_{DMEM,tot}$, was 55.8 mg/L (measured $[Mg^{2+}]_{DMEM}$ per day was 0.765 mM which compared favorably with the nominal value of 0.8 mM [32]; $[Mg^{2+}]_{DMEM,tot}$ = 0.765 mmol L^{-1} * 24.305 mg $mmol^{-1}$ * 3 = 55.8 mg/L). The immersion media volume was 3 mL (0.003 L), the average daily rate was computed from a 3 day period, and the computed rate (mg day^{-1}) was either normalized by wire replicate V_0 (cm^3) or SA_0 (cm^2).

In vivo average daily degradation rates (mass loss rates) for the ZSr41 and P-Mg pins were calculated based on volumetric change from 3-D reconstructions. The *in vivo* degradation rates, either normalized by initial volume (V_0) or by initial surface area (SA_0), were calculated according to the following equations (Eq. 6.2a and 6.2b, respectively):

$$\frac{Avg.Daily\ Deg.\ Rate}{Unit\ Initial\ Vol} = \frac{(V_0 - V_{47}) \times \rho}{47\ day \times V_0} \quad (Eq.\ 6.2a)$$

$$\frac{Avg.Daily\ Deg.\ Rate}{Unit\ Initial\ Surf.Area} = \frac{(V_0 - V_{47}) \times \rho}{47\ day \times SA_0} \quad (Eq.\ 6.2b)$$

Only volumetric values at day 47 (V_{47}) were used to calculate the average daily degradation rates. Eq. 6.2 was first calculated for each wire replicate for each group (ZSr41, P-Mg) and then a mean value was obtained. Volumetric values (cm^3) were obtained from the 3-D reconstructed pins using the Volume function in IMARIS®. The weight density of each pin was either ρ_{ZSr41} = 1.90x10^3 mg cm^{-3} or $\rho_{P\text{-}Mg}$ = 1.74x10^3 mg cm^{-3}, the average daily rate was computed from a 47 day period, and the computed rate (mg day^{-1}) was either normalized by wire replicate V_0 (cm^3) or SA_0 (cm^2).

Additionally, the *in vitro* and *in vivo* average daily degradation rates per unit area for ZSr41 and P-Mg pins from this study were compared with published *in vitro* degradation rates from the following studies with ZSr41 alloys: ZSr41 and P-Mg sheets in direct exposure co-culture method (i.e., Transwell® inserts) with H9

human embryonic stem cells (H9-hESCs) in mTeSR® media (average from 3 days) [2]; ZSr41 and P-Mg sheets in the direct culture method (i.e., cells were seeded directly onto sample surface) with human umbilical vein endothelial cells (HUVECs) in EGM^{TM}-2 media (average from 1 day) [4]; and, ZSr41 and P-Mg sheets in the direct culture method with BMSCs in DMEM media (average from 3 days) [5].

6.2.7. Statistical analyses

Electrochemical, cytocompatibility, and *in vitro* degradation experiments were run in triplicate. Sample sizes for *in vivo* measurements are outlined in Table 6.1. All data sets were tested for normal distribution and homogeneous variance. Parametric data sets were analyzed using one-way analysis of variance (ANOVA) followed by the Tukey HSD *post hoc* test. Data sets with normal distribution but heterogeneous variance were analyzed using one-way ANOVA (homogeneous variance not assumed) followed by the Games-Howell *post hoc* test. Non-parametric data sets were analyzed using the Kruskal-Wallis test followed by either the Nemenyi *post hoc* test (equal sample sizes) or the Dunn *post hoc* test (unequal sample sizes). Statistical significance was considered at $p < 0.05$.

6.3. Results

6.3.1. Surface characterization of ZSr41 alloys

Figure 6.1 summarizes results for surface characterization of polished, and autoclaved ZSr41 and P-Mg pins. The SEM micrographs (1,000x) in Figure 6.1a and 6.1b show the polished surfaces of the ZSr41 and P-Mg pins, respectively. These micrographs confirmed the presence of a network of secondary β-phase (white web-like structures) on the ZSr41 pin but not on P-Mg. Standard-less EDS surface elemental composition analysis (Figure 6.1a and 6.1b, insets, tables) confirmed the presence of Zn and Sr on the ZSr41 pin but not on P-Mg. Specifically, the ZSr41 pin had 4.0 wt. % Zn and 0.9 wt. % Sr along with residual oxides (1.1 wt. %) in a Mg matrix; in contrast, P-Mg only had residual oxides (1.5 wt. %) in a Mg matrix. Likewise, XRD results confirmed crystalline Mg, $Mg_{17}Sr_2$, Mg_7Zn_3, SrO, and ZnO (Figure 1a') and crystalline Mg, $Mg(OH)_2$, and MgO (Figure 6.1b') on the polished surfaces of ZSr41 and P-Mg, respectively. The SEM micrographs (160x) in Figure 6.1c and 6.1d show the autoclaved surfaces of the ZSr41 and P-Mg pins, respectively. These micrographs showed the nucleation of micron-scale oxide structures predominantly on the surface of the ZSr41 pin and to a much lower extent on P-Mg. Additional SEM micrographs (Figure 6.1c and 6.1d, insets, SEM micrographs; 500x) of a side-view at the periphery of the ZSr41 and P-Mg pins, respectively, show that the oxide structures on the ZSr41 pin self-assembled to a height of approximately 35 μm. Standard-less EDS surface

elemental composition analysis after autoclaving (Figure 6.1c and 6.1d, insets, tables) confirmed an oxide-enriched surface for ZSr41, and to a lower extent P-Mg. Specifically, the oxygen content on the surface of ZSr41 increased to 36.6 wt. % after autoclaving; meanwhile, the Zn and Sr content remained in close proximity to the nominal value. Likewise, the oxygen content on the surface of P-Mg pin was 18.2 wt. % after autoclaving. XRD results after autoclaving confirmed crystalline Mg, $Mg_{17}Sr_2$, $Mg(OH)_2$, SrO, and $(Zn_{0.85}Mg_{0.15})O$ (Figure 6.1c') and crystalline Mg, $Mg(OH)_2$, $Mg_2O(OH)_2$ and MgO (Figure 6.1d') on the polished and autoclaved surfaces of ZSr41 and P-Mg, respectively.

6.3.2. Corrosion properties of ZSr41 alloys from electrochemical testing

PDP curves obtained for the as-polished samples showed that the initial corrosion (or degradation) behavior of the ZSr41 and P-Mg pins was similar (Figure 6.2). PDP results for embedded, polished, and autoclaved samples were not included due to deterioration of the epoxy resin as a result from exposure to water vapor during autoclaving. The median PDP trace with the most representative corrosion potential (E_{corr}) and corrosion current density (J_{corr}) for each sample type was plotted in Figure 6.2a. A qualitative assessment of the PDP curves indicated that the as-polished ZSr41 sample was slightly more cathodic when compared to P-Mg. Furthermore, assessment of the linear anodic (b_a) and cathodic (b_c) portions of the PDP curves gave indication that ZSr41 and P-Mg had similar half-reaction characteristics. ANOVA was used to confirm statistically significant differences in

the E_{corr} [F (1, 4) = 9.4064, p = 3.74x10^{-2}] values calculated by Tafel extrapolation from the PDP curves (Figure 6.2b). *Post hoc* pairwise comparisons confirmed that the E_{corr} of ZSr41 (-1.60±0.03 V; mean±SD) was significantly more cathodic (p < 0.05) when compared with P-Mg (-1.66±0.01 V). Significant differences in J_{corr} values calculated by Tafel extrapolation (Figure 6.2c) were not confirmed between the mean value for ZSr41 (33.77±3.60 mA cm^{-2}; mean±SD) and P-Mg (45.40±8.23 mA cm^{-2}).

6.3.3. Cytocompatibility of ZSr41 pins in co-culture with BMSCs

Cytocompatibility of ZSr41 and P-Mg pins with BMSCs was evaluated through cell adhesion on the culture plates up to 3 days after co-culture with the pins and results are summarized in Figure 6.3a-6.3d. Figure 6.3a shows representative fluorescence images of BMSCs attached to the culture plates at R_1 location during D1, D2, and D3 post-incubation; similar images were obtained at R_0 and R_2 during the same incubation intervals. The DAPI-stained nuclei were used to quantify BMSC adhesion density at locations R_0, R_1, and R_2 inside each well during each incubation interval and results are plotted in the histograms shown in Figures 6.3b-6.3d, for each respective location. ANOVA was used to confirm statistically significant differences for BMSC adhesion density at location R1 at D3 [F (2, 6) = 14.179, p = 5.326x10^{-3}]; family-wise comparison of BMSC adhesion densities at all other locations and time points did not yield statistically significant differences. *Post hoc* pairwise comparisons confirmed that the mean BMSC adhesion density

in co-culture with ZSr41 (22.12±1.37x10^3 cells cm^{-2}; mean±SE) was significantly lower (p < 0.01) when compared with the BMSCs-only positive control (29.92±0.79x10^3 cells cm^{-2}) at D3. A comparison between cell adhesion densities at each location for each group showed a general trend of increasing densities with increasing incubation time.

6.3.4. *In vitro* degradation of ZSr41 pins in co-culture with BMSCs in DMEM

Results for the *in vitro* degradation of the ZSr41 and P-Mg pins during D1-D3 incubation intervals are summarized in the histograms in Figure 6.3e-6.3g. Sample mass (Figure 6.3e), media pH (Figure 6.3f), and Mg^{2+} ion concentration in media ([Mg^{2+}]; Figure 6.3g) are important indicators of the degradation of Mg-based materials [9]. ANOVA showed statistically significant differences in the mean percent final mass (M_f/M_0x100; Figure 6.3e) of ZSr41 and P-Mg at D2 [$F(1, 4) = 10.027$, $p = 3.397\text{x}10^{-2}$] and D3 [$F(1, 4) = 17.126$, $p = 1.44\text{x}10^{-2}$]; no significant family-wise differences were confirmed at D1. *Post hoc* pairwise comparisons confirmed a statistically lower final mass percentage at D2 (p < 0.05) for ZSr41 (97.94±0.71%; mean±SD) compared with P-Mg (101.74±1.95%), and at D3 (p < 0.05) for ZSr41 (96.62±0.70%) compared with P-Mg (99.98±1.22%). Similarly, ANOVA (without homogeneous variance) confirmed statistically significant differences in the mean pH of the incubation media at D1 [$F(3, 8) = 88.645$, $p = 2.723\text{x}10^{-6}$], and ANOVA (with homogeneous variance) confirmed differences at D2 [$F(3, 17) = 71.028$, $p = 8.01\text{x}10^{-10}$] and D3 [$F(3, 4) = 13.314$, $p = 2.37\text{x}10^{-2}$]

(Figure 6.3f). *Post hoc* pairwise comparisons at D1 confirmed a significantly more alkaline media for ZSr41 (8.19±0.03; mean±SD) compared with P-Mg (8.01±0.01; $p < 0.001$), BMSCs-only positive control (7.99±0.01; $p < 0.001$), and DMEM-only blank reference (8.07±0.03; $p < 0.01$); likewise, the media of BMSC was significantly lower compared with P-Mg ($p < 0.001$) and DMEM ($p < 0.05$). At D2, *post hoc* comparisons confirmed a significantly more alkaline media ($p < 0.001$) for ZSr41 (8.10±0.03) compared with P-Mg (7.97±0.01), BMSC (7.93±0.02), and DMEM (7.99±0.01); likewise, the media of BMSCs was significantly lower ($p < 0.01$) compared with DMEM. At D3, *post hoc* comparisons confirmed a significantly more alkaline media ($p < 0.05$) for ZSr41 (8.05±0.02) compared with P-Mg (7.94±0.02), BMSC (7.94±0.03), and DMEM (7.98±0.00). Additionally, the Kruskal-Wallis test for non-parametric data confirmed statistically significant differences in the mean $[Mg^{2+}]$ at D1 [X^2 (3, N = 30) = 26.124, $p = 8.984 \times 10^{-6}$], ANOVA (without homogeneous variance) confirmed significant differences at D2 [F (3, 9) = 278.720, $p = 4.374 \times 10^{-9}$], and ANOVA (with homogeneous variance) confirmed significant differences at D3 [F (3, 8) = 3034.9, $p = 1.46 \times 10^{-12}$] (Figure 6.3g). *Post hoc* pairwise comparisons at D1 confirmed a significantly higher $[Mg^{2+}]$ ($p < 0.001$) for ZSr41 (6.92±1.32 mM; mean±SD) compared with P-Mg (1.61±0.13 mM), BMSC (0.78±0.01 mM), and DMEM (0.77±0.00 mM). At D2, *post hoc* comparisons confirmed a significantly a significantly higher $[Mg^{2+}]$ ($p < 0.001$) for ZSr41 (6.00±0.45 mM) compared with P-Mg (1.41±0.14 mM), BMSC (0.70±0.03 mM), and DMEM (0.74±0.01 mM); likewise, a significantly higher $[Mg^{2+}]$ ($p < 0.001$) was

confirmed for P-Mg compared with BMSC and DMEM. At D3, *post hoc* comparisons confirmed a significantly a significantly higher [Mg^{2+}] ($p < 0.001$) for ZSr41 (4.77±0.06 mM) compared with P-Mg (1.32±0.03 mM), BMSC (0.71±0.10 mM), and DMEM (0.79±0.02 mM); furthermore, a significantly higher [Mg^{2+}] ($p < 0.001$) was confirmed for P-Mg compared with BMSC and DMEM.

Additionally, the Zn^{2+} and Sr^{2+} ion concentrations ([Zn^{2+}] and [Sr^{2+}], respectively) in the culture media were also measured to ensure concentrations remained below cytotoxic levels reported in literature. Results for [Zn^{2+}] and [Sr^{2+}] during D1-D3 incubation intervals are summarized in the histograms in Figure 6.3h and 6.3i, respectively. The Kruskal-Wallis test confirmed statistically significant differences in the mean [Zn^{2+}] at D1 [X^2 (3, N = 30) = 18.503, $p = 3.464x10^{-4}$], at D2 [X^2 (3, N = 21) = 13.355, $p = 3.929x10^{-4}$], and D3 [X^2 (3, N = 12) = 6.590, $p = 8.619x10^{-4}$] (Figure 6.3h). *Post hoc* pairwise comparisons at D1 confirmed a significantly higher [Zn^{2+}] ($p < 0.001$) for ZSr41 (39.83±6.65 µM; mean±SD) compared with P-Mg (3.03±3.12 µM), BMSC (2.12±0.38 µM), and DMEM (2.06±0.15 µM). At D2, *post hoc* comparisons confirmed a significantly higher [Zn^{2+}] ($p < 0.001$) for ZSr41 (39.02±4.75 µM) compared with P-Mg (1.79±0.56 µM), BMSC (1.87±0.35 µM), and DMEM (2.19±0.18 µM). Similarly, at D3 *post hoc* comparisons confirmed a significantly higher [Zn^{2+}] ($p < 0.001$) for ZSr41 (38.33±2.78 µM) compared with P-Mg (2.36±0.53 µM), BMSC (2.28±0.57 µM), and DMEM (2.43±0.11 µM). In addition, the Kruskal-Wallis test confirmed statistically significant differences in the mean [Sr^{2+}] at D1 [X^2 (3, N = 30) = 21.077, p =

$1.015x10^{-4}$], while ANOVA (without homogeneous variance) confirmed statistically significant differences at D2 [F (3, 9) = 60.005, $p = 2.237x10^{-6}$] and at D3 [F (3, 4) = 25.795, $p = 6.019x10^{-4}$] (Figure 6.3i). *Post hoc* pairwise comparisons at D1 confirmed a significantly higher [Sr^{2+}] ($p < 0.001$) for ZSr41 (20.83±5.30 µM; mean±SD) compared with P-Mg (1.22±2.31 µM), BMSC (0.22±0.45 µM), and DMEM (0.38±0.66 µM). At D2, *post hoc* comparisons confirmed a significantly higher [Sr^{2+}] ($p < 0.001$) for ZSr41 (13.95±2.35 µM) compared with P-Mg (0.24±0.59 µM), BMSC (1.20±1.56 µM), and DMEM (0.12±0.21 µM). Similarly, at D3 *post hoc* comparisons confirmed a significantly higher [Sr^{2+}] ($p < 0.001$) for ZSr41 (16.43±2.81 µM) compared with P-Mg (1.12±0.64 µM), BMSC (0.13±0.23 µM), and DMEM (0.51±0.88 µM).

Figure 6.4 summarizes results for surface characterization of ZSr41 and P-Mg pins after 3 days in co-culture with BMSCs in DMEM culture media. The SEM micrographs (65x) in Figure 6.4a and 6.4b were obtained from the center (lengthwise) of the pins and show the corroded surfaces of the ZSr41 and P-Mg, respectively. These micrographs indicate that the surface of ZSr41 showed signs of aggressive localized corrosion, but P-Mg did not. In contrast, SEM micrographs obtained from the ends of the pins (Figure 6.4a and 6.4b, insets) showed an inverse behavior where P-Mg showed more aggressive localized corrosion compared with ZSr41. After immersion in DMEM, XRD results confirmed crystalline Mg, $Ca_{0.3}Sr_{0.7}O$, $Zn(OH)_2$, MgO and HA (Figure 6.4a') and crystalline Mg, $Ca(OH)_2$, $Mg_5O_4(OH)_2$, $Mg_2PO_4(OH)$, $Ca_3(PO_4)_2$, and HA (Figure 6.4b') on the

corroded surfaces of ZSr41 and P-Mg, respectively. Standard-less EDS surface elemental composition analysis (Figure 6.4c) confirmed the presence of Zn and Sr on the ZSr41 pin but not on P-Mg, a higher oxide content on ZSr41 compared with P-Mg, and a Ca/P at.%/at. % ratio closer to that of HA for ZSr41 compared with P-Mg. Specifically, the ZSr41 pin had (in atomic %) 71.2% O, 20.1% Mg, 0.4% Zn, 0.1% Sr, 3.5% Ca, 2.7% P, and 2.1% Na, Cl, and K; the P-Mg had 61.1% O, 30.0% Mg, 2.5% Ca, 5.7% P, and 0.8% Na, Cl, and K. Based on these values, the Ca/P at.%/at. % ratio for ZSr41 and P-Mg was 1.31 and 0.44, respectively; in comparison, the theoretical stoichiometric ratio for HA is 1.67.

6.3.5. Weekly *in situ* monitoring of the *in vivo* degradation of ZSr41 intramedullar pins

Figure 6.5 summarizes results from weekly *in situ* measurements to monitor the *in vivo* degradation of intramedullar ZSr41 and P-Mg tibial pins throughout an implantation period of 47 days. Figure 6.5a shows representative *in situ* μCT images from the proximal tibia for all groups at selected time points throughout the 47-day study. The same animal within each group was imaged at each time point and each representative μCT image was obtained from the mid-diaphysis of the proximal tibia at a 5 mm distance from the tibial plateau. These images confirmed aggressive peri-implant cortical bone formation in response to the degradation of ZSr41 intramedullar pins, and to a lesser extent also for P-Mg, starting from D12 all throughout D47. The μCT images also confirmed the presence of peri-implant

hydrogen gas pockets (dark spots) inside the bone tunnel for both ZSr41 and P-Mg groups throughout D47. In addition, peri-implant gas-induced cavities were also observed in the cortical bone region for the ZSr41 and P-Mg groups up to D47.

The histograms in Figure 6.5b-6.5d summarize the Mg^{2+}, Zn^{2+}, and Sr^{2+} ionic concentrations in the collected blood serum, respectively, up to 42 days post-implantation of ZSr41 and P-Mg intramedullar pins. Results from statistical analyses on measured ionic concentrations in the blood serum along with significant differences and reported values (mean±SD) are summarized in Table 6.2. Although several significant differences were confirmed throughout the 47-day study, the significant differences of merit (i.e. where ZSr41 was significantly higher compared with either P-Mg, Sham, or both) were as follows: at D3, the Mg^{2+} concentration for ZSr41 was significantly higher compared with Sham; at D0, D3, D5, D7, and D21 the Sr^{2+} concentration for ZSr41 was significantly higher compared with Sham. At D35 and D42, no significant differences were obtained for any of the groups for any of the ions measured.

6.3.6. Peri-implant bone remodeling resulting from ZSr41 intramedullar pin degradation

Figure 6.6 summarizes visualization of the 3D reconstructed VOIs along with quantification of peri-implant bone remodeling and volumetric implant change throughout the 47-day implantation period of ZSr41 and P-Mg intramedullar pins.

Figure 6.6a shows representative images of 3D reconstructions of the endosteum of the proximal tibia with ZSr41 or P-Mg implants compared with the Sham control. To illustrate the sequential bone remodeling, each image corresponds to the same animal within each group. These images show that the peri-implant proximal tibia for ZSr41 and P-Mg increased in volume. However, in the case of ZSr41, the aggressive bone remodeling at D7, D28, and D47 was accompanied by the formation of a large amount of hydrogen-gas-induced cavities in the peri-implant endosteum of the proximal tibia. In contrast, gas-induced cavities were observed to a much lesser extent on the endosteum of the proximal tibia with P-Mg implants, and were not observed at all in the Sham control. The histograms shown in Figure 6.6b-6.6d summarize the quantification of the peri-implant bone volume (trabecular and cortical) at D12, 28, and D47 post-implantation, respectively. Results from D12 (Figure 6.6b) showed that the volume of both trabecular and cortical peri-implant bone regions was similar for all groups. At D28 (Figure 6.6c), the trabecular bone volume remained statistically indistinguishable for all groups; however, ANOVA confirmed statistically significant differences in the mean cortical bone volume [$F(2, 13) = 5.797$, $p = 1.586 \times 10^{-2}$]. Specifically, *post hoc* pairwise comparison showed that the peri-implant cortical bone volume for ZSr41 ($1.07 \pm 0.14 \times 10^{2}$ mm^3; mean±SD) was significantly higher ($p < 0.05$) when compared with the Sham control ($0.83 \pm 0.05 \times 10^{2}$ mm^3). At D47 (Figure 6.6d), ANOVA confirmed statistical differences in the volumes of peri-implant trabecular bone [$F(2, 11) = 4.634$, $p = 3.469 \times 10^{-2}$] and cortical bone [$F(2, 11) = 63.486$, $p = 9.10 \times 10^{-7}$]. *Post hoc* pairwise

comparisons of trabecular volume confirmed a significantly higher value ($p < 0.05$) for ZSr41 ($1.49\pm0.34\text{x}10^{2}$ mm^3) compared with the Sham control ($0.84\pm0.19\text{x}10^{2}$ mm^3). Likewise, *post hoc* comparisons confirmed a significantly higher cortical bone volume ($p < 0.001$) for ZSr41 ($1.71\pm0.20\text{x}10^{2}$ mm^3) compared with P-Mg ($0.90\pm0.10\text{x}10^{2}$ mm^3) and the Sham control ($0.77\pm0.10\text{x}10^{2}$ mm^3).

The histograms shown in Figure 6.6e-6.6g summarize the quantification of the weight density for peri-implant muscle, trabecular bone, and cortical bone, as well as the weight density of the ZSr41 and P-Mg implants at D12, 28, and D47 post-implantation. At D12 (Figure 6.6e), ANOVA confirmed statistically significant differences only for the weight density of the trabecular bone region [$F(2, 9) = 10.14$, $p = 4.949\text{x}10^{-3}$] and *post hoc* pairwise comparisons showed that P-Mg (1.60 ± 0.03 g cm^{-3}; mean±SD) was significantly lower ($p < 0.01$) when compared with ZSr41 (1.67 ± 0.02 g cm^{-3}) and Sham control (1.66 ± 0.02 g cm^{-3}). At D28 (Figure 6.6f), the Kruskal-Wallis test confirmed statistically significant differences in the mean weight density of the trabecular bone region [X^2 (2, N = 16) = 10.488, $p = 5.28\text{x}10^{-3}$] and ANOVA (without homogeneous variance) confirmed significant differences in the mean weight density of the cortical bone [$F(2, 6) = 8.622$, $p = 1.643\text{x}10^{-2}$]. Specifically, *post hoc* pairwise comparisons showed that the weight density of the peri-implant trabecular region around P-Mg (1.58 ± 0.02 g cm^{-3}) was significantly lower ($p < 0.01$) compared with the Sham control (1.65 ± 0.01 g cm^{-3}). Likewise, *post hoc* comparisons showed that the weight density of the peri-implant cortical region around ZSr41 (1.81 ± 0.03 g cm^{-3}) was significantly lower compared

with P-Mg (1.85±0.02 g cm^{-3}; $p < 0.05$) and Sham control (1.87±0.01 g cm^{-3}; $p < 0.01$). At D47 (Figure 6.6g), ANOVA confirmed statistically significant differences only for the weight density of the cortical bone region [$F(2, 11) = 12.304$, $p = 1.564 \times 10^{-3}$] and *post hoc* pairwise comparisons showed that ZSr41 (1.80±0.04 g cm^{-3}) was significantly lower ($p < 0.01$) when compared with P-Mg (1.86±0.01 g cm^{-3}) and Sham control (1.88±0.02 g cm^{-3}). In all cases, the weight density of the peri-implant muscle region was always 1.55-1.56 g cm^{-3}. Likewise, the weight density for the cortical region of the Sham control at all time points was 1.86-1.88 g cm^{-3} which is in good agreement with published values in literature of 1.80-1.92 g cm^{-3} [33].

Figure 6.6h shows representative images of 3D reconstructions of ZSr41 and P-Mg intramedullar pins during the 47-day implantation in the proximal rat tibia. To illustrate the sequential *in situ* implant degradation, each image corresponds to the same implant within each group. For the ZSr41 group, none of the implants had complete and/or pristine µCT scans at all time points (Table 6.1). Rat #7 in the ZSr41 group had the most complete set with only a fraction of the implant missing at D7 (missing portion is represented with dashed lines). A qualitative comparison of the 3D reconstructed implants shows that the ZSr41 intramedullar pin degraded much quicker compared with the P-Mg pin. The ZSr41 implant showed a homogeneous thinning from all sides (i.e. homogeneous bulk corrosion) up to D28. Analysis at D39 showed fragmentation and loss of mechanical continuity of the ZSr41 implant. At D47, the residual ZSr41 implant was found in one large and two

smaller fragments. In contrast, the P-Mg pin showed localized bulk corrosion as indicated by thinning primarily in the center along the length of the implant. Likewise, up to D47 the P-Mg pin did not lose mechanical continuity by fragmenting into smaller pieces. The histogram shown in Figure 6.6i summarizes the quantification of the percent volume of the implants (at each time point) relative to their paired initial volume throughout the 47-day implantation. The volume percent for the Sham control pertains to the volume of the pre-drilled cavity only since implants were not placed in this group. Due to the absence of replicate data (Table 6.1), statistical analysis for the percent volume for the following were not included: ZSr41 and P-Mg at D3 ($n_{D3,ZSr41}$ = 2 and $n_{D3,P\text{-}Mg}$ = 2), ZSr41 at D7 ($n_{D7,ZSr41}$ = 1), and Sham at D39 ($n_{D39,Sham}$ = 0). ANOVA confirmed significant differences in the mean percent volume at D7 [$F(1, 6) = 693.66$, $p = 1.98 \times 10^{-7}$], D12 [$F(2, 9) = 60.53$, $p = 6.03 \times 10^{-6}$], D28 [$F(2, 15) = 203.94$, $p = 1.33 \times 10^{-11}$], D39 [$F(1, 8) = 102.7$, $p = 7.69 \times 10^{-6}$], and D47 (without homogeneous variance) [$F(2, 8) = 182.911$, $p = 3.908 \times 10^{-7}$]. *Post hoc* pairwise comparisons showed the following significant differences in the percent volume: at D7, Sham (17.96±4.36%) was significantly lower ($p < 0.001$) than P-Mg (89.03±3.18%); at D12, Sham (11.44±3.43%) was significantly lower ($p < 0.001$) than ZSr41 (59.25±13.89%) and P-Mg (80.38±6.52%), and ZSr41 was significantly lower ($p < 0.05$) than P-Mg; at D28, Sham (8.35±3.45%) was significantly lower ($p < 0.001$) than ZSr41 (36.05±5.58%) and P-Mg (70.85±6.60%), and ZSr41 was significantly lower ($p < 0.001$) than P-Mg; at D39, ZSr41 (29.43±6.11%) was significantly lower ($p < 0.001$) than P-Mg

(61.14±3.41%); and at D47, Sham (3.18±1.81%) was significantly lower than ZSr41 (13.01±6.58%; $p < 0.05$) and P-Mg (58.10±6.53%; $p < 0.001$), and ZSr41 was significantly lower ($p < 0.001$) than P-Mg.

6.3.7. Surface characterization of dissected ZSr41 intramedullar pins

Results for surface characterization of ZSr41 and P-Mg intramedullar pins after they were dissected from the tibiae in which they were implanted for 47 days are summarized in Figure 6.7. The montages in Figure 6.7a and 6.7b show optical photos of the residual dissected implants along with SEM images (50x) and corresponding elemental distribution maps (for Mg, Ca, and P) obtained through EDS. The SEM micrographs show that both ZSr41 and P-Mg samples were aggressively corroded; however, the residual ZSr41 pin did not show as many surface cracks compared with P-Mg sample which indicated homogeneous corrosion on ZSr41 and localized corrosion on P-Mg. The EDS elemental distribution maps show that the deposition of Ca and P, along with residual Mg, was evenly distributed on the surface of the dissected ZSr41 and P-Mg implants. Standard-less EDS surface elemental composition analysis (Figure 6.7c) confirmed the presence of Zn and Sr on the residual ZSr41 pin but not on P-Mg, approximately equal C and O content on both dissected implants, and a higher Ca/P at.%/at. % for ZSr41 compared with P-Mg. Specifically, the ZSr41 pin had (at. %) 49.91%C, 39.57% O, 3.02% Mg, 0.73% Zn, 0.03% Sr, 3.18% Ca, 2.84% P, and 0.72% Na, Cl, and K; the P-Mg implant had 53.65% C, 37.97% O, 4.80%

Mg, 1.30% Ca, 1.77% P, and 0.51% Na, Cl, and K. Based on these values, the Ca/P at.%/at. % ratio for ZSr41 and P-Mg was 1.12 and 0.73. Additionally, XRD analysis (Figure 6.7d) confirmed crystalline Mg, $Mg(OH)_2$, and HA on the surface of the dissected implants. A reference spectrum for HA in the rat tibia (i.e. crushed bone into fine powder) is included in Figure 6.7d to show overlap of HA peaks with spectra from experimental groups. Likewise, a single peak for elemental P was detected on the surface of ZSr41, but not on P-Mg or reference bone.

6.3.8. Elemental mapping analysis on transverse cross-sections at the implant-tissue interface

Figure 6.8 summarizes results for elemental mapping analysis on dissected tibia cross-sections to characterize the implant-tissue interface *in situ* at 47 days post-implantation. The montage in Figure 6.8a shows SEM images (50x) and corresponding EDS elemental distribution maps (for Mg, Zn, Sr, Ca, and P) obtained from resin-embedded transverse cross-sections cut at the mid-diaphysis of the proximal tibia at a distance of 5 mm from the tibial plateau. The Mg distribution map for ZSr41 shows that, at this anatomical location, the ZSr41 intramedullar pin was completely resorbed without traces of Mg enrichment in the peri-implant tissue. In contrast, the Mg map for P-Mg showed the cross-section of the residual intramedullar pin (indicated by white arrow). The absence of Mg mapping of the peri-implant bone region surrounding the P-Mg implant was due to the drastically higher Mg content in the pin compared with the surrounding bone.

The Mg map for the Sham control confirmed the expected Mg distribution in cortical bone. Elemental distribution maps of Zn and Sr for all groups confirmed the presence of these two elements in cortical bone without significant enrichment of peri-implant tissue surrounding the ZSr41 pin. Elemental distribution maps of Ca and P for ZSr41 confirmed circumferential aggressive remodeling of mineralized peri-implant bone in response to the degradation of the ZSr41 intramedullar pin. The Ca and P maps for P-Mg confirmed a mineralized layer at the implant-tissue interface along with normal trabeculae in the intramedullar bone tunnel. The Ca and P maps for the Sham control confirmed the expected mineralized distribution in cortical and trabecular bone. Furthermore, triplicate EDS point analyses were measured in the cortical region for all groups (indicated by white stars in P maps) and in the new bone formed around the ZSr41 implant (indicated by white arrowheads in P maps) in order to determine the peri-implant bone mineral quality as indicated by the Ca/P at. %/at. % ratio. Results for the Ca/P ratio from EDS point analyses are summarized in the histogram in Figure 6.8b. ANOVA confirmed statistically significant differences in the mean Ca/P ratio of the mineralized bone regions of interest [$F(3, 8) = 32.007$, $p = 8.34 \times 10^{-5}$]. *Post hoc* pairwise comparisons showed a significantly lower Ca/P ratio ($p < 0.001$) for the cortical bone region surrounding the ZSr41 intramedullar pin (1.25±0.03; mean±SD) compared with the new bone region surrounding the ZSr41 implant (1.56±0.04), peri-implant cortical bone in P-Mg (1.55±0.03), and cortical bone in the Sham control (1.39±0.07). Likewise, P-Mg was significantly higher ($p < 0.01$) compared with the Sham control.

6.3.9. Histological evaluation of the proximal tibia

Optical images of undecalcified histology sections obtained from the proximal tibia in which the ZSr41 and P-Mg intramedullar pins were implanted for 47 day are shown in Figure 6.9. Longitudinal saggital and transverse plastic-embedded undecalcified sections were obtained and stained with either Toluidine blue (blue stains for cell nucleus and structure, purple stains for collagen, and tray stains for bone) or Goldner's trichrome (green stains for mineralized bone, red stains for unmineralized osteoid, and brownish-gray stains for bone marrow cells). Figure 6.9a shows longitudinal saggital sections (2.5x magnification) of the proximal tibia for ZSr41, P-Mg, and Sham control. The Toluidine blue-stained longitudinal sections of ZSr41 and P-Mg confirmed the formation of hydrogen-gas-induced cavities in the peri-implant region (indicated by red arrows) in which bone marrow cells were absent. In contrast, the trabecular bone tunnel of the Sham control showed a healthy amount of bone marrow cells. The small vacancies in the bone tunnel of the Sham control are artifacts of chemical treatment during section preparation and pertain to healthy amounts of adipose cells [34]; adipose cell vacancies were observed in the bone tunnel of P-Mg and Sham, but not in ZSr41. In addition, the Golder trichrome-stained longitudinal section of ZSr41 confirmed aggressive bone remodeling (indicated by white arrowhead) in response to the degradation of the intramedullar implant. Additionally, unmineralized osteoid was observed in the bone tunnel adjacent to the P-Mg implant (indicated by black arrowhead). Comparison of the trabecular bone region of all groups shows a lack

of evenly-distributed trabeculae in ZSr41, abnormally distributed trabeculae near the gas pockets for P-Mg, and normal and healthy trabeculae distribution in the Sham control. Figure 6.9b shows transverse sections of the proximal tibia obtained 6 mm away from the tibial plateau (2.5x magnification) for ZSr41, P-Mg, and Sham control. The transverse sections (both stains) confirmed aggressive bone remodeling, bone tunnel enlargement, hydrogen-gas-induced cavity formation, and discontinuity and/or thinning of the annular cortical bone structure in the ZSr41 and P-Mg groups, but not for the Sham control. Analysis of cell structure did not show abnormal enlargement of cells indicating hyperplastic bone enlargement (as opposed to hypertrophic growth). Specifically, the Toluidine blue-stained transverse sections confirmed hydrogen-gas-induced cavities with absent marrow cells in both implant groups (indicated by red arrows) but not in the Sham control. Cartilage formation was observed in the center of the bone tunnel where the P-Mg implant was placed. The Goldner trichrome-stained transverse sections confirmed circumferential aggressive remodeling of mineralized peri-implant bone in response to the degradation of the ZSr41 intramedullar pin (indicated by white arrowheads). Bone remodeling inside the bone tunnel was also observed for P-Mg but not to the same extent when compared with ZSr41. Additionally, unmineralized osteoid was observed in the bone tunnel for both implant groups (indicated by black arrowhead) but not in the Sham control. The presence of unmineralized osteoid in close proximity to the implant (or where the implant was originally placed) and bone formation away from the implant could indicate stimulation of

bone formation both near the implant and further away within the bone tunnel [35]. Furthermore, in all cases, infiltration of inflammatory cells was not observed.

6.3.10. Degradation rates of ZSr41

Figure 6.10 summarizes results from the measured *in vitro* and *in vivo* degradation rates from this study along with a comparison with published *in vitro* degradation rates for ZSr41 and P-Mg. Figure 6.10a shows a scatter plot of ZSr41 and P-Mg implant V_i (measured from 3D reconstructed VOIs) as a function of time (in days) during the 47-day implantation period. The linear-fitted curves for each group show the decreasing volume and highlight the difference in initial implant volume. The inset in Figure 6.10a shows a scatter plot with a normalized implant volume (relative to V_0) as a function time (in weeks). The linear-fitted curve of the normalized volume highlights the faster degradation rate of ZSr41 (-0.12 cm^3 cm^{-3} $weeks^{-1}$; $R^2 = 0.99$) when compared with P-Mg (-0.07 cm^3 cm^{-3} $weeks^{-1}$; $R^2 = 0.95$). Extrapolation of these curves indicated that the ZSr41 and P-Mg intramedullar pins will completely degrade in 8 and 14 weeks, respectively, when implanted in the rat tibia bone tunnel. Figure 6.10b shows the average daily degradation rate for the ZSr41 and P-Mg pins measured in this study (both *in vitro* and *in vivo*) and normalized by the corresponding V_0. ANOVA confirmed statistically significant differences in the mean average daily degradation rates relative to V_0 [$F(3, 12) = 177.34$, $p = 3.35 \times 10^{-10}$]. *Post hoc* pairwise comparisons showed that the *in vivo* average daily degradation rates of ZSr41 (35.64±2.67 mg cm^{-3} d^{-1}) and P-Mg

(16.24±1.83 mg cm^{-3} d^{-1}) were both significantly higher ($p < 0.001$) when compared with their *in vitro* counterparts in DMEM (24.39±1.58 mg cm^{-3} d^{-1} and 3.79±0.52 mg cm^{-3} d^{-1}, respectively). Additionally, the average daily degradation rate of ZSr41 was significantly higher ($p < 0.001$) compared with P-Mg for both *in vitro* and *in vivo* measurements. Since corrosion rates are typically associated with exposed surface area [7, 10, 36], the average daily degradation rate was also calculated relative to SA_0 of the ZSr41 and P-Mg pins, and results are shown in Figure 6.10c. ANOVA confirmed statistically significant differences in the mean average daily degradation rates relative to SA_0 [$F(3, 12) = 199.79$, $p = 1.66 \times 10^{-10}$]. *Post hoc* pairwise comparisons showed that the *in vivo* average daily degradation rates of ZSr41 (0.98±0.08 mg cm^{-2} d^{-1}) and P-Mg (0.39±0.04 mg cm^{-2} d^{-1}) were both significantly higher ($p < 0.001$) when compared with their *in vitro* counterparts in DMEM (0.69±0.04 mg cm^{-2} d^{-1} and 0.09±0.01 mg cm^{-2} d^{-1}, respectively). Additionally, the average daily degradation rate of ZSr41 was significantly higher ($p < 0.001$) compared with P-Mg for both *in vitro* and *in vivo* measurements. Figure 6.10d shows a comparison between the average daily degradation rates relative to SA_0 measured in this study and *in vitro* degradation rates of ZSr41 in various cell culture media (with respective cell types) reported in literature [2, 4, 5]. Although the comparative histogram includes several variables, in the context of alloy design and optimization, this table helps illustrate the range of *in vitro* degradation rates of the ZSr41 alloy. Collectively, the comparative results show a lower *in vitro* degradation rate in DMEM of rolled and aged ZSr41 sheets compared

with the as-drawn pins and indicate that implementation of processing techniques could dramatically reduce the ZSr41 alloy degradation rate to meet clinical requirements.

6.4. Discussion

The *in vitro* degradation of ZSr41 pins and their cytocompatibility with BMSCs was investigated using the co-culture method. We also examined the biocompatibility and *in vivo* degradation of ZSr41 intramedullar pins implanted in rat tibiae for 47 days. Hereafter we will discuss: factors that influenced the *in vitro* and *in vivo* degradation of ZSr41 alloys, the cytocompatibility of as-drawn ZSr41 pins with BMSCs, and the biological implications of a considerably fast-degrading ZSr41 intramedullar implant. Though originally intended for orthopedic implant applications, the fast-degrading as-drawn ZSr41 wires presented in this study (under current alloy processing parameters) did not meet clinical requirements (in terms of degradation rate). Thus, the discussion of the *in vivo* degradation rate of ZSr41 will not focus on performance compared with other alloys whose degradation rate is superior compared with commercial Mg. Rather, the discussion will focus on the utility of a fast-degrading alloy to illustrate the host response to high dissolution rates and concomitant degradation products at the implantation site.

6.4.1. The degradation of ZSr41 pins and intramedullar implants

The degradation (i.e. corrosion) rate of the ZSr41 alloy was likely mediated by the electrochemical behavior between the α-Mg matrix and second-phase precipitates (composition and dispersion). Previous studies indicated that crystalline Mg-Zn-Sr alloys showed segregation of Zn and Sr predominantly in the precipitated phases accompanied by an α-matrix with ~4 wt. % Zn [1, 37, 38]. Specifically, previous studies from our group [1] confirmed through EDS and XRD analysis the presence of $Mg_{17}Sr_2$, a binary $Zn_{13}Sr$ phase, and a variety of Mg-Zn binary phases in as-cast Mg-4Zn-1Sr alloy sheets. The EDS and XRD results from this study (Figure 6.1a') on as-drawn ZSr41 wire confirmed the presence of the $Mg_{17}Sr_2$ phase and a binary Mg-Zn phase. Microstructurally, previous studies from our group [1, 4] showed that the second phases in rolled and heat-treated Mg-4Zn-1Sr alloy sheets consisted of dispersed round particles (a few microns in diameter). The microstructure of the as-drawn ZSr41 wires used in this study appeared as interconnected networks of secondary β-phase (white web-like structures; Figure 6.1a). Based on a systematic comparison between distinct rolled and heat-treated Mg-4Zn-xSr alloys [4], we suggested the importance of the Zn/Sr at. % ratio in dictating composition and morphology of the distinctive β-phases, both of which are critical factors for micro-galvanic corrosion (i.e. corrosion resistance of the alloy). However, in order to understand the β-phase-mediated corrosion, in-depth TEM analysis as well as micro-galvanic measurements are required to accurately identify the composition/distribution and quantify the standard electrode potential,

respectively, of the β-phases in the as-drawn ZSr41 wires. Detailed discussions on the evolution of the microstructure during solidification, grain size, and mechanical properties of the Mg-Zn-Sr alloy system can be found in Refs. [1, 37, 38], and a thermodynamic evaluation with phase diagrams are presented in Ref. [39].

The *in vitro* degradation rate of the ZSr41 pins in DMEM was significantly higher compared with the P-Mg control. Results from PDP measurements and Tafel extrapolation (Figure 6.2) showed that the initial corrosion response of the as-polished ZSr41 and P-Mg pins had similar characteristics (i.e. similar E_{corr} values and J_{corr} in the same order of magnitude). Even though the E_{corr} value for ZSr41 was significantly lower compared with P-Mg (Figure 6.2b), it is the J_{corr} value (which did not show significant differences; Figure 6.2c) which is directly proportional to the corrosion rate. Results from the *in vitro* degradation obtained through co-culture in DMEM for 3 days showed significantly higher values for final percent mass (relative to initial mass; Figure 6.3e), pH of incubation media (Figure 6.3f), and $[Mg^{2+}]$ in the culture media (Figure 6.3g) of ZSr41 starting at day 2 of incubation; in contrast, at day 1, only the pH and $[Mg^{2+}]$ were significantly higher. Final mass of Mg-based biomaterials can be influenced by the deposition of degradation products and the pH is influenced by the absence of 5% CO_2 environment (since measurements are typically taken outside of incubator) needed for optimal $NaHCO_3$-mediated buffering [7]. Thus, the significantly higher $[Mg^{2+}]$ in the media of ZSr41 indicated a significantly higher *in vitro* degradation rate

compared with P-Mg as early as day 1 of incubation. Qualitatively, surface characterization of the ZSr41 and P-Mg pins after the 3-day *in vitro* degradation (Figure 6.4) showed considerable aggressive localized corrosion and a heavily-oxidized surface on ZSr41 compared with P-Mg. Both of these surface characterization parameters supported the faster *in vitro* degradation of ZSr41 compared with P-Mg. To our knowledge, this is the first report on the degradation of as-drawn ZSr41 wires; however, published literature using rolled and heat-treated ZSr41 sheets showed that the *in vitro* degradation rates of the ZSr41 alloy (Mg-4Zn-1Sr, wt. %) was superior compared with commercial Mg when incubated in r-SBF for 15 days [1] and in mTeSR® media for 3 days [2], but only comparable to commercial Mg when incubated in EGM^{TM}-2 media for 1 day [4], in DMEM media for 3 days [5], and in human blood and plasma for 2 hours [3]. Results from distinct *in vitro* degradation studies for ZSr41 alloys are summarized in Figure 6.10d. It should be noted that the different *in vitro* degradation rates observed for ZSr41 alloys in distinct cell culture media are likely primarily affected by the HCO_3^- ion concentration in the culture media [5, 40, 41]. Kirkland et al. provided a comprehensive summary of *in vitro* degradation rates (mg cm^{-2} day^{-1}) of various Mg-based biomaterials [36] with which the *in vitro* results from our study compare favorably. In fact, the *in vitro* degradation rates for the P-Mg control and ZSr41 pins obtained in our study rank in the lower end and middle segment, respectively, compared with a variety of Mg-based biomaterials incubated for 3, 7 and 14 days in Minimum Essential Medium (MEM) without serum [36]. Additionally, although

not strictly an indicator of degradation rate, the ease with which the ZSr41 pins oxidized after autoclaving compared with the P-Mg control (Figure 6.1c and 6.1d), could also be indicative of the higher tendency of the as-drawn ZSr41 pins to corrode. Interestingly, in addition to HA, a variety of oxide and hydroxide phases formed on the surfaces of both ZSr41 and P-Mg pins after *in vitro* degradation. Although ZSr41 had a Ca/P ratio closer to that of HA (compared with P-Mg), the calculated Ca/P ratio is only a rough estimate of the actual HA ratio on the surface of each pin since Ca or P was found in other phases. Therefore, an in-depth study (e.g. through x-ray photoelectron spectroscopy) is necessary to quantify the percent of each phase identified through XRD (Figure 6.4a' and 6.4b') in order to accurately assess the Ca/P ratio and mineral quality of the HA found on the surfaces of ZSr41 and P-Mg pins after *in vitro* degradation.

The *in vivo* degradation rate of the ZSr41 was studied for the first time and, when used as intramedullar implants placed in rat tibiae for 47 days, the degradation rate of ZSr41 was significantly higher compared with the P-Mg control. Results from weekly μCT scans (Figure 6.5a) along with corresponding 3D-reconstructed VOIs (Figure 6.6h) showed a considerably faster degradation rate for the ZSr41 intramedullar pins compared with the P-Mg control. Quantification of the percent volume at each time point relative to the initial volume (Figure 6.6i) confirmed a significantly faster degradation rate for ZSr41 implants compared with the P-Mg control as early as day 12. Due to the lack of statistical power, significant differences could not be confirmed for earlier time points but the trend of faster

degradation for ZSr41 compared with P-Mg was observed as early as day 3. The measured *in situ* volumetric percentage was then confirmed through analysis of dissected implants (Figure 6.7a and 6.7b), elemental mapping of the tissue-implant interface (Figure 6.8), and histological evaluation (Figure 6.9). All of which qualitatively confirmed near-complete resorption of the ZSr41 intramedullar pin but considerable residues of the P-Mg implant. Surface characterization of the dissected implant through SEM, EDS, and XRD (Figure 6.7) showed the formation of Mg, $Mg(OH)_2$ and HA and results are in agreement with previous evaluations of Mg-Sr intramedullar implants placed in mice femora [14] and Mg-Ca intramedullar implants placed in rabbit femora [42]. To our knowledge, this is the first report on the *in vivo* implantation of ZSr41 alloys; however, the degradation performance of the as-drawn ZSr41 pins in the present study (i.e. complete resorption in approximately 8 weeks) did not meet clinical requirements. In fact, to our knowledge, these ZSr41 pins rank among the faster-degrading Mg alloys tested *in vivo* and reported in published literature. Nevertheless, the corrosion behavior of the as-drawn ZSr41 pins could be enhanced via surface modifications or coatings.

The *in vivo* average daily degradation rates of both ZSr41 and P-Mg intramedullar pins were significantly higher compared with their *in vitro* counterparts. These results are in agreement with previous studies that reported higher *in vivo* degradation rates, compared with their *in vitro* (via immersion) counterparts, for rolled Mg-2Sr [14] and extruded Mg-6Zn [43] intramedullar implants, and for high-purity Mg (99.99 wt. %) transcortical screws [15].

Specifically, for the Mg-2Sr study, Gu et al. compared the *in vitro* degradation rate obtained from the immersion of implants in Hank's solution during 500 hours of immersion with the *in vivo* degradation rate obtained from implantation in the femoral shaft of C578L/6 mice for 4 weeks [14]. Likewise, for the Mg-6Zn study, Zhang et al. compared the *in vitro* degradation rate obtained from the immersion of implants in SBF during 3 and 30 days with the *in vivo* degradation rate obtained from implantation in the femoral shaft of New Zealand white rabbits for 14 weeks [43]. Similarly, Han et al. compared the *in vitro* degradation rate obtained from the immersion of implants in modified SBF during 4 and 16 weeks with the *in vivo* degradation rate obtained from transcortical implantation in fractured femoral condyles of New Zealand white rabbits for 4 and 24 weeks [15]. Collectively, however, results where the *in vivo* degradation is higher compared with *in vitro* immersion contrast dramatically a wide body of literature that shows the opposite trend. A recent comprehensive review by Martinez Sanchez et al. showed that for many Mg alloys, the *in vivo* degradation rate could be as much as 9 times lower compared with results from *in vitro* immersion tests [10]. Although Martinez Sanchez et al. accurately pointed out the intrinsic effect of implantation site on the measured *in vivo* degradation rate, the systematic review fell short of highlighting the importance of implantation site along with method and time periods considered to measure the corrosion rate. In this study, as well as those presented as comparison [14, 15, 43], the Mg-based implants were placed in anatomical regions rich in vasculature which very likely exacerbated the *in vivo* corrosion rates.

Willbold *et al.* showed that the *in vivo* degradation of AZ31 screws was largely dependent on the implantation site [44]. Likewise, a growing body of literature supports a faster corrosion rate of Mg-based implants in the trabecular region, which is rich in vasculature and body fluids, compared with cortical bone [11, 12, 14, 45, 46]. Our methods for measurement of *in vitro* and *in vivo* corrosion (immersion in complete culture media and *in situ* µCT, respectively) are in accordance with the recommendations presented by Martinez Sanchez et al. to provide accurate and continuous corrosion measurements. Thus, our evaluation of *in vitro* with *in vivo* corrosion rates compared with published literature is meant to complement efforts, such as those of Martinez Sanchez et al., to establish comprehensive correlations/models to bridge the growing gap between *in vitro* and *in vivo* tests. In doing so, we seek to make benchtop experiments more relevant and avoid unnecessary animal experiments.

6.4.2. The cytocompatibility of as-drawn ZSr41 pins in co-culture with BMSCs

A significant reduction in BMSC adhesion density on the culture plates at R_1 after 3 days of co-culture with ZSr41 pins, compared with the BMSCs-only control, gave first indication of possible detrimental effects due to the significantly faster *in vitro* degradation rate of ZSr41 (compared with P-Mg). Results of the 3-day *in vitro* evaluation of the cytocompatibility of ZSr41 pins in co-culture with BMSCs (Figure 6.3a-6.3d) showed that although ZSr41 showed signs of significantly faster

degradation as early as day 1 (compared with P-Mg), it was not until day 3 that negative effects on BMSC adhesion density were observed. Furthermore, a comparison of BMSC adhesion density at all three locations evaluated (R_0, R_1, and R_2) showed a significant reduction only at R1 (Figure 6.3b-6.3d); however, the mean adhesion density for ZSr41 at all three locations was the lowest compared with P-Mg and the BMSCs-only positive control. Since rat-derived BMSC viability is not affected *in vitro* by supplemented Mg^{2+} ion concentrations up to 27.6 mM [7], and since during the 3-day culture period the daily [Mg^{2+}] in the culture media did not exceed 7 mM, it is reasonable to conclude that the significant reduction in BMSC adhesion density was likely due to the significant increase in media alkalinity. We should mention that the $NaHCO_3$-CO_2 buffering system can effectively buffer sharp increases in media pH in very short time periods [7], indicating that the actual pH during degradation was likely higher than what was measured for the media collected (Figure 6.3f). In fact, previous results from our group showed that media pH of 9.5 significantly reduced BMSC adhesion density *in vitro* [7]. Previously, our group introduced the direct *in vitro* culture method designed for Mg-based materials to study interactions and possible cytotoxic effects at the cell-biomaterial interface [7]. In the direct culture method, cells are seeded directly onto the sample surface, but also seeded surrounding the sample; in doing so, we can evaluate cells (i) in direct contact with the sample, and (ii) in indirect contact with the sample. Thus, the direct culture method complements traditional immersion-based methods (i.e. ISO 10993) and provides a more

physiologically relevant model to study Mg-based biomaterials. In a previous study, we investigated the cytocompatibility of rolled and aged Mg-4Zn-xSr (x = 0.15, 0.5, 1.0, and 1.5 wt. %) alloy sheets using the direct culture method with BMSCs [5]. Results from this study showed that the Mg-4Zn-1Sr alloys (i.e. ZSr41) remained largely cytocompatible with BMSCs both in direct and indirect contact with the samples up to 3 days. In fact, there were no significant differences in BMSC adhesion density compared with the glass reference and cells-only positive control. It should be pointed out that the degradation rate of the rolled and aged ZSr41 sheets in DMEM was approximately one-third compared with that of the as-drawn pins (Figure 6.10d). Thus, it is reasonable to conclude that the reduced BMSC adhesion density reported in this study was related to the fast degradation rate (and concomitant induced alkalinity) and not to the alloying elements in the Mg-Zn-Sr alloys. In fact, solubilized [Mg^{2+}], [Zn^{2+}], and [Sr^{2+}] in the media during the 3-day *in vitro* degradation of the ZSr41 pins (Figure 6.3g-6.3i) were all below the therapeutic daily dosages (TDD) and LD50 reported in literature [2]. Although first indications of cytotoxicity were observed in this study for the as-drawn ZSr41 pins with BMSCs, previous studies verified the cytocompatibility of Mg-Zn-Sr alloys with H9-hESCs [2], fibroblasts [3, 38], HUVECs [4], osteoblasts [47], and BMSCs [5]. Thus, Mg-Zn-Sr crystalline ternary alloys with slower degradation rates (compared with ZSr41 as-drawn pins) should be further studied for orthopedic implant applications.

6.4.3. Host response at the implantation site to fast-degrading ZSr41 intramedullar implants

The fast degradation rate of the ZSr41 intramedullar pins induced aggressive bone remodeling throughout the 47-day implantation in the rat tibia. While a growing body of literature converges on the ability of Mg-based implants to increase peri-implant bone formation in animal models [11, 14, 15, 42, 45, 46, 48-51], only a few studies have focused on host response to fast degradation rates of Mg-based biomaterials (either due to intrinsic material properties or anatomical placement, as pointed out in Section 6.4.1) [11, 51]. Three main discussion points will be presented pertaining to the host response to fast-degradation characteristics of intramedullar ZSr41 pins: (i) hydrogen-gas-induced damage on surrounding tissue persisted throughout the degradation of the intramedullar implants; (ii) aggressive remodeling along with a significant increase in peri-implant bone volume was measured for ZSr41 compared with P-Mg and Sham groups; and (iii) the quality of the newly-formed peri-implant bone was distinct for ZSr41 compared with the Sham group.

Hydrogen gas released during the fast degradation of ZSr41 implants induced damage on peri-implant cortical bone tissue and bone marrow cells. The formation of hydrogen gas pockets inside the bone tunnel was observed via μCT scans for both implant groups (Figure 6.5a). Damage to the peri-implant cortical bone region caused by released hydrogen gas, which showed up as cavities, was visualized in

the 3-D reconstructed bone segments (Figure 6.6a, top row). Analysis of these results showed that damage to the cortical bone was most prominent in the ZSr41 group compared with the P-Mg group. In contrast, no damage was observed in the 3-D reconstructions for the Sham control group. Since no animals were sacrificed during intermediate time points, the damage was verified via histological analysis only at day 47 post-implantation (Figure 6.9). Both Toluidine blue and Goldner trichrome stained sections confirmed the presence cavities in the peri-implant cortical bone region for the ZSr41 group, along with the permanence of acellular pockets for both implant groups. Previous studies showed damage to the peri-implant cortical bone region (although they attributed some of the occurrences to segmentation artifacts) caused by the degradation of Mg-based implants [14, 51]. More recently, Kraus et al. and Wang et al. studied Mg-alloys as implant materials and reported on the effects of gas accumulation on bone healing [11, 16]. Starting from an inflammatory response evaluation, both studies indicated a lack of inflammatory cell infiltration, which is consistent with published literature for a variety of Mg alloys evaluated up to 36 weeks post-implantation [11, 16, 44-46, 50, 52]. Subsequently, during weeks 4 through 12 post-implantation, Kraus et al. observed substantial peri-implant gas and gas-induced cavity formation via µCT scans, 3-D reconstructions, and histological analysis. The authors suggested that accumulation of hydrogen gas pressure induced mechanical stress during the cortical bone reparative phase resulting in altered callus formation. From week 12, when most of the Mg alloy implant was resorbed and hydrogen gas evolution

reduced, Kraus et al. observed quick bone remodeling and healing of bone defects up to week 24 when near-complete restoration was observed [11]. In a separate study, Wang et al. reported that hydrogen gas formation resulting from the degradation of Mg-Zn-Zr alloys caused cavity formation in peri-implant cortical bone with the largest cavities occurring 8-12 weeks post implantation. At 24 weeks post-implantation, μCT scans, 3-D reconstructions, and histological analyses confirmed an improvement in trabecular and cortical bone characteristics along with a reduction in local bone damage. The authors indicated that the gradually-disappearing gas cavities were filled with newly regenerated bone, cartilage, and fibrous tissue [16]. Wang et al. pointed out that the main concern regarding hydrogen gas formation did not pertain to bone remodeling (which is achieved following cavity formation), but rather to the loosened contact at the implant-tissue interface which would reduce the effectiveness of the Mg-based fixation device. Interestingly, although the time frames for cavity formation (up to week 12 post-implantation) and bone healing (12-24 weeks post-implantation) were similar for both studies, it should be noted that the degradation time frames for the alloys used were drastically distinct. Specifically, the ZX50 alloy used by Kraus et al. was almost completely resorbed in 12 weeks whereas the Mg-Zn-Zr alloy used by Wang et al. lasted well over 6 months. Therefore, our results of observed hydrogen gas formation and hydrogen-gas-induced defects in the peri-implant cortical bone region surrounding the ZSr41 intramedullar pins are well in agreement with the studies by Kraus et al. and Wang et al. since production of large quantities of

hydrogen gas would be expected during the *in vivo* degradation of the continuously fast-degrading of the ZSr41 alloy. Additionally, our results show for the first time that the accumulation of degradation products (hydrogen gas or local alkalization) resulting from fast degradation of Mg-based biomaterials caused a drastic reduction in the amount of peri-implant bone marrow cells. In fact, previous *in vitro* studies showed a reduction in rat-derived BMSC viability in response to increased alkalinity [7]. By comparison, we could speculate an onset of quick bone remodeling following complete resorption of the ZSr41 pins (approximately 8 weeks post-implantation); however, the reduced amount of BMSCs could potentially have an impact on the rate or overall effectiveness of the remodeling process. Furthermore, our results from the *in vivo* degradation of P-Mg also confirmed that the degradation rate is a critical factor to control adverse reactions during bone remodeling at the implant site. Specifically, although hydrogen gas pockets were observed up to 47 days (approximately 7 weeks) post-implantation of P-Mg, the reduced degradation rate (compared with ZSr41) induced drastically fewer defects in the peri-implant bone during the healing process. Remarkably, in all cases reported in literature despite the degradation rate of the Mg-based implant used, it is widely accepted that the gas produced from the *in vivo* degradation of the Mg-based biomaterial is gradually absorbed by the host tissue without noticeable systemic or animal mobility effects.

A significantly increased peri-implant bone volume was measured for ZSr41, compared with P-Mg and Sham groups, despite adverse reactions caused by

hydrogen gas production. A qualitative analysis of the *in situ* 2-D µCT scans (Figure 6.5a, top row) along with a quantification of the 3-D reconstructed peri-implant bone volume regions (Figure 6.6a) at day 12 (Figure 6.6b), day 28 (Figure 6.6c), and day 47 (Figure 6.6d) confirmed significantly higher volumes for peri-implant trabecular and cortical bone regions surrounding the ZSr41 intramedullar pins compared with the P-Mg and Sham groups at day 47 post-implantation. The increased peri-implant bone formation measured around the ZSr41 intramedullar pins at day 47 was confirmed through a qualitative EDS analysis on resin-embedded undecalcified cross sections which showed aggressive remodeling characterized by cortical bone formation at the site of implantation and resorption (Figure 6.8a, top row). Similarly, EDS and XRD analyses of the dissected ZSr41 residual implant confirmed HA formation on the implant surface (Figure 6.7), which was indicative of bone formation at the tissue-implant interface. Furthermore, histological analysis of undecalcified plastic-embedded sections (Figure 6.9) confirmed the formation of mineralized woven bone at the site where the ZSr41 implant was placed and resorbed. The presence of unmineralized osteoid tissue at the site of implantation and resorption of the ZSr41 pin gave evidence of the presence of osteoblasts and subsequent osteogenesis [35]. Numerous studies showed an increase in peri-implant bone volume [11, 14-16, 42, 45, 48-50, 53, 54] caused by an increase in osteoblastic and/or osteoclastic activity in response to the release of Mg^{2+} ions resulting from degradation of Mg-based implants [11, 15, 42, 49, 50, 53]. It was suggested that reactive bone hyperplasia was the cause of

increased peri-implant bone growth induced by the degradation of Mg-containing biodegradable implants [51]. In our case, it is also likely that osteoblastic activity was further enhanced by Sr^{2+} ions released during the degradation of ZSr41, as indicated by previous studies on Mg-Sr alloys for orthopedic implant applications [14, 53]. Our results also showed that while the degradation of the ZSr41 intramedullar caused an increase in peri-implant bone volume, a systemic increase of Mg^{2+}, Sr^{2+}, or Zn^{2+} ions concentration in the blood serum for the ZSr41 group was not detected (Figure 6.5b-6.5d, respectively). Similarly, previous studies showed that the *in vivo* degradation of Mg-based implants did not cause an increase in Mg^{2+} ion concentration in the blood [14, 42, 45, 46]. In fact, previous studies also evaluated the response of visceral organ function to the degradation of Mg-based implants and confirmed minimal/no effect on liver function and no effect on kidney function, among others [46, 53, 54]. Although some significant differences were observed between the ZSr41, P-Mg, and Sham groups, it should be noted that these differences were within a very narrow range, all values were well under therapeutic daily dosages [2], and the slight variations could have resulted from slight differences in the amount of food intake. Furthermore, even though a significant increase in peri-implant bone volume surrounding the P-Mg implant was not measured (compared with the Sham control at any of the evaluated time points; Figure 6.6b-6.6d), the following data gave qualitative evidence of bone remodeling induced by the degradation of the P-Mg pin: the 2-D µCT scans (Figure 6.5a, middle row) showed cortical bone remodeling surrounding

the pin at days 12 and 28; the mean trabecular and cortical bone volumes (Figure 6.6b-6.6d) was higher for P-Mg compared with the Sham group, though not statistically significant due to large standard deviation; EDS and XRD analyses of the dissected pin confirmed HA on the surface of the P-Mg implant (Figure 6.7); EDS cross-sectional analysis confirmed a layer of Ca and P (most likely HA based on EDS and XRD analyses of the dissected implant) at the tissue-implant interface (Figure 6.8a, middle row); and, histological analysis confirmed the formation of woven bone and osteoid tissue at the site of implantation/resorption of the P-Mg implant (Figure 6.9), both important indicators of osteoblastic activity. The overall bone remodeling response to the degradation of the ZSr41 intramedullar pin can be described as a result from two parallel reactions: one in which an ion-induced stimulation led to bone growth, and another in which hydrogen gas formation led to cavity formation and bone damage [11, 16]. In that regard, the net gain in peri-implant bone volume surrounding Mg-based implants (i.e. ZSr41 and P-Mg intramedullar pins) is described by ion-induced stimulation dominating over hydrogen-gas-induced cavity formation, even for rapidly degrading alloys such as ZX50 [11] or ZSr41 presented in this study.

Our results showed for the first time that although a significant net increase in peri-implant volume resulted from the rapid degradation of ZSr41 intramedullar implants, the quality of the newly formed bone was significantly inferior when compared with the Sham control. Weight density values obtained from voxel grayscale intensity of the 3-D reconstructed peri-implant cortical VOIs (Figure 6.6f-

6.6g) showed significantly lower values for ZSr41 when compared with P-Mg and Sham at 28 and 47 days post-implantation. Interestingly, the significantly lower weight density values for the ZSr41 pertained to the peri-implant cortical region of significantly higher volume (i.e. newly formed bone stimulated whose growth was stimulated by the degradation of the ZSr41 pin). The mineral quality of the bone was further evaluated using point EDS analyses on resin-embedded cross-sections harvested at day 47 post-implantation which showed a significantly lower Ca/P at. %/at. % ratio for the cortical bone surrounding the ZSr41 implant compared with newly formed bone at the site of ZSr41 implant resorption, with cortical bone surrounding the P-Mg implant, and with cortical bone in the Sham control. To our knowledge, only Kraus et al. reported on the bone remodeling response to a rapidly degrading ZX50 alloy which was completely resorbed in approximately 12 weeks [11], and an evaluation of bone weight density, bone mineral density (BMD), or bone mineral content (BMC) was not included in their study. Likewise, Gu et al. observed distinct Ca/P ratios in newly formed peri-implant bone which they attributed to bone remodeling [14]. We speculate that the drastically fast degradation of as-drawn ZSr41 intramedullar pins stimulated bone remodeling through reactive bone hyperplasia; however, the remodeling process was too aggressive and the surplus of bone would have reduced mechanical stress values (i.e. constant loading with increase in bone cross sectional area) necessary for proper bone healing according to Wolff's law [55]. It is also a possibility that even though ion release during ZSr41 degradation resulted in a net bone volume

gain, the loss in mineral quality could be correlated with the concomitant high amounts of hydrogen gas released during the rapid degradation of ZSr41 intramedullar pins. In contrast, previous studies evaluating bone quality in response to the *in vivo* degradation of Mg alloys (with complete resorption lasting well into several months) did not report adverse effects on BMD [14, 15] or tissue mineral density (TMD) [16]. Taken together, our results from the host response to the fast-degrading ZSr41 intramedullar pins at the implantation site showed for the first time that a Mg alloy with resorption time of approximately 8 weeks was able to stimulate a significant net bone growth. However, in parallel, hydrogen gas accumulation induced considerable damage on peri-implant bone and the newly formed bone did not show proper mineral quality, which might have been due to reduced mechanical stresses necessary for proper bone healing.

6.5. Conclusions

This article reports for the first time: the *in vitro* degradation of as-drawn ZSr41 pins and their cytocompatibility with BMSCs using the co-culture method, and the biocompatibility and *in vivo* degradation of as-drawn ZSr41 intramedullar pins implanted in rat tibiae for 47 days. Given the drastically-fast *in vivo* degradation rate of the ZSr41 implants, we presented the utility of a fast-degrading alloy to illustrate the host response to high dissolution rates and concomitant degradation products at the implantation site. The following major conclusions were drawn from the present study:

1. In this study, the as-drawn ZSr41 pins showed a significantly faster *in vitro* degradation rate compared with the P-Mg control after 3 days of incubation in DMEM media in co-culture with BMSCs. First signs of reduced BMSC adhesion density were observed at day 3, indicating cytotoxicity possibly due to an increase in media alkalinity resulting from the rapid *in vitro* degradation of the as-drawn ZSr41 pins.

2. The *in vivo* degradation rate of the ZSr41 was studied for the first time and, when used as intramedullar implants placed in rat tibiae for 47 days, the degradation rate of ZSr41 was significantly higher compared with the P-Mg control.

3. The *in vivo* average daily degradation rates of both ZSr41 and P-Mg intramedullar pins were significantly higher compared with their *in vitro* counterparts. The significantly faster *in vivo* degradation rate likely resulted from placement in the highly-vascularized intramedullar region. Although a growing body of literature for Mg-based implants supports slower *in vivo* degradation rates compared with *in vitro* results, our results agree with other intramedullar implant studies suggesting that implant placement is a critical factor to consider when correlating *in vitro* with *in vivo* results.

4. Our results from the host response to the fast-degrading ZSr41 intramedullar pins at the implantation site showed for the first time that the ZSr41 alloy (with resorption time of approximately 8 weeks) was able to stimulate a significant

net bone growth. However, in parallel, hydrogen gas accumulation induced considerable damage on peri-implant bone and the newly formed bone did not show proper mineral quality, which might have been due to reduced mechanical stresses necessary for proper bone healing. Thus, properly engineering the degradation rate of Mg-based implants is a critical factor to control adverse reactions during bone remodeling at the implant site.

6.6. Figures and tables

Figure 6.1: Characterization of ZSr41 and P-Mg pins.
SEM micrographs and surface elemental composition quantified through EDS area analysis, and corresponding x-ray diffraction patterns, respectively, for: (a) and (a') polished ZSr41; (b) and (b') polished P-Mg; (c) and (c') autoclaved ZSr41; and, (d) and (d') autoclaved P-Mg. SEM insets in (c) and (d) are side-views of the surfaces respective to each sample. Original magnification: (a) and (b), 1,000x; (c) and (d), 160x; insets in (c) and (d), 500x. Scale bar = 50 µm for all images.

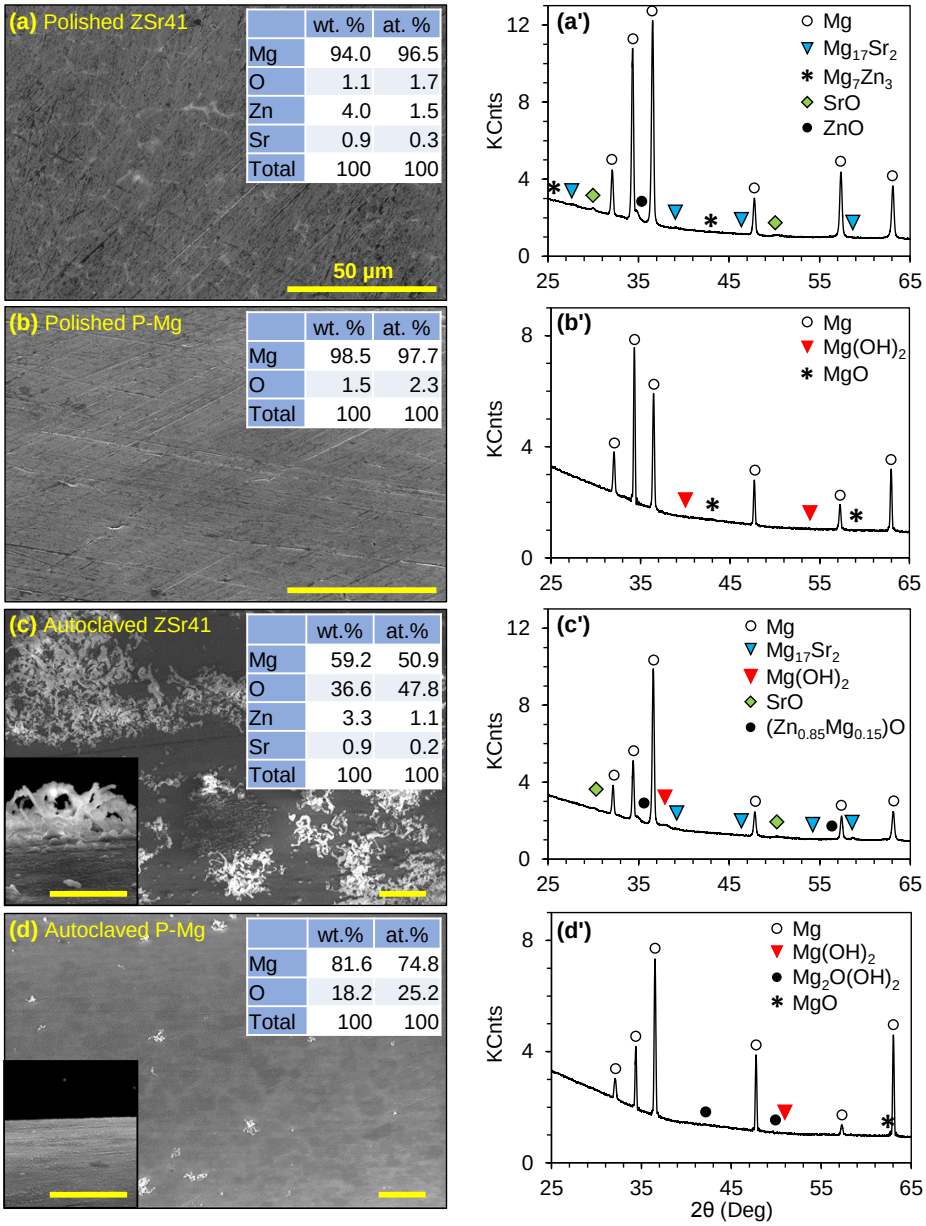

Figure 6.2: Electrochemical polarization testing results of ZSr41 and P-Mg pins. (a) potentiodynamic polarization response of polished metallic samples using r-SBF at 37°C as the electrolyte; and (b) corrosion potential and (c) corrosion current density obtained from Tafel-type extrapolation (ASTM G102-89) of potentiodynamic polarization curves; values are mean ± SD, n = 3, **p* < 0.05.

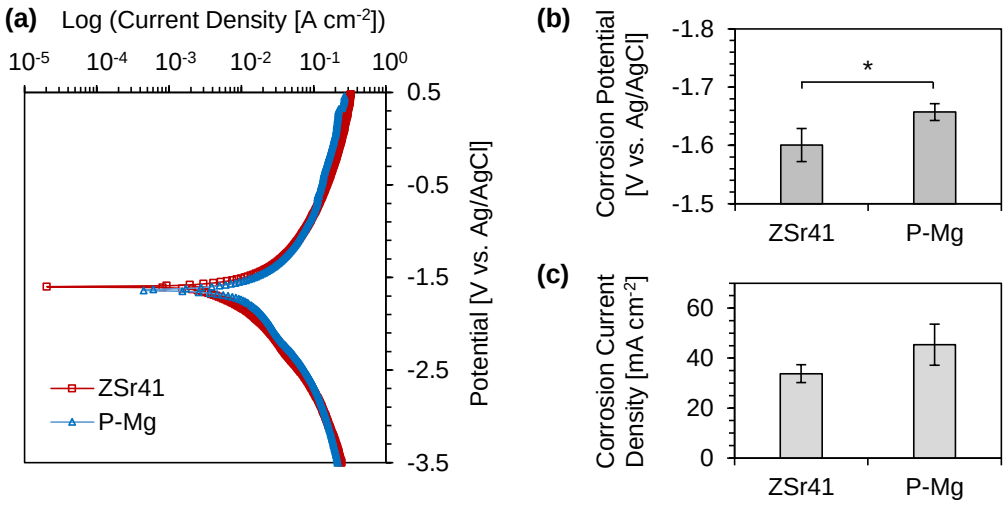

Figure 6.3: *In vitro* cytocompatibility and degradation of ZSr41 and P-Mg pins in co-culture (i.e. utilizing Transwell® inserts) with BMSCs during 3 day period (D1, D2, D3).

At each day interval, culture media was collected, measured, and replaced with fresh media. BMSC and DMEM designate cells-only positive control and blank culture media groups, respectively. (a) Representative fluorescence images of BMSCs adhered at plate location R_1 (3.5 mm from center of well) after co-culture with pins. Blue: DAPI stained nuclei. Green: Alexa Fluor® 488 stained cytoskeleton. Scale bar = 200 µm for all images. Original magnification: 10x. (b)-(d) BMSC adhesion density on culture plates at well center (R_0), 3.5 mm from well center (R_1), and 7.0 mm from well center (R_2), respectively. (e) Percent final mass (M_f) relative to initial mass of the pins (M_0). (f) pH of BMSC culture media incubated with pins. (g)-(i) Mg^{2+}, Zn^{2+}, and Sr^{2+} ion concentration, respectively, in BMSC culture media incubated with pins. Values in: (b)-(d) are average ± SE, and (e)-(i) average ± SD. (b)-(e) n = 3 for all groups and time points, and (f)-(i) n = 9 at D1, n = 6 at D2, n = 3 at D3 for all groups. *$p < 0.05$, **$p < 0.01$, ***$p < 0.001$.

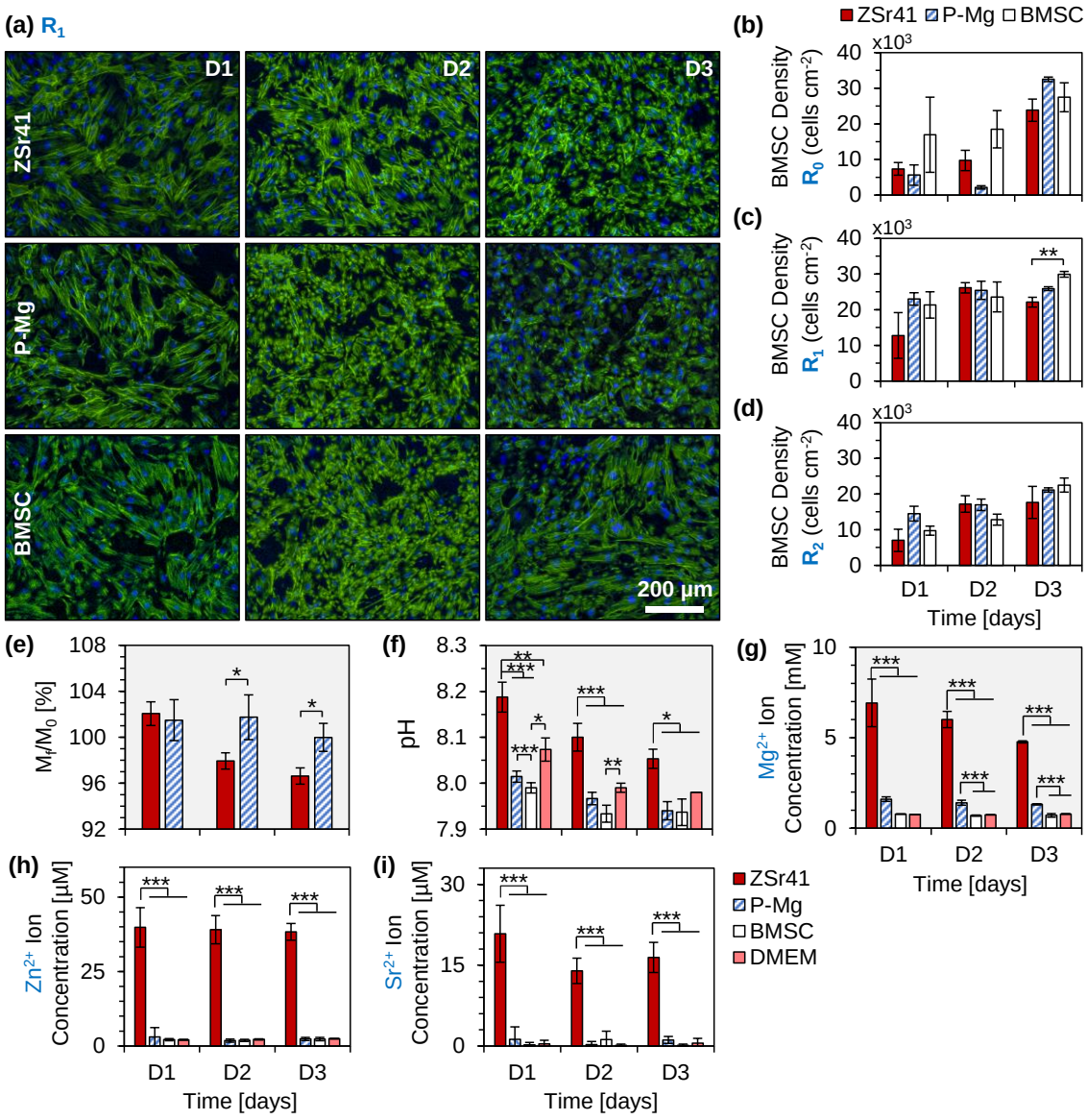
(a) R1
D1
D2
D3
ZSr41
P-Mg
BMSC
200 µm
(b)
ZSr41 P-Mg BMSC
x10³
BMSC Density R0 (cells cm-2)
(c)
BMSC Density R1 (cells cm-2)
(d)
BMSC Density R2 (cells cm-2)
Time [days]
(e)
Mt/M0 [%]
(f)
pH
(g)
Mg2+ Ion Concentration [mM]
(h)
Zn2+ Ion Concentration [µM]
(i)
Sr2+ Ion Concentration [µM]
ZSr41
P-Mg
BMSC
DMEM

Figure 6.4: Characterization of ZSr41 and P-Mg pins after *in vitro* degradation in co-culture with BMSC culture media during 3 day period.
High-area SEM micrographs and corresponding x-ray diffraction patterns, respectively, for: (a) and (a') ZSr41, and (b) and (b') P-Mg. SEM insets in (a) and (b) represent degradation that occurred at pin end segments. Original magnification: 65x, and scale bar = 500 µm for all images. (c) Surface elemental composition (at. %) quantified through EDS area analysis on (a) and (b) at 65x magnification.

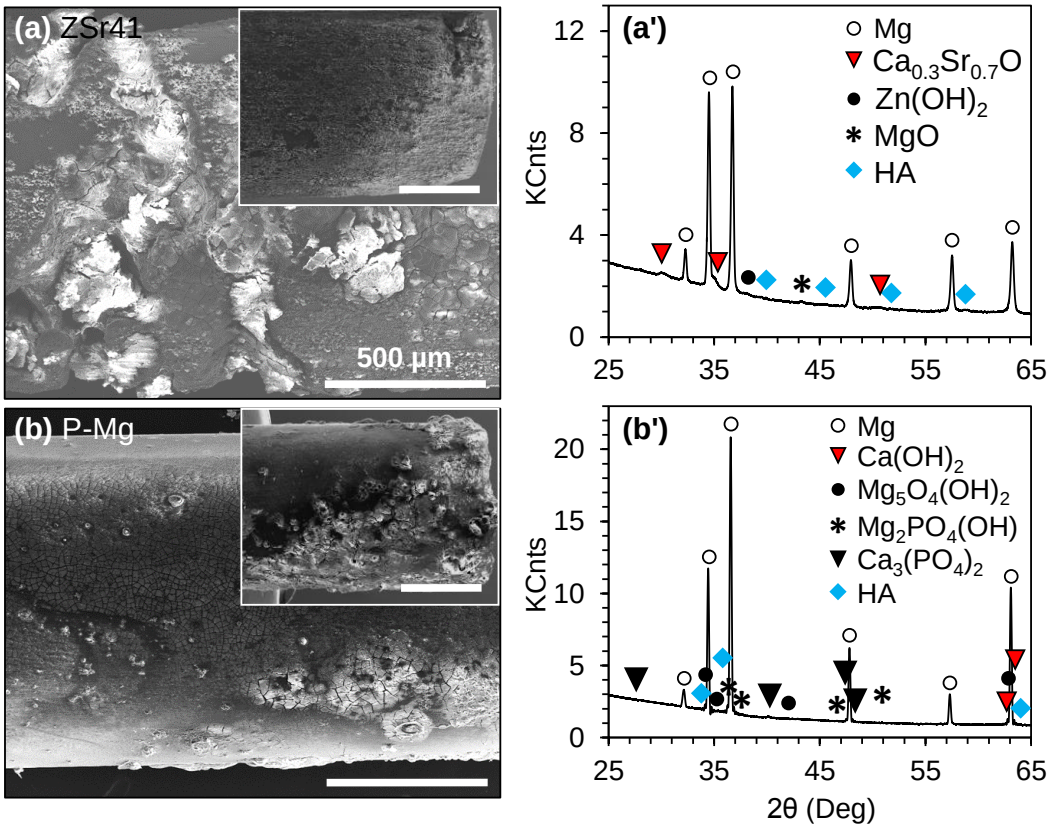

Figure 6.5: Weekly *in situ* measurements to monitor the *in vivo* degradation of intramedullar ZSr41 and P-Mg tibial pins throughout an implantation period of 47 days.

Sham designates control group with intramedullar cavity but no intramedullar pin implant. (a) Representative transverse 2-D µCT images obtained from the proximal tibia (at the mid-diaphysis 5 mm from the tibial plateau) with implanted intramedullar pins in 12-week old Sprague Dawley rats. Scale bar = 3 mm. (b)-(d) Mg^{2+}, Zn^{2+}, and Sr^{2+} ion concentration, respectively, in rat blood serum during implantation of intramedullar pins. Values are average ± SD; n = 6 for all groups during all time points. *$p < 0.05$, **$p < 0.01$, ***$p < 0.001$.

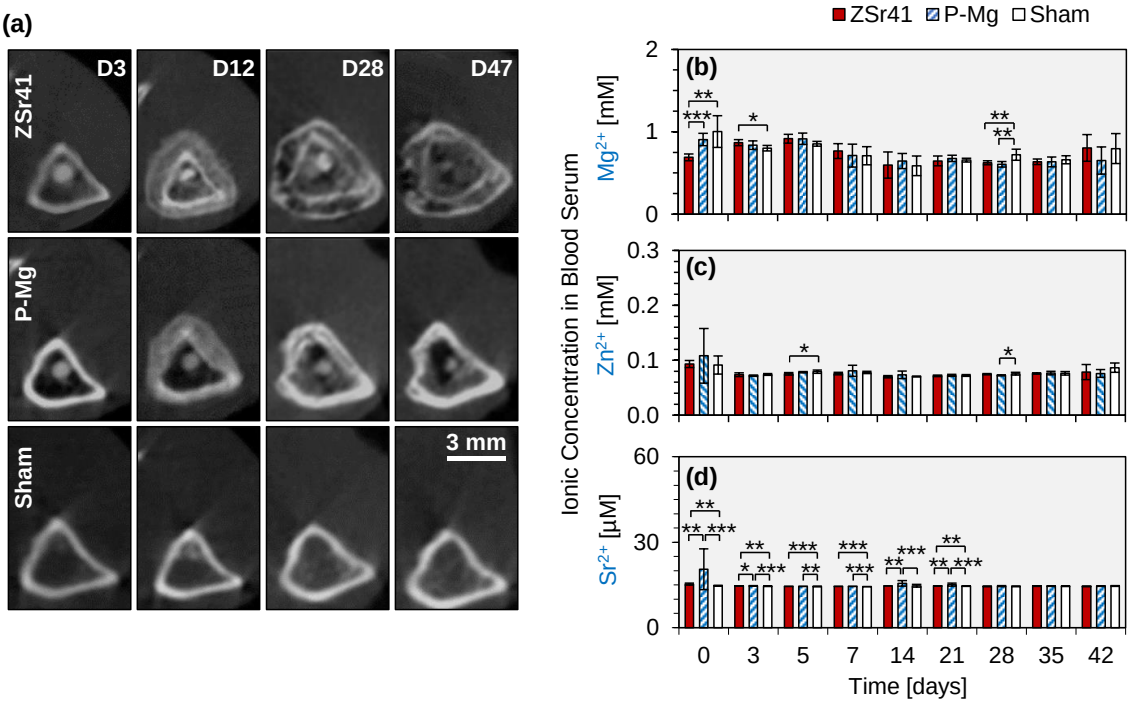

Figure 6.6: Bone remodeling of the proximal tibia in response to the degradation of intramedullar ZSr41 and P-Mg tibial pins throughout an implantation period of 47 days.

3-D structures were all reconstructed from µCT data in IMARIS® using the volume of interest (VOI) technique with an optimized threshold based on statistical analysis. Sham designates control group with intramedullar cavity but no intramedullar pin implant. (a) Representative 3-D VOI of the proximal tibia at 7, 28, and 47 days post-implantation of intramedullar pins. (b)-(d) Volume of the trabecular and cortical peri-implant bone regions of the proximal tibial diaphysis (defined between tibial tuberosity and 12.82 ± 50 mm distally from tibial plateau) at (b) 12, (c) 28, and (d) 47 days post-surgery. (e)-(g) Weight density (*i.e.* not bone mineral density) of muscle, and trabecular and cortical peri-implant bone regions specified in (b)-(d). The theoretical physical densities of ZSr41 (1.90 g cm^{-3}) and P-Mg (1.74 g cm^{-3}) and corresponding voxel grayscale intensity values at day 0 for the pins were used as calibration phantoms to calculate the physical density of each VOI. (h) Representative 3-D VOI of the intramedullar ZSr41 and P-Mg pins at select time points post-implantation. The dotted line in the VOI of ZSr41 pin at day 7 outlines a missing region of the implant caused by a misaligned µCT scan. Scale bar = 2 mm for all images. (i) Percent implant volume at each time point (V_i; i = 0, 3, 7, 12, 28, 39, and 47 days) relative to initial volume of each implant (V_0). The volume for Sham indicates the volume of the pre-drilled cavity. Values are average ± SD; see Table 1 for sample size for each group at each time point. *p < 0.05, **p < 0.01, ***p < 0.001.

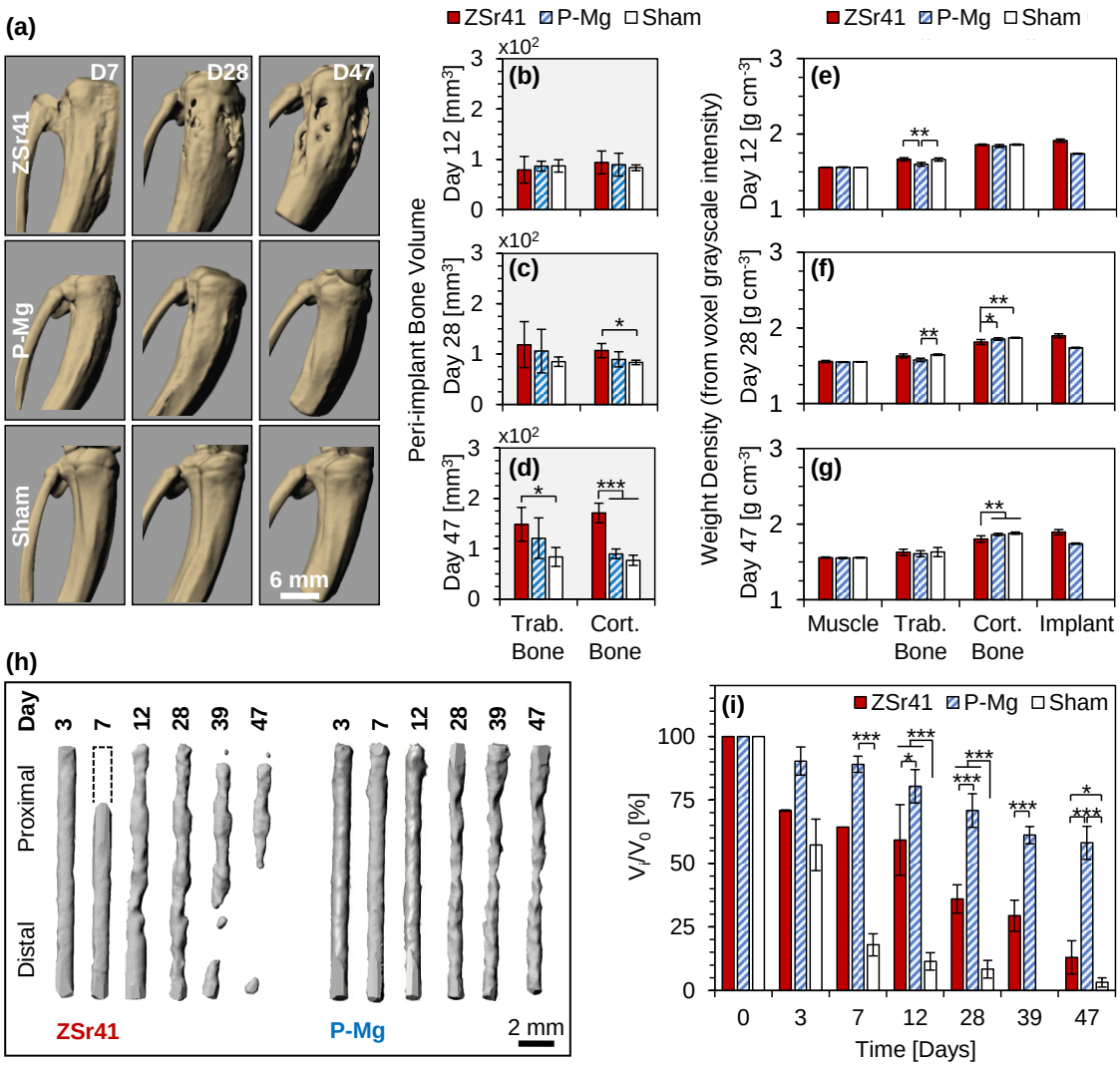
(a)
D7
D28
D47
ZSr41
P-Mg
Sham
6 mm
ZSr41 P-Mg Sham
Peri-implant Bone Volume
(b)
(c)
(d)
Day 12 [mm³]
Day 28 [mm³]
Day 47 [mm³]
x10²
Trab. Bone
Cort. Bone
Weight Density (from voxel grayscale intensity)
(e)
(f)
(g)
Day 12 [g cm⁻³]
Day 28 [g cm⁻³]
Day 47 [g cm⁻³]
Muscle
Trab. Bone
Cort. Bone
Implant
(h)
Day
3
7
12
28
39
47
Proximal
Distal
ZSr41
P-Mg
2 mm
(i)
ZSr41 P-Mg Sham
V_t/V_0 [%]
Time [Days]

Figure 6.7: Characterization of dissected residual ZSr41 and P-Mg intramedullar pins after implantation in rat tibiae during 47 days.
(a) and (b) Montage containing optical image of dissected pin, high-area SEM micrographs, and corresponding surface elemental distribution maps (Mg, Ca, and P) for (a) ZSr41 and (b) P-Mg. Original magnification: 50x, and scale bar = 500 µm for all images. Red rectangle indicates region of analysis on implant. (c) Surface elemental composition (at. %) quantified through EDS area analysis on SEM micrographs in (a) and (b) at 50x magnification. (d) X-ray diffraction patterns of the surface of the dissected residual ZSr41 and P-Mg implants, along with diffraction pattern for pulverized 19-week old rat tibia. Inset in (d) represents a close-up of the 46-52 Deg region of the spectra.

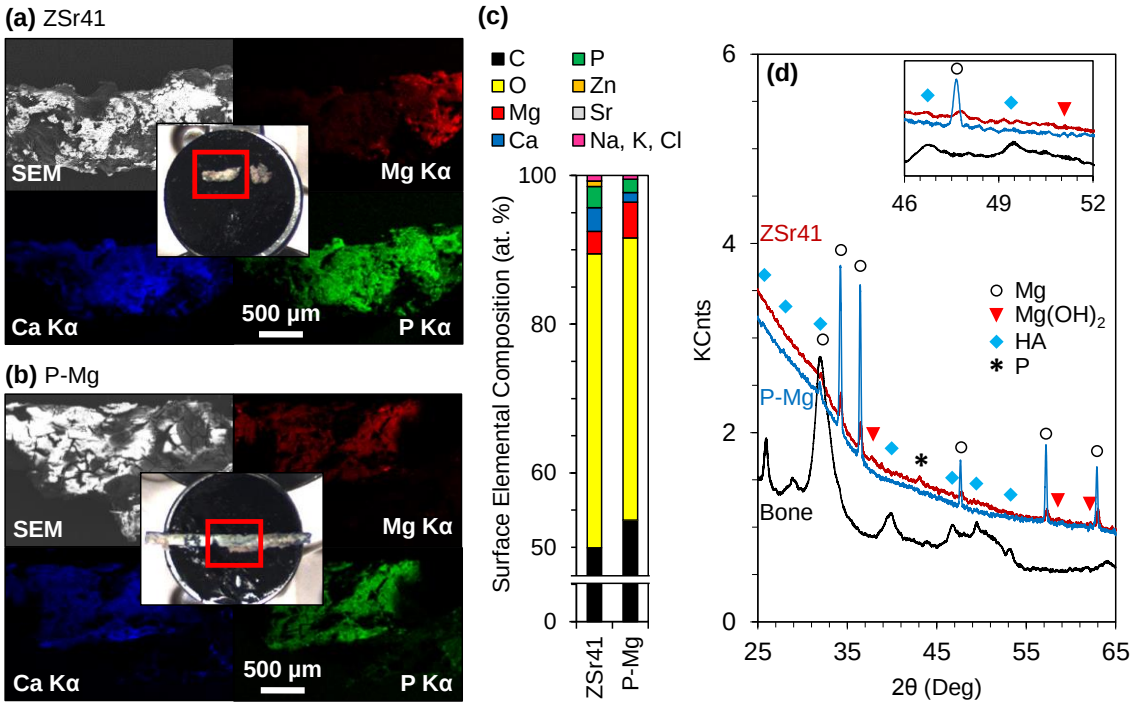

Figure 6.8: Elemental mapping analysis on epoxy-embedded transverse cross-sections obtained at the mid-diaphysis 5 mm from the tibial plateau with implanted intramedullar pins after implantation during 47 days.
Sham designates control group with intramedullar cavity but no intramedullar pin implant. (a) Montage containing composite SEM micrographs and corresponding surface elemental distribution maps (Mg, Zn, Sr, Ca, and P) for transverse cross-sections. At this anatomical location, the ZSr41 implant was completely resorbed, whereas a residual P-Mg implant with high Mg concentration was observed (indicated by white arrow in Mg Kα map for P-Mg). Original magnification: 50x, and scale bar = 1 mm for all images. (b) Quantification of Ca/P (at.%/at. %) ratio from EDS analyses at cortical bone regions indicated with white stars in P Kα distribution maps in (a). ZSr41 New Bone designates newly formed cortical bone fractions in the peri-implant bone tunnel (indicated with white arrowheads). Values are average ± SD; n = 3 for all groups. ***p* < 0.01, ****p* < 0.001.

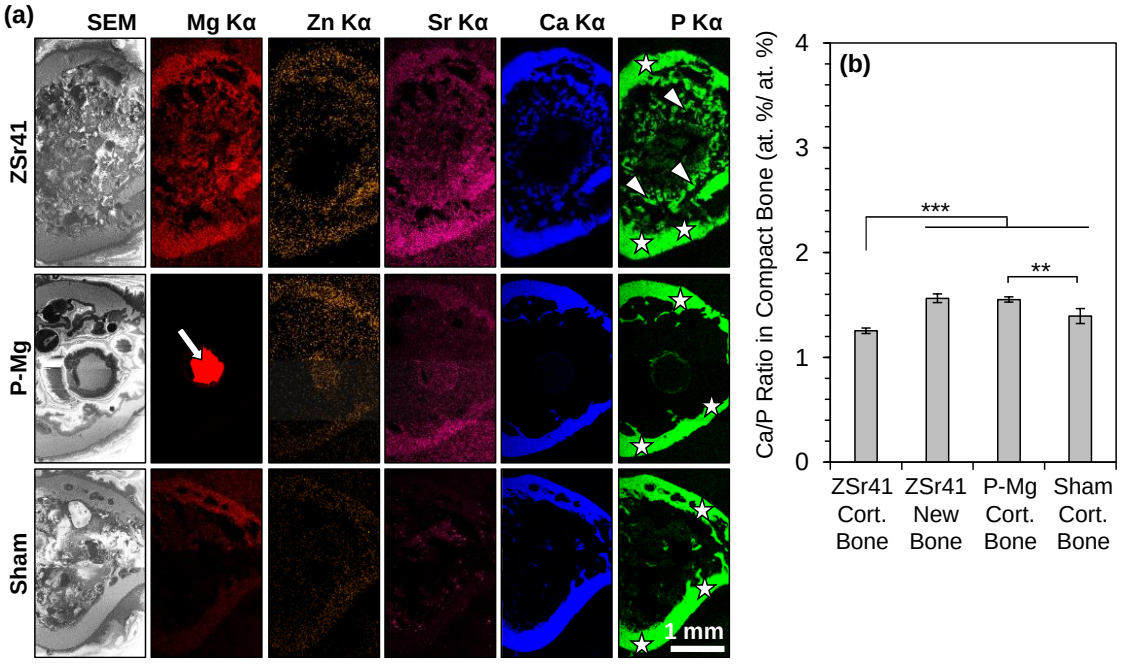

Figure 6.9: Representative histology of plastic-embedded undecalcified thin sections of tissue harvested 47 days post-implantation.

Sections were cut: (a) longitudinally along the saggital plane of the proximal tibia, and (b) transversally at the mid-diaphysis 6 mm from the tibial plateau. Sections were stained with Toluidine Blue (blue = cell structure, purple = collagen, and gray = bone) and Goldner Masson Trichrome (green = mineralized bone, red = unmineralized osteoid, and brownish-gray = bone marrow cells). Images were obtained at an original magnification of 2.5x; scale bar = 2 mm for all images. White arrowheads indicate new bone formation; black arrowheads indicate unmineralized osteoid; and, red arrows indicate hydrogen gas-induced cavities and absence of bone marrow cells.

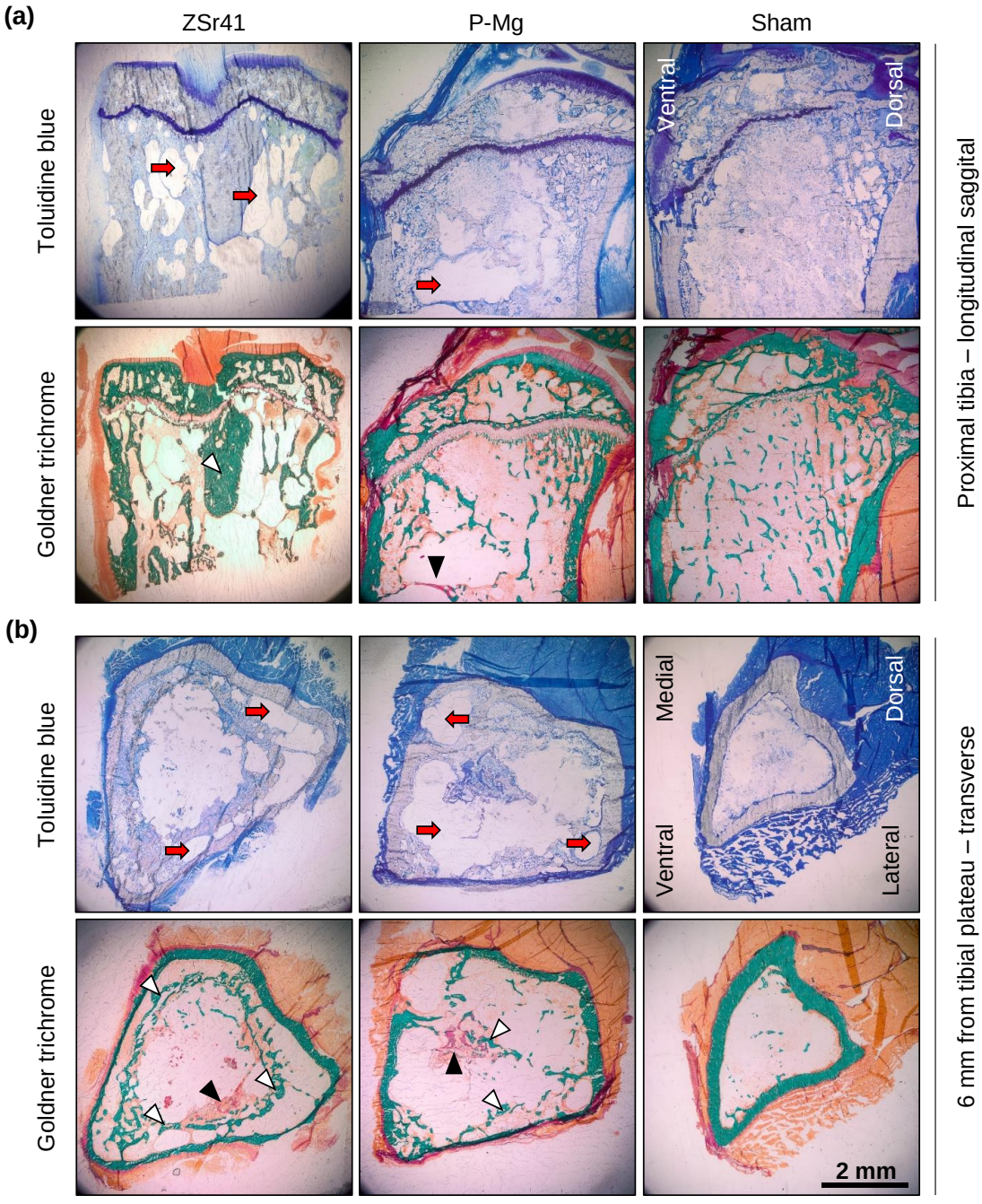
(a)
ZSr41
P-Mg
Sham
Toluidine blue
Goldner trichrome
Ventral
Dorsal
Proximal tibia – longitudinal saggital
(b)
Toluidine blue
Goldner trichrome
Medial
Dorsal
Ventral
Lateral
2 mm
6 mm from tibial plateau – transverse

Figure 6.10: Analysis of the *in vitro* and *in vivo* degradation of ZSr41 alloys. (a) Intramedullar pin volume during the implantation in the rat tibia as a function of time in days. Inset in (a) represents ratio of implant volume (V_i) at each time point relative to the initial implant volume (V_0) as a function of time in weeks. (b) and (c) Comparison of the average daily *in vitro* and *in vivo* degradation rates (mass loss rates) of ZSr41 and P-Mg pins relative to the (b) initial volume of the pins (V_0), or (c) initial surface area of the pins (SA_0). The average daily *in vitro* degradation rates were calculated from Mg^{2+} ion concentration in media and averaged over a 3 day period. The average daily *in vivo* degradation rates were calculated from volumetric values obtained from 3-D reconstructions and averaged over a 47 day period. Values are mean ± SD, n=3 for in vitro, and n=5 for in vivo; ***$p < 0.001$. (d) Average daily *in vitro* and *in vivo* degradation rates per unit SA_0 of ZSr41 and P-Mg pins from this study compared with published *in vitro* values [2, 4, 5]. The color of each bar designates the model system (*i.e.* media type, cell type, culture configuration, culture time) and the icon above each bar designates material properties (*i.e.* geometry, purity, processing, and for Mg, commercial source).

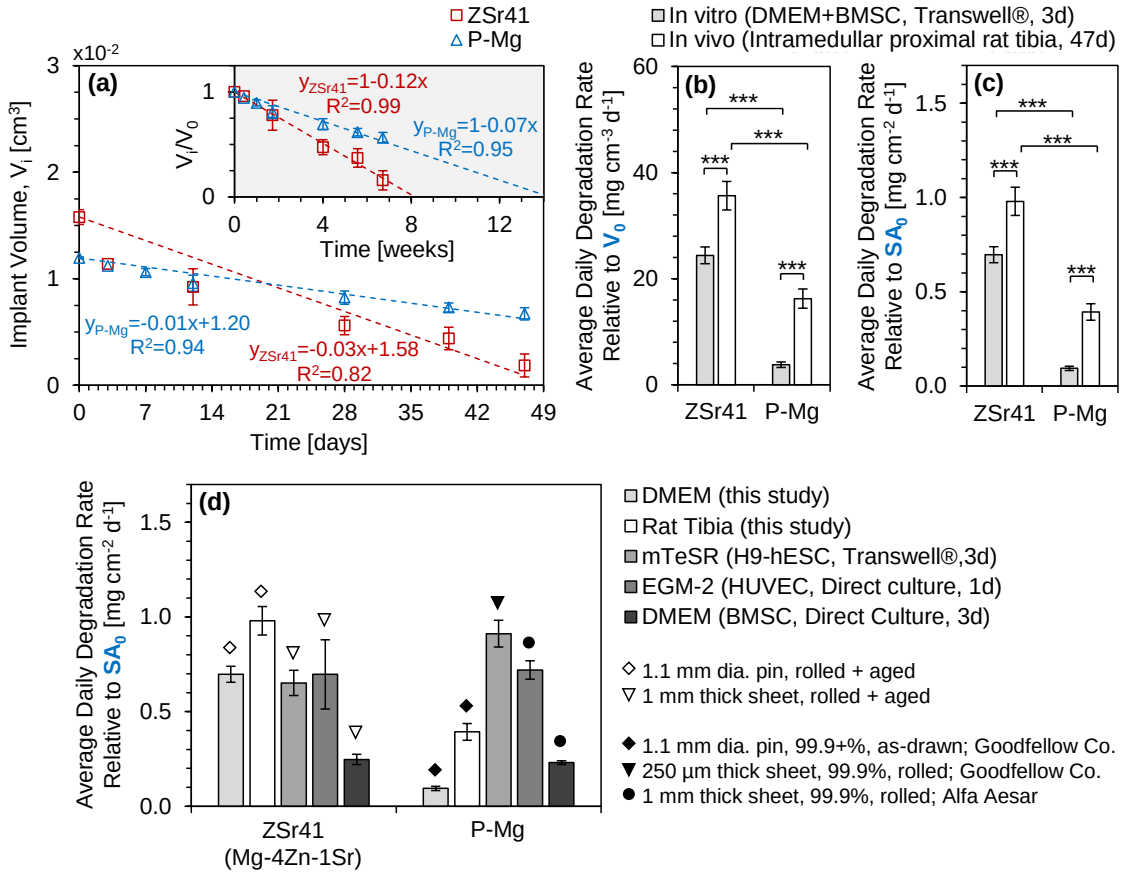

Table 6.1: Designated animals per group and data collected from each specimen to investigate the biocompatibility and *in vivo* degradation of ZSr41 intramedullar pins.

Rat ID	Group	Blood collected at all time points	µCT remarks	Time points (day #) with complete µCT scans for 3D reconstruction and analysis of peri-implant bone	Time points (day #) with complete µCT scans for 3D reconstruction and analysis of implant	Destructive testing technique *post mortem*
1	P-Mg	Yes		12, 28, 39	3, 7, 12, 28, 39, 47	Implant surface analysis (SEM/EDS/XRD)
2	P-Mg	Yes		12, 28, 39	-, -, 12, 28, 39, 47	Implant surface analysis (SEM/EDS/XRD)
3	P-Mg	Yes		12, 28, 39	3, 7, 12, 28, 39, 47	Histology
4	P-Mg	Yes	Implant placed partially outside of bone tunnel	N/A	N/A	N/A
5	P-Mg	Yes		12, 28, 39	-, 7, 12, 28, 39, 47	Histology
6	P-Mg	Yes		--, 28, 39	-, 7, --, 28, 39, 47	Bone-implant interface (SEM & EDS elemental mapping)
7	ZSr41	Yes		12, 28, --	3, -, 12, 28, 39, 47	Histology
8	ZSr41	Yes		12, 28, 39	-, -, 12, 28, 39, 47	Implant surface analysis (SEM/EDS/XRD)
9	ZSr41	Yes	Implant placed partially outside of bone tunnel	N/A	N/A	N/A
10	ZSr41	Yes		12, 28, 39	-, -, 12, 28, 39, 47	Histology
11	ZSr41	Yes		12, 28, 39	-, -, 12, 28, 39, 47	Bone-implant interface (SEM & EDS elemental mapping)
12	ZSr41	Yes		--, 28, 39	3, 7, --, 28, --, 47	Implant surface analysis (SEM/EDS/XRD)
13	Sham	Yes		--, 28, 39	3, -, --, 28, --, 47	Bone-implant interface (SEM & EDS elemental mapping)
14	Sham	Yes		12, 28, --	3, 7, 12, 28, --, 47	Histology
15	Sham	Yes		--, 28, 39	3, 7, --, 28, --, 47	Histology
16	Sham	Yes		12, 28, 39	3, 7, 12, 28, --, 47	
17	Sham	Yes		12, 28, 39	-, -, 12, 28, --, 47	
18	Sham	Yes		12, 28, 39	3, 7, 12, 28, --, 47	

Table 6.2: Results from statistical analyses on measured Mg^{2+}, Sr^{2+}, and Zn^{2+} ionic concentrations in collected blood serum.

Ion	Time point	Family-wise test	Family-wise statistics summary	*Post hoc* pairwise comparison (measured values, mean±SD)	Significance
Mg^{2+} [mM]	D0	ANOVA (w/o homogeny. variance)	$F(2, 8) = 22.806$, $p = 4.168 \times 10^{-4}$	ZSr41 (0.69±0.04) < P-Mg (0.91±0.07)	$p < 0.001$
				ZSr41 (0.69±0.04) < Sham (1.00±0.19)	$p < 0.01$
	D3	ANOVA	$F(2, 15) = 3.809$, $p = 4.59 \times 10^{-2}$	ZSr41 (0.87±0.04) > Sham (0.80±0.03)	$p < 0.05$
	D28	ANOVA	$F(2, 15) = 11.457$, $p = 9.452 \times 10^{-4}$	ZSr41 (0.62±0.02) < Sham (0.72±0.07)	$p < 0.01$
				P-Mg (0.60±0.03) < Sham (0.72±0.07)	$p < 0.01$
Zn^{2+} [mM]	D5	ANOVA	$F(2, 15) = 4.601$, $p = 2.766 \times 10^{-2}$	ZSr41 (75.49±2.32) < Sham (79.35±2.89)	$p < 0.05$
	D28	ANOVA	$F(2, 15) = 4.722$, $p = 2.567 \times 10^{-2}$	P-Mg (72.55±1.03) < Sham (75.49±2.55)	$p < 0.05$
Sr^{2+} [µM]	D0	Kruskal-Wallis	$X^2(2, N = 18) = 14.749$, $p = 6.272 \times 10^{-4}$	P-Mg (20.54±7.16) > Sham (14.74±0.13)	$p < 0.001$
				ZSr41 (15.31±0.33) < P-Mg (20.54±7.16)	$p < 0.01$
				ZSr41 (15.31±0.33) > Sham (14.74±0.13)	$p < 0.05$
	D3	Kruskal-Wallis	$X^2(2, N = 18) = 13.345$, $p = 1.265 \times 10^{-3}$	P-Mg (14.71±0.08) > Sham (14.55±0.05)	$p < 0.001$
				ZSr41 (14.64±0.02) > Sham (14.55±0.05)	$p < 0.01$
				ZSr41 (14.64±0.02) < P-Mg (14.71±0.08)	$p < 0.05$
	D5	ANOVA	$F(2, 15) = 14.526$, $p = 3.097 \times 10^{-4}$	ZSr41 (14.51±0.02) > Sham (14.46±0.02)	$p < 0.001$
				P-Mg (14.50±0.01) > Sham (14.46±0.02)	$p < 0.01$
	D7	ANOVA	$F(2, 15) = 21.873$, $p = 3.583 \times 10^{-5}$	ZSr41 (14.50±0.02) > Sham (14.43±0.01)	$p < 0.001$
				P-Mg (14.48±0.02) > Sham (14.43±0.01)	$p < 0.001$
	D14	Kruskal-Wallis	$X^2(2, N = 18) = 10.152$, $p = 6.245 \times 10^{-3}$	P-Mg (15.58±1.00) > Sham (14.72±0.46)	$p < 0.001$
				ZSr41 (14.68±0.04) < P-Mg (15.58±1.00)	$p < 0.01$
	D21	Kruskal-Wallis	$X^2(2, N = 18) = 15.158$, $p = 5.111 \times 10^{-4}$	P-Mg (15.15±0.53) > Sham (14.55±0.03)	$p < 0.001$
				ZSr41 (14.66±0.03) < P-Mg (15.15±0.53)	$p < 0.01$
				ZSr41 (14.66±0.03) > Sham (14.55±0.03)	$p < 0.01$

6.7. References

[1] Guan RG, Cipriano AF, Zhao ZY, Lock J, Tie D, Zhao T, et al. Development and Evaluation of a Magnesium-Zinc-Strontium Alloy for Biomedical Applications – Alloy Processing, Microstructure, Mechanical Properties, and Biodegradation. Mater Sci Eng, C. 2013;33:3661-9.

[2] Cipriano AF, Zhao T, Johnson I, Guan R-G, Garcia S, Liu H. In vitro degradation of four magnesium–zinc–strontium alloys and their cytocompatibility with human embryonic stem cells. J Mater Sci Mater Med. 2013;24:989-1003.

[3] Nguyen TY, Cipriano AF, Guan RG, Zhao ZY, Liu H. In vitro interactions of blood, platelet, and fibroblast with biodegradable Magnesium-Zinc-Strontium alloys. J Biomed Mater Res, A. 2015;103:2974–86.

[4] Cipriano AF, Sallee A, Guan R-G, Zhan-Yong Z, Tayoba M, Cortez MC, et al. Cytocompatibility and Early Inflammatory Response of Human Endothelial Cells in Direct Culture with Mg-Zn-Sr Alloys. Submitted to Biomaterials. 2015.

[5] Cipriano AF, Sallee A, Guan R-G, Zhao Z-Y, Lin A, Liu H. A comparative study on the degradation of Mg-4Zn-xSr alloys and their cytocompatibility using the direct culture method. Submitted to Acta Biomaterialia. 2015.

[6] Kirkpatrick CJ, Mittermayer C. Theoretical and practical aspects of testing potential biomaterials in vitro. J Mater Sci Mater Med. 1990;1:9-13.

[7] Cipriano AF, Sallee A, Guan R-G, Zhao Z-Y, Tayoba M, Sanchez J, et al. Investigation of magnesium–zinc–calcium alloys and bone marrow derived mesenchymal stem cell response in direct culture. Acta Biomater. 2015;12:298-321.

[8] Witte F, Fischer J, Nellesen J, Crostack H-A, Kaese V, Pisch A, et al. In vitro and in vivo corrosion measurements of magnesium alloys. Biomaterials. 2006;27:1013-8.

[9] Kirkland NT, Birbilis N, Staiger MP. Assessing the corrosion of biodegradable magnesium implants: A critical review of current methodologies and their limitations. Acta Biomater. 2012;8:925-36.

[10] Sanchez AHM, Luthringer BJC, Feyerabend F, Willumeit R. Mg and Mg alloys: How comparable are in vitro and in vivo corrosion rates? A review. Acta Biomater. 2015;13:16-31.

[11] Kraus T, Fischerauer SF, Hänzi AC, Uggowitzer PJ, Löffler JF, Weinberg AM. Magnesium alloys for temporary implants in osteosynthesis: In vivo studies of their degradation and interaction with bone. Acta Biomater. 2012;8:1230-8.

[12] Erdmann N, Angrisani N, Reifenrath J, Lucas A, Thorey F, Bormann D, et al. Biomechanical testing and degradation analysis of MgCa0.8 alloy screws: A comparative in vivo study in rabbits. Acta Biomater. 2011;7:1421-8.

[13] Hofstetter J, Martinelli E, Pogatscher S, Schmutz P, Povoden-Karadeniz E, Weinberg AM, et al. Influence of trace impurities on the in vitro and in vivo degradation of biodegradable Mg–5Zn–0.3Ca alloys. Acta Biomater. 2015;23:347-53.

[14] Gu XN, Xie XH, Li N, Zheng YF, Qin L. In vitro and in vivo studies on a Mg–Sr binary alloy system developed as a new kind of biodegradable metal. Acta Biomater. 2012;8:2360-74.

[15] Han P, Cheng P, Zhang S, Zhao C, Ni J, Zhang Y, et al. In vitro and in vivo studies on the degradation of high-purity Mg (99.99wt.%) screw with femoral intracondylar fractured rabbit model. Biomaterials. 2015;64:57-69.

[16] Wang J, Jiang H, Bi Y, Sun Je, Chen M, Liu D. Effects of gas produced by degradation of Mg–Zn–Zr Alloy on cancellous bone tissue. Mater Sci Eng, C. 2015;55:556-61.

[17] Xin Y, Hu T, Chu PK. In vitro studies of biomedical magnesium alloys in a simulated physiological environment: A review. Acta Biomater. 2011;7:1452-9.

[18] Liu H. The effects of surface and biomolecules on magnesium degradation and mesenchymal stem cell adhesion. J Biomed Mater Res A. 2011;99:249-60.

[19] Johnson I, Perchy D, Liu H. In vitro evaluation of the surface effects on magnesium-yttrium alloy degradation and mesenchymal stem cell adhesion. J Biomed Mater Res A. 2011;100A:477–85.

[20] Rickard DJ, Sullivan TA, Shenker BJ, Leboy PS, Kazhdan I. Induction of Rapid Osteoblast Differentiation in Rat Bone Marrow Stromal Cell Cultures by Dexamethasone and BMP-2. Dev Bio. 1994;161:218-28.

[21] Fischer J, Pröfrock D, Hort N, Willumeit R, Feyerabend F. Reprint of: Improved cytotoxicity testing of magnesium materials. Mater Sci Eng, B. 2011;176:1773-7.

[22] Cipriano AF, De Howitt N, Gott SC, Miller CT, Rao MP, Liu H. Bone Marrow Stromal Cell Adhesion and Morphology on Micro- and Sub-Micropatterned Titanium. J Biomed Nanotechnol. 2014;10:660-8.

[23] Larsen LB, Madsen JE, Høiness PR, Øvre S. Should Insertion of Intramedullary Nails for Tibial Fractures Be With or Without Reaming?: A Prospective, Randomized Study With 3.8 Years' Follow-up. J Orthop Trauma. 2004;18:144-9.

[24] Rammelt S, Illert T, Bierbaum S, Scharnweber D, Zwipp H, Schneiders W. Coating of titanium implants with collagen, RGD peptide and chondroitin sulfate. Biomaterials. 2006;27:5561-71.

[25] Otto TE, Patka P, Haarman HJTM, Klein CPAT, Vriesde R. Intramedullary bone formation after polylactic acid wire implantation. J Mater Sci Mater Med. 1994;5:407-10.

[26] De Aza PN, Luklinska ZB, Santos C, Guitian F, De Aza S. Mechanism of bone-like formation on a bioactive implant in vivo. Biomaterials. 2003;24:1437-45.

[27] Butz F, Ogawa T, Chang TL, Nishimura I. Three-dimensional bone-implant integration profiling using micro-computed tomography. Int J Oral Maxillofac Implants. 2006;21:687-95.

[28] Bernhardt R, van den Dolder J, Bierbaum S, Beutner R, Scharnweber D, Jansen J, et al. Osteoconductive modifications of Ti-implants in a goat defect model: characterization of bone growth with SR μCT and histology. Biomaterials. 2005;26:3009-19.

[29] Morinaga K, Kido H, Sato A, Watazu A, Matsuura M. Chronological Changes in the Ultrastructure of Titanium-Bone Interfaces: Analysis by Light Microscopy, Transmission Electron Microscopy, and Micro-Computed Tomography. Clin Implant Dent Relat Res. 2009;11:59-68.

[30] Sheng MHC, Baylink DJ, Beamer WG, Donahue LR, Lau KHW, Wergedal JE. Regulation of bone volume is different in the metaphyses of the femur and vertebra of C3H/HeJ and C57BL/6J mice. Bone. 2002;30:486-91.

[31] Gruber HE. Adaptations of Goldner's Masson Trichrome Stain for the Study of Undecalcified Plastic Embedded Bone. Biotech Histochem. 1992;67:30-4.

[32] Nguyen TY, Liew CG, Liu H. An In Vitro Mechanism Study on the Proliferation and Pluripotency of Human Embryonic Stems Cells in Response to Magnesium Degradation. PLoS ONE. 2013;8:e76547.

[33] Lai YM, Qin L, Hung VWY, Chan KM. Regional differences in cortical bone mineral density in the weight-bearing long bone shaft—A pQCT study. Bone.36:465-71.

[34] Chatterjee S. Artefacts in histopathology. Journal of Oral and Maxillofacial Pathology : JOMFP. 2014;18:S111-S6.

[35] Mavrogenis A, Dimitriou R, Parvizi J, Babis G. Biology of implant osseointegration. J Musculoskelet Neuronal Interact. 2009;9:61-71.

[36] Kirkland NT, Lespagnol J, Birbilis N, Staiger MP. A survey of bio-corrosion rates of magnesium alloys. Corros Sci. 2010;52:287-91.

[37] Brar HS, Wong J, Manuel MV. Investigation of the mechanical and degradation properties of Mg–Sr and Mg–Zn–Sr alloys for use as potential biodegradable implant materials. J Mech Behav Biomed Mater. 2012;7:87-95.

[38] Li H, Peng Q, Li X, Li K, Han Z, Fang D. Microstructures, mechanical and cytocompatibility of degradable Mg–Zn based orthopedic biomaterials. Mater Design. 2014;58:43-51.

[39] Aljarrah M, Aghaulor U, Medraj M. Thermodynamic assessment of the Mg–Zn–Sr system. Intermetallics. 2007;15:93-7.

[40] Walker J, Shadanbaz S, Kirkland NT, Stace E, Woodfield T, Staiger MP, et al. Magnesium alloys: Predicting in vivo corrosion with in vitro immersion testing. J Biomed Mater Res, B. 2012;100B:1134-41.

[41] Willumeit R, Feyerabend F, Huber N. Magnesium degradation as determined by artificial neural networks. Acta Biomater. 2013;9:8722-9.

[42] Li Z, Gu X, Lou S, Zheng Y. The development of binary Mg–Ca alloys for use as biodegradable materials within bone. Biomaterials. 2008;29:1329-44.

[43] Zhang S, Zhang X, Zhao C, Li J, Song Y, Xie C, et al. Research on an Mg–Zn alloy as a degradable biomaterial. Acta Biomater. 2010;6:626-40.

[44] Willbold E, Kaya AA, Kaya RA, Beckmann F, Witte F. Corrosion of magnesium alloy AZ31 screws is dependent on the implantation site. Mater Sci Eng, B. 2011;176:1835-40.

[45] Xu L, Yu G, Zhang E, Pan F, Yang K. In vivo corrosion behavior of Mg-Mn-Zn alloy for bone implant application. J Biomed Mater Res, A. 2007;83A:703-11.

[46] Zhang E, Xu L, Yu G, Pan F, Yang K. In vivo evaluation of biodegradable magnesium alloy bone implant in the first 6 months implantation. J Biomed Mater Res, A. 2009;90:882-93.

[47] Wang J-L, Mukherjee S, Nisbet DR, Birbilis N, Chen X-B. In vitro evaluation of biodegradable magnesium alloys containing micro-alloying additions of strontium, with and without zinc. J Mater Chem B. 2015;3:8874-83.

[48] Witte F, Kaese V, Haferkamp H, Switzer E, Meyer-Lindenberg A, Wirth CJ, et al. In vivo corrosion of four magnesium alloys and the associated bone response. Biomaterials. 2005;26:3557-63.

[49] Witte F, Ulrich H, Palm C, Willbold E. Biodegradable magnesium scaffolds: Part II: Peri-implant bone remodeling. J Biomed Mater Res, A. 2007;81A:757-65.

[50] Xu L, Pan F, Yu G, Yang L, Zhang E, Yang K. In vitro and in vivo evaluation of the surface bioactivity of a calcium phosphate coated magnesium alloy. Biomaterials. 2009;30:1512-23.

[51] Wang YB, Xie XH, Li HF, Wang XL, Zhao MZ, Zhang EW, et al. Biodegradable CaMgZn bulk metallic glass for potential skeletal application. Acta Biomater. 2011;7:3196-208.

[52] Witte F, Ulrich H, Rudert M, Willbold E. Biodegradable magnesium scaffolds: Part 1: Appropriate inflammatory response. J Biomed Mater Res, A. 2007;81A:748-56.

[53] Tie D, Guan R, Liu H, Cipriano A, Liu Y, Wang Q, et al. An in vivo study on the metabolism and osteogenic activity of bioabsorbable Mg–1Sr alloy. Acta Biomater. 2016;29:455-67.

[54] Sun Je, Wang J, Jiang H, Chen M, Bi Y, Liu D. In vivo comparative property study of the bioactivity of coated Mg–3Zn–0.8Zr alloy. Mater Sci Eng, C. 2013;33:3263-72.

[55] Wolff J. Das gesetz der transformation der knochen. DMW-Deutsche Medizinische Wochenschrift. 1892;19:1222-4.

Chapter 7 - Preparation, degradation, and cytocompatibility of anodically oxidized MgO surface treatments for biomedical applications

7.1. Background

The first objective of this study was to engineer anodically oxidized surface treatments for commercial pure Mg (99.9% purity). Second, we investigated the *in vitro* degradation of the surface-treated Mg using electrochemical methods and through long-term immersion studies in revised simulated body fluid (r-SBF) and Dulbecco's Modified Eagle Medium (DMEM). Third, we utilized the physiologically relevant and comprehensive direct culture *in vitro* method [1-6] to investigate the degradation, cytocompatibility, and cell-biomaterial interface between surface-treated Mg and bone marrow derived mesenchymal stem cells (BMSCs) cultured in DMEM. While the direct culture method has helped elucidate cellular responses at the interface with non-surface treated Mg alloys [1, 7, 8], to our knowledge, this is the first comprehensive report to focus on BMSC interactions at the cell-biomaterial interface with anodically oxidized bulk Mg substrates. Results from this study demonstrate the potential of anodic oxidation to modulate the degradation rates of Mg-based biomaterials, as well as the utility of the direct culture method to study the cell-biomaterial interface to optimize bioactive properties of hybrid Mg-based biomaterials for biomedical implant applications.

7.2. Materials and methods

7.2.1. Synthesis of anodically oxidized surface treatments

7.2.1.1. Preparation of Mg working electrodes

Commercially pure Mg sheets (99.9%, As-rolled, 1.0 mm thick, Cat# 40604; Alfa Aesar, Ward Hill, MA, USA) were utilized throughout this study. To prepare the working electrodes used for anodization, the Mg sheets were cut into 10 x 10 mm squares, connected to copper wire using copper tape, and embedded in epoxy resin (Cat# ULTRA-3000R-32; Pace Technologies, Tucson, AZ, USA) as the working electrode (1 cm^2 area exposed; Figure 7.1a: 1-4). Embedding the Mg-based samples in epoxy resin ensured exposure of a single 10 x 10 mm surface, as well as provided insulation for the electrical connection between the sample and the copper wire. The 10 x 10 mm exposed surfaces of the embedded Mg samples were ground with SiC abrasive paper (Ted Pella Inc. Redding, CA, USA) up to 1200 grit, fine polished up to 0.25 µm with polycrystalline diamond paste (Physical Test Solutions, Culver City, CA, USA), and ultrasonically cleaned in acetone and ethanol prior to electrochemical tests.

7.2.1.2. Electrochemical setup

All electrochemical tests were performed using a three-electrode cell configuration connected to a potentiostat (Model 273A; Princeton Applied Research, Oak Ridge, TN, USA) controlled through PowerSuite 2.50.0 software

(Princeton Applied Research). A 3-D printed electrode holder designed for compatibility with Nalgene® Griffin 50 mL beakers (Cat# Z130931; Sigma-Aldrich, St. Louis, MO, USA) was used to ensure a parallel-plate electrode configuration and fix a distance of 1 cm between the working and counter electrodes (Figure 7.1a: 5 and 6). In the three-electrode cell the epoxy-embedded Mg electrode (anode), platinum foil (cathode), and Ag/AgCl were used as working, counter, and reference electrodes, respectively (Figure 7.1a: 7). The anodically surface treatments were generated using 30 mL of a 10 M KOH electrolyte [9, 10], which was prepared using deionized water and analytical-grade reagents. All experiments were carried out at room temperature, with constant stirring to ensure electrolyte homogeneity, and all potentials are in reference to Ag/AgCl electrode.

7.2.1.3. Anodic linear polarization

In order to identify the electrochemical processes of Mg in a 10 M KOH electrolyte, and therefore identify potentials that could be used to generate anodically oxidized surface treatments, an anodic linear potential sweep was performed from -1.7 to 2.3 V vs Ag/AgCl at a rate of 10 mV s^{-1}.

7.2.1.4. Potentiostatic anodization

Potentiostatic anodization was carried out at applied potentials in the passivation region approximating trans-passive oxidation, where the primary product in the passivation layer is $Mg(OH)_2$ [9, 11]. Thus, based on results from

the anodic polarization, the anodically oxidized surface treatments were generated at applied potentials of 1.8, 1.9, or 2.0 V vs Ag/AgCl; the suffix “A” designates “as-anodized”. All anodization processes lasted for 2 hr [9, 10], during which transient current density measurements (2 points per second) were recorded using a digital multimeter (Model 2100; Keithley Instruments, Cleveland, OH, USA) interfaced with a desktop PC. The anodized samples were subsequently spray-rinsed with 200-proof ethanol and dried with Nitrogen gas prior to surface characterization and annealing. Optical photographs were recorded to compare macro-scale homogeneity of surface treatment coverage.

7.2.1.5. Annealing of anodized Mg samples

In preparation for annealing, the anodized Mg samples were removed from the epoxy mount using a horizontal lathe equipped with a cutting tool. The anodized Mg substrates were subsequently annealed at 450 °C for 6 hr [9, 10] using an inductive furnace (F47915; Thermo Fisher Scientific, Waltham, MA, USA) controlled by a PID microcontroller (Micromega; Omega Engineering, Inc., Stamford, CT, USA) to convert the $Mg(OH)_2$ surface treatments to compact crystalline MgO by a dehydration reaction. The suffix “AA” designates “anodized and annealed”. The annealing cycle consisted of an initial heating ramp of 100 °C/hr, followed by 6 hr at 450 °C, and cooling to room temperature. An initial heating ramp was utilized to avoid the sudden collapse of the $Mg(OH)_2$ crystal

structure, thereby maximizing preservation of the $Mg(OH)_2$ surface topography in the final MgO product [12].

7.2.2. Microstructure characterization

The microstructure and elemental composition/distribution of the A and AA surface treatments were characterized using a scanning electron microscope (SEM; Nova NanoSEM 450, FEI Co., Hillsboro, OR, USA) equipped with an X-Max50 detector and AZtecEnergy software (Oxford Instruments, Abingdon, Oxfordshire, UK). The A and AA sample surfaces were sputter coated (Model 108, Cressington Scientific Instruments Ltd., Watford, UK) with platinum/palladium at 20 mA and 40 sec sputter time. Surface elemental composition and distribution were analyzed with energy dispersive x-ray spectroscopy (EDS). SEM images and EDS analyses were acquired with an accelerating voltage of 20 kV. To determine the thickness of the surface treatments, the anodized samples were cut in half, mounted at 90°, sputter coated, visualized using SEM, and analyzed using EDS for elemental composition and distribution.

7.2.3. Preparation of anodized and annealed samples for potentiodynamic polarization, immersion, or cell culture experiments

All tests of the anodically oxidized surface treatments were carried out only in the AA condition. Since the surface treatments were only synthesized on a single 10 x 10 mm face of the 1-mm-thick Mg sheet, the samples were re-embedded and

encapsulated in epoxy resin using a custom-built compression mold (Figure 7.4a:1 & 2) to ensure that tests were confined to the AA surfaces. 3-D printed molds were designed and developed to gravity-cast stamps of polydimethylsiloxane (PDMS; Sylgard® 184, Dow Corning Corp., Auburn, MI, USA). The PDMS stamps (Ø8 mm) came into contact with the surface treated Mg samples under compression to protect the surfaces from the epoxy resin during the re-embedding/encapsulation process (Figure 7.4b) to expose a 2-D working surface (Ø8 mm; 0.50 cm^2 exposed area). Non-treated, polished (up to 0.25 µm with polycrystalline diamond paste) 10 x10 mm Mg sheets were used as a control for all experiments. Likewise, non-culture treated glass slides (Cat#12-544-1, Fisher Scientific, Hampton, NH, USA) with a thickness of 1 mm were cut into 10 x 10 mm squares and used as a reference for immersion and cell culture experiments.

For potentiodynamic polarization (PDP) measurements, the AA or Mg control samples were prepared as follows: a PDMS circular well was used to confine the resin (Figure 7.4b: 1), copper tape and wire were assembled on the reverse side of the AA or Mg control substrates on top of a glass spacer (Figure 7.4b: 2), compression was applied on the assembly via the PDMS stamp, and 1 mL of epoxy resin was added and cured at 70 °C for 2 hours (Figure 7.4b: 3) to yield the geometry shown in Figure 7.4b: 4. The circular geometry (OD Ø25.4 mm) was designed to ensure that the PDP samples were compatible with the 3-D printed electrode holder and 3-electrode cell setup (Figure 7.1a: 5-7). Prior to PDP

measurements, the re-embedded AA and Mg control samples were wiped with acetone and soaked in 200-proof ethanol for 20 minutes.

For immersion or cell culture experiments the AA, Mg control, and Glass samples were prepared in a similar configuration for PDP measurements but without the electrical connection. Specifically, rather than using copper tape and wire, a double-sided bio-adhesive (Cat# TM8710A; MACtac North America, Stow, OH, USA) was used to secure the substrates to a glass spacer. Additionally, a square (14 x 14 mm) PDMS well was used to confine 400 µL of epoxy resin; this sample geometry/size ensure sample compatibility with standard 12-well culture plates (Figure 7.4b: 4, green square). Curing the epoxy resin at 70 °C for 2 hours was fundamental to ensure that cell viability was not affected by epoxy monomer residues (results not shown). Prior to immersion or cell culture experiments, the re-embedded AA, Mg control, and glass samples were wiped with acetone, soaked in 200-proof ethanol for 10 minutes, individually weighed (M_o), photographed, and sterilized under ultraviolet (UV) radiation for 2 hr on each side.

7.2.4. Corrosion behavior via electrochemical testing

Anodic PDP curves of the 1.8, 1.9, and 2.0 AA samples were obtained using the electrochemical setup described in section 2.1.2. The working electrodes were the re-embedded AA or Mg control samples (with electrical connection and in circular geometry). r-SBF at pH 7.4 was used as the electrolyte and maintained at 37.5 °C during PDP scans. The composition of r-SBF is the same as human blood

plasma and details for preparation are described elsewhere [13]. PDP scans were obtained without equilibration of the working electrode. The potential was anodically scanned from -3.5 to 0.5 V vs Ag/AgCl at a scanning rate of 20 mV s^{-1}. Values for corrosion potential (E_{corr}) and corrosion current density (J_{corr}) were extrapolated from the PDP curves according to ASTM G102-89 standard. Optical photographs were obtained post-electrochemical testing to compare the surfaces.

7.2.5. Degradation of 1.9 AA through immersion in r-SBF and/or DMEM

7.2.5.1. Experimental setup for immersion method

Collectively, microstructure characterization and corrosion behavior via electrochemical testing showed that 1.9 AA samples yielded a superior surface treatment compared with 1.8 AA and 2.0 AA (see results). Thus, the degradation of 1.9 AA samples was further investigated through separate 9-day (216-hr) immersions in r-SBF and/or DMEM (Sigma Aldrich, St. Louis, MO, USA) supplemented with 10% fetal bovine serum (FBS; HyClone, Logan, UT, USA) and 1% penicillin/streptomycin (P/S; Invitrogen, Grand Island, NY, USA). Hereafter, DMEM + 10% FBS + 1% P/S is referred to as DMEM. The prepared 1.9 AA, Mg control, and glass samples were placed in standard 12-well cell culture treated plates and incubated in 3 mL of r-SBF or DMEM under standard cell culture conditions (i.e., 37 ºC, 5%/95% CO2/air, humidified sterile environment) up to 9 days (216 hrs). A blank reference designated as “rSBF” or “DMEM” group consisted r-SBF or DMEM alone, respectively. The time points of interest for

immersion in r-SBF were selected as: 1, 2, 4, 8, 12, and 24 hrs, and then every 24-hr interval up to 216 hrs (day 9); the time points for immersion in DMEM were selected as 24-hr intervals up to 216 hrs (day 9).

The following details were repeated at each designated immersion time point for both immersion solutions (i.e. r-SBF and/or DMEM). In order to more closely mimic *in vivo* conditions where the circulation system regularly takes away soluble degradation products from the local site of implantation [14], the immersion solution was collected for analysis and replenished with 3 mL of fresh solution (pH 7.4, 37 ºC). Optical photographs of the samples were obtained when immersed in solution (just before collecting the immersion solution), and also after the solution was collected (before replenishing with fresh solution); the only exception was time 0 when the samples were photographed before immersion and immediately after immersion. These photographs are referred as “immersed in [solution]” or “with [solution] removed”, respectively, where [solution] indicates either r-SBF or DMEM. Photographs of the immersed samples allowed us to qualitatively assess hydrogen gas evolution while photographs of the samples with the solution removed allowed us to compare macro-scale localized corrosion on the surfaces of the samples. At the conclusion of the immersion experiments, the samples were dried in an oven at 37 ºC for 3 days, individually weighed (M_f), and photographed (designated as “Dry”).

7.2.5.2. *In vitro* degradation of 1.9 AA through immersion in r-SBF and/or DMEM

At each designated immersion time point, the *in vitro* degradation of the 1.9 AA and Mg control samples was evaluated through measurements of pH and ionic concentrations of the collected immersion solutions, and through the change in mass of each sample. The pH of the immersion solution at each time point was measured immediately after collection using a calibrated pH meter (Model SB70P, VWR). The concentration of Mg^{2+} and Ca^{2+} ions ($[Mg^{2+}]$ and $[Ca^{2+}]$, respectively) in the collected solution was measured using inductively coupled plasma optical emission spectroscopy (ICP-OES; Optima 8000, Perkin Elmer, Waltham, MA, USA). In order to minimize matrix effects in ICP-OES, the collected r-SBF or DMEM aliquots were diluted to 1:100 solutions in DI water. Ionic concentrations were then obtained from calibration curves generated using Mg and Ca standards (Perkin Elmer) diluted to ranges of 0.5-5.0 and 0.1-1.0 mg/L, respectively. Finally, the initial (M_o) and final masses of each sample (M_f) were used to calculate the ratio of the final/initial dry mass of each sample (M_f/M_o).

7.2.5.3. Microstructure characterization post-immersion in r-SBF and/or DMEM

The microstructure and elemental composition/distribution of the post-immersion dry and sputter-coated 1.9 AA and Mg control samples (surface and

cross-section) was evaluated using SEM and EDS, respectively, following details described in section 2.2.

7.2.6. BMSC responses in direct culture with 1.9 AA

7.2.6.1. Preparation of BMSC culture

Following a protocol approved by the University of California at Riverside (UCR) Institutional Animal Care and Use Committee (IACUC), BMSCs were harvested from three-week-old female Sprague Dawley rat weanlings after euthanasia by CO_2. Specific details regarding BMSC extraction, isolation and culture were described previously [15]. Briefly, the bone marrow from the femora and tibiae of rat weanlings was flushed out using DMEM, filtered through a 70-μm nylon strainer, the collected BMSCs cultured in DMEM under standard cell culture conditions, and passaged twice for culture with the prepared 1.9 AA, Mg control, and glass samples.

7.2.6.2. Direct culture of BMSCs with 1.9 AA

Specific details pertaining to the direct culture method were described previously [1]. Briefly, all the prepared samples were placed in standard 12-well cell culture treated plates and rinsed with 3 mL of DMEM to calibrate the osmotic pressure. Subsequently, BMSCs (P2) were seeded directly onto the surfaces of the samples at a density of $4x10^4$ cells cm^{-2} and incubated in 3 mL of DMEM (pH 7.4) under standard cell culture conditions for 24 hr. A positive control, designated

as "BMSC" group, consisted of BMSCs cultured only with DMEM in the wells, i.e. without any samples; likewise, a blank reference designated as “DMEM” group consisted DMEM alone. Similar to the details described in section 2.5.1, optical photographs of the samples were obtained before cell culture (0 hr), immediately after addition of cells (0 hr, direct culture), and just before collecting the cell media at the designated endpoint (24 hr, direct culture).

7.2.6.3. In vitro degradation of 1.9 AA in the BMSC culture

Following the procedure outlined in section 2.5.2, the *in vitro* degradation of the 1.9 AA and Mg control samples following the 24-hr cell culture was evaluated through measurements of pH and [Mg^{2+}] in the collected media; the [Ca^{2+}] in the collected media was also measured.

7.2.6.4. Quantification of BMSC adhesion under direct vs. indirect contact

BMSC adhesion and morphology on the surface of the samples (*direct contact* with the sample) and on culture plate surrounding the respective samples (*indirect contact* with the sample; designated as “Plate”) was evaluated after 24 hr of incubation through fluorescence microscopy. The samples and wells were washed with phosphate buffered saline (PBS) to remove non-adherent cells. Subsequently, adherent cells (on sample surfaces and plates) were fixed with 4% formaldehyde (10% neutral buffered formalin; VWR, Radnor, PA, USA) and stained with 4',6-diamidino-2-phenylindole dilactate (DAPI; Invitrogen) nucleic acid

stain and Alexa Flour® 488-phalloidin F-actin stain for fluorescence imaging. Adherent cells on the sample surface and on the culture plate surrounding the sample were visualized using a fluorescence microscope (Eclipse Ti and NIS software, Nikon, Melville, NY, USA) with a 10x objective lens at the same exposure condition and analyzed using Image J (NIH, Bethesda, MD, USA). BMSC adhesion density per group per location (i.e. sample or plate) was quantified by counting the DAPI-stained cell nuclei at five random locations normalized by unit area. BMSC morphology was qualitatively assessed based on F-actin fluorescence. Subsequently, the samples were dried in an oven at 37 ºC for 3 days, individually weighed (M_f), and photographed (designated as “Dry”). The initial (M_o) and final masses of each sample (M_f) were used to further assess the *in vitro* degradation by calculating the ratio of the final/initial dry mass of each sample (M_f/M_o).

7.2.6.5. Characterization of the BMSC-1.9 AA interface (i.e. direct contact)

The interface between the BMSC monolayer and 1.9 AA, Mg, and/or glass samples after 24 hr of incubation was visualized using SEM while distribution maps of surface elemental composition were acquired with EDS. The samples for SEM/EDS analysis were washed with PBS to remove non-adherent cells; adherent cells on the samples were fixed with 3% glutaraldehyde in 0.1 M potassium phosphate buffer for 1 hr. After fixation, the samples washed with PBS, serially dehydration in increasing ethanol concentration (50%, 75%, 90%, 2x100%; 10 min each), critical-point dried (Autosamdri-815, Tousimis Research Corp., Rockville,

MD, USA), and sputter coated (Model 108, Cressington Scientific Instruments Ltd., Watford, UK) with platinum/palladium at 20 mA and 40 sec sputter time.

7.2.7. Degradation rates of 1.9 AA

In vitro average daily degradation rates (mass loss rates) for the 1.9 AA and Mg samples were calculated based on measured [Mg^{2+}] in the culture media (r-SBF, DMEM, or BMSC+DMEM). The *in vitro* degradation rates, normalized by initial surface area (SA_0), were calculated according to the following equation (Eq. 7.1):

$$(Eq.7.1)\ \ Avg.Daily\ Deg.\ Rate = \frac{\left\{[Mg^{2+}]_{sample,total} - [Mg^{2+}]_{blank\ ref,total}\right\} \times 0.003\ L}{number\ of\ days \times SA_0}$$

Eq. 7.1 was first calculated for each individual sample replicate for each group (e.g. 1.9 AA replicate 1, 1.9 AA replicate 2, […], Mg replicate 1, etc.) and then a mean value was obtained. In Eq. 1, $[Mg^{2+}]_{sample,\ total}$ and $[Mg^{2+}]_{blank\ ref,\ total}$ refer to the total concentration for each individual sample replicate per group and blank reference, respectively, summed from all time points; in both cases, these values were obtained through ICP-OES measurements (mg/L). The difference between $[Mg^{2+}]_{sample,\ total}$ and $[Mg^{2+}]_{blank\ ref,\ total}$ effectively subtracts the background from the reference solution, where the remainder pertains specifically to Mg^{2+} ions from sample degradation. Furthermore, the immersion media volume was 3 mL (0.003 L), the number of days was either 9 (for immersion in r-SBF or DMEM) or 1 (for

cell culture in BMSC+DMEM), and the computed rate (mg day^{-1}) was normalized by individual sample replicate SA_0 (0.486±0.026 cm^2 for 1.9 AA and 0.471±0.037 cm^2 for Mg; compared with the nominal 0.5 cm^2 from PDMS stamp footprint).

7.2.8. Statistical analyses

All experiments described above were done in triplicate. All data sets were tested for normal distribution and homogeneous variance. Parametric data sets were analyzed using one-way analysis of variance (ANOVA) followed by the Tukey HSD *post hoc* test. Statistical significance was considered at $p < 0.05$.

7.3. Results

7.3.1. Synthesis of anodically oxidized surface treatments

Figure 7.1 shows the experimental setup and synthesis of anodically oxidized surface treatments on Mg using 10 M KOH as the electrolyte. Figure 7.1a provides a pictorial representation of the method used to prepare Mg working electrodes along with the 3-electrode cell used to control the anodization parameters (see sections 7.2.1.1 and 7.2.1.2 for details). Figure 7.1b shows the median trace obtained during the anodic linear polarization, which was used to identify electrochemical processes of Mg in the 10 M KOH electrolyte. Three distinct regions (which indicated unique oxidation processes) were identified: (i) cathodic process (-1.7 V to -0.5 V), (ii) passivation process (-0.5 V to 2.0 V), and (iii) trans-passive process (+2.0 V to +2.3 V). These regions indicated that the anodic

oxidation of Mg in a 10 M KOH electrolyte was characteristic of an active-passive metal and our results are in agreement with the electrochemical regions observed for Mg-Zn-Ca alloys during the anodic polarization in a 10 M KOH electrolyte [11]. Previous studies showed the formation of a $Mg(OH)_2$ passivation layer during potentiostatic anodization in the passivation region (-0.5 V to 2.0 V) [9-11]. Lei et al. showed the synthesis of barrier-type MgO surface treatments on Mg-Zn-Ca alloys through anodization in the passivation region followed by annealing [9, 10]. Thus, potentiostatic anodization was carried out at the upper boundary of the passivation region to first generate $Mg(OH)_2$ surface treatments, specifically at applied potentials of 1.8, 1.9, or 2.0 V vs Ag/AgCl.

Figure 7.1c shows transient current density curves obtained during the potentiostatic anodization at the three applied potentials of interest. Additionally, the photographs in Figure 7.1c show that anodization of Mg at 1.8, 1.9, or 2.0 V vs Ag/AgCl resulted in macroscopic large-scale homogeneous surface treatments. Comparison of the transient current density curves showed a dramatic increase during the synthesis of 2.0 A compared with 1.8 A and 1.9 A, which likely resulted from border-line behavior approximating transpassive oxidation. Previous studies showed that anodization in the transpassive region led to increased current density due to oxygen evolution and transpassive metal dissolution [9, 11, 16], all of which were observed in our experiments. Additionally, the general profile of all transient current density curves showed an initial spike followed by a delay preceding an exponential increase (ramp) to finally reach a pseudo steady-state current density,

which likely caused by an electrical double layer capacitance [17]. For all three transient current density plots, we quantified the time to reach the ramp end (t_{RE}), and the current densities at the ramp end (J_{RE}) and immediately before stopping the anodization (J_{120}); Figure 7.1d shows mean values for t_{RE}, while Figure 7.1e shows mean values for J_{RE} and J_{120}. Collectively, the parameters t_{RE}, J_{RE}, and J_{120} were used as benchmark indicators and indices of quality control during synthesis to ensure sample reproducibility.

7.3.2. Microstructure characterization

Figure 7.2 shows results from surface and cross-sectional characterization of the as-anodized 1.8 A, 1.9 A, and 2.0 A samples. Figure 7.2a summarizes results from surface characterization through a montage of SEM images (150x magnification) and corresponding EDS elemental surface distribution maps for Mg and O (Kα lines). The SEM images confirmed the large-scale homogeneous coverage of the surface treatments at all three applied potentials. Furthermore, the SEM images confirmed that only the 1.8 A sample showed residual polish lines along with crater-like defects in the surface treatment. The EDS maps showed homogeneously distributed elemental Mg and O on the surfaces of the 1.9 A and 2.0 A samples, as well as localized elemental Mg hot-spots on the surface of the 1.8 A sample. The insets in the top row of Figure 7.2a show high-magnification (40,000x) SEM images of the surface morphology of the as-anodized samples. These images confirmed the ability of anodization to generate distinct nano- and

sub-micro-scale topographies on the surface of Mg in as little as 100 mV differences in the applied potential. Additionally, the histogram in Figure 7.2b shows the surface elemental composition (in at. %) obtained from EDS analyses at 150x magnification. Primarily, Mg and O content was detected on the surfaces of all three samples, as well as carbon (C) and traces of potassium (K; < 0.27 at. %). A semi-quantitative comparison of the O/Mg at. % ratio showed that the 1.9 A sample had ratio of 2, which was indicative of the stoichiometric ratio for $Mg(OH)_2$.

Figure 7.2c shows SEM images (5,000x magnification) and corresponding overlaid EDS elemental surface distribution maps for Mg and O (Kα lines), which were used for cross-sectional characterization of the as-anodized samples. The inset in the top row of Figure 7.2c shows a high-magnification (30,000x) SEM image of the surface treatment thickness for the 1.8 A sample. Collectively, this analysis confirmed that the surface treatments were confined to the top layer of the bulk Mg substrate, where the thicknesses were 144±40 nm for 1.8 A, 940±319 nm for 1.9 A, and 2.81±0.93 μm for 2.0 A. Furthermore, the SEM images also showed cracks propagating through the surface treatment of the 2.0 A sample and into the bulk Mg substrate.

Figure 7.3 shows results from surface characterization of the anodized and annealed 1.8 AA, 1.9 AA, and 2.0 AA samples. Figure 7.3a summarizes results from surface characterization through a montage of SEM images (150x magnification) and corresponding EDS elemental surface distribution maps for Mg

and O (Kα lines). The SEM images and EDS maps showed that the surface treatments on the 1.8 AA and 1.9 AA samples remained largely homogeneous, but the 2.0 AA sample showed signs of crack propagation and delamination throughout the surface. The insets in the top row of Figure 7.3a show high-magnification (40,000x) SEM images of the surface morphology of the anodized and annealed samples. These images showed that the as-anodized nano- and sub-micro-scale topographies were largely influenced by the annealing procedure; in fact, the topographical features were best conserved on the 1.8 AA sample but completely disappeared on the 2.0 AA sample. Additionally, the histogram in Figure 7.3b shows the surface elemental composition (in at. %) obtained from EDS analyses at 150x magnification. Elemental Mg, O, C, and K, prevailed on the surfaces of all samples after annealing but the range of O/Mg at. % ratio was greater compared with the as-anodized samples. A semi-quantitative comparison of the O/Mg at. % ratio showed that the 1.8 AA sample had ratio of 0.586, the 1.9 AA sample had a ratio of 3.193, and the 2.0 AA sample had a ratio of 1.904.

7.3.3. Corrosion properties from electrochemical testing

The re-embedding method used to prepare the samples for potentiodynamic polarization, immersion, or cell culture experiments (Figure 7.4a and 7.4b) provided a highly reproducible way of ensuring that all tests were directed only to the treated surfaces.

PDP curves obtained for the 1.8 AA, 1.9 AA, 2.0 AA, and Mg control samples showed that the initial *in vitro* corrosion (or degradation) behavior of the anodized-annealed samples and pure Mg control were similar (Figure 7.4c-7.4e). The median PDP trace with the most representative corrosion potential (E_{corr}) and corrosion current density (J_{corr}) for each sample type was plotted in Figure 7.4c. The inset in the PDP graph shows a close-up of the most anodic segment of the potentials scanned and the photographs show the sample surfaces post-electrochemical testing. Comparison of the PDP traces showed that all surface treated samples and the Mg control had comparable cathodic segments. While a considerable portion of the anodic segment of the traces remained relatively comparable for all groups, a close inspection of the most anodic portion (inset) indicated that all AA samples showed an anodic oxidation shoulder near +0.35 V vs Ag/AgCl but the Mg control did not. Qualitative assessment of the surfaces post-electrochemical testing gave further evidence of distinct electrochemical processes on the surfaces of all AA samples compare with the Mg control. Values for E_{corr} and J_{corr} were obtained from Tafel extrapolation of the PDP curves (Figure 7.4d and 7.4e, respectively). E_{corr} values for all AA samples were similar when compared with the Mg control (Figure 7.4d). ANOVA showed significant differences only for J_{corr} values of the metallic samples studied [F (3, 11) = 4.536, $p = 2.652 \times 10^{-2}$] (Figure 7.4e). Specifically, *post hoc* pairwise comparisons showed that the average J_{corr} value for 1.9 AA (5.23±2.17 mA cm^{-2}; mean±SD) was

significantly lower when compared with 2.0 AA (9.20±0.60 mA cm^{-2}) and Mg control (8.09±1.10 mA cm^{-2}), but not compared with 1.8 AA (7.54±1.56 mA cm^{-2}).

7.3.4. Degradation of 1.9 AA through immersion in r-SBF and DMEM

Figure 7.5 summarizes results from the immersion of the 1.9 AA and Mg control samples in r-SBF for 9 days (216 hrs). Figure 7.5a shows photographs of the samples at select time points during the immersions study either immersed in r-SBF or with r-SBF removed to qualitatively evaluate hydrogen gas evolution and macro-scale surface degradation, respectively. These photographs showed that hydrogen gas evolution was likely reduced on the surface of the 1.9 AA group when compared with the Mg control during the initial 48 hrs of immersion. Qualitatively, the photographs also showed that the anodized and annealed treatment (white region) remained on the surface up to 2 hrs after immersion; thereafter the surface treatment turned into a black product. Comparison of the Dry samples at the conclusion of the study showed a much more homogenously-corroded 1.9 AA sample compared with the Mg control. Analysis of the pH during the immersion study (Figure 7.5b) showed that during the initial 2 hrs of immersion, the surface treatment on the 1.9 AA group inhibited the increase in media alkalinity compared with the Mg control. From the 4 hr time point onward, ANOVA confirmed a significant increase in the pH of the collected r-SBF for the 1.9 AA group compared with the Mg control. Similarly, ANOVA confirmed a significant increase in the $[Mg^{2+}]$ of the collected r-SBF (Figure 7.5c) for the 1.9 AA group compared

with the Mg control at all time points. In contrast, analysis of the [Ca^{2+}] in the collected immersion solution (Figure 7.5d) did not reveal any significant differences among any of the groups. Due to the large amount of *post hoc* pairwise comparisons, asterisks in Figure 7.5b and 7.5c indicate statistical differences only between 1.9 AA and the Mg control at all time points during the 9 day immersion in r-SBF, while Table 7.1 shows corresponding tabulated results for measured values and statistical analyses. Figure 7.5e shows SEM images (150x) of the 1.9 AA and Mg control samples at the conclusion of the 9 day immersion and after drying. Both samples had a similar appearance in terms of corrosion-induced cracks and accumulation of degradation products. Quantification of the ratio of the final/initial dry mass of each sample (M_f/M_o) yielded 0.976±0.012 and 0.983±0.001 for the 1.9 AA and Mg control samples, respectively. Additionally, the histogram in Figure 7.5f shows the surface elemental composition (in at. %) obtained from EDS analyses at 150x magnification. Elemental Mg, O, C, calcium (Ca), phosphorus (P), and trace amounts of sodium (Na), K, and chloride (Cl), prevailed on the surfaces of all samples after immersion in r-SBF. Interestingly, the 1.9 AA showed a higher percentage of Ca (5.83%) and P (5.52%) deposition compared with the Mg control (2.36% and 3.80%, respectively).

Figure 7.6 summarizes results from the immersion of the 1.9 AA and Mg control samples in DMEM for 9 days (216 hrs). Figure 7.6a shows photographs of the samples at select time points during the immersions study either immersed in DMEM or with DMEM removed. Similar to the immersion study in r-SBF, the

photographs showed that hydrogen gas evolution was likely reduced on the surface of the 1.9 AA group when compared with the Mg control during the initial 72 hrs of immersion. Additionally, comparison of the Dry samples at the conclusion of the study, again, showed a much more homogenously-corroded 1.9 AA sample compared with the Mg control. ANOVA confirmed a significant increase in the pH of the collected DMEM for the 1.9 AA group compared with the Mg control only during the initial 24 hrs (Figure 7.6b). Similarly, ANOVA confirmed a significant increase in the $[Mg^{2+}]$ of the collected DMEM (Figure 7.6c) for the 1.9 AA group compared with the Mg control at all time points, especially during the initial 24 hrs of immersion. In contrast, analysis of the $[Ca^{2+}]$ in the collected immersion solution (Figure 7.6d) did not reveal any significant differences among any of the groups. Due to the large amount of *post hoc* pairwise comparisons, asterisks in Figure 7.6b and 7.6c indicate statistical differences only between 1.9 AA and the Mg control at all time points during the 9 day immersion in DMEM, while Table 7.2 shows corresponding tabulated results for measured values and statistical analyses. Figure 7.6e shows SEM images (150x and 15,000x) of the 1.9 AA and Mg control samples at the conclusion of the 9 day immersion and after drying. Low magnification SEM images showed that both samples had a similar appearance in terms of corrosion-induced cracks and accumulation of degradation products. However, high magnification SEM images showed the formation of spherical sub-micro scale structures on the surface of the 1.9 AA samples but not on the surface of the Mg control. Quantification of the ratio of the final/initial dry mass of each

sample (M_f/M_o) yielded 0.993±0.003 and 0.999±0.002 for the 1.9 AA and Mg control samples, respectively. Additionally, the histogram in Figure 7.6f shows the surface elemental composition (in at. %) obtained from EDS analyses at 150x magnification. Elemental Mg, O, C, Ca, P, and trace amounts of Na, K, and Cl, prevailed on the surfaces of all samples after immersion in DMEM. In contrast to the differences obtained after the immersion in r-SBF, after immersion in DMEM both 1.9 AA and Mg control samples had similar percentages of Ca and P on their surfaces.

Figure 7.7 shows a montage of SEM images and EDS elemental surface distribution maps used to perform the cross-sectional analysis of the 1.9 AA and Mg control samples after immersion in r-SBF (Figure 7.7a) and DMEM (Figure 7.7b) for 9 days (216 hrs). Comparison of SEM images showed that the passivation layer on the 1.9 AA samples was considerably thicker after immersion in both r-SBF and DMEM, compared with the Mg control. In r-SBF the passivation layer on the 1.9 AA sample was 92.1±9.6 µm compared with 18.9±4.5 µm for the Mg control; similarly, in DMEM the passivation layers were 39.7±5.4 µm and 4.9±1.3 µm for the 1.9 AA group and Mg control, respectively. An overlay of the EDS elemental surface distribution maps for Mg and O (Kα lines) confirmed the thickening of the passivation layer on the surface of the 1.9 AA samples. Interestingly, EDS elemental surface distribution maps for Ca and P (Kα lines) showed that the thick passivation layer on 1.9 AA after immersion in r-SBF and DMEM was also enriched with Ca and P.

7.3.5. Evaluation of 1.9 AA in the direct culture with BMSCs in DMEM for 24 hrs

Results from the *in vitro* degradation of the 1.9 AA and Mg control samples in direct culture with BMSCs in DMEM for 24 hrs are summarized in Figures 7.8a-7.8d. Figure 7.8a shows photographs of the samples before direct culture with BMSCs in DMEM, immediately after seeding BMSCs, immediately before collecting the media for analysis, and after drying for 3 days. Similar to the results from immersion studies, the photographs showed that hydrogen gas evolution was likely reduced on the surface of the 1.9 AA group when compared with the Mg control at 0 and 24 hrs. Comparison of the Dry samples confirmed more homogeneous degradation on the surface of the 1.9 AA sample compared with the Mg control. The histogram in Figure 7.8b showed that the ratio of the final/initial dry mass of the metallic samples (M_f/M_o) was similar. Additionally, analysis of the pH of the collected media (Figure 7.8c) did not confirm statistically significant differences; however, in general terms, the pH in the media of the 1.9 AA and Mg control groups showed a higher mean value compared with the Glass reference, BMSC control, and DMEM blank reference. Furthermore, ANOVA confirmed a significant increase in the [Mg^{2+}] of the collected media after 24 hrs of incubation with the samples [F (4, 15) = 40.536, p = 7.144×10^{-8}] but not in the [Ca^{2+}] of the media (Figure 7.6c). *Post hoc* pairwise comparisons showed that the [Mg^{2+}] of the 1.9 AA group (4.64±1.07 mM) was significantly higher ($p < 0.001$) when compared with the Mg control (1.96±0.37 mM), Glass reference (0.67±0.02 mM), BMSC

positive control (0.68±0.01 mM), and DMEM blank reference (0.72±0.03 mM); likewise, the [Mg^{2+}] of the Mg control was significantly higher ($p < 0.05$) when compared with the Glass reference and BMSC positive control.

Results from the quantification of BMSC adhesion and morphology under *direct* and *indirect* contact with the 1.9 AA and Mg control samples in direct culture in DMEM for 24 hrs are summarized in Figures 7.8e and 7.8f. Figure 7.8e shows fluorescence images of BMSCs attached onto the culture plates (i.e. *indirect* contact) after 24 hrs of incubation. Attached and viable cells were observed in all groups and the morphology of these cells indicated normal growth and isotropic spreading. Results of BMSC adhesion density both under *direct* and *indirect* contact with the surfaces of 1.9 AA, Mg control, Glass reference, and BMSC positive control are summarized in Figure 7.8f. ANOVA did not confirm statistically significant differences in the mean cell adhesion density under either *direct* or *indirect* contact with the samples. Specifically, ANOVA for BMSC adhesion density under *direct* contact with the sample surface approached significance [F (2, 7) = 4.996, $p = 4.488 \times 10^{-2}$] and *post hoc* pairwise comparison showed $p = 0.06$ for both 1.9 AA ($1.41 \pm 0.13 \times 10^4$ cells cm^{-2}) and Mg control ($1.37 \pm 0.17 \times 10^4$ cells cm^{-2}) when compared with the Glass reference ($1.97 \pm 0.14 \times 10^4$ cells cm^{-2}).

Figure 7.9 summarizes results from the characterization of the BMSC-biomaterial interface with the 1.9 AA and Mg control samples in direct culture with BMSCs in DMEM for 24 hrs. Distinct changes in surface topography and elemental

composition for the 1.9 AA group and Mg control, when compared with the glass reference, were observed through the SEM and EDS analysis of the BMSC-biomaterial interface. Furthermore, a qualitative assessment of BMSC morphologies in response to the characteristics of the substrate interface was used to determine BMSC-biomaterial interactions. Figure 7.9a shows the characterization of the BMSC-biomaterial interface for 1.9 AA, Mg control, and Glass reference at an original magnification of 150x (top row), 1,000x (bottom row), and 5,000x (insets in bottom row). The color mapping in each image represents surface elemental distribution measured by EDS, where red = Mg, yellow = O, green = C, purple = Ca, orange = P, white = Si, and pink = Na, K and Cl. Degradation-induced surface cracks were most prominent (distribution and size) on the 1.9 AA sample compared with the Mg control. BMSC spreading on the 1.9 AA was largely anisotropic (i.e. compact spherical-shaped cell bodies [18]), compared with a higher degree of isotropic spreading on the Mg control sample, and complete isotropic spreading on the Glass reference. High magnification SEM images (5,000x magnification) indicated that the BMSCs adhered on the 1.9 AA sample showed a lack of cell protrusions (filopodia and lamellipodia) extending at the interface, whereas BMSCs on the Mg control and Glass reference showed a healthy amount of cell protrusions. Figure 7.9b summarizes the elemental composition (in at. %) results obtained from EDS analyses at 150x magnification. Elemental Mg, O, C, Ca, P, and trace amounts of Na, K, and Cl, prevailed on the surfaces of both metallic samples after direct culture with BMSCs in DMEM.

Specifically, the surface of the 1.9 AA sample had a much higher percent content of O (49.12%), Ca (4.68%), and P (9.175), when compared with the Mg control (27.44%, 0.63%, and 4.18%, respectively). The cumulative total percent content of Na, K, and Cl was also higher for 1.9 AA compared with the Mg control (2.39% and 0.76%, respectively). It is likely that the presence and co-localization (results not shown) of O, Ca, and P resulting from the degradation of both Mg-based metallic materials indicated mineral deposition induced by the corrosion process. Additionally, the C content on all three samples was attributed to adhered cells, proteins, and extracellular matrix produced by cells.

7.3.6. Degradation rates of 1.9 AA

Figure 7.10 summarizes results from the measured average daily *in vitro* degradation rates from this study obtained from immersion in r-SBF for 9 days, immersion in DMEM for 9 days, and direct culture with BMSCs in DMEM for 1 day (24 hrs). Since corrosion rates are typically associated with exposed surface area [1, 19, 20], the average daily degradation rate was calculated relative to the exposed SA_0 of the 1.9 AA and Mg control samples (after re-embedding in epoxy resin using the compression mold). ANOVA confirmed statistically significant differences in the mean average daily degradation rates relative to SA_0 [F (5, 15) = 72.895, p = 5.528×10^{-10}]. *Post hoc* pairwise comparisons showed significant differences in three distinct clusters. First, the average daily degradation rate of 1.9 AA was significantly faster ($p < 0.001$) in r-SBF (1.03±0.09 mg cm^{-2} day^{-1})

compared with DMEM (0.40±0.05 mg cm^{-2} day^{-1}) and with BMSCs in DMEM (0.54±0.11 mg cm^{-2} day^{-1}). Second, the average daily degradation rate of the Mg control was significantly faster ($p < 0.05$) in r-SBF (0.31±0.07 mg cm^{-2} day^{-1}) compared with DMEM (0.14±0.00 mg cm^{-2} day^{-1}) and with BMSCs in DMEM (0.17±0.01 mg cm^{-2} day^{-1}). Third, the average daily degradation rate of 1.9 AA was significantly faster ($p < 0.001$) compared with the Mg control after immersion in r-SBF for 9 days, immersion in DMEM for 9 days, and direct culture with BMSCs in DMEM for 1 day (24 hrs).

7.4. Discussion

7.4.1. Anodically oxidized surface treatments for biomedical applications

Since the early 2000's, several studies have focused on developing environmentally and toxic-free anodic oxidation processes for Mg-based materials. Interestingly, many studies focused on utilizing KOH- or NaOH-based electrolytes to anodize commercially pure Mg and Mg alloys to improve the corrosion resistance for a variety of applications [9-11, 21-26]. Blawert et al. and Yabuki et al. conveniently summarized many of these studies and provided discussions on parameters influencing film formation, including stabilization due to electrolyte additives and/or alloying elements [22, 25]. Several studies focused on developing anodically oxidized surface treatments specifically for biomedical applications, where the degradation was investigated through immersion in SBF for 30 days [23], immersion in adjusted Hank's solution for 40 hours [24], dynamic incubation

(300 RPM rotation) in Eagle's minimum essential medium (E-MEM) supplemented with 10% FBS for 24 hrs [26], and immersion in Hank's solution for 3 days [10]. Anodization of Mg-based biomaterials has also been utilized to produce high aspect ratio MgO nano-whiskers [27], self-ordered oxy-fluoride nanoporous/tubular layers [28], and fluorinated-oxides using micro-arc oxidation [29]. Specifically, the anodization and annealing parameters used in this study were based on the work by Cai et al [11] and Lei et al. [9, 10].

Despite the absence of improvement in degradation resistance, several aspects of the anodically oxidized surface treatments presented in this study compare favorably with published literature. Although results from PDP measurements (Figure 7.4c-7.4e) and from the initial response during the immersion in r-SBF (Figures 7.5b) gave indication of an initial improvement in degradation resistance, $[Mg^{2+}]$ measurements from the 9-day immersion tests in r-SBF (Figure 7.5c) and DMEM (Figure 7.6c), as well as the 24-hr direct culture with BMSCs in DMEM (Figure 7.8d) showed that the anodically oxidized and annealed surface treatments from this study were not able to mitigate the rapid degradation compared with pure Mg. Interestingly, a considerably faster degradation rate was observed during the initial 24 hrs of incubation of the 1.9 AA samples in DMEM, which was followed by a much slower degradation during subsequent time periods up to day 9 (Figures 7.2b and 7.2c). Likewise, H_2 gas evolution was likely reduced from the surfaces of the 1.9 AA samples during incubation in both r-SBF (Figure 7.5a) and DMEM (Figure 7.6a). Hiromoto et al. reported an similar response,

where a considerably higher degradation rate was observed during the initial 24 hours of incubation of anodized and anodized-autoclaved surface treatments on pure Mg (99.95%) in E-MEM + FBS [26]. Even though our anodization and annealing processing parameters were similar to those used by Lei et al. to improve the degradation resistance of Mg 5.5-6.5% Zn 1.0-1.5%Ca alloys [9, 10], it is reasonable to speculate that the alloying elements could influence the stability of the anodic film. In fact, previous studies reported that aluminum ions contained in Mg alloys AZ31 and AZ91 led to the formation of aluminum oxide in the anodically oxidized surface films, which helped improve passivation [21, 30]. Additionally, the transient current density responses measured during the synthesis of our anodic oxide treatments (Figure 7.1c) were similar to the results reported by Hiromoto et al. in which the authors anodized commercial pure Mg (99.95%) using a 1 M NaOH as the electrolyte at applied potentials of 2, 7, and 20 V for 10 min [24]. Furthermore, the surface morphology as well as the propagation of cracks through the film of the 2.0 A sample (Figures 7.2a and 7.2c, respectively) resembled their samples anodized at 7 V. In a follow up study, Hiromoto et al. reported an increase in anodic film thickness with increasing applied potential [26], which was in agreement with our results (Figure 7.2c). Moreover, our results showed that the anodic films were enriched with Ca and P post-immersion in r-SBF and DMEM (Figure 7.7), which compared favorably with results from two studies by Hiromoto et al. [24, 26]. Interestingly, Hiromoto et al. used glow discharge optical emission spectroscopy (GD-OES) to show that C adsorption,

likely from proteins and amino acids, was limited only to the outermost layer of the anodically oxidized films [26]. In addition, our results showed that the thickness of the passivation film on the 1.9 AA samples post-immersion in r-SBF and DMEM (Figure 7.7) was considerably greater when compared with the passivation film on the Mg control. These results suggest a distinct mode of degradation for the 1.9 AA samples since localized pitting and undermining, which are characteristic of Mg-based biomaterials [31, 32], was replaced by a continuous growth of the passivation film.

One of the major contributions of this study to the field of anodic films on Mg-based biomaterials for biomedical applications is the detailed description of the highly reproducible methods utilized. Published literature gives very sparse details on electrode preparation, post-treatment handling, and sample preparation following post-treatments. Thus, the images presented in Figures 7.1a, 7.4a, and 7.4b, provide a detailed representation of sample geometry, condition, and experimental setup utilized in this study. Most remarkable were the large-scale homogeneous surface treatments (Figure 7.1c) and highly reproducible results (Figure 7.1d-7.1e) obtained from implementing our electrode preparation process combined with the precise control of the electrode configuration setup. Likewise, the re-embedding process (Figure 7.4a-7.4b) allowed us to confidently assess and confine PDP, immersion, and cell culture experiments only on the treated surfaces. We are confident that the methods for electrode preparation presented in this study can be implemented towards a variety of electrochemical methods to prepare

surface treatments and/or coatings on Mg-based biomaterials, as well as to study these electrodes using a variety of *in vitro* experiments. In order to enhance the effectiveness of anodization to improve the corrosion resistance of Mg-based biomaterials future studies should focus on investigating pre-treatment methods including acid activation, alkali cleaning, or fluoride activation [33], and/or post-treatment methods such as hydrothermal treatments to seal off pores, cracks, and flaws present in the anodic films [26, 34].

7.4.2. 1.9 AA in the direct culture with BMSCs

Adhesion and morphology of BMSCs under indirect contact was largely unaffected by the solubilized degradation products of the 1.9 AA samples. Our results from the direct culture *in vitro* study showed that BMSC adhesion and morphology under indirect contact with the 1.9 AA samples were largely unaffected by solubilized degradation products (Figure 7.8e-7.8f), despite the significantly faster degradation rate when compared with the Mg control (Figure 7.10). Previous studies by our group investigating BMSC responses to solubilized degradation products of Mg-xZn-0.5Ca alloys and Mg-4Zn-xSr alloys using the direct culture method showed that both adhesion and morphology of BMSCs under indirect contact were largely unaffected up to 72 hrs of culture [1, 7]. In fact, we previously showed that BMSC adhesion and morphology were not detrimentally affected when cultured in DMEM transiently adjusted to pH 9.0 or when supplemented with 27.6 mM of Mg^{2+} ions [1]. In another study using the direct culture method with

human umbilical vein endothelial cells (HUVECs), we showed that HUVECs under indirect contact were also largely unaffected by solubilized degradation products from Mg-4Zn-xSr alloys, incubation in EGM^{TM}-2 media transiently adjusted to pH 9.0, or in EGM^{TM}-2 media supplemented with 27.6 mM of Mg^{2+} ions [8]. In all cases mentioned above, including results from this study, cells under *indirect* contact with Mg-based biomaterials were not detrimentally affected by solubilized degradation products. Collectively, these results highlight the importance of the direct culture method where the indirect contact aspect (which is analogous to traditional ISO 10993-based tests) is complimented by the direct contact aspect of the *in vitro* method.

Although BMSC adhesion at the cell-biomaterial interface was not significantly reduced, a qualitative assessment of cell morphology showed anisotropic spreading at the interface with the 1.9 AA samples. Our results from fluorescence image quantification did not confirm a significant reduction of BMSC adhesion at the cell biomaterial interface with the 1.9 AA sample compared with the Mg control and Glass reference (Figure 7.8f). However, the qualitative assessment of the cell-biomaterial interface using SEM and EDS showed that BMSC spreading on the 1.9 AA was largely anisotropic (i.e. compact spherical-shaped cell bodies; Figure 7.9a, top row), compared with the Mg control and Glass reference samples which had BMSCs with higher degrees isotropic spreading. The lack of filopodia and lamellipodia of BMSCs adhered on the 1.9 AA (Figure 7.9a, bottom row), compared with the Mg control and Glass reference, gave indication of unhealthy

and perhaps even loosely adhered BMSCs. Results from the Mg control in this study agreed with results from a previous study where we showed continuous growth and proliferation of BMSCs on the Mg control up to 72 hrs of incubation under direct contact [1]. Thus, the unhealthy morphology of the BMSCs at the interface with the 1.9 AA samples gave indication of detrimental effects induced by the rapid degradation of hybrid biomaterial. In fact, in a previous study we demonstrated that BMSC viability at the cell-biomaterial interface after 72 hrs of incubation was dependent on degradation rate, where an average daily degradation rate greater than approximately 0.30 mg cm^{-2} day^{-1} resulted in a significant reduction in BMSC viability [7]. Although a 72 hr direct culture would be necessary to compare BMSC viability at the interface with the 1.9 AA samples, it is reasonable to speculate that the rapid degradation rate of 1.9 AA in DMEM with BMSCs after 24 hrs (0.54±0.11 mg cm^{-2} day^{-1}) was responsible for the unhealthy morphology. Since [Mg^{2+}] in the media did not exceed 27.6 mM [1], we hypothesize that either localized alkalinity, change in surface topography, or compound formation at the dynamic interface induced by the rapid degradation caused the observed BMSC unhealthy morphology. Recently, Jiang et al. prepared fluorinated-oxides using micro-arc oxidation through a process the authors termed micro-arc fluorination (MAF) [29]. The MAF process used saturated NH_4HF_2 as the electrolyte and applied potentials of 120-200 V for 3 min to treat the surface of pure Mg (>99.93%). The authors used this sparking-dependent process to improve the corrosion resistance and cell adhesion of MC3T3-E1 immortalized murine

osteoblasts at the interface with the spark-oxidized Mg. Despite the considerable differences in applied potential and electrolyte composition compared with the process described in this study, results from the MAF-treated surfaces illustrate the potential of anodization to control the degradation and engineer the cell-biomaterial interface for biomedical implant applications.

7.5. Conclusions

This article reported on the detailed preparation of anodically oxidized surface treatments for commercial pure Mg (99.9% purity), on the *in vitro* degradation of the surface-treated Mg, and on the cytocompatibility and cell-biomaterial interface between surface-treated Mg and BMSCs using the physiologically relevant and comprehensive direct culture *in vitro* method. The following major conclusions were drawn from the present study:

1. Despite the absence of improvement in long-term degradation resistance, the surface treatments prepared in this study provided initial degradation resistance in r-SBF, a considerably high degradation rate during the initial 24 hrs of immersion in DMEM followed by a much lower rate up to day 9, and likely reduced H_2 gas production. Furthermore, a distinct mode of degradation for the 1.9 AA samples was observed where localized pitting and undermining was replaced by a continuous growth of a passivation film enriched with Ca and P.
2. One of the major contributions of this study to the field of anodic films on Mg-based biomaterials for biomedical applications is the detailed description of the

highly reproducible methods utilized. We are confident that the methods for electrode preparation presented in this study can be implemented towards a variety of electrochemical methods to prepare surface treatments and/or coatings on Mg-based biomaterials, as well as to study these electrodes using a variety of *in vitro* experiments.

3. Results from the direct culture *in vitro* study showed that adhesion and morphology of BMSCs under indirect contact was largely unaffected by the solubilized degradation products of the 1.9 AA samples. In contrast, although BMSC adhesion at the cell-biomaterial interface was not significantly reduced, a qualitative assessment of cell morphology showed anisotropic spreading at the interface with the 1.9 AA samples. We hypothesize that either localized alkalinity, change in surface topography, or compound formation at the dynamic interface induced by the rapid degradation of the 1.9 AA samples caused the BMSC unhealthy morphology.
4. Results from this study demonstrate the potential of anodic oxidation to modulate the degradation rates of Mg-based biomaterials, as well as the utility of the direct culture method to study the cell-biomaterial interface to optimize bioactive properties of hybrid Mg-based biomaterials for biomedical implant applications.

7.6. Figures and tables

Figure 7.1: Experimental setup and synthesis of anodized Mg using 10 M KOH as the electrolyte.
(a) Working electrode preparation and experimental setup: 1. Front side of Mg substrate, 2. Reverse side of Mg substrate showing electrical connection with copper tape and wire, 3. Electrical components placed in casting mold, 4. Mg working electrode (1 cm^2 exposed area), 5. Rendering of custom-designed three-electrode holder with fixed 10 mm spacing between working and counter electrodes, 6. Rendering of electrode holder placed in anodization container, 7. Optical photograph of three-electrode cell (Working: Mg; Counter: Pt foil; Reference: Ag/AgCl) used for the anodization of Mg. (b) Anodic polarization plot of Mg obtained at a scan rate of 10 mV s^{-1}. Labels indicate distinct oxidation processes. (c) Current density obtained during a 2 hr potentiostatic anodization at applied potentials of 1.8, 1.9, or 2.0 V vs Ag/AgCl. Ramp End (ER) designates the end of exponential current density increase at each potential. Optical photographs represent the as-anodized surface at each applied potential; scale bar = 5 mm. (d) Time (minutes) to reach RE at each applied potential. (e) Current density at RE (J_{RE}) and at the conclusion of the 2 hr (120 min) anodization (J_{120}) at each applied potential. The parameters t_{RE}, J_{RE}, and J_{120} were used as quality control indicators during sample synthesis to ensure sample reproducibility.

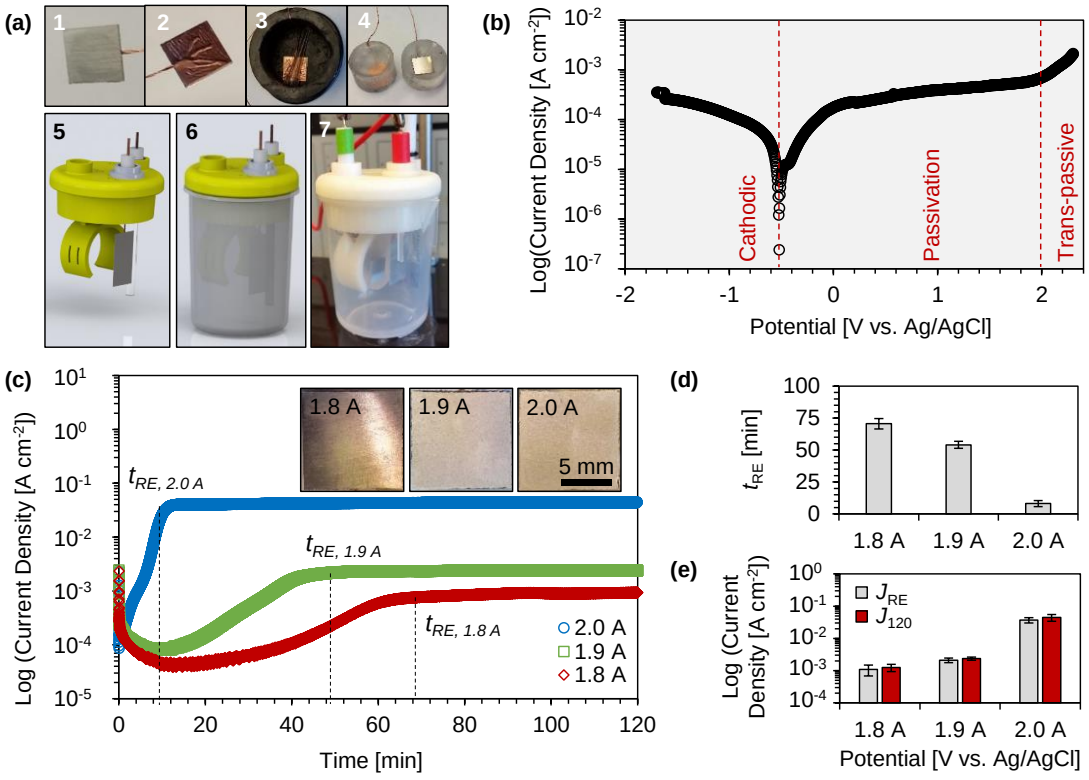

Figure 7.2: Surface and cross-sectional characterization of as-anodized Mg samples prepared at applied potentials of 1.8, 1.9, or 2.0 V vs Ag/AgCl.
(a) Montage of SEM images and corresponding EDS elemental surface distribution maps (Kα lines) for Mg and O on the anodized surface. SEM images and maps were obtained at an original magnification of 150x; scale bar = 200 µm for all images and maps. Insets in the SEM images in (a) show high-magnification SEM images (40,000x original magnification) of sub-micron-scale topography on the anodized surface of each sample; scale bar = 500 nm for all SEM images (insets). (b) Surface elemental composition (at. %) quantified through EDS area analysis on (a) at 150x magnification and corresponding O/Mg at. %/at. % ratio. (c) Montage of SEM images and corresponding EDS elemental surface distribution maps (Kα lines) for Mg and O (overlay) on the cross section of the anodized samples. SEM images and maps were obtained at an original magnification of 5,000x; scale bar = 5 µm for all images and overlaid maps. The inset in the SEM image (c, 1.8) shows a high-magnification SEM image (30,000x original magnification) of the thin oxide on the surface of 1.8; scale bar = 1 µm. The thickness of each oxide (mean ±SD; denoted by double arrows) is tabulated in each SEM image.

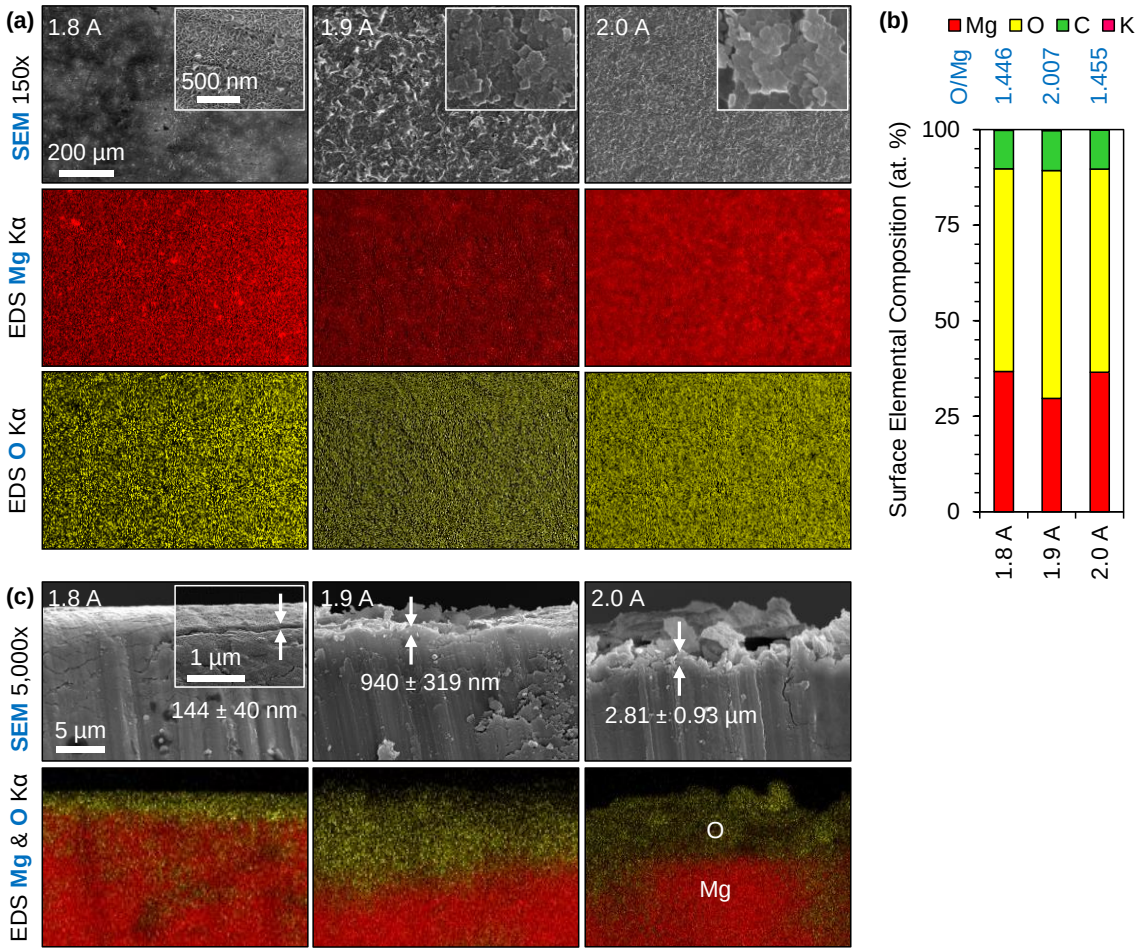

Figure 7.3: Surface characterization of anodized-annealed (AA) Mg samples. After anodization at applied potentials of 1.8, 1.9, or 2.0 V vs Ag/AgCl the anodized substrates were removed from the epoxy and annealed at 450 °C for 6 hrs (heat ramp 100 °C/Hr; cool to RT in open air). (a) Montage of SEM images and corresponding EDS elemental surface distribution maps (Kα lines) for Mg and O on the AA surface. SEM images and maps were obtained at an original magnification of 150x; scale bar = 200 µm for all images and maps. Insets in the SEM images in (a) show high-magnification SEM images (40,000x original magnification) of sub-micron-scale topography on the AA surface of each sample; scale bar = 500 nm for all SEM images (insets). (b) Surface elemental composition (at. %) quantified through EDS area analysis on (a) at 150x magnification and corresponding O/Mg at. %/at. % ratio.

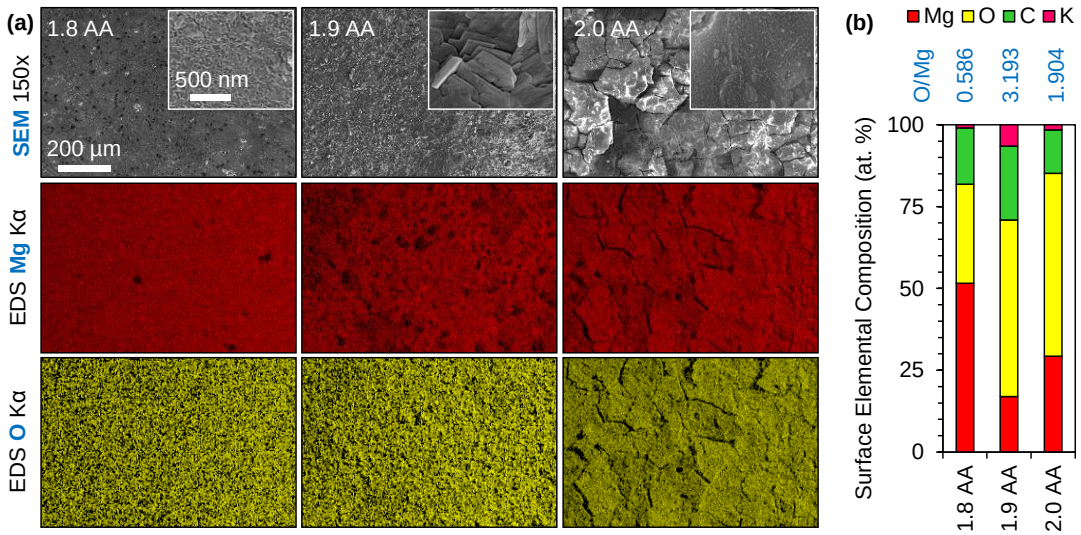

Figure 7.4: Electrode preparation and results from electrochemical polarization testing of AA Mg and pure Mg control samples.
(a) Custom-designed compression mold to re-embed AA samples in order to eliminate edge defects: 1. rendering of mold, and 2. assembled device. (b) Schematic diagram illustrating sample preparation process using the custom-designed compression mold: 1. Compression mold component layout to make electrodes for potentiodynamic polarization (PDP) measurements, 2. Electrode components were stacked on each other and held in place by the compressive force applied by the lid of the mold, 3. Epoxy resin was added and cured to encapsulate the electronic components and the PDMS stamp isolated a circular region on the electrode to yield the working surface, and 4. Re-embedded samples used for PDP measurements. The Ø25.4 mm diameter was used to make the electrodes compatible with the custom-designed electrode holder (Figure 1), while the working surface (Ø8 mm; 0.50 cm^2 exposed area) was constrained by the 10x10 mm AA or pure Mg substrate. The same process was used to prepare the samples for immersion or cytocompatibility (without a wire or copper tape) and were encapsulated by a square 14x14 mm mold for compatibility with standard 12-well tissue culture plates. (c) PDP response of AA Mg and pure Mg control re-embedded samples using rSBF at 37 °C as the electrolyte. Inset in (c) shows secondary anodic oxidation region in AA samples. Optical photographs show samples after PDP measurements; scale bar = 4 mm for all images. (d) and (e) corrosion potential and corrosion current density, respectively, of AA Mg and pure Mg control re-embedded samples obtained from Tafel extrapolation (ASTM G102-89) of PDP curves; values are mean ± SD, n = 3, *p < 0.05.

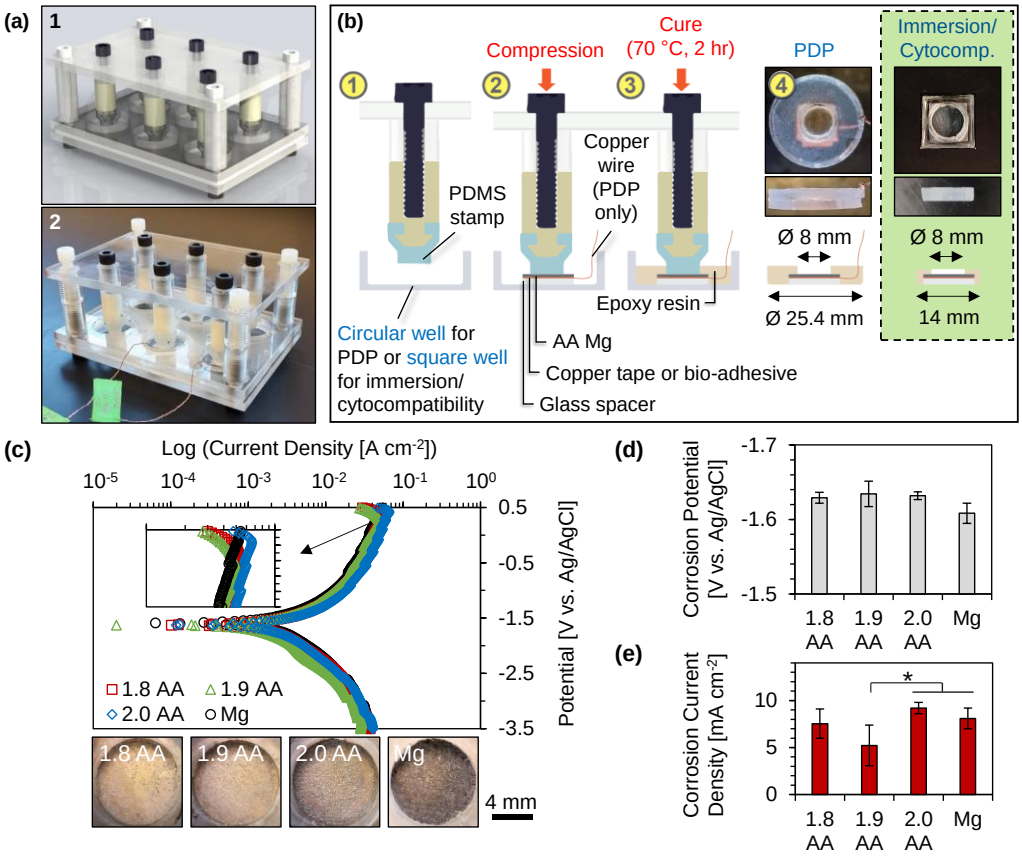

Figure 7.5: The degradation of 1.9 AA and pure Mg control samples through immersion in rSBF for 9 days (216 hrs) under standard cell culture conditions. Glass samples were used as a reference material, and rSBF-only was used as a blank reference. (a) Optical photographs of the samples at select time points during the immersion study. Top two rows are photos of the samples immersed in rSBF (to show hydrogen gas evolution), while the two bottom rows are photos of the samples with the rSBF removed (to show corrosion on the sample surface). The "Dry" samples were dried at 37 °C for two days before imaging. Scale bar = 4 mm for all images. Measured (b) pH, (c) $[Mg^{2+}]$, and (d) $[Ca^{2+}]$ of the collected media from each incubation interval with each sample. At each prescribed time point, the immersion rSBF was collected and replenished with fresh solution. (e) SEM images (150x original magnification) of the 1.9 AA and pure Mg control samples at the conclusion of the immersion study. Scale bar = 250 µm for both images. M_f/M_o is the ratio of the final/initial dry mass of each sample. (f) Surface elemental composition (at. %) quantified through EDS area analysis on (e) at 150x magnification. All values are mean ± SD, n = 3; *$p < 0.05$, **$p < 0.01$, and ***$p < 0.001$ for 1.9 AA compared with pure Mg control.

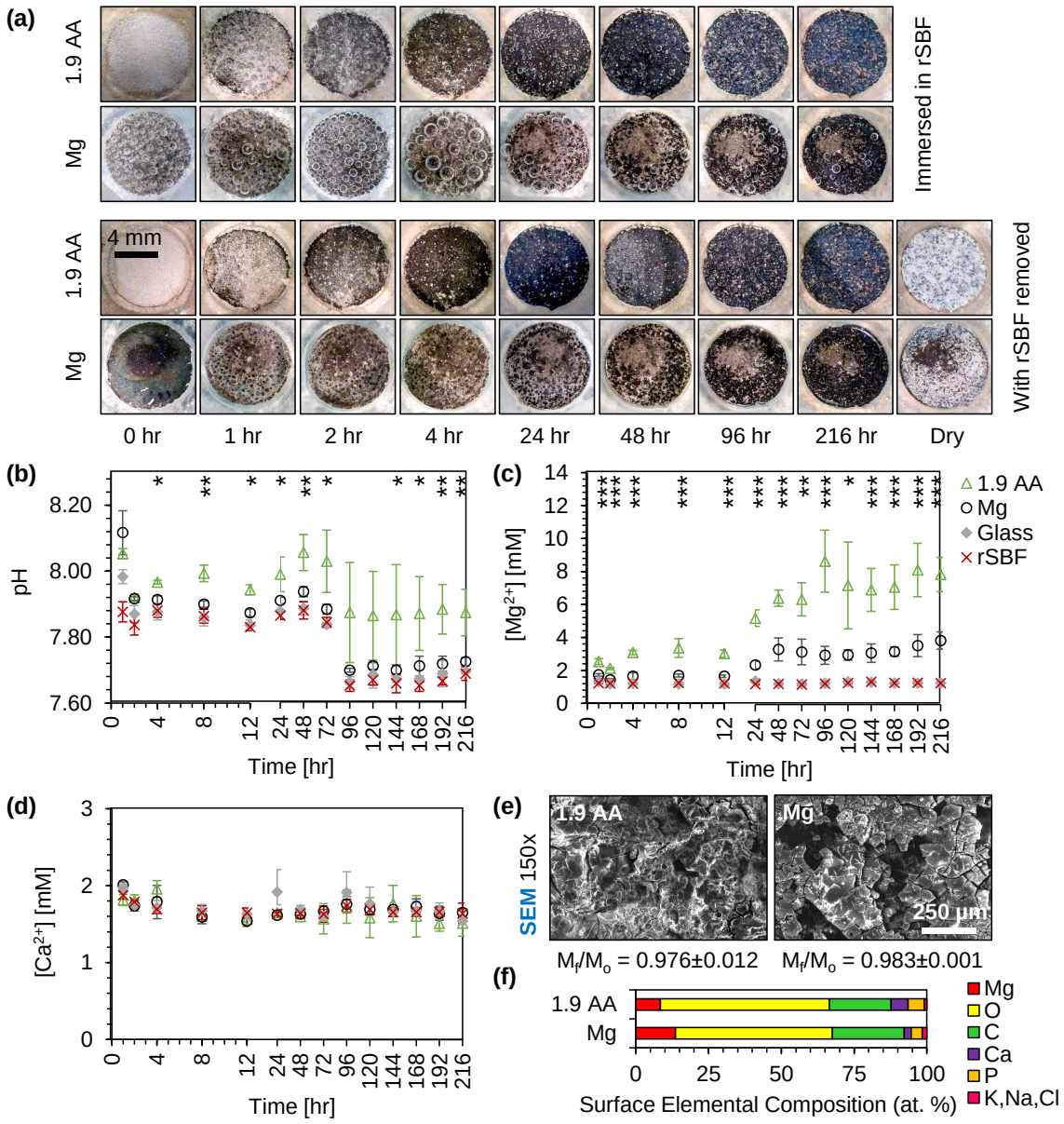
(a)
1.9 AA
Mg
Immersed in rSBF
4 mm
With rSBF removed
0 hr
1 hr
2 hr
4 hr
24 hr
48 hr
96 hr
216 hr
Dry
(b)
pH
Time [hr]
(c)
[Mg2+] [mM]
Time [hr]
1.9 AA
Mg
Glass
rSBF
(d)
[Ca2+] [mM]
Time [hr]
(e)
SEM 150x
1.9 AA
Mg
250 μm
Mf/Mo = 0.976±0.012
Mf/Mo = 0.983±0.001
(f)
1.9 AA
Mg
Surface Elemental Composition (at. %)
Mg
O
C
Ca
P
K,Na,Cl

Figure 7.6: The degradation of 1.9 AA and pure Mg control samples through immersion in DMEM for 9 days (216 hrs) under standard cell culture conditions. Glass samples were used as a reference material, and DMEM-only was used as a blank reference. (a) Optical photographs of the samples at select time points during the immersion study. Top two rows are photos of the samples immersed in DMEM (to show hydrogen gas evolution), while the two bottom rows are photos of the samples with the DMEM removed (to show corrosion on the sample surface). The "Dry" samples were dried at 37 °C for two days before imaging. Scale bar = 4 mm for all images. Measured (b) pH, (c) $[Mg^{2+}]$, and (d) $[Ca^{2+}]$ of the collected media from each incubation interval with each sample. At each prescribed time point, the immersion DMEM was collected and replenished with fresh solution. (e) SEM images (150x and 15,000x original magnification) of the 1.9 AA and pure Mg control samples at the conclusion of the immersion study. Scale bar = 250 µm and 2 µm for 150x and 15,000x images, respectively. M_f/M_o is the ratio of the final/initial dry mass of each sample. (f) Surface elemental composition (at. %) quantified through EDS area analysis on (e) at 150x magnification. All values are mean ± SD, n = 4; *$p < 0.05$, **$p < 0.01$, and ***$p < 0.001$ for 1.9 AA compared with the pure Mg control.

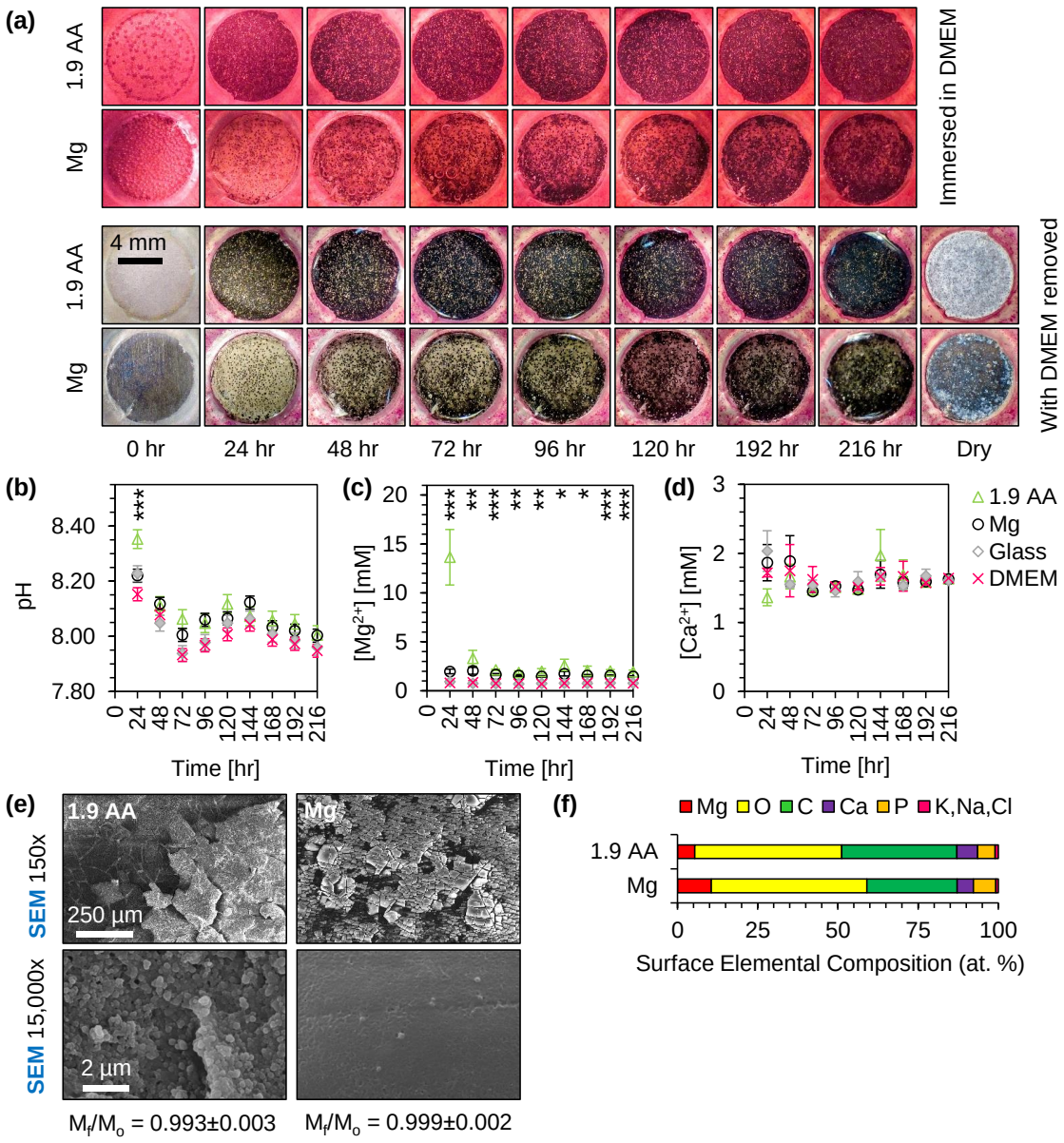
(a)
1.9 AA
Mg
Immersed in DMEM
4 mm
With DMEM removed
0 hr
24 hr
48 hr
72 hr
96 hr
120 hr
192 hr
216 hr
Dry
(b)
pH
Time [hr]
(c)
[Mg2+] [mM]
Time [hr]
(d)
[Ca2+] [mM]
Time [hr]
1.9 AA
Mg
Glass
DMEM
(e)
SEM 150x
SEM 15,000x
250 µm
2 µm
Mf/Mo = 0.993±0.003
Mf/Mo = 0.999±0.002
(f)
Mg O C Ca P K,Na,Cl
Surface Elemental Composition (at. %)

Figure 7.7: Cross-sectional analysis after the degradation of 1.9 AA and pure Mg control samples through immersion in (a) rSBF or (b) DMEM for 9 days (216 hrs) under standard cell culture conditions.
(a) and (b) are montages of SEM images and corresponding EDS elemental surface distribution maps (Kα lines) for Mg and O (overlay), Ca, and P on the cross section of the degraded samples. SEM images and maps were obtained at an original magnification of 500x; scale bar = 100 µm for all images and maps. The thickness of each oxide (mean ±SD; denoted by double arrows) is tabulated in each SEM image.

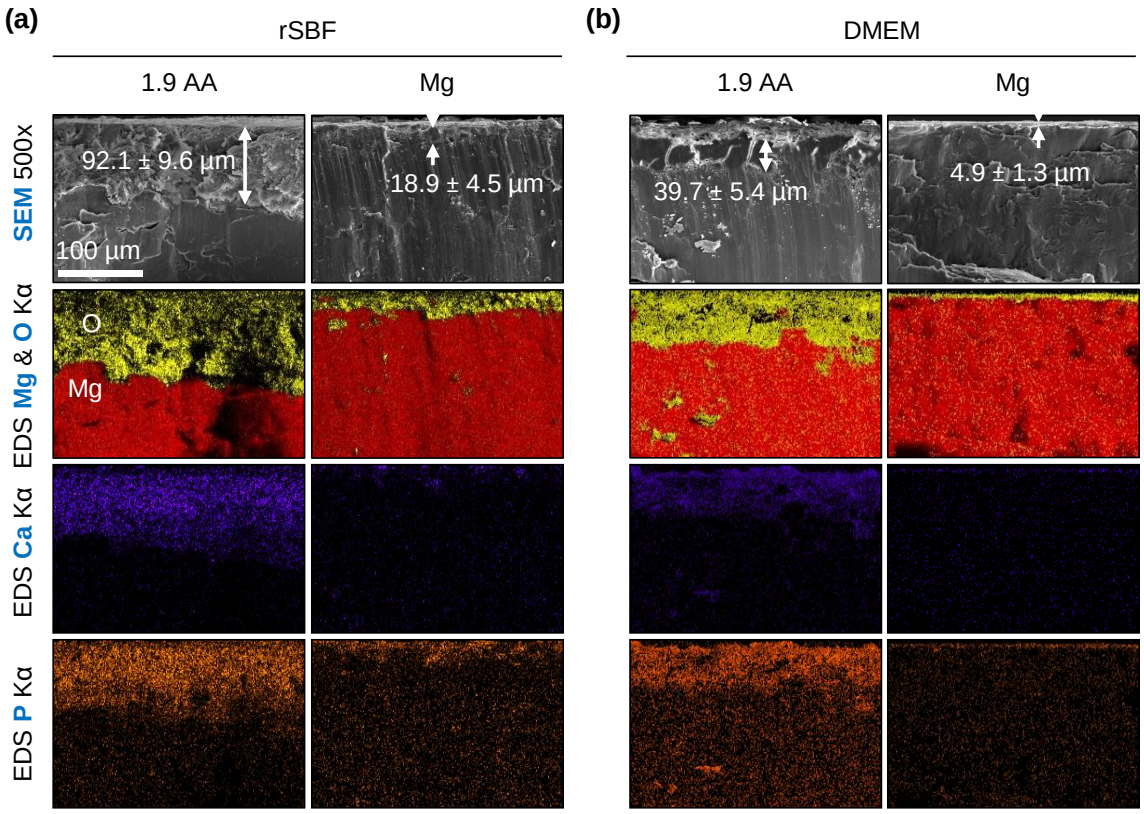

Figure 7.8: The cytocompatibility of 1.9 AA and pure Mg control samples in the direct culture with BMSCs in DMEM for 24 hrs.
Glass samples were used as a reference material, BMSC-only was used as the positive control, and DMEM-only was used as a blank reference. (a) Optical photographs of the samples during the cytocompatibility study. The photos of the samples immersed in DMEM show hydrogen gas evolution. The "Dry" samples were dried at 37 °C for two days before imaging. Scale bar = 4 mm for all images. (b) Change in mass of the samples. M_f/M_o is the ratio of the final/initial dry mass of each sample. Measured (c) pH and (d) solubilized ionic concentrations ($[Mg^{2+}]$ and $[Ca^{2+}]$) of the collected BMSC culture media incubated with each sample. (e) Fluorescence images of BMSCs adhered on the culture plates surrounding the samples. Blue color indicates DAPI stained nuclei and green color indicates Alexa Fluor® 488-phalloidin stained F-actin (cytoskeleton). Scale bar = 200 µm for all images. Original magnification: 10x. (f) BMSC adhesion density directly on the sample surface (Sample) or on the culture plates surrounding the samples (Plate). Values in (b), (c), and (d) are mean ± SD, n = 4; values in (f) are mean ± SE; n = 4; *$p < 0.05$, ***$p < 0.001$, ‡$p = 0.06$.

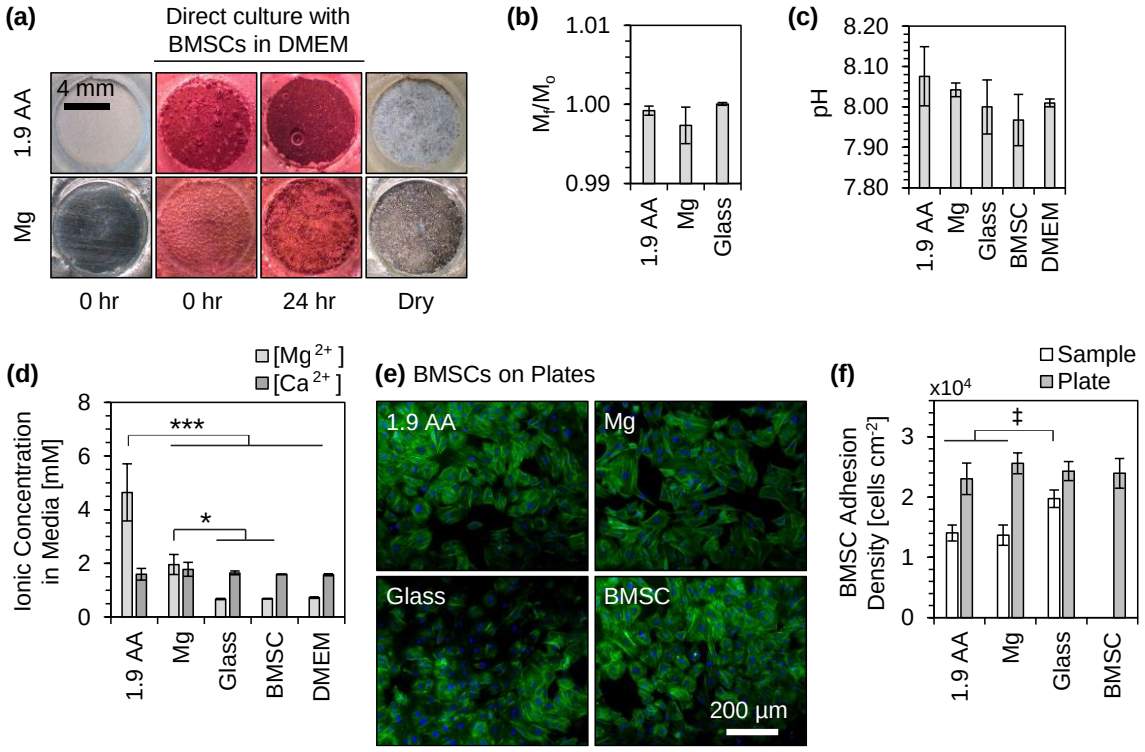

Figure 7.9: Cell-biomaterial characterization of 1.9 AA and pure Mg control samples after the direct culture with BMSCs in DMEM for 24 hrs.
Glass samples were used as a reference material. (a) Overlay of SEM images and corresponding EDS elemental surface distribution color mapping (Kα lines) for: Mg (red), C (green), O (yellow), Ca (purple), P (orange), Si (white), and Na, K, and Cl (pink). The SEM/EDS images were obtained at an original magnification of: 150x with scale bar = 200 µm (top row), and 1,000x with scale bar = 20 µm (bottom row). Insets in the bottom row are SEM images taken at 5,000x original magnification with scale bar = 5 µm for all images. The color key in (a, top row, Mg) is the same for all 1.9 AA and Mg SEM/EDS images. (b) Surface elemental composition (at. %) based on EDS quantification on 150x images (a, top row).

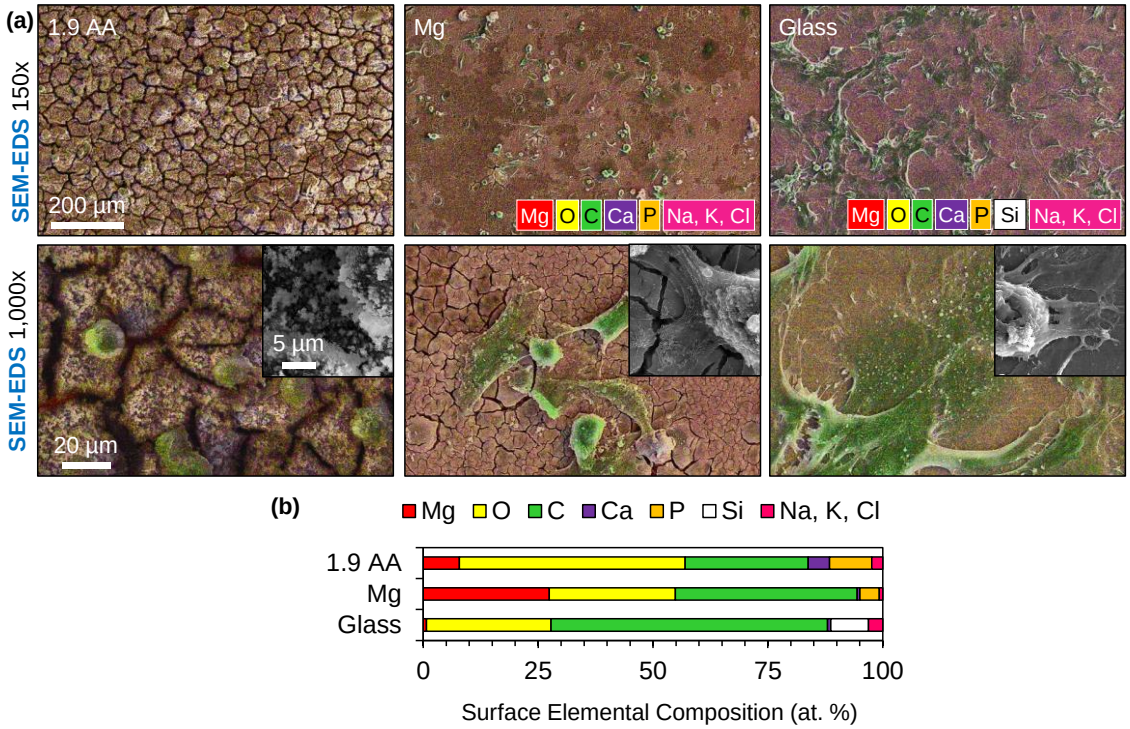

Figure 7.10: Average daily *in vitro* degradation rates (mass loss rates) of 1.9 AA and pure Mg control samples relative to the initial surface area (SA_0).
The average daily *in vitro* degradation rates were calculated from Mg^{2+} ion concentration in media and averaged over the total incubation time for each medium (i.e., 9 days in rSBF and DMEM, or 1 day for BMSC+DMEM). Values are mean ± SD, n=3 for experiments in rSBF, and n = 4 for experiments in DMEM and BMSC+DMEM; *$p < 0.05$, and ***$p < 0.001$.

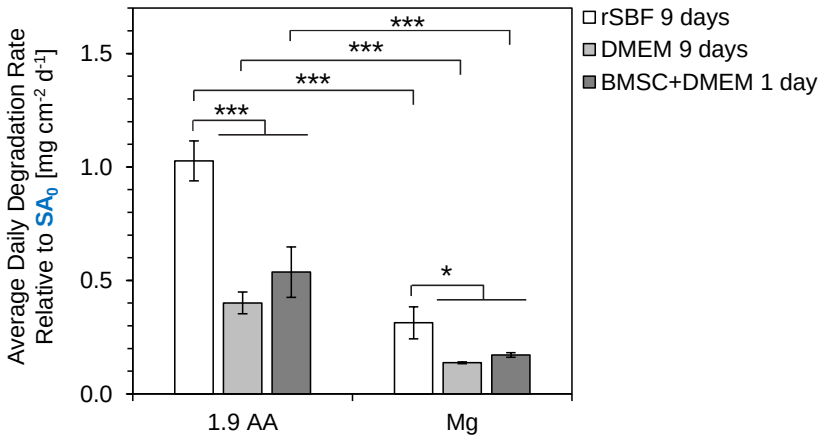

Table 7.1: Results from ANOVA on measured pH and [Mg^{2+}] in collected r-SBF during 9 day immersion. Post hoc results only for the comparison between 1.9 AA and Mg control.

	Time point [hrs]	Family-wise statistics summary	*Post hoc* pairwise comparison (measured values, mean±SD)	p value
pH	4	$F(3, 8) = 17.435$, $p = 7.205 \times 10^{-4}$	1.9 AA (8.05±0.02) > Mg (8.12±0.07)	$p < 0.05$
	8	$F(3, 8) = 24.827$, $p = 2.092 \times 10^{-4}$	1.9 AA (7.92±0.01) > Mg (7.92±0.01)	$p < 0.01$
	12	$F(3, 8) = 20.556$, $p = 4.078 \times 10^{-4}$	1.9 AA (7.97±0.01) > Mg (7.91±0.01)	$p < 0.05$
	24	$F(3, 8) = 10.866$, $p = 3.405 \times 10^{-3}$	1.9 AA (7.99±0.03) > Mg (7.90±0.01)	$p < 0.05$
	48	$F(3, 8) = 18.242$, $p = 6.169 \times 10^{-4}$	1.9 AA (7.94±0.02) > Mg (7.87±0.01)	$p < 0.01$
	72	$F(3, 8) = 10.162$, $p = 4.194 \times 10^{-3}$	1.9 AA (7.99±0.05) > Mg (7.91±0.01)	$p < 0.05$
	144	$F(3, 8) = 7.820$, $p = 9.182 \times 10^{-3}$	1.9 AA (8.06±0.06) > Mg (7.94±0.02)	$p < 0.05$
	168	$F(3, 8) = 8.543$, $p = 7.09 \times 10^{-3}$	1.9 AA (8.03±0.10) > Mg (7.88±0.02)	$p < 0.05$
	192	$F(3, 8) = 14.831$, $p = 1.244 \times 10^{-3}$	1.9 AA (7.87±0.15) > Mg (7.70±0.02)	$p < 0.01$
	216	$F(3, 8) = 16.337$, $p = 8.989 \times 10^{-4}$	1.9 AA (7.87±0.11) > Mg (7.71±0.03)	$p < 0.01$
[Mg^{2+}] [mM]	1	$F(3, 8) = 99.526$, $p = 1.129 \times 10^{-6}$	1.9 AA (2.54±0.18) > Mg (1.72±0.08)	$p < 0.001$
	2	$F(3, 8) = 166.17$, $p = 1.522 \times 10^{-7}$	1.9 AA (2.12±0.06) > Mg (1.43±0.07)	$p < 0.001$
	4	$F(3, 8) = 142.37$, $p = 2.791 \times 10^{-7}$	1.9 AA (3.08±0.12) > Mg (1.64±0.22)	$p < 0.001$
	8	$F(3, 8) = 38.793$, $p = 4.102 \times 10^{-5}$	1.9 AA (3.36±0.56) > Mg (1.69±0.09)	$p < 0.001$
	12	$F(3, 8) = 154.07$, $p = 2.048 \times 10^{-7}$	1.9 AA (3.02±0.22) > Mg (1.65±0.07)	$p < 0.001$
	24	$F(3, 8) = 121.12$, $p = 5.255 \times 10^{-7}$	1.9 AA (5.26±0.51) > Mg (2.41±0.24)	$p < 0.001$
	48	$F(3, 8) = 98.781$, $p = 1.162 \times 10^{-6}$	1.9 AA (6.48±0.50) > Mg (3.36±0.70)	$p < 0.001$
	72	$F(3, 8) = 43.733$, $p = 2.622 \times 10^{-5}$	1.9 AA (6.41±1.01) > Mg (3.20±0.78)	$p < 0.01$
	96	$F(3, 8) = 38.451$, $p = 4.239 \times 10^{-5}$	1.9 AA (8.74±1.89) > Mg (3.01±0.55)	$p < 0.001$
	120	$F(3, 8) = 13.134$, $p = 1.856 \times 10^{-3}$	1.9 AA (7.26±2.64) > Mg (3.02±0.32)	$p < 0.05$
	144	$F(3, 8) = 41.661$, $p = 3.144 \times 10^{-5}$	1.9 AA (6.99±1.30) > Mg (3.14±0.56)	$p < 0.001$
	168	$F(3, 8) = 47.625$, $p = 1.959 \times 10^{-5}$	1.9 AA (7.15±1.36) > Mg (3.23±0.28)	$p < 0.001$
	192	$F(3, 8) = 40.756$, $p = 3.413 \times 10^{-5}$	1.9 AA (8.20±1.62) > Mg (3.60±0.67)	$p < 0.001$
	216	$F(3, 8) = 85.577$, $p = 2.027 \times 10^{-6}$	1.9 AA (7.92±1.05) > Mg (3.90±0.52)	$p < 0.001$

Table 7.2: Results from ANOVA on measured pH and [Mg^{2+}] in collected DMEM during 9 day immersion. Post hoc results only for the comparison between 1.9 AA and Mg control.

	Time point [hrs]	Family-wise statistics summary	*Post hoc* pairwise comparison (measured values, mean±SD)	p value
pH	24	$F(3, 12) = 40.568$, $p = 1.473 \times 10^{-6}$	1.9 AA (8.35±0.03) > Mg (8.22±0.03)	$p < 0.001$
[Mg^{2+}] [mM]	24	$F(3, 12) = 76.421$, $p = 4.344 \times 10^{-8}$	1.9 AA (13.65±2.84) > Mg (1.97±0.24)	$p < 0.001$
	48	$F(3, 12) = 29.015$, $p = 8.781 \times 10^{-6}$	1.9 AA (3.32±0.80) > Mg (2.04±0.36)	$p < 0.01$
	72	$F(3, 12) = 249.44$, $p = 4.502 \times 10^{-11}$	1.9 AA (2.14±0.08) > Mg (1.66±0.11)	$p < 0.001$
	96	$F(3, 12) = 153.49$, $p = 7.787 \times 10^{-10}$	1.9 AA (1.86±0.17) > Mg (1.56±0.08)	$p < 0.01$
	120	$F(3, 12) = 74.457$, $p = 5.036 \times 10^{-8}$	1.9 AA (1.99±0.27) > Mg (1.46±0.07)	$p < 0.01$
	144	$F(3, 12) = 25.837$, $p = 1.602 \times 10^{-5}$	1.9 AA (2.59±0.63) > Mg (1.75±0.25)	$p < 0.05$
	168	$F(3, 12) = 27.848$, $p = 1.087 \times 10^{-5}$	1.9 AA (2.06±0.45) > Mg (1.55±0.11)	$p < 0.05$
	192	$F(3, 12) = 200.15$, $p = 1.645 \times 10^{-10}$	1.9 AA (2.00±0.16) > Mg (1.56±0.06)	$p < 0.001$
	216	$F(3, 12) = 134.63$, $p = 1.671 \times 10^{-9}$	1.9 AA (1.94±0.17) > Mg (1.45±0.08)	$p < 0.001$

7.7. References

[1] Cipriano AF, Sallee A, Guan R-G, Zhao Z-Y, Tayoba M, Sanchez J, et al. Investigation of magnesium–zinc–calcium alloys and bone marrow derived mesenchymal stem cell response in direct culture. Acta Biomater. 2015;12:298-321.

[2] Rickard DJ, Sullivan TA, Shenker BJ, Leboy PS, Kazhdan I. Induction of Rapid Osteoblast Differentiation in Rat Bone Marrow Stromal Cell Cultures by Dexamethasone and BMP-2. Dev Bio. 1994;161:218-28.

[3] Fischer J, Pröfrock D, Hort N, Willumeit R, Feyerabend F. Reprint of: Improved cytotoxicity testing of magnesium materials. Mater Sci Eng, B. 2011;176:1773-7.

[4] Xin Y, Hu T, Chu PK. In vitro studies of biomedical magnesium alloys in a simulated physiological environment: A review. Acta Biomater. 2011;7:1452-9.

[5] Liu H. The effects of surface and biomolecules on magnesium degradation and mesenchymal stem cell adhesion. J Biomed Mater Res A. 2011;99:249-60.

[6] Johnson I, Perchy D, Liu H. In vitro evaluation of the surface effects on magnesium-yttrium alloy degradation and mesenchymal stem cell adhesion. J Biomed Mater Res A. 2011;100A:477–85.

[7] Cipriano AF, Sallee A, Guan R-G, Zhao Z-Y, Lin A, Liu H. A comparative study on the degradation of Mg-4Zn-xSr alloys and their cytocompatibility using the direct culture method. Submitted to Acta Biomaterialia. 2015.

[8] Cipriano AF, Sallee A, Guan R-G, Zhan-Yong Z, Tayoba M, Cortez MC, et al. Cytocompatibility and Early Inflammatory Response of Human Endothelial Cells in Direct Culture with Mg-Zn-Sr Alloys. Submitted to Biomaterials. 2015.

[9] Lei T, Ouyang C, Tang W, Li L-F, Zhou L-S. Preparation of MgO coatings on magnesium alloys for corrosion protection. Surf Coat Tech. 2010;204:3798-803.

[10] Lei T, Ouyang C, Tang W, Li L-F, Zhou L-S. Enhanced corrosion protection of MgO coatings on magnesium alloy deposited by an anodic electrodeposition process. Corros Sci. 2010;52:3504-8.

[11] Cai Z, Lu D, Li W, Liang Y, Zhou H. Study on anodic oxidation of magnesium in 6M KOH solution by alternative current impedance. Int J Hydrogen Energy. 2009;34:467-72.

[12] Ding Y, Zhang G, Wu H, Hai B, Wang L, Qian Y. Nanoscale Magnesium Hydroxide and Magnesium Oxide Powders: Control over Size, Shape, and Structure via Hydrothermal Synthesis. Chemistry of Materials. 2001;13:435-40.

[13] Iskandar ME, Aslani A, Liu H. The effects of nanostructured hydroxyapatite coating on the biodegradation and cytocompatibility of magnesium implants. J Biomed Mater Res, A. 2013;101A:2340-54.

[14] Cipriano AF, Zhao T, Johnson I, Guan R-G, Garcia S, Liu H. In vitro degradation of four magnesium–zinc–strontium alloys and their cytocompatibility with human embryonic stem cells. J Mater Sci Mater Med. 2013;24:989-1003.

[15] Cipriano AF, De Howitt N, Gott SC, Miller CT, Rao MP, Liu H. Bone Marrow Stromal Cell Adhesion and Morphology on Micro- and Sub-Micropatterned Titanium. J Biomed Nanotechnol. 2014;10:660-8.

[16] Bettini E, Leygraf C, Pan J. Nature of current increase for a CoCrMo alloy:" transpassive" dissolution vs. water oxidation. International Journal of Electrochemical Science. 2013;8:11791-804.

[17] Lockett V, Horne M, Sedev R, Rodopoulos T, Ralston J. Differential capacitance of the double layer at the electrode/ionic liquids interface. Physical Chemistry Chemical Physics. 2010;12:12499-512.

[18] Dubin-Thaler BJ, Giannone G, Döbereiner H-G, Sheetz MP. Nanometer Analysis of Cell Spreading on Matrix-Coated Surfaces Reveals Two Distinct Cell States and STEPs. Biophys J. 2004;86:1794-806.

[19] Sanchez AHM, Luthringer BJC, Feyerabend F, Willumeit R. Mg and Mg alloys: How comparable are in vitro and in vivo corrosion rates? A review. Acta Biomater. 2015;13:16-31.

[20] Kirkland NT, Lespagnol J, Birbilis N, Staiger MP. A survey of bio-corrosion rates of magnesium alloys. Corros Sci. 2010;52:287-91.

[21] Ono S, Kijima H, Masuko N. Microstructure and Voltage-Current Characteristics of Anodic Films Formed on Magnesium in Electrolytes Containing Fluoride. Mater Trans. 2003;44:539-45.

[22] Blawert C, Dietzel W, Ghali E, Song G. Anodizing Treatments for Magnesium Alloys and Their Effect on Corrosion Resistance in Various Environments. Adv Eng Mater. 2006;8:511-33.

[23] Song G. Control of biodegradation of biocompatable magnesium alloys. Corros Sci. 2007;49:1696-701.

[24] Hiromoto S, Shishido T, Yamamoto A, Maruyama N, Somekawa H, Mukai T. Precipitation control of calcium phosphate on pure magnesium by anodization. Corros Sci. 2008;50:2906-13.

[25] Yabuki A, Sakai M. Anodic films formed on magnesium in organic, silicate-containing electrolytes. Corros Sci. 2009;51:793-8.

[26] Hiromoto S, Yamamoto A. Control of degradation rate of bioabsorbable magnesium by anodization and steam treatment. Mater Sci Eng, C. 2010;30:1085-93.

[27] Hahn R, Brunner JG, Kunze J, Schmuki P, Virtanen S. A novel approach for the formation of Mg(OH)2/MgO nanowhiskers on magnesium: Rapid anodization in chloride containing solutions. Electrochem Commun. 2008;10:288-92.

[28] Turhan MC, Lynch RP, Jha H, Schmuki P, Virtanen S. Anodic growth of self-ordered magnesium oxy-fluoride nanoporous/tubular layers on Mg alloy (WE43). Electrochem Commun. 2010;12:796-9.

[29] Jiang HB, Kim YK, Ji JH, Park IS, Bae TS, Lee MH. Surface modification of anodized Mg in ammonium hydrogen fluoride by various voltages. Surf Coat Tech. 2014;259, Part B:310-7.

[30] Murakami K, Hino M, Nakai K, Kobayashi S, Saijo A, Kanadani T. Mechanism of Corrosion Protection of Anodized Magnesium Alloys. Mater Trans. 2008;49:1057-64.

[31] Song GL, Atrens A. Corrosion mechanisms of magnesium alloys. Adv Eng Mater. 1999;1:11-33.

[32] Song G, Atrens A. Understanding Magnesium Corrosion—A Framework for Improved Alloy Performance. Adv Eng Mater. 2003;5:837-58.

[33] Turhan MC, Lynch R, Killian MS, Virtanen S. Effect of acidic etching and fluoride treatment on corrosion performance in Mg alloy AZ91D (MgAlZn). Electrochim Acta. 2009;55:250-7.

[34] Gray JE, Luan B. Protective coatings on magnesium and its alloys — a critical review. J Alloy Compd. 2002;336:88-113.

Chapter 8 – Conclusions and future research

8.1. Summary of major conclusions

The major conclusions of this dissertation are presented in parallel to the research objectives presented in section 1.4:

1. The composition and morphology of the second phases in each of the as-cast Mg-xZn-0.5Ca alloys or Mg-4Zn-xSr (x = 0.15, 0.5, 1.0, 1.5 wt. %) alloys played pivotal roles in modulating the degradation properties. It is likely that the Zn/Sr at. % ratio, similar to the role of Zn/Ca at. %, played a critical role in the morphology and composition of second phases. Collectively, the Mg-4Zn-1.0Sr alloy showed the slowest corrosion compared with all other Mg-Zn-Sr alloys studied. Even though the anodically oxidized surface treatments on Mg did not improve the corrosion resistance in physiologically relevant solutions, the tools and processes developed can be implemented to study other coatings and surface treatments for Mg-based materials for biomedical applications.

2. The direct culture method was established to probe cellular behaviors at the dynamic cell-biomaterial interface with Mg-based materials in physiologically relevant conditions, thereby providing a more comprehensive *in vitro* method for examining bioresorbable materials compared with current standards. Factors that influence the behavior of Mg-based and/or screening ability of the direct culture method include: (i) buffer capacity (i.e. HCO_3^- concentration) of

the culture media and induced degradation rate (i.e. DMEM < mTeSR®1 < EGM^{TM}-2), (ii) sensitivity of cells to solubilized degradation by-products (i.e. BMSC < HUVEC < H9-hESC), (iii) the tolerance of cells (i.e. BMSC or HUVEC) to highly alkaline media (pH 9.0) or elevated [Mg^{2+}] (27.6 mM) without adverse effects on viability or morphology, and (iv) other cellular behavior (i.e. inflammatory response by HUVECs) in response to elevated concentrations of solubilized by-products from the alloying elements (i.e. Zn^{2+} ions).

3. The direct culture method (BMSC/DMEM for 72 hrs) was used to demonstrate that the *in vitro* degradation rates of the Mg-xZn-0.5Ca alloys were lower compared with the Mg-4Zn-xSr alloys and anodically oxidized Mg. Likewise, we demonstrated an inverse relationship between mean percent BMSC viability at the cell-biomaterial interface and alloy average daily degradation rate, which likely resulted from a degradation-induced change in surface topography and/or hydrogen gas release. Likewise, despite confirming BMSC adhesion at the interface with anodically oxidized Mg after 24 hrs, the morphology of these cells was abnormal and unhealthy (compact cell bodies with no filopodia extensions). Additionally, HUVEC adhesion at the cell-biomaterial interface showed minimal adhesion after 24 hrs of culture, which indicated a higher sensitivity of HUVECs compared with BMSCs. In contrast, solubilized by-products from the degradation of Mg-xZn-0.5Ca alloys, Mg-4Zn-xSr alloys, or anodically oxidized Mg did not cause detrimental effects on the adhesion density of BMSCs or HUVECs under *indirect contact*.

4. The Mg-4Zn-1.0Sr alloy showed a significantly faster *in vivo* degradation rate compared with commercially pure Mg control when placed as intramedullar pins in the rat tibia. Contrary to a growing body of literature, the *in vivo* degradation rate was significantly higher compared to the *in vitro* counterpart for Mg-4Zn-1.0Sr alloy and Mg intramedullar implants, suggesting that implant placement is a critical factor to consider when correlating results from *in vitro* models to *in vivo* measurements. Furthermore, host response evaluation showed for the first time that the fast-degrading Mg-4Zn-1.0Sr alloy (with resorption time of approximately 8 weeks) stimulated a significant net bone growth. However, hydrogen-gas-induced damage and improper mineral quality in the *de novo* peri-implant bone were also observed.

5. Collectively, the results and conclusions of this dissertation supported the promising potential of bioresorbable Mg-based biomaterials for musculoskeletal implant applications. It is likely that the solution that enables clinical translation of Mg-based biomaterials will be a combination of alloys, surface treatments, and/or coatings. Furthermore, this dissertation provided design guidelines and *in vitro* tools to screen and optimize: alloy composition, degradation rates, cytocompatibility, and cellular responses at the cell-biomaterial interface to fine tune Mg-based biomaterials for specific implant applications.

8.2. Future research

Future directions include utilization of the direct culture method to screen the degradation rates, cytocompatibility and cell-biomaterial interactions with other Mg alloys designed for biomedical applications, including crystalline binary Mg-xSr and ternary Mg-1Ca-xSr (x = 0.2, 0.5, 1.0, and 2.0 wt. % Sr) alloys. In doing so, we seek to create a library of alloy performance for a variety of biomedical applications. Additionally, further *in vitro* studies on long-term functions of BMSCs (e.g., osteogenic differentiation, gene expression, etc.) in response to the dynamic interface with Mg-based biomaterials will enable us to enhance the utility of the direct culture model. Likewise, we plan to optimize the direct culture *in vitro* method so that the degradation rates more accurately predict the implant-placement-specific *in vivo* behavior. Furthermore, we plan optimize the anodically oxidized surface treatments in order to enhance the corrosion resistance of Mg and Mg alloys; especially because the mode of degradation can be modulated through the implementation of this surface treatment. Moreover, we will implement the tools and methods used to synthesize and characterize the anodically oxidized Mg to generate a variety of coatings including electrophoretic deposition of MgO nanoparticles and graphene-based layers, which can be used biomedical implant or sensor applications.